

## INFORMATION TO USERS

This manuscript has been reproduced from the microfilm master. UMI films the text directly from the original or copy submitted. Thus, some thesis and dissertation copies are in typewriter face, while others may be from any type of computer printer.

**The quality of this reproduction is dependent upon the quality of the copy submitted.** Broken or indistinct print, colored or poor quality illustrations and photographs, print bleedthrough, substandard margins, and improper alignment can adversely affect reproduction.

In the unlikely event that the author did not send UMI a complete manuscript and there are missing pages, these will be noted. Also, if unauthorized copyright material had to be removed, a note will indicate the deletion.

Oversize materials (e.g., maps, drawings, charts) are reproduced by sectioning the original, beginning at the upper left-hand corner and continuing from left to right in equal sections with small overlaps. Each original is also photographed in one exposure and is included in reduced form at the back of the book.

Photographs included in the original manuscript have been reproduced xerographically in this copy. Higher quality 6" x 9" black and white photographic prints are available for any photographs or illustrations appearing in this copy for an additional charge. Contact UMI directly to order.

U·M·I

University Microfilms International  
A Bell & Howell Information Company  
300 North Zeeb Road, Ann Arbor, MI 48106-1346 USA  
313/761-4700 800/521-0600



Order Number 9509404

**Bedload transport of mixed-size sediments by wind**

Shaw, Susan Calder, Ph.D.

University of Washington, 1994

Copyright ©1994 by Shaw, Susan Calder. All rights reserved.

**U·M·I**  
300 N. Zeeb Rd.  
Ann Arbor, MI 48106



**BEDLOAD TRANSPORT OF MIXED-SIZE SEDIMENTS**

**BY WIND**

**by**

**Susan Calder Shaw**

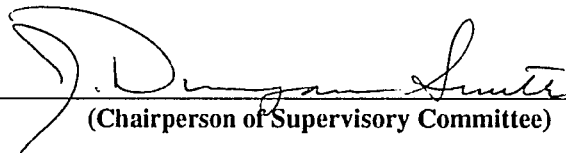
**A dissertation submitted in partial fulfillment  
of the requirements for the degree of**

**Doctor of Philosophy**

**University of Washington**

**1994**

Approved by \_\_\_\_\_

  
(Chairperson of Supervisory Committee)

Program Authorized  
to Offer Degree \_\_\_\_\_

Department of Geological Sciences

Date \_\_\_\_\_

June 3, 1994

© Copyright 1994

Susan Calder Shaw

**Doctoral Dissertation**

In presenting this dissertation in partial fulfillment of the requirements for the Doctoral degree at the University of Washington, I agree that the Library shall make its copies freely available for inspection. I further agree that extensive copying of this dissertation is allowable only for scholarly purposes, consistent with "fair use" as prescribed in the U.S. Copyright Law. Requests for copying or reproduction of this dissertation may be referred to University Microfilms, 1490 Eisenhower Place, P.O. Box 975, Ann Arbor, MI 48106, to whom the author has granted "the right to reproduce and sell (a) copies of the manuscript in microform and/or (b) printed copies of the manuscript made from microform".

Signature *Susan Calder Braun*

Date *June 3, 1994*

University of Washington

Abstract

**BEDLOAD TRANSPORT OF MIXED-SIZE SEDIMENTS BY WIND**

by Susan Calder Shaw

Chairperson of the Supervisory Committee: Professor J. Dungan Smith  
Department of Geological Sciences

Natural sediments contain a range of particle sizes. The physics of bedload transport of natural sediment, therefore, is complicated by variability in response to the fluid of the different grain-size fractions in motion, and by the nature of the collisions between moving grains and particles of disparate mass composing the sediment bed. This work presents a theoretical model capable of predicting the mechanics of motion of poorly sorted sediments in the bedload layer and the evolution of particle-scale topography of the sediment surface. The model consists of four components that are coupled to predict the bedload-transport rates of grain-size fractions within a mixture. They are: (1) a computer-generated sediment bed that reproduces the grain size-frequency distribution and fully characterizes the physical properties of both the bed surface and subsurface; (2) a saltation component that describes the ballistic trajectories of moving grains; (3) a collisional algorithm that treats the behavior of grain-grain interactions at the bed in the presence of fluid forces on the grains, by tracking the position of each moving grain relative to the sediment surface, such that the exact location and geometric configuration of the collision site is known; and, (4) a fluid-mechanical element that predicts the extraction of momentum from the wind by each grain-size fraction and by the entire saltating mass, as a function of position in the flow. The model can be used to predict bedload-discharge rates for a large range of flow conditions, sediment properties, and grain-size frequency distributions, and, thereby, permits reliable computation of sediment fluxes beyond the range of available experimental data.

Bedload flux of the sediment mixture is determined by calculating the product of particle velocity times grain concentration for each size fraction and integrating over the height of the bedload layer to yield volume discharges of each fraction; the total bedload flux is the sum of the fluxes for each grain-size fraction. Model predictions compare well with measurements made by Yamasaka and Ikeda (1988) for the same grain-size frequency distribution. A bedload-transport



equation, derived from regressions on model-predicted, fractional transport rates, is presented for use in calculating size-by-size and bulk sediment fluxes.

Model predictions of grain saltation parameters, including particle lift-off speeds and angles, agree with empirical data on particle motion in granular mixtures. The model quantifies some of the experimental observations of mixed-size sediment transport that have been discussed qualitatively in the literature, including modifications of grain-collision behavior with variations in surface sorting, and it lays the foundation for examination of the origin and characteristics of eolian sedimentary structures. It also predicts significant variations in transport rates and collision histories between homogeneous and inhomogeneous sediment mixtures, particularly at low transport rates. The demonstrated sensitivity of grain-bed and grain-fluid interactions to the size-frequency distribution of the sediment mixture emphasizes the importance of accurately accounting for grain-size variations in numerical models of processes involving heterogeneous sediments.

## TABLE OF CONTENTS

LIST OF FIGURES .....	iii
LIST OF TABLES .....	vi
1. INTRODUCTION .....	1
1.1 Mixed-grain sediment-transport systems .....	2
1.2 Need for a theoretical model to describe mixed-grain sediment transport .....	5
1.3 Components of the model .....	7
2. THE SEDIMENT BED .....	12
2.1 Grain-size distributions .....	15
2.2 Bed-generation algorithm .....	24
2.3 Characteristics of the sediment surface .....	33
2.4 Comparison with measured sediment beds .....	46
2.5 Summary .....	59
3. THE FLUID MECHANICS OF EOLIAN SEDIMENT-TRANSPORTING FLOWS .....	63
3.1 Effects of bed roughness .....	65
3.2 Form of the wind-velocity profile .....	79
3.3 Momentum extraction from the wind by mixed-size grains .....	83
3.4 Numerical modelling approach. I: Saltation of mixed-size grains .....	85
3.5 Numerical modelling approach. II: Setting the boundary conditions .....	92
3.6 Numerical modelling approach. III: Quantifying momentum extraction .....	105
3.7 Calculated momentum-extraction profiles .....	116
3.8 Summary .....	136

4. GRAIN COLLISIONS WITH THE BED .....	140
4.1 Numerical model of mixed-grain collisions .....	142
4.2 Model predictions of collisional dynamics .....	157
4.3 Comparison with measured statistics .....	192
4.4 Summary .....	197
5. MODEL CALCULATIONS OF MIXED-GRAIN BEDLOAD TRANSPORT .....	201
5.1 Theoretical calculations of bedload transport .....	203
5.2 Comparison of calculated fluxes with bedload-transport measurements .....	206
5.3 Summary .....	218
6. SUMMARY AND CONCLUSIONS .....	219
LIST OF REFERENCES .....	227

## LIST OF FIGURES

Number	Page
2.1 Grain-frequency distribution data .....	16
2.2 Grain-size distribution predicted by model, Great Sand Dunes sample .....	20
2.3 Grain-size distribution predicted by model, wind-tunnel experimental sample .....	22
2.4 Relationship between particle angle-of-repose and grain size .....	26
2.5 Initial construction of a computer-generated sediment bed .....	28
2.6 Geometric relationships between grains composing the sediment bed .....	30
2.7 Example of a computer-generated sediment bed .....	32
2.8 Sediment-bed section prior to fluid flow .....	34
2.9 Force balance on a grain resting on the bed .....	36
2.10 Grain clusters formed on the computer-generated bed surface .....	40
2.11 Evolution of the sediment-bed surface with increasing fluid shear .....	41
2.12 Representative bed section used to calculate grain angles-of-repose .....	49
2.13 Calculated grain angles-of-repose .....	50
2.14 Comparison of calculated grain angles-of-repose with Miller and Byrne data .....	53
2.15 Comparison of calculated grain angles-of-repose with Kirchner <i>et al.</i> data .....	54
2.16 Calculated grain pocket-geometry angles of the bed interior .....	57
2.17 Porosity characteristics of the sediment-bed interior .....	58
3.1 Computer-generated sediment bed used for transport calculations .....	67
3.2 Fluid-mechanical surface ( $z = 0$ ) of computer-generated bed .....	74
3.3 Velocity profile over the nonmoving, poorly sorted bed .....	77
3.4 Velocity profile over the nonmoving surface, with viscous-sublayer correction .....	81
3.5 Velocity profiles of the flow interior, sediment-transport layer, and near-bed region .....	82
3.6 Typical trajectory of a grain saltating across the poorly sorted sediment bed .....	89

3.7 Model predictions of the critical shear stress for initiation of grain saltation .....	98
3.8 Dependency of the critical shear stress of saltation on grain size and transport stage .....	102
3.9 Predicted vertical profiles of sediment concentration, drag force, and the product $F_*C_*$ .....	111
3.10 Curve smoothing applied to momentum-extraction profiles .....	120
3.11 Momentum-extraction profiles of individual grains transported over mixed-grain bed .....	122
3.12 Momentum-extraction profiles of each grain-size fraction normalized by $D_{50}$ .....	123
3.13 Momentum-extraction profiles of representative size fractions within the mixture .....	125
3.14 Momentum-extraction profile of the mixture and examples of curve iteration .....	128
3.15 Comparison of momentum-extraction profiles at successive transport stages .....	129
3.16 Relationships of momentum extraction, transport stage, and height of the bedload layer .....	131
3.17 Comparison of momentum-extraction profiles for uniform and mixed-size mixtures .....	133
3.18 Variations in wind-velocity profiles with changes in amount of momentum extraction .....	135
4.1 Collision geometry between a moving grain and the poorly sorted sediment surface .....	144
4.2 Predicted modes of grain transport across a poorly sorted bed .....	160
4.3 Predicted grain impact speeds vs. lift-off speeds for the sediment mixture .....	165
4.4 Examples of predicted collisions between moving grains and grains composing the bed .....	168
4.5 Predicted outcomes of collisions between uni-sized grains .....	174
4.6 Predicted outcomes of collisions between grains of unequal size .....	175
4.7 Comparison of impact speeds for a grain colliding with a mixed-size vs. uni-sized bed....	177
4.8 Comparison of lift-off speeds for a grain colliding with a mixed-size vs. uni-sized bed ...	178
4.9 Comparison of hop heights for a grain colliding with a mixed-size vs. uni-sized bed .....	179
4.10 Comparison of hop lengths for a grain colliding with a mixed-size vs. uni-sized bed ....	180
4.11 Comparison of impact angles for a grain colliding with a mixed-size vs. uni-sized bed .....	181
4.12 Comparison of lift-off angles for a grain colliding with a mixed-size vs. uni-sized bed .....	182
4.13 Comparison of impact speeds for three size fractions composing the sediment mixture .....	185
4.14 Comparison of lift-off speeds for three size fractions composing the sediment mixture .....	186
4.15 Comparison of hop heights for three size fractions composing the sediment mixture ....	187

4.16 Comparison of the number of trajectories per sequence for three size fractions .....	190
4.17 Comparison of total distance travelled per grain for three size fractions .....	191
4.18 Comparison of impact and lift-off speeds for $D_{50}$ grains at three transport stages .....	193
5.1 Measured bedload-transport rates for size fractions of a poorly sorted mixture .....	208
5.2 Measured bedload-transport rates, replotted in terms of the transport stage .....	211
5.3 Comparison of measured and model-predicted bedload-transport rates .....	212
5.4 Bedload-transport curves derived for model-predicted results using equation 5.6 .....	214
5.5 Comparison of mixed-size bulk transport rates with uniform-size transport rates .....	216

## LIST OF TABLES

Number	Page
2.1 Comparison of empirical and model-predicted sediment-bed porosities .....	60
4.1 Sizes of saltating grains relative to the sizes of grains they eject from the bed .....	171
4.2 Comparison of measured and model-predicted statistics of grain-grain collisions .....	195
5.1 Comparison of semi-empirical and model-predicted shear stress values .....	209

## ACKNOWLEDGMENTS

I have been very fortunate to have had four excellent advisors during my education: my father, Bill Calder, who first introduced me to science during many years of field adventures in remote places, captured my imagination with natural history lessons, and taught me patience and perseverance in research endeavors; my undergraduate advisor, Andrew Knoll, who educated me in the rigors of independent research and what it takes to be a good teacher; Patricia Wiberg, who has shared her time over many years and miles to teach me computer and quantitative methods, and who also freely shared ideas, numerical algorithms, and friendship; and hardly least, my advisor Jim Smith, whose guidance, support, and encouragement have been unsurpassed. I sincerely thank Jim for his exceptional teaching and his strong friendship. I would also like to thank my graduate faculty representative, Estella Leopold, who has been an enthusiastic supporter and advisor, and a source of much inspiration. I am indebted to committee members Patricia Wiberg and David Jay, who have been very supportive with advice, financial backing, and technical assistance, and who provided valuable editorial comments on this dissertation. I owe a great deal of thanks to committee members Tom Dunne, Bernard Hallet, and Jody Bourgeois for their encouragement, support, and the numerous great field trips they each have led. I have learned a great deal from all of you. My employers at the Washington Department of Natural Resources have been exceptionally supportive of my graduate school endeavors, graciously allowing me many months of leave time to complete my dissertation. I thank my many colleagues there for being so encouraging of my personal goals and for their reminders regarding the importance of humor. Many fellow graduate students and friends have contributed to the contents and the culmination of this work. I particularly would like to thank Nathan Schumaker, who helped me set up a deluxe computing facility in the backwoods of the Olympic Peninsula. I also appreciate the help and friendship of Leal Mertes, Rob Thomas, Liane White, Scott Horton, the Young-Bergs, and the many other colleagues and close friends. I could not have accomplished this work without the unquestioning support and love of my family - the Calders, Shaws, Stapletons, and Cranes - and my husband, David, who deserves a second Ph.D. for helping me through this one. This work was supported in part by NSF grants OCE-8310712 and OCE-8700659, a Chevron Graduate Scholarship, and a Graduate Faculty Fellowship from the Department of Geological Sciences, University of Washington.



## **DEDICATION**

to my parents, Bill and Lorene,  
and to my brother, Bill,  
for all the adventures among the elephantheads and monkeyflowers -  
thanks for showing me the way;

and to David,  
for new adventures at the top of the forest canopy -  
thanks for helping me stay that way.

## Chapter 1: Introduction

During the last decade, the number of studies dealing with windblown sediments has increased dramatically and contributed to a greater understanding of the physical processes associated with erosion, transport, and deposition in eolian environments. With rising worldwide concerns over desertification and the finite capacity of hydrocarbon reserves in eolian stratigraphic traps, among other critical resource considerations, the field of eolian studies has evolved into a multidisciplinary one, with researchers from diverse earth- and life- science fields seeking to define better the basic dynamics of eolian processes. The number of new books and edited conference proceedings produced in the last few years (e.g. Barndorff-Nielsen *et al.*, 1985a; Nickling, 1986; El-Baz and Hassan, 1986; Frostick and Reid, 1987; Kocurek, 1988; Hesp and Fryberger, 1988; Siever, 1988; Thomas, 1989; Fryberger *et al.*, 1990; Nordstrom, 1990; Pye and Tsoar, 1990; Barndorff-Nielsen and Willetts, 1991) attests to the rapid expansion of basic and applied eolian research. Covered in these volumes is a broad range of topics, from the physics of sand and dust erosion, transport, deposition and diagenesis, to recent advances in the sedimentology and mineralogy of windblown deposits, geomorphology of modern bedforms and landforms on Earth and other planets, dynamics of ecological change in eolian systems, impact of human activity on natural processes, micrometeorology of eolian environments, reconstruction of past depositional settings, and particle-fluid dynamical interpretations of eolian sedimentary structures.

Numerical modelling of transport and deposition phenomena on a sand-particle scale has contributed significantly to the understanding of grain motion and aerodynamics over plane beds and individual, simple, small-scale bedforms. These studies have relied largely on wind-tunnel measurements of grain movement and transport rates for their motivation and verification. Thus far, physically and mathematically based models of eolian transport mechanics have characterized sand populations in the most elemental manner possible, namely as particles of uniform size and shape mobilized under steady, uniform aerodynamic conditions. These simplifications have been made to resolve the fundamental nature of particle and fluid motion prior to introduction of stochastic complexities of heterogeneous sand composition, grain irregularities, and flow discontinuities

into the problem. These foundation models, however, have not yet reached a level of sophistication necessary for entirely predicting the dynamics of granular interactions and bedform behavior observed in field or experimental studies. One reason is that natural sediments in any transporting environment always contain a range of grain sizes. The interaction of multiple size fractions and their differential momentum exchange with the wind ultimately dictates: (1) the spatial and temporal variability in sediment fluxes; (2) the generation of bed-surface protrusions giving rise to bed instabilities that form small-scale sedimentary features like ripples; and (3) the patterns of grain sorting and packing that produce distinctive stratigraphic laminae in modern and ancient eolian deposits. Therefore, one critical link between studies of particle-fluid energetics and the physical interpretation of erodible-bed morphology, so far incompletely made, lies in understanding the dynamics of heterogeneous sediment mixtures.

At present, there are no comprehensive, physically based models of eolian, mixed-size sediment transport that can reproduce the complex interactions between the air, the moving sand populations, and the evolving bed topography. The work presented in this dissertation is intended as a step in that direction.

### **1.1 Mixed-grain sediment-transport systems**

Bedload-discharge rates in any natural eolian environment are modified by the nature of the interactions between the solid and fluid components. As individual sand grains accelerate from the bed surface, they extract momentum from the air, thereby modifying the wind-velocity profile near the ground and the ability of the air to sustain energetically moving grains. In mixed-grain sediment systems, there is no single air threshold velocity for granular transport, but rather a suite of threshold velocities in which each value corresponds to a discrete grain-size fraction present in the sediment mixture. Modification of the wind profile through momentum exchange varies as a function of the number of grains in transit from each size fraction, at successive heights above the bed surface. Sands from an inhomogeneous sample are mobilized and transported at rates quite different than grains of the same dimension in a uniform-sized sample, as has been shown experimentally in both air (e.g. Bagnold, 1941; Gerety and Slingerland, 1983) and in water (e.g. Gilbert, 1914; Iseya and

Ikeda, 1987; Wilcock and Southard, 1989). In addition, the ability of a moving grain to eject others during collision with the bed surface depends on the relative masses of the particles involved. Hence, the degree of sorting of the particle mixture directly dictates the complexity of both the grain-fluid and grain-grain interactions during a sediment-transport event. To describe the mechanics of heterogeneous sediment transport, therefore, requires an accurate assessment of the sediment properties of the mixture.

Eolian sediments are classified in four distinct groups (e.g. Siever, 1988), based on their grain-size frequency distribution and dominant transport mode: lag or interdune accumulations, dune sands, loess, and dust. Lag accumulations, interdune deposits, and sand sheets typically contain poorly sorted, coarse sediments (e.g. pebbles, granules, coarse sands) that have been winnowed of their finer fraction and might move only episodically by individual grains creeping or rolling along the surface. Dune sands generally are composed of more well-sorted particles, with a median grain size of 0.125mm to 0.50mm (i.e. fine to medium sands), which move as bedload by rolling or hopping across the bed surface. Loess, consisting mainly of 0.01mm to 0.07mm grains (i.e. silt), usually is transported as suspended load. Dust, which includes the finest silt and clay fractions (<0.01mm), frequently is carried in suspension over hundreds of kilometers (Pye and Tsoar, 1990). Examples of these four sediment types are numerous throughout eolian depositional environments, although intergradational deposits form in marginal systems, as, for example, in the high desert environment of central Washington State where isolated dunefields merge with loess deposited regionally during the Pleistocene glaciation. Given the abundance of eolian sands in the modern and ancient geologic record, this dissertation treats the case of dune-size sediments.

Eolian ripples and dunes, with relatively few exceptions, are composed of grains of sand size (i.e. 2mm to 0.063mm on the Udden-Wentworth scale). These sand particles migrate primarily by saltation, that is, by the hopping of grains across the bed in a series of strongly asymmetric trajectories. A second mode of transport accounting for approximately one-quarter of the total bedload flux (e.g. Bagnold, 1941; Anderson *et al.*, 1991) is surface creep. This is the mechanism whereby grains skip across the bed in short trajectories, rarely losing contact with its surface. The differences between surface creep and saltation are gradational, and it can be difficult to segregate the two, espe-

cially under field or experimental observation. However, it is conjectured (e.g. Anderson *et al.*, 1991) that saltating particles receive most of their forward momentum through dynamic exchange with the horizontal component of the wind-velocity profile, while those in surface creep move forward through impact with saltating grains returning to the bed. At low transport stages where the local boundary shear stress just exceeds the critical value for initiating particle motion, grains can roll short distances downwind along the bed surface. Rolling is a minor transport mode in sand mixtures, though, largely associated either with incipient motion at the onset or end of a wind gust, or with particles dislodged by a glancing collision that imparts insufficient momentum to propel them upward from the bed. At high transport stages where the fluid shear velocity exceeds particle settling velocities, grains may be propelled aloft through a combination of upward momentum gained from energetic collisions with bed-surface grains, and turbulent fluctuations in the vertical component of the wind-stream, resulting in particle suspension. This dissertation addresses the bedload mechanics of rolling, creeping, and saltation under low to moderate transport regimes (i.e. the ratio of the boundary shear stress to the critical shear stress for grain motion,  $T_*$ , is less than 8), the average conditions under which lower plane and impact-rippled beds develop.

The variation in particle sizes and densities across a sandy surface plays a leading role in the evolution of bed texture (e.g. particle packing) because the bed-surface sedimentology directly controls the grain-wind and grain-grain interactions responsible for the generation of texture. The ability of wind-accelerated, saltating grains to eject particles from the sand bed through impact dislodgment depends closely on the size-frequency distribution and packing geometry of grains composing the bed, as well as the ratios of masses between a saltating grain and a stationary particle with which it collides. Sand grains of particular sizes become selectively entrained or deposited across a surface with irregular topography, resulting in development of particle-sorting patterns that can vary both spatially and temporally. The effect of small particles becoming trapped in the interstices between larger grains and of big grains moving nearly continuously down beds effectively smoothed by infilling of pocket irregularities with small grains has been well-documented in wind-tunnel motion photography.

Grain sorting patterns can vary widely in the direction of downwind transport. For example,

on a typical windward dune face, where transport occurs primarily through creep and saltation, sorting patterns grade from poorly sorted, coarse sands at the base to gradually finer, better-sorted sands up the stoss side (e.g. Bagnold, 1941; Folk, 1971). Local variations may also occur between rippled and non-rippled surfaces on a dune face or planar bed, as well as between internal stratigraphic laminae of individual secondary bedforms. Active bedload-transport zones on windward dune faces typically contain fairly narrowly distributed, unimodal sands, from which the finer fractions (e.g. silts, dust, clay) have been winnowed through transport. Conversely, interdune flats and other deflation areas comprise broadly distributed, usually bimodal deposits of coarse lag grains and interstitial fines that have been dropped from the suspension layer (e.g. Binda, 1983). For example, of nearly 500 inland and coastal dune samples collected worldwide (see Ahlbrandt, 1979), sands were found to be moderately well-sorted ( $\sigma_1$  sorting values of 0.5 - 0.7, where  $\sigma_1$  is the inclusive graphic standard deviation) with a mean particle size in the fine-sand range (0.13mm to 0.35 mm). The best sorting appears to occur in fine sands, as they are most easily mobilized through saltation and surface creep. The sand samples modelled in this work are of similar to slightly coarser sorting characteristics than those summarized by Ahlbrandt (1979).

## 1.2 Need for a theoretical model to describe mixed-grain sediment transport

The purpose of this work is to formulate a theoretical model for the transport of eolian sediment mixtures as bedload. A clear understanding of the dynamics of mixed-grain-size sediment motion is of fundamental importance to many diverse areas of geological science and engineering, where solutions to sedimentologic and geomorphologic problems require a detailed physical knowledge of the mechanics of erosion, dispersion, and accumulation of sediments with a variety of compositions.

For example, sediment-transport models, coupled with bedform-generation algorithms, provide a means for reconstructing the evolution of sedimentary textures and small-scale structures found in ancient and modern sands, as a basis for paleoenvironmental interpretations. Sedimentary structures are valuable tools for identifying depositional environments. Fine-scale laminations or "translatent strata", which are produced by migrating wind ripples, represent the most common

microstructure found in eolian deposits, and they have been used extensively in analyses of outcrops and cores to discriminate between wind- and water- generated deposits (Hunter, 1977; Kocurek and Dott, 1981; Rubin and Hunter, 1987). Each lamina is formed by a single migrating ripple that is maintained largely by collisions of energetically moving grains with a less-energetic population of surface grains propelled forward by these impacts. Numerical models are essential for predicting the physics of collisions between particles of different sizes and the nature of grain ejections from the bed surface. A model that reconstructs the depositional mechanics of sand deposits also is applicable to the study of fluid migration through porous media. Fine laminations in eolian strata can reduce the permeability of the rock to fluid migration across laminations, thereby affecting hydrocarbon production in ancient eolian sandstones (Fryberger and Schenk, 1988). The degree of bed porosity in modern sediments can also govern the dispersion of groundwater and groundwater contaminants (Freeze and Cherry, 1979).

Another goal of eolian studies is to predict the flux rates of grain-size fractions within naturally distributed mixtures, and thereby to address erosion concerns in arid and semi-arid environments. These include migration of dunefields into arable regions, soil loss to croplands, and deflation of desert surfaces, which result in long-term ecological change. The interactions between the wind and transported sediments, which vary depending on grain size, ultimately dictate the spatial and temporal variability in sediment fluxes. Variability in the flux rates of individual size fractions leads to lateral and vertical sorting of the sediment bed, thereby influencing the textural and compositional characteristics of depositional surfaces. Calculating sediment fluxes in poorly sorted sediments, therefore, necessitates accurately predicting the size-frequency distributions and densities of sand particles that will be entrained, transported, and deposited simultaneously under varying atmospheric conditions.

The importance of a quantitative model, moreover, lies in its ability to predict aerodynamic and particle-transport phenomena for a spectrum of flow and sedimentological conditions that cannot be measured adequately, if at all, in laboratory or natural settings. For example, the few wind-tunnel measurements procured of sediment-transport parameters in mixed-size materials (e.g. grain-collision geometries, particle velocities, particle-ejection distributions, sediment fluxes) have

been necessarily limited to lower transport-stage ( $1.0 < T_* < 3.0$ ) conditions for which detailed observations of near-bed particle motion could physically be made without high sediment concentrations obscuring the near-bed field of view. As significant sediment erosion and accumulation typically occur during stronger flow events, when opportunities to make field measurements are rare and the deposits left behind present only an incomplete record of active transport processes, a physically complete, predictive model is especially useful in reconstructing the coevolution of grain motion, bed configuration, and air flow that existed during a given transport event.

### 1.3 Components of the model

The mixed-grain bedload model presented in this dissertation includes four algorithms for predicting sediment-bed packing and porosity, the characteristics of individual and composite particle motion under a variety of aerodynamic and sedimentologic conditions, the structure of the wind-velocity profile within the saltation layer during transport, and the discharge rates of each grain-size fraction within a sediment mixture. These components are also required of a homogeneous bedload-transport model. In the mixed-grain case, however, they must be treated in a sophisticated manner to address the collision mechanics of grains of unequal mass, the effective roughness for the flow imposed by grains of different sizes moving within the bedload layer, and the dynamics of momentum exchange for each grain-size fraction in transport.

The building block of this model is a theoretical algorithm for specifying the geometric configurations of inhomogeneous sediment beds, which fully characterizes the grain size-frequency distribution and the physical properties of the bed surface and subsurface. This component is then coupled with others for grain-bed and fluid-bed interactions to evaluate the behavior of grains of different sizes under a range of transport conditions. This algorithm also can be used to quantify spatial and temporal variations in grain sorting and packing during sediment movement. Two-dimensional beds are composed of poorly sorted sediment mixtures, by randomly distributing grains from measured grain-size frequency distributions in the manner described in Chapter 2. Computed sediment beds are developed to any desired multi-grain-diameter thickness. They are allowed to evolve as the size-frequency distribution of the moving particles above the bed is



adjusted automatically to accommodate eroded and deposited grains at the surface, thus accounting for any changes in bed-surface sedimentology that result from the transport process. Computed granular-bed configurations are compared with available measurements of grain packing and bed-pocket geometries, as well as photomicrographs of experimentally developed deposits (e.g. Pryor, 1973; Beard and Weyl, 1973; Ahlbrandt, 1979; Fryberger and Schenk, 1981; Schenk, 1983) to demonstrate the validity of the model.

A second component characterizes the near-bed aerodynamic conditions and the interactions between the wind and individual grains as they begin to move and then to saltate in sequences of trajectories across the bed. The fluid-solid dynamical component couples a collisional algorithm, describing the mechanics of grain-bed interactions, with the equations of motion for a sediment grain in a transporting airstream, to predict saltation behavior. The nature of successions of trajectories made by individual grains as functions of time, elevation above the bed, and distance travelled downwind are calculated using the saltation model of Wiberg and Smith (1985).

The fluid-dynamical component of the model also contains an algorithm for evaluating the modification of the near-bed vertical profile of wind velocity as a result of momentum exchange between the fluid and the saltating grains. This strong interaction is largely responsible for shaping the vertical profiles of sediment concentration for each grain-size fraction and, consequently, the bedload-flux profiles for each fraction. Hence, to predict transport rates in heterogeneous sediments, it is necessary to determine the structure of the near-bed fluid velocity field under diverse flow and sediment conditions, as well as the form of the boundary-roughness parameter ( $z_o$ ), which relates the geometry of the sediment bed to the height of the bedload layer. Methods for computing the vertical profile of downwind velocity and the roughness parameter have not previously been formulated for poorly sorted materials. Since the structure of the wind velocity profile is not known *a priori*, a numerical expression is developed herein to calculate the profile shape iteratively. The calculation is constrained by the fact that, in order for saltating grains to achieve equilibrium with the flow, each grain terminating motion on the bed is replaced, on average, by a particle ejected from the bed. Determination of the velocity profile requires a knowledge of the critical shear stress at which momentum reduction becomes significant and below which the flow cannot sustain grain sal-

tation. This critical shear stress for initiation of saltation is dependent on grain size, as well as on the total local fluid shear stress. The values of the critical stresses for each sediment component also are found iteratively. Through each iteration, the sediment-concentration and fluid-velocity profiles are calculated by individual size fraction and then summed to obtain the integrated profiles for the particular sediment-mixture and airflow conditions. Once the modified velocity profile is known precisely, the exact height of the saltation layer and the value of the roughness coefficient ( $z_0$ ) enhanced by sediment transport can be computed.

A third component of the model addresses collisions between moving grains and the computer-generated sediment bed, in the presence of fluid forces acting on the colliding grains and particles composing the bed surface. The ability of a grain to eject a stationary particle on the bed surface depends on the impact angle and speed of the incoming grain, the point of collision between grains of unequal size or between a grain and a bed-surface pocket, and the ratio of grain masses involved in the collision. This model is modified from one developed earlier (Calder, 1987) for uniform-grain ballistics and is described in Chapter 4. Collisions are stochastic in nature; the exact location of contact between saltating and stationary grains, as well as the magnitude of the impact angle and speed, are not known at first. Posing the granular arrangement of the bed particles explicitly, however, permits a deterministic solution to the grain-bed collision problem. The ballistic paths and energetics of particle trajectories are determined by the saltation algorithm; as each grain moves across the bed, its position is traced relative to known points along the bed surface, such that when the grain approaches the bed, its collision with the first stationary grain it meets can be calculated exactly. The characteristics of grain rebound and ejection of particles from the bed surface are predicted by the model and depend on the geometry and energetics of the collision. This algorithm does not rely on experimental statistics of trajectory parameters, other than for independent verification of results. Model predictions of collision outcomes are compared with the available empirical information for similar size-frequency distributions procured by Willetts and Rice (1985a, 1989) and Nickling (1988).

Coupling of the sediment bed, ballistic, grain-fluid interaction, and grain-bed collisional algorithms permits calculation of sediment fluxes for specific size fractions under flow conditions

of interest. The coupling of these components is addressed in Chapter 5. Fractional transport rates are then summed to derive bedload transport rates for the entire sediment mixture. In order to test the mixed-grain bedload model, theoretical results are compared with a unique set of high-precision, wind-tunnel data obtained by Yamasaka and Ikeda (1988). Whereas numerous empirical studies of sediment transport in water have been conducted, the experiments of Yamasaka and Ikeda represent the only ones for which fractional transport rates were measured. Most of the existing modelling efforts on the mechanics of sand mixtures have been aimed at creating transport functions for total bedload discharge. Although based on physical principles for the relationships between shear velocities and total mass flux, these models (e.g. Bagnold, 1936, 1941; Chepil, 1945; Zingg, 1953; Kawamura, 1964; Williams, 1964; Hsu, 1973, 1974; White, 1979; Hsu and Blanchard, 1991) employ empirical coefficients that limit their range of applicability to those sediment-transport conditions under which the data were collected. Furthermore, Sarre (1987) found in a comparison of several of these transport equations, that they predict widely varying sand-transport rates for single values of grain size and shear velocity ( $u_*$ ). The advantage of this numerical model, therefore, is that it can be used to predict bedload-discharge rates for a large range of flow conditions, sediment properties, and grain-size frequency distributions, and it thereby permits reliable computation of sediment fluxes beyond the range of available experimental data.

This bedload-transport model provides an alternative hypothesis to the grain splash-function models of Ungar and Haff (1987), Anderson and Haff (1988, 1991), Werner (1990), McEwan and Willetts (1991), and others, which treat grain collisions statistically, based to varying degree on observations of grain collisions in wind tunnels. In their models, the fluid mechanics of grain motion are decoupled from the collision process, and greater emphasis is placed on ascertaining the numbers of grains ejected by a single collision and on calculating the contact forces between all bed particles associated with grain impact (e.g. Haff and Anderson, 1993). Alternatively, this model emphasizes the complex coupling of the fluid-mechanical and collisional processes, whereby collisions are described in an average sense by the dominant interactions between impacting grains, the few grains at the bed surface with which they have direct contact, and fluid forces acting on the grains. Both modelling approaches need to approximate certain aspects of the sediment-transport

process, so that a basic, general model can be developed. Ultimately, a numerical model that incorporates the full complexities of the coupled fluid-mechanical and collisional elements, without general approximations, may be developed; however, that stage has not yet been reached.

The contribution of this work, therefore, is a unified theory for the fluid- and particle- transport dynamics of sediment mixtures in wind. Necessary input information to run the computational algorithms are the grain-size frequency distribution of the mixed sediment of interest, the fluid and particle densities, the fluid viscosity, and the boundary shear stress. This model is not limited to any particular fluid environment, other than those represented by quasi-steady, quasi-uniform flows. The bed-generation algorithm accommodates unimodal and multi-modal grain-frequency distributions and, with some modifications, can be adapted readily to address very different sedimentologies, e.g. the poorly sorted mixtures of boulders, pebbles, and sand characteristic of fluvial environments and eolian lag deposits. The effect of particle-scale irregularities of the bed surface obstructing the near-bed flow can be treated following a technique derived by Wiberg and Smith (1987a, 1991) for fluvial sediments, which has been incorporated into the fluid-mechanical component of the mixed-grain eolian model. Furthermore, the model can be extended to analyze the flux of particles of each size fraction into suspension, by coupling the bedload flux calculations for each size fraction with the component equations for suspended load transport. In addition, the model lays the basic framework for future explorations of the variations in sediment movement associated with differences in fluid properties, as well as the effects of mixed-density particle distributions and grain shapes on heterogeneous-sediment transport rates.

## Chapter 2: The Sediment Bed

The size and spatial arrangement of particles composing a wind-deposited bed exert a direct control on sediment flux rates by governing the geometries of grain-bed collisions and, thereby, the success of saltating particles in rebounding and ejecting immobile grains from the depositional surface. Unless the exact configuration of the granular bed is specified, it is impossible to predict the actual geometry of a particular collision. Furthermore, the dynamics of subsequent trajectories of any rebounding or ejected grains are extremely sensitive to the mechanical properties of the collision. To model the fundamental mechanics of grain-bed interactions, therefore, an algorithm is required that reconstructs the basic aspects of sediment-bed morphologies.

Very few attempts have been made to model theoretically the geometries of granular-bed configurations. Most previous work has concentrated on materials of uniform size, primarily to make the problem more tractable from an experimental and computational standpoint (e.g. Deresiewicz, 1958; Mitha *et al.*, 1986; Werner and Haff, 1986, 1988; Werner, 1990; Anderson and Haff, 1991). In mechanical and chemical engineering, numerical models of mixed-size spheres or disks have been developed to examine the internal stress fields in mobile granular aggregates. Serrano and Rodriguez-Ortiz (1973) and Cundall and Strack (1979) both formulated discrete-particle models in which interactions between all spheres in a rigid-walled container were traced in two dimensions as disturbances originating at its boundaries propagated through the interior. Dynamic equilibrium was considered to be achieved when the internal forces of the shearing medium were balanced. These numerical experiments were performed in the absence of fluid flow, for a relatively small number of weightless spheres (i.e. <500).

Recently, Jiang and Haff (1993) have introduced molecular models in the sedimentological arena, by adding water flow as the shearing force. These PDM, or particle dynamics method, models apply explicit Newtonian mechanics to describe intergranular contact forces (i.e. frictional, elastic), which can be coupled with models of particle and fluid motion to investigate grain migration within and away from the sediment bed. Jiang and Haff generated initial beds by gravitationally settling about 100 disks of two sizes onto a solid surface and allowing them to come to rest through inter-

granular dissipation of kinetic energy. By incorporating algorithms to describe the motion of solid and fluid components, they were able to examine preliminarily the sorting and vertical mixing of bed particles, as well as the behavior of particle trajectories and mass fluxes within the saltation layer. More recently, Haff and Anderson (1993) have utilized the PDM model to investigate the sensitivity of grain response, following eolian saltation impacts on a simulated mixed-grain bed, to the choice of intergranular dynamical properties. Because they considered intergranular dynamics to be independent of fluid forces, their study had no aerodynamical component. The authors' development of test sediment beds followed the approach of Jiang and Haff, in which they used particles of two diameters to represent the desired distribution of grains in the simulated bed and deposited them gravitationally between two fixed walls to create an initial accumulation. To aid in more rapid dissipation of kinetic energy, so that particles reach a terminal velocity quickly and settle on the growing bed, they imposed a zero-velocity condition on all particles.

Examples of granular beds shown in this work are composed in a different physical manner. This bed-generation algorithm constructs granular beds in two dimensions from measured frequency distributions of grain size. The use of real distributions as model input allows direct testing of simulated-bed characteristics, such as grain spacing, packing, and sorting, against their measured counterparts, to determine how accurately the model simulates natural sediment-bed configurations. Grain packing and orientation directly influence bed microtopography, which, in turn, affects the interaction between the air mass, the moving particles, and grain-bed collisions within the near-bed region. Therefore, a bed-generation model that describes the full size distribution of a sediment mixture is desired in a unified theory for mixed-grain bedload transport.

Particles, chosen randomly from the grain-size distribution, are arranged according to basic arguments of Euclidean geometry for tangency of coplanar objects, to form the initial sediment bed. Initial beds are constructed in the absence of fluid flow, such that the model does not impose structural and sorting patterns commonly developed by wind working of deposits. Computed sediment beds can be employed in two modes, either as: (1) short beds with periodic boundaries, a technique common to the sediment-bed algorithms cited above, where grains leaving the downwind boundary are re-entered at the same speed and elevation on the upwind side to simulate continuous

transport within one bed cross-section; and (2) "infinite" or extended beds, where the histories of individual saltating particles and any grains they set into motion are traced downwind continuously. The first approach provides computational efficiency and is appropriate particularly when considering the evolution of bed morphology in a localized reach, wherein only a representative sample of the bed is needed. The latter approach is advantageous for sediment-transport calculations, particularly for comparisons with measured data, because the probability distributions of the bed grains and, therefore, of the particles ejected into the saltation layer, are more likely to represent the full size-frequency distribution of the mixture than found in a shorter segment of the bed surface. The algorithm, however, is not limited computationally in the number of particles employed, as are the PDM-based models. Multi-particle-thick beds are subsequently subjected to fluid-imposed shear stresses of increasing strength, to quantify changes in bed topography and grain-transport behavior from the threshold of fluid motion to full-scale, steady, horizontally uniform airflow.

The first step in generating a computerized sediment bed is to construct a randomly composed, granular deposit in the absence of fluid flow. Most natural sand beds possess some inherent lateral or vertical sorting associated with antecedent transport events, upon which new windblown grains are dispersed stochastically. The objective of creating sediment beds initially unworked by fluid flow, however, is to observe the development of sorting patterns as the wind begins to blow and to quantify appropriately the fluid and particle mechanics responsible for their growth, rather than assuming some internal bed structure qualitatively or arbitrarily. Prior to sediment-transport calculations, the bed surface is smoothed of any artificial protuberances created by grain placement in the absence of fluid and collisional forces; this is achieved by subjecting the bed to weak airflows below the critical shear-velocity threshold. Computer-derived sediment beds are tested against available observations of the geometric properties and surface-roughness characteristics of natural and laboratory-generated, unworked sediment beds. This forms the basis for later analyses of the morphometric variation in bed configurations under marginal through moderate sediment-transporting flows.

## 2.1 Grain-size distributions

The two grain-size distributions used as examples in this work were obtained from a dune crest in Great Sand Dunes National Monument, southern Colorado (Ahlbrandt, 1979, Fig. 22c) and from dried fluvial sands used in wind-tunnel experiments performed in Japan (Yamasaka and Ikeda, 1988, Fig. 1). The former distribution is reproduced in Figure 2.1a and the latter in Figure 2.1c. These samples were chosen with different purposes in mind, the former to verify the bed-construction algorithm and the latter to test the ability of the integrated transport model to predict measured sediment-discharge rates.

The Great Sand Dunes sample represents one of a relatively few for which grain-size frequency distributions are given in discrete size fractions and additional information on bed packing and porosity is available. Few measurements have been reported for both bed grain-size distributions and packing geometries of typical, well-sorted windblown deposits. Instead, most grain-size data are presented as moment statistics (i.e. mean, sorting, skewness, kurtosis) for the purpose of differentiating eolian-dune from beach or fluvial sands (e.g. Shepard and Young, 1961; Folk, 1971; Bigarella, 1972; Binda, 1983; Bui *et al.*, 1989), and from which it is difficult to reconstruct the original frequency distribution of each phi-size fraction. These studies generally do not contain any detailed sedimentological analysis of the deposits from which grain samples were taken. Several field and wind-tunnel investigations, however, have been conducted of dune-crest sediments from Great Sand Dunes National Monument (e.g. Burford, 1961; Ahlbrandt, 1979; Fryberger *et al.*, 1979; Andrews, 1981; Fryberger and Schenk, 1981; Schenk, 1983; personal data), in which grain-size frequency distributions are plotted and information on bed packing can be obtained from measurements and photomicrographs of experimentally produced strata.

Unfortunately, bedload-transport rates were not measured in the wind-tunnel studies of Great Sand Dunes sediment. To verify the dynamical components of the transport theory, model predictions of bedload discharge are compared with the Japanese wind-tunnel data sets. Whereas the morphological details of their experimentally produced sediment beds were not reported, Yamasaka and Ikeda (1988) do present the only known published eolian data in which transport rates of each grain-size fraction of the sediment sample were measured. Given the present lack of



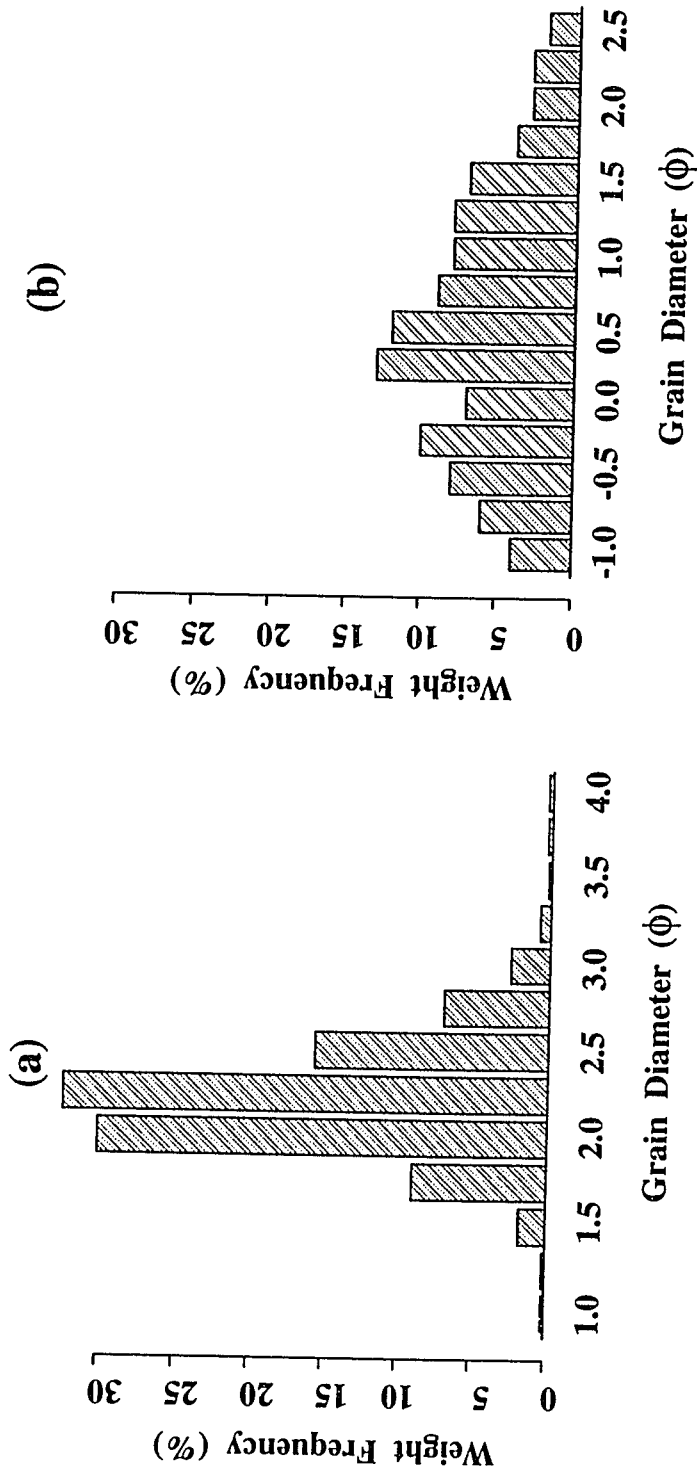


**Figure 2.1** Grain-frequency distribution data. (a) Weight-frequency-percent histogram of a dune-crest sand sample, Great Sand Dunes National Monument, Colorado (from Ahlbrandt, 1979); median grain size ( $\phi_{50}$ ) = 2.1  $\phi$  = 0.23mm. (b) For comparison, weight-frequency-percent data of Yamasaka and Ikeda (1988); data are presented in their paper in a cumulative-frequency-percent curve (see Figure 2.1c) and are regraphed here in histogram form; median grain size ( $\phi_{50}$ ) = 0.51  $\phi$  = 0.70mm.

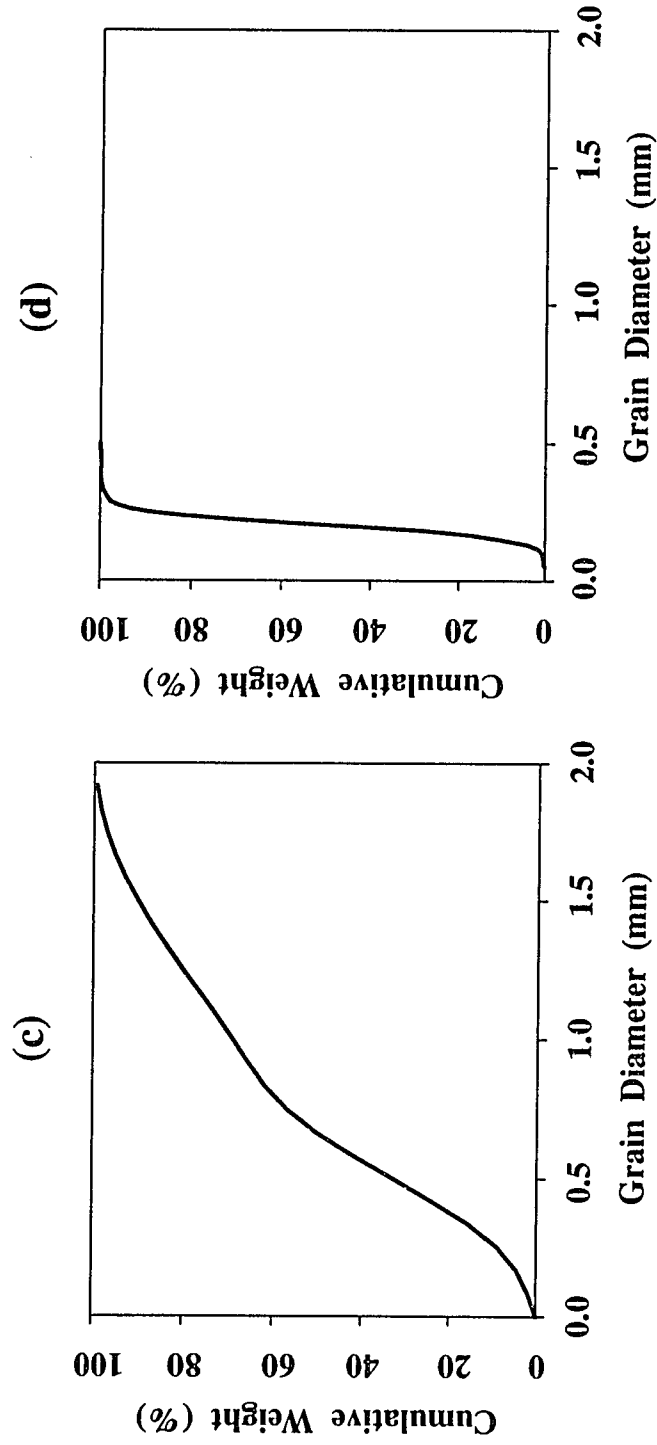


**Figure 2.1 continued** Grain-frequency distribution data. (c) Cumulative weight-frequency-percent curve presented by Yamasaka and Ikeda (1988) for their experimental sand sample; median grain size ( $D_{50}$ ) = 0.70mm. (d) For comparison, cumulative-weight-percent data of the Great Sand Dunes sample; data are presented in Ahlbrandt (1979) in a frequency-percent histogram (see Figure 2.1a) and are regraphed here as a cumulative-percent curve; median grain size ( $D_{50}$ ) = 0.23mm.

empirical, mixed-grain-size data with which to evaluate predicted flow and sediment-transport mechanics at the level of detail necessary for testing the numerical algorithms, comparison of measured and theoretical bedload transport rates provides one of the only means for verifying the ability of the model to predict the transport behavior of grain mixtures.

Measurements of grain-size distributions in natural deposits are usually reported in the form of frequency histograms or cumulative-percentage frequency curves. Conventionally, histograms plot grain diameter, measured in millimeter or phi units, against weight percent which represents the weight of each sediment fraction converted to a percentage of the total sample (Figure 2.1a, b). Size analytical techniques, such as mechanical sieving or electronic particle counters, usually partition size fractions into 1/4 phi units. Cumulative frequency curves show the variation in weight percentage as a continuous function of grain size, so that several meaningful statistical parameters can be displayed graphically; for example, the sample median is that grain size ( $\phi_{50}$ ) for which half of the particles, by weight, are coarser and half are finer (Figure 2.1c, d). Traditionally, grain-size histograms of natural eolian sediments have been approximated by Gaussian probability functions, or log-normal probability curves when using the logarithmic phi scale. More recently, microsedimentological analyses of natural sands (e.g. Bagnold and Barndorff-Nielsen, 1980; Barndorff-Nielsen, *et al.*, 1982; Fieller *et al.*, 1984; Flenley, 1985; Christiansen and Hartmann, 1988), have demonstrated that both eolian and subaqueous grain-size distributions conform more closely to log-hyperbolic density functions. These studies suggest that log-normal approximations tend to remove the true asymmetry of real sediment distributions and underestimate the low frequencies of the extreme, or "tail", end members.

Although the computer algorithm described here can accommodate size-frequency distributions in any statistical representation (i.e. logarithmic probability functions, cumulative frequency curves, histograms), the use of original data is preferred over probability density functions fit to them. Probability-distribution plots typically are employed to smooth or simplify grain-size data so that comparisons can be made between statistical characteristics (e.g. sorting, skewness) of different samples. The objective here, however, is to reproduce as completely as possible the exact size-frequency distribution of a sample, so that the relationships between the

various size fractions in producing sediment-bed packing and porosity can be evaluated. The finer and coarser fractions, which often are under-represented even in the log-hyperbolic suite of distributions (Flenley *et al.*, 1987), provide the sample inhomogeneity that promotes variability in sediment-bed morphologies.

Using weight-frequency-percent data from any measured sample as input (e.g. Figure 2.1a-d), the computational model determines, based on the weight of each size fraction reported, the number of grains that may exist in each size class (e.g. 1/4 phi unit). A total sample weight is assumed unless otherwise specified; with medium sands, for example, a sample chosen to weigh 0.5-1.0 kg will yield approximately 2000-5000 particles as input to the bed-generation routine. Since the dimensions of each grain in each size class are not known *a priori*, the average grain size of each class is used to generate an initial probability distribution of grain numbers per size fraction. The number of grains of average size that can exist in each size class is determined by comparing the measured or estimated weight of each fraction with the calculated weight as grains are added to the sample, until these values coincide. This method provides an initial distribution of the number of grains that are expected in each grain-size class.

From this nonuniform distribution of expected grain numbers, an iterative routine produces a randomly sorted sample containing grains with the full range of permitted sizes in each class. This routine employs a multiplicative-congruential generator method (Kennedy and Gentle, 1980), where (0,n) random numbers, representing individual sand grains, are normally distributed about a sample mean. Because most sand-size frequency distributions are asymmetric about the mean, however, this approach has been modified to account for sample skewness. Rather than distributing random deviates uniformly about the mean, the left and right limbs of the sample grain-size distribution are treated as discrete probability functions with the same mean but different standard deviations. Hence, an expected grain-number frequency distribution can be defined by two density-function curves, one applied to the left asymptote of the distribution and the other to the right asymptote. A fifth-order polynomial equation is used to compute each curve so that the low-frequency classes and tail-end members are preserved in the distribution. In Figure 2.2a, two curve segments A and B are shown for the Great Sand Dunes grain-size distribution [sample mean ( $\phi_m$ )

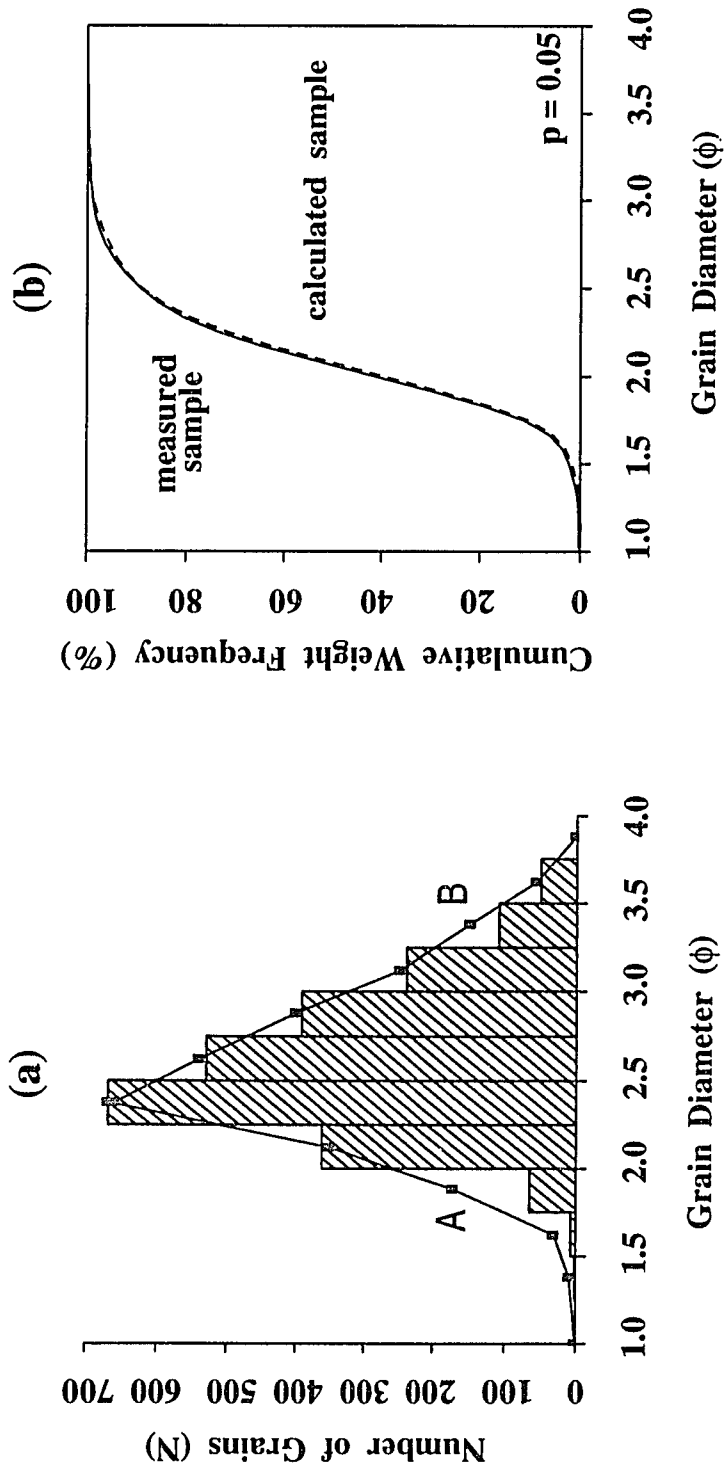


**Figure 2.2** Grain-size distribution characteristics of the Great Sand Dunes sample predicted by the model. (a) Frequency histogram of grain-size classes by number, rather than by weight, predicted from the measured weight-percent data presented in Figure 2.1a. This distribution was computed using a random-number generator routine, in which density-function curves A and B bound the nonuniform dispersment of random variates (grain sizes) about the sample mean (see text). (b) Comparison of the measured cumulative weight-frequency distribution with predicted results. Weight percents were calculated from the frequency predictions of grain number shown in (a) to verify the model's ability to generate the correct number of appropriately weighted grains per size class; results show a standard error of  $p = 0.05$ . For this case,  $\phi_{16} = 2.44\phi$  [0.18mm],  $\phi_{50} = 2.08\phi$  [0.23mm],  $\phi_{84} = 1.80\phi$  [0.30mm].

=  $2.1\phi$ ]. Curves A and B have been truncated at the sample mean. Curve A represents  $(\phi_m - x)$  sample variates with a standard deviation of  $0.40\phi$ ; curve B denotes  $(\phi_m + x)$  variates with a standard deviation of  $0.47\phi$ . These curves bound the distribution of grain sizes produced by the random-number generator.

Random numbers, representing nominal grain diameters, are added to the calculated distribution using a modified congruential-generator technique (Marsaglia's Polar Method; see Kennedy and Gentle, 1980, p. 133-264). This method generates two independent random numbers  $(n_1, n_2)$  transformed as variates  $(v_1 = 2n_1 - 1$  and  $v_2 = 2n_2 - 1)$ , from which values of the x-axis of the distribution are determined:

$$x = v_1 \left[ -2 \ln (v_1^2 + v_2^2) / (v_1^2 + v_2^2) \right]^{1/2} . \quad (2.1)$$

The grain diameter  $(\phi)$  is equal to:

$$\phi = x (\sigma_A - \phi_m); \quad \phi = x (\sigma_B + \phi_m); \quad (2.2)$$

where  $\sigma_A$  and  $\sigma_B$  are the standard deviations of probability-density functions A and B, and  $\phi_m$  is the sample mean. In addition to the weight-frequency-percent distribution, this algorithm requires two random seeds as input variables. Random-number generation proceeds iteratively until each size class of the distribution is filled with the appropriate number of grains to yield a sand sample whose size fractions correspond in weight to those of the original weight-frequency-percent distribution. Randomly produced grains are listed sequentially in a file for input to the bed-construction algorithm.

Examples of grain-number frequency distributions of particle size calculated by the model are plotted as histograms in Figures 2.2a and 2.3a. In both cases, curves (A, B), which were employed to delimit the dispersal of generated random variates, are shown with the final model prediction of grain-number statistics. Points on the curves represent the initially expected numbers of grains of average size in each class, based on size-fraction weight limits. Comparison of these values with the final number of grains in each class shows some variability between the anticipated and predicted outcome, due to the fact that the random assortment of grains composing the fraction contained either more coarse grains or fine grains than the expected average. Since the coarser grains in a particular class weigh more than the finer ones, the permitted weight of each fraction

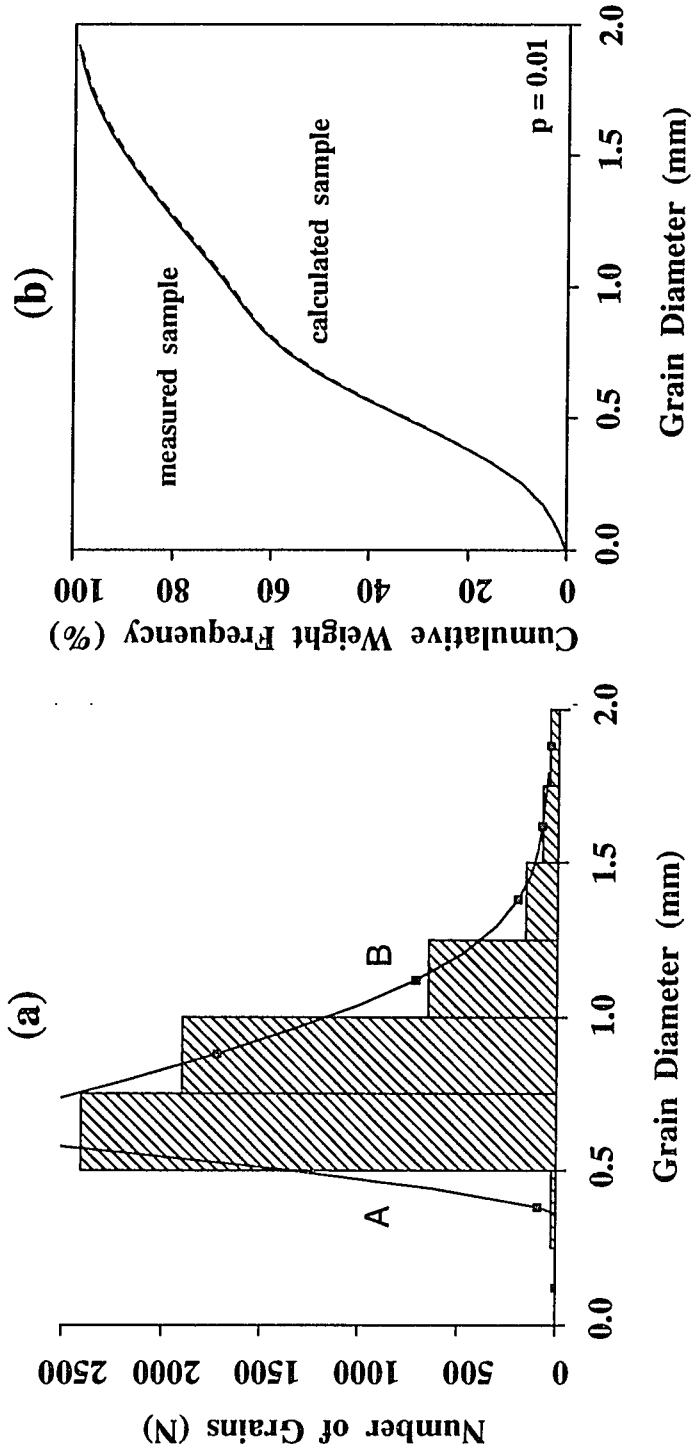


**Figure 2.3** Model predictions of grain-size distribution characteristics of the experimental sands used by Yamasaka and Ikeda (1988). (a) Frequency histogram of grain-size classes by number, rather than by weight, predicted from the measured weight-percent data shown in Figure 2.1c. Probability density-function curves A and B were used to limit the non-uniform distribution of random variates (grain sizes) in the routine used to compute the grain-size histogram (see text). Grains of discrete size are then chosen randomly from this distribution to build successive layers of the sediment bed. (b) Comparison of the measured cumulative weight-frequency curve with that calculated from the predicted grain-number frequency distribution. Differences between the two curves show a standard error of  $p = 0.01$ . For the measured and predicted samples,  $D_{16} = 0.32\text{mm}$ ,  $D_{50} = 0.68\text{mm}$ , and  $D_{84} = 1.35\text{mm}$ .

may be achieved with relatively fewer coarse grains than expected if all the grains were of mean size. The converse holds in size classes where the model predicted more fine grains than estimated using the mean grain size. The final predicted grain-number frequencies correlate with the expected frequency curves (A, B) at a 98% confidence interval.

The distribution of grain numbers per size fraction presented in Figure 2.2a was generated from the weight-frequency-percent histogram of Great Sand Dunes fine-to-medium sands shown in Figure 2.1a. Assuming a total weight of 20 grams, given that the original weight of the collected sample was not reported, this sample produced approximately 2500 sand grains with a slight skew toward the finer fraction (e.g. sorting of the finer fraction is 47% (i.e.  $\sigma/m = 0.47$ ), compared with 40% of the finer tail). Weight-frequency percents for each phi fraction calculated from this output of randomly generated grain sizes (Figure 2.2b) correlate with the measured weight probability densities for corresponding fractions at the 95% confidence interval. Grain statistical parameters determined from the measured and predicted weight-frequency distributions agree closely:

<u>measured sample</u>	<u>calculated sample</u>
$\phi_{16} = 2.56$ [D <sub>16</sub> = 0.17mm]	$\phi_{16} = 2.44$ [D <sub>16</sub> = 0.18mm]
$\phi_{50} = 2.10$ [D <sub>50</sub> = 0.23mm]	$\phi_{50} = 2.08$ [D <sub>50</sub> = 0.23mm]
$\phi_{84} = 1.80$ [D <sub>84</sub> = 0.30mm]	$\phi_{84} = 1.80$ [D <sub>84</sub> = 0.30mm]

Grain statistical parameters calculated from the grain-number frequency distribution rather than by weight, however, exhibit slightly greater sample variance, with  $\phi_{16} = 2.76$  (D<sub>16</sub> = 0.15mm),  $\phi_{50} = 2.32$  (D<sub>50</sub> = 0.20mm), and  $\phi_{84} = 1.85$  (D<sub>84</sub> = 0.28mm). The median grain size by number of grains weights the nominal diameter of each particle equally. Because there are many more fine grains in a size fraction of a given weight than coarse grains in a class of comparable weight, grain-number frequency distributions in most cases are skewed toward the finer size fractions. Hence, grain-statistical parameters (e.g. the median) computed by number of grains for a poorly sorted sediment sample may be considerably smaller than the corresponding statistics calculated by weight. Originally, grain-size percentile measures were defined on the basis of grain weight (e.g. Lindholm, 1987), although some studies prefer to report statistical parameters of particle size as a function of grain number, perhaps resulting from the sample-collection methods used (e.g. Miller and Byrne, 1966). Given the differences shown above in the percentiles computed by grain weight



versus number, however, it is evident that these two statistical methods are not interchangeable. To maintain a basis for comparison of the empirical and theoretical results of this study, sample statistics will be given henceforth by weight percentile.

Figure 2.3 compares theoretical grain-distribution results for the sand sample used experimentally by Yamasaka and Ikeda (1988). This sample is noticeably more negatively skewed than the previous example (e.g. compare Figures 2.1a and 2.1b), with a fine-tail sorting of 18% and a coarse-tail sorting of 47% (Figure 2.3a). The weight-frequency curve calculated from the predicted grain-number probability distribution is nearly identical to the measured curve, at the 99% confidence level. Grain statistical parameters are essentially the same:

measured sample

$D_{16} = 0.32\text{mm}$   
 $D_{50} = 0.68\text{mm}$   
 $D_{84} = 1.35\text{mm}$

calculated sample

$D_{16} = 0.32\text{mm}$   
 $D_{50} = 0.68\text{mm}$   
 $D_{84} = 1.36\text{mm}$

## 2.2 Bed-generation algorithm

Once a size-frequency distribution by grain number has been generated from a specified weight-percent probability distribution, particles are selected randomly from it and placed sequentially along the evolving surface of a two-dimensional sediment bed. The initial layer of grains is deposited on a flat surface, which serves as the foundation for successive bed layers. Ten to 30 layers of grains typically provide a sufficiently thick, inhomogeneously arrayed bed for evaluating the mechanics of sediment transport and the subsequent topographic evolution of the bed surface.

Particles are represented as spheres of nominal diameter (e.g. a sphere with the same volume as the natural grain) and quartz density ( $\rho_s = 2.65 \times 10^3 \text{ kg/m}^3$ ). Spherical particle shapes are a suitable approximation in a large percentage of eolian environments, in which the asperities of sand grains are removed over time by intergranular abrasion, fracturing during collision, and chemical weathering (e.g. silica dissolution). Fourier-shape analyses and other computerized micrographic evaluations of sand samples from natural deposits demonstrate that grains become particularly well-rounded in the active sediment-transport zones of dunefields that are derived from older, weathered

sedimentary units (Mazzullo *et al.*, 1986; Pye and Tsao, 1990). Most of the sand comprising the Great Sand Dunes system derives from Precambrian granites and Paleozoic sandstones that have been continuously reworked and rounded by a combination of marine, fluvial, alluvial, and eolian processes (Johnson, 1967; Andrews, 1981).

In the model, the basal layer of grains is deposited on a horizontal surface to avoid imposing initial microtopographic irregularities that might influence the geometric array of overlying particles. Grains are selected sequentially from a file of particle diameters, obtained using the previously described random-number generator routine, and placed in an appropriate geometric configuration with other grains in the bed. In the basal layer of the bed only, this arrangement is determined by the angle of repose ( $\phi_o$ ) of a given particle and its diameter ( $D$ ) relative to the average diameter of the grains composing the bed ( $k_s$ ); see Figure 2.4a. The particle angle of repose, also called the friction or bed-pocket-geometry angle, is a fluid-mechanical measure of the ability of a resting particle to move upward and out of a pocket formed by adjacent stationary grains. At any value of the boundary shear stress, a stable bed-pocket geometry is one in which the combined forces of effective particle weight and intergranular friction, acting to keep a particle in its pocket, outweigh the combined, fluid-induced forces of lift and drag promoting its entrainment. Fluid forces acting on a resting grain are reduced if its protrusion relative to the top of the pocket is minimized.

At present, no analytical theorem exists for predicting the bed-pocket-geometry angle between grains of disparate size, largely due to the difficulties encountered in measuring micro-scale properties of natural beds and to the stochastic nature of grain packing and relative protrusion in poorly sorted sediments. The bed-generation algorithm, therefore, employs the semi-empirical method of Wiberg and Smith (1987b) to set the realistic spacing of grains at the base of the bed. Nonetheless, the manner in which grains are distributed across the basal plane is relatively unimportant because any topographic expressions of the basal layer are masked by successive layers of grains comprising the bed.

Wiberg and Smith (1987b) developed a geometric expression for  $\phi_o$  from analyses of grain angle-of-repose measurements made by Miller and Byrne (1966) for test grains of varied diameter

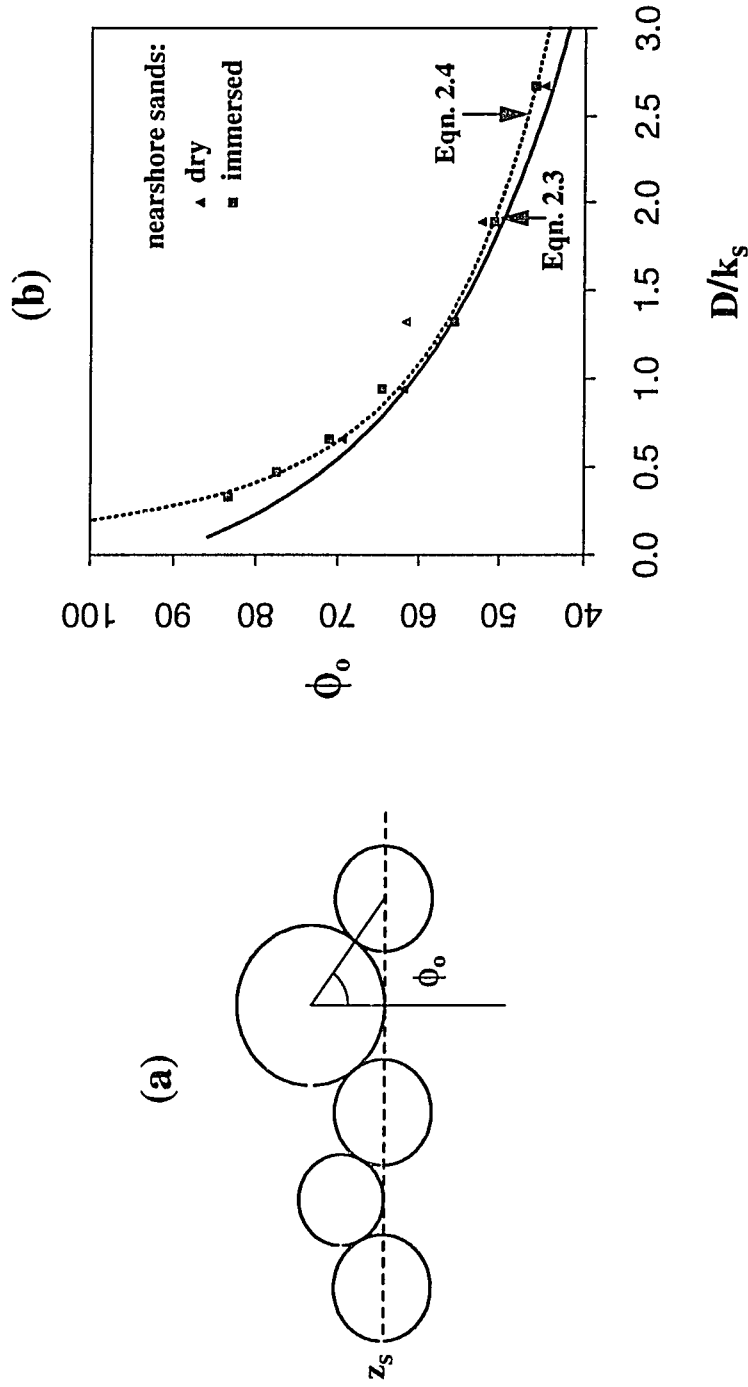


**Figure 2.4** Relationships between the particle angle-of-repose,  $\phi_o$ , and the ratio of grain size to the average size of particles composing the bed,  $D/k_s$ . (a) The angle of repose  $\phi_o$  of a particle resting in a bed pocket, where  $z_s$  is the average level of the bottom of the grain before it begins to roll from the pocket. (b)  $\phi_o$  as a function of  $D/k_s$ , from the experiments of Miller and Byrne (1966) for sub-rounded, nearshore sands. The dashed curve shows their regression-equation fit to the data; the solid curve denotes the geometric relationship of Wiberg and Smith (1987b). For  $D/k_s > 0.5$ , the latter provides a good approximation of the Miller and Byrne data (see text equation 2.3); for  $D/k_s < 0.5$ , the dashed curve (text equation 2.4) is appropriate. [After Wiberg and Smith, 1987b, Fig. 6.]

positioned randomly on different types of natural sediment beds. Sediments, both dry and wetted, were adhered to a tiltable plane, which allowed measurement of the angle at which loose, test grains rolled from their pockets. Experiments were conducted with beds composed of angular grains (crushed quartzite), sub-rounded grains (nearshore sands), and spheres. Wiberg and Smith re-analyzed the empirical data to obtain the following geometric relationship for grain angles of repose as a function of test grain diameter ( $D_m$ ) and the average diameter of the bed grains ( $k_s$ ):

$$\phi_o = \text{acos} \left[ \frac{D_m/k_s + z_s}{D_m/k_s + 1} \right] \quad (2.3)$$

where  $z_s$  is the average level of the bottom of the grain residing in the bed pocket (Figure 2.4a) and the subscript  $m$  denotes the sediment component of interest from the frequency distribution of grain sizes. For the sub-rounded grain class, which bears the closest resemblance to natural eolian sands, this expression agrees most closely with the experimental data if  $(D_m/k_s) > 0.5$  and  $z_s = -0.02$  (Figure 2.4b). For  $(D/k_s) < 0.5$ , the bed-pocket angle  $\phi_o$  is given by the power-law relationship (Miller and Byrne, 1966):

$$\phi_o = c_o (D_m/k_s)^{-\beta} \quad (2.4)$$

where the regression coefficients  $c_o = 61.5$  and  $\beta = 0.3$ .

A representative basal bed section, composed from the Great Sand Dunes particle-frequency distribution, is shown in Figure 2.5a. In this example, randomly chosen grains are spaced according to the  $\phi_o$  vs.  $D_m/k_s$  relationship, in which the average bed-grain diameter  $k_s = D_{50} = 0.23\text{mm}$ . These grains are denoted as dashed disks or circles in the figure; solid-lined disks signify overlying grains of diameter  $D_m$ .

Successive layers of the bed are formed by adding grains from the calculated size-frequency distribution and placing them in geometrically viable positions relative to the rest of the bed grains. Each grain,  $D_m$ , added to the developing bed surface is permitted to move from pocket to pocket, in the downwind direction, until a stable geometric configuration (described in the next paragraph) is encountered. Once that grain is situated, the next grain from the randomly composed distribution list is placed in the first available downwind pocket that can accommodate it geometrically. This

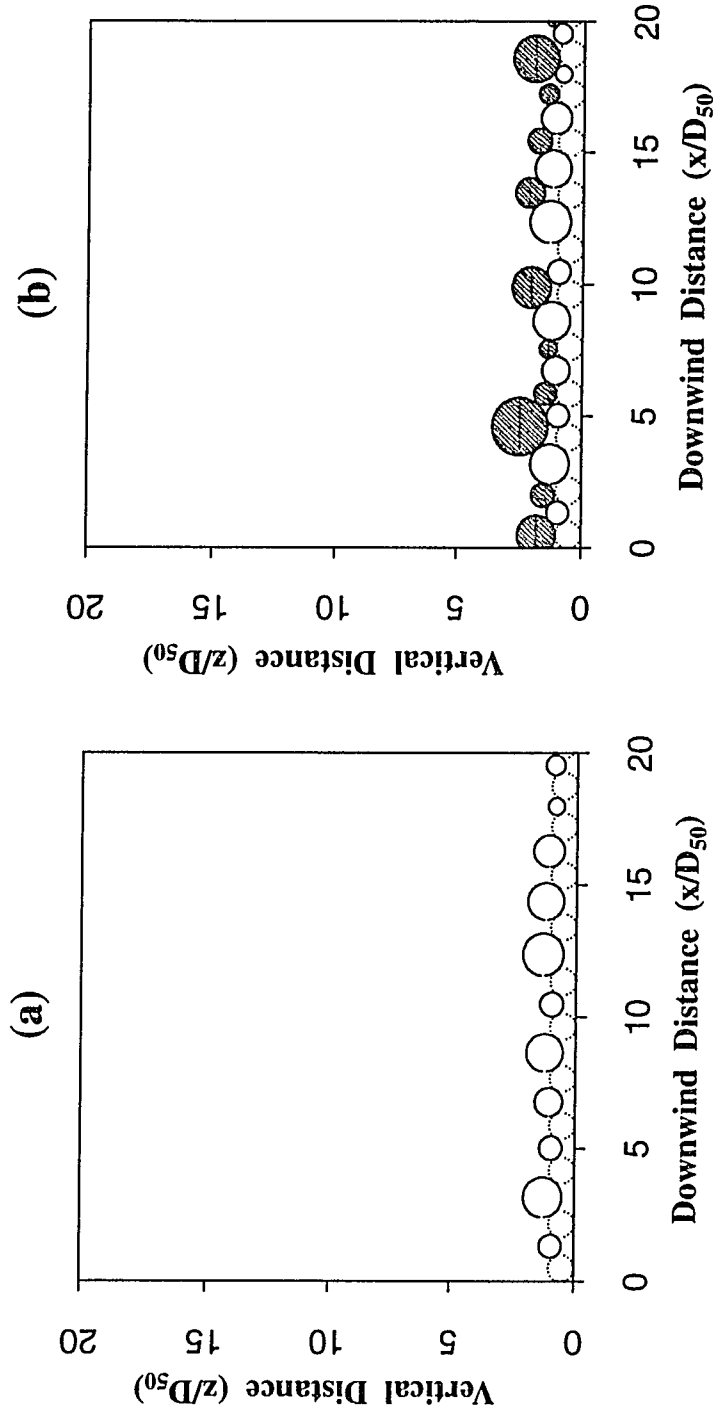


**Figure 2.5** Computer-generated bed section in the initial stages of construction. (a) Grains forming the basal layer of the bed are deposited on a flat surface and spaced according to the relationship between the bed angle of repose,  $\phi_0$ , and the ratio of grain diameter to average bed-particle diameter,  $D/k_s$ . Solid-lined disks denote grains chosen at random from a grain-size frequency distribution and deposited as the bed basal layer; dashed disks are the average-sized bed particles,  $k_s$ , used to position the basal-layer grains. (b) The same bed configuration shown in (a) but with an added layer of grains, denoted as hatched disks. Selected at random from the grain-size frequency distribution, these grains are deposited in surface pockets between bed particles, according to a geometric algorithm that relates the incoming grain dimensions to the size, spacing and orientation of the pocket-forming grains (see text). Great Sand Dunes sample;  $D_{50} = 0.23\text{mm}$ .

strategy effectively produces superposed layers of grains, in which pockets left vacant at one level are filled or covered with particles from successive layers. In Figure 2.5b, particles forming the first layer developed above the bed base are shown as hatched disks. Note that all available pockets were not filled, because grains selected from the distribution were too large to fit within them. This pocket selection-and-rejection behavior of particles also has been documented in photographic analyses of incipient grain motion in wind tunnels (e.g. Bagnold, 1941; Chepil, 1959; Nickling, 1988).

The potential for a chosen grain to reside in a pocket created by surrounding bed particles depends on its diameter relative to the size, spacing, and orientation of pocket grains. A pocket is defined by a bed grain and any other downwind grains  $D_{1,\dots,n}$  whose exposed surfaces cumulatively form a concavity that can accommodate an incoming grain with no overlapping of particles. Stable pocket configurations are located by positioning an introduced grain between two, coplanar bed particles whose surfaces are exposed to the incoming particle, such that the x-coordinate of its center lies between the upwind ( $x_1$ ) and downwind ( $x_2$ ) bed-grain centers, and the incoming grain does not overlap with any other grains composing the sediment bed. If overlap occurs, then the incoming grain moves to the next potential pocket formed by grains with centers  $[x_2, z_2]$  and  $[x_3, z_3]$ , and so forth. Figure 2.6 illustrates a typical configuration in which two bed particles with centers  $[x_1, z_1]$  and  $[x_2, z_2]$  create a potential pocket for an incoming grain with center  $[x_p, z_p]$ . Coordinates  $[x_p, z_p]$  are defined by the intersection of two circles with radii  $r_1$  and  $r_2$ , where  $r_1$  equals the sum of the radii of grain  $[x_1, z_1]$  and the incoming grain, and  $r_2$  is the summed radii of grain  $[x_2, z_2]$  and the incoming grain. This configuration establishes a triangle with sides of length  $r_1$ ,  $r_2$ , and  $p = \overline{x_1 x_2}$ , which can be used to solve for the center coordinates of the newly added grain. This is accomplished by computing the magnitude of angle  $A$  and triangle lengths  $r_1$ ,  $r_2$ ,  $d$ , and  $p = [(x_2 - x_1)^2 + (z_2 - z_1)^2]^{1/2} = p_1 + p_2$ . Length  $d$ , perpendicular to  $\overline{x_1 x_2}$ , forms two right triangles, such that  $p_1^2 = r_1^2 - d^2$  and  $p_2^2 = r_2^2 - d^2$ . Solving for  $p_1$  and  $p_2$  in terms of  $r_1$ ,  $r_2$ , and  $p$  gives:

$$p_1 = \frac{r_2^2 - r_1^2 - p^2}{-2p} \quad ; \quad p_2 = \frac{r_2^2 - r_1^2 + p^2}{2p} \quad . \quad (2.5)$$

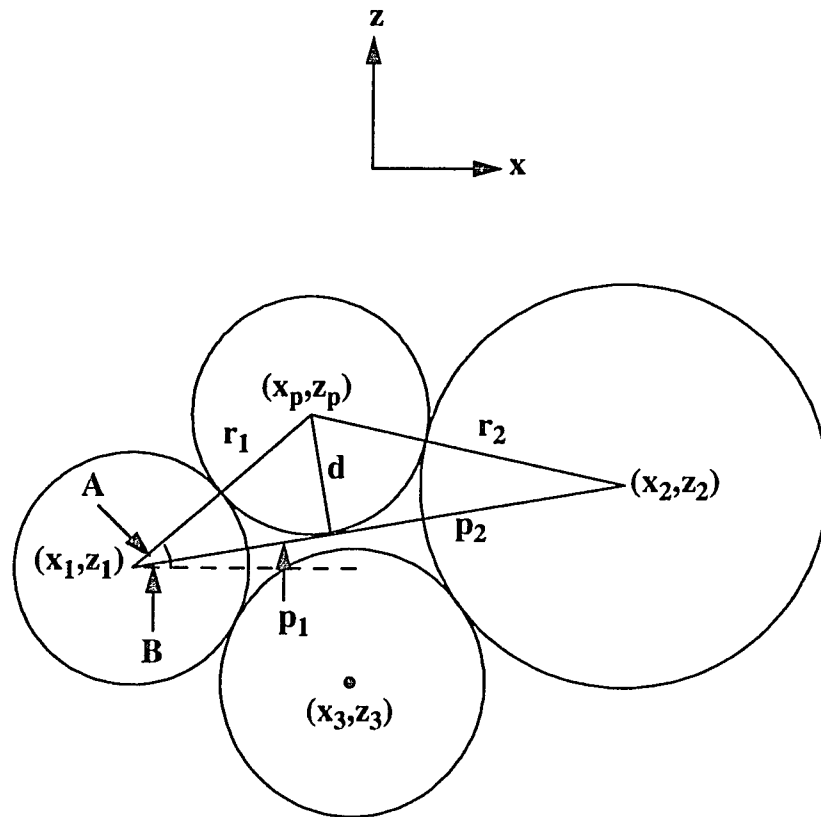


**Figure 2.6** Definition of the geometric relationships between bed grains, for determining whether a given bed pocket can accommodate an incoming grain. Grains with center coordinates  $[x_1, z_1]$ ,  $[x_2, z_2]$ , and  $[x_3, z_3]$  denote pocket-forming bed particles. The introduced particle has center  $[x_p, z_p]$ . A triangle formed by lengths  $p = \overline{x_1 x_2}$  and the summed radii of the incoming grain with the upwind ( $r_1$ ) and downwind ( $r_2$ ) bed particles, respectively, is used to solve for the values of  $[x_p, z_p]$ . This calculation also requires finding the length of triangle sides  $d$ ,  $p_1$ , and  $p_2$ , as well as the magnitude of angle  $A$ . The slope of  $\overline{x_1 x_2}$  relative to the bed-normal, or  $x$ -, axis is specified by angle  $B$ . Once  $[x_p, z_p]$  is found, the potential for overlap of the incoming grain with all other grains in the bed is assessed; if overlap occurs, this grain is moved to the next available pocket and the new geometric configuration is evaluated in a similar manner.

Length  $d$  is found by substitution of (2.5) into  $d^2 = r_1^2 - p_1^2 = r_2^2 - p_2^2$ :

$$d = \left[ \frac{(r_1 + r_2 + p) (r_1 + r_2 - p) (r_1 + p - r_2) (r_2 + p - r_1)}{4p^2} \right]^{\frac{1}{2}} . \quad (2.6)$$

The magnitude of angle  $A$  is:

$$\begin{aligned} \angle A &= \left( \operatorname{atan} \left( \frac{d}{p_1} \right) + \angle B \right) && \text{if } (p_2 \geq d) \\ &\text{or} && \\ \angle A &= \pi - \left( \operatorname{atan} \left( \frac{d}{p_1} \right) + \angle B \right) && \text{if } (p_2 < d) ; \end{aligned} \quad (2.7)$$

where  $\angle B$  is the divergence of  $\overline{x_1 x_2}$  from the x-axis of the bed plane. The new position of the center of the incoming grain has coordinates:

$$x_p = (\cos A \cdot r_1) \pm x_1 ; \quad z_p = (\sin A \cdot r_1) \pm z_1 . \quad (2.8)$$

This grain will remain in its new pocket provided that it is not superimposed on other particles, in this case with grain  $[x_3, z_3]$  (Figure 2.6). The only constraint imposed on this geometric formula is that a particle added to the bed layer must touch two bed grains, not just one. One grain perched freely on the convex surface of another is not physically realistic and, furthermore, would create a pocket with an implausible orientation in relation to the bed-normal direction.

With this grain-geometry algorithm, sediment beds may be constructed to any specified thickness and length. Figure 2.7 shows a typical bed section approximately 20 grain layers, or 14  $D_{50}$ , thick and 30  $D_{50}$  long. The basal layer of  $D_{50}$  grains is excluded graphically and from the bed-geometry (e.g. grain packing) calculations. The resulting sediment beds exhibit irregular granular arrangements with relatively loose packing. The grain-packing arrangement displayed in this figure obtains largely from the working hypothesis of the model, in which grains are placed sequentially in appropriate pockets, leaving some pockets empty and, thus, producing an internal structure with open interstitial networks. An alternative hypothesis would be to fill each identified pocket with a grain selected especially for it from the distribution, rather than randomly testing pockets and



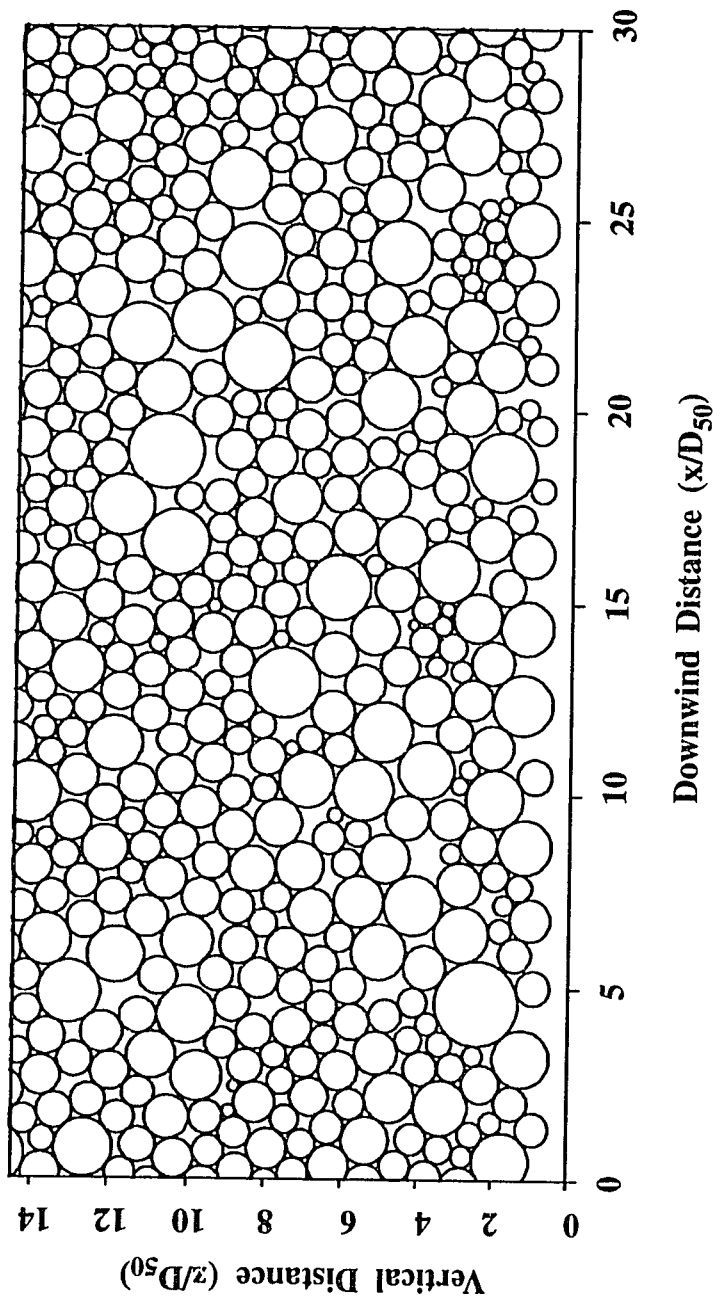


**Figure 2.7** Example of a computer-generated, two-dimensional, sediment bed. Downwind and vertical axes are nondimensionalized by  $D_{50}$  of the grain-size frequency distribution. This bed section has a downwind length of  $30 D_{50}$  and a vertical thickness of  $15 D_{50}$ . Grains, represented as disks, are packed in irregular, relatively loose arrays separated by interstitial pore space. [Great Sand Dunes sand sample;  $D_{50} = 0.23\text{mm}$ ,  $D_{16} = 0.18\text{mm}$ ,  $D_{84} = 0.30\text{mm}$ .]

bypassing them if grain overlap occurs. Employing this method, however, results in very tightly packed beds whose bed-pocket geometries and interstitial volumes compare unfavorably with measured statistics for the same size-frequency distributions.

### 2.3 Characteristics of the sediment surface

The bed cross-section graphed in Figure 2.8 illustrates a characteristic of some sediment surfaces produced by the geometric formula discussed above. Grains deposited as the final surface layer occasionally are left perched in unnatural positions, often as the top grain of a precariously constructed pile or cluster of particles. If bed construction were continued to greater heights above this surface, these isolated particles would become surrounded and stabilized by other grains. When they form the bed surface, however, they are exposed to the fluid flow, which will transport them readily to a more sheltered bed pocket.

This phenomenon of grain perching has been reported from the initial preparation of sand beds in wind tunnels for sediment-transport experiments, where grains laid along the tunnel floor in the absence of a fluid flow form artificial micro-piles (Greeley *et al.*, 1977; Nickling, 1988). These piles result in spurious measurements of particle initial motion and typically are removed prior to experimentation by raising the air velocity toward the threshold for particle motion and then dropping it back to zero. In a similar manner, the computer-generated sediment bed is smoothed of its unrealistic grain protuberances by applying a flow-induced, local boundary shear stress to its surface and then incrementally increasing the stress until the unstably positioned grains are re-situated. These grains, for example the solid particles shown in Figure 2.8, usually topple into more stable bed-pocket geometries at shear stresses that are one-half to one order of magnitude below their respective critical shear stresses for initial motion.

The bed-smoothing algorithm used to remove unbalanced surface grains contains a fluid mechanical element that evaluates, for each incremental value of the instantaneous, local boundary shear stress ( $\tau_b$ ), the potential for each grain to move out of the bed pocket in which it resides and migrate downwind to the next closest stable pocket geometry. The relocated grain can be remobilized, at the same increment of  $\tau_b$ , if its new pocket collapses through removal of adjacent

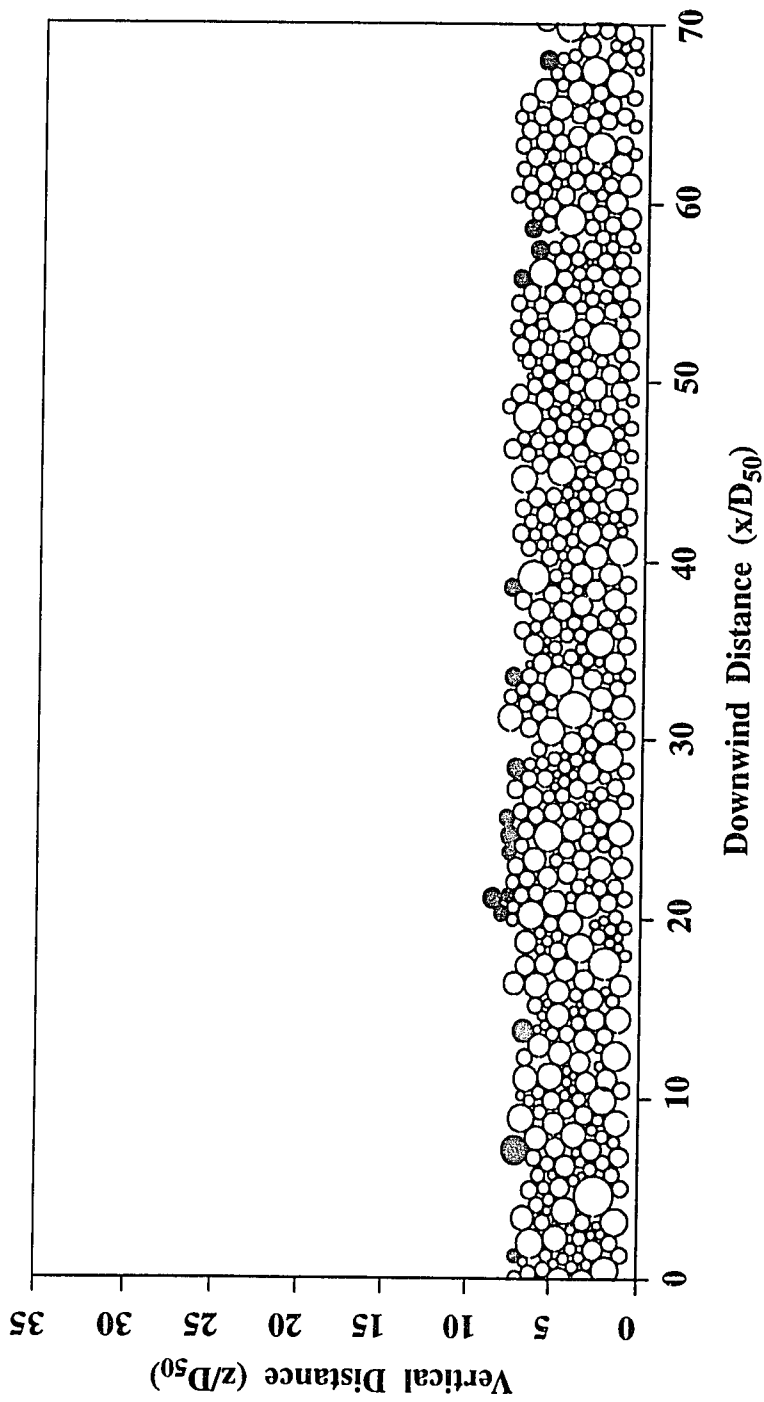
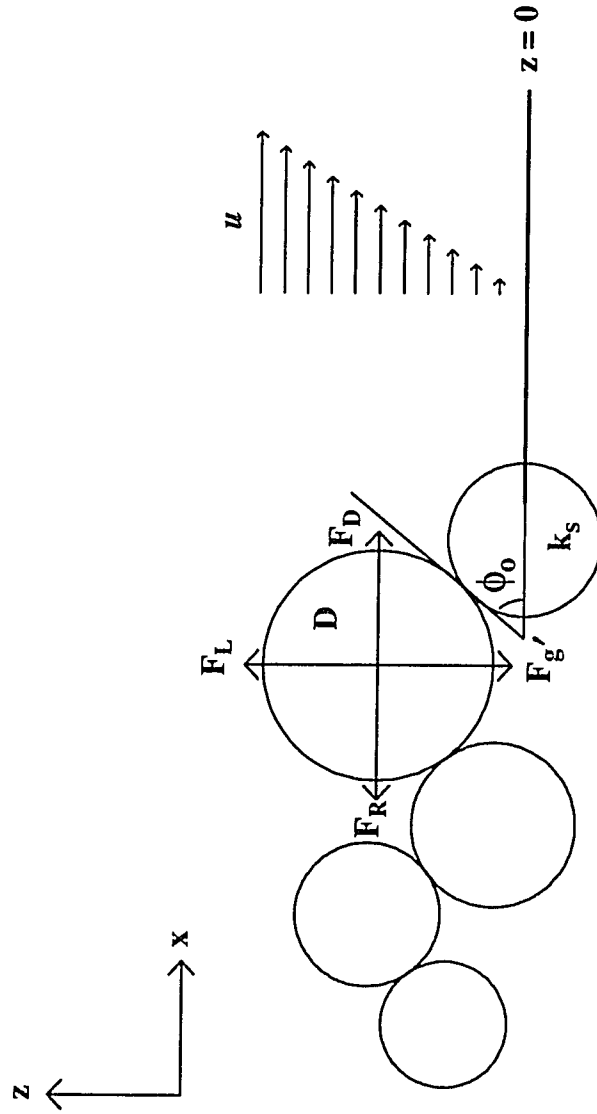


Figure 2.8 Example sediment bed with a downwind length of  $70 D_{50}$  and a thickness of about  $8 D_{50}$ . Solid disks denote grains left perched on the surface by terminating bed construction prior to filling the adjacent bed pockets. Perched grains are redistributed into more stable bed-pocket configurations by sweeping the bed with low-velocity flows, well below the threshold velocities required to initiate rolling or saltation fluid mechanically. Once the sediment surface has been smoothed of irregular grain arrangements, a fully posed fluid-mechanical element is coupled with the bed-generation formula to transport bed particles. [Great Sand Dunes sample;  $D_{50}=0.23\text{mm}$ ]

particles. The flow-induced stress is applied to the entire bed; grains below the first few layers comprising the sediment surface, however, are unaffected until  $\tau_b$  significantly exceeds the critical value for grain motion and subsurface grains become exposed through erosion of overlying particles.

The mechanics of grain initial motion have been formulated explicitly for subaqueous sediment transport (Wiberg and Smith, 1985, 1987b), whereby particle initial conditions are specified in terms of the fluid and body forces acting on individual grains, the particle angles of repose, and the  $D/k_s$  relationship. Although true initial motion is not being considered in this case, because grains are being removed from unnatural positions at flow velocities well below those required to propel grains into the airstream, the mechanics of particle first motion can be employed to redistribute grains objectively and in a physically accurate manner. It has been established, both theoretically and empirically, that the dynamical behavior of moving grains in water versus air differs considerably, as a result of the thousand-fold decrease in fluid density. Fluid-mechanical forces on sedimentary particles due to lift, drag, and relative acceleration scale with the fluid density, whereas inertial forces scale with the sediment density. Consequently, collisional forces on grains become relatively more important in air, whereas fluid-mechanical forces primarily govern grain behavior in water. The physical mechanisms by which a grain begins to pivot upward and eject from its bed pocket, however, are similar in both fluids. Initial motion depends largely on the particle angle of repose, the closeness of grain packing, the immersed density of the grain, and the upward- and outward- directed forces acting on it, which can be characterized similarly for both water and air.

The forces acting on a sediment grain that rests on a flat bed are those of gravity ( $F_g$ ); lift and drag due to fluid motion over the bed ( $F_L$  and  $F_D$ ); and a force resisting grain motion, acting on the particle as a result of the bed geometry,  $F_R = [(F_g - F_B - F_L) \tan \phi_o]$ , where the force terms in parentheses represent the particle's effective weight (gravity minus buoyancy and lift) and  $\phi_o$  is the particle angle of repose discussed previously (see Figure 2.9). Following the approach of Wiberg and Smith (1987b), the point at which a sediment grain first begins to move can be quantified by balancing the forces resisting motion against those promoting downwind acceleration:



**Figure 2.9** Force balance on a grain resting in a bed-surface pocket, where  $F_L$ ,  $F_D$ ,  $F_g'$ , and  $F_R$  are the forces of lift, drag, gravitational acceleration, and resistance due to the particle effective weight, the ratio of  $D/k_s$ , and the bed-pocket angle  $\phi_0$ . The mean flow velocity is  $u$ , which varies linearly with  $z$  from  $z=0$  through the near-bed, viscous sublayer in which the bed grains are submerged. The zero-velocity reference is placed at the center of the pocket grain,  $k_s$ , unless the particle of interest is part of a larger, perched pile of grains (see text).

$$(F_{g'} - F_L) \tan \phi_o = F_D . \quad (2.9)$$

$F_{g'}$  denotes the immersed weight of the grain, equivalent to  $(F_g - F_B) = (\rho_s - \rho)gV$ , where  $\rho_s$  is the sediment density,  $\rho$  is the air density,  $g$  is gravitational acceleration, and  $V$  is the grain volume.

The lift force acts on a grain as a result of normal and tangential stresses applied to the grain surface, and is expressed as:

$$F_L = \frac{1}{2} c_L \tau_b [f^2(z_T/z_o) - f^2(z_B/z_o)] A_x , \quad (2.10)$$

where  $c_L = 0.2$  is the lift coefficient,  $z_T$  and  $z_B$  are the heights of the top and bottom of the grain, respectively, as it rests on the bed,  $z_o$  is the bed-roughness parameter, and  $A_x$  is the cross-sectional area of the grain in the plane normal to the lift force. Terms  $[f^2(z_T/z_o)]$  and  $[f^2(z_B/z_o)]$  are fluid velocity-profile functions, defining the velocity gradient across the surface of the particle from top to bottom. They obtain from the relationship of the vertical profile of downwind velocity  $u(z)$  to the shear velocity  $u_*$ ; i.e.,  $f(z/z_o) = u(z)/u_*$ , where  $u_* = [\tau_b / \rho]^{1/2}$ .

The drag force,  $F_D$ , similarly depends on the velocity-profile function  $f(z/z_o)$ , averaged over the grain cross-section, and can be written as:

$$F_D = \frac{1}{2} c_D \tau_b \langle f^2(z/z_o) \rangle A_x \quad (2.11)$$

where  $c_D$  is the drag coefficient. The coefficient  $c_D$  is calculated from the experimental relationship for spheres as a function of the particle Reynolds number  $Re = [\langle u \rangle D / \nu]$ , where  $\langle u \rangle$  is the vertically averaged velocity,  $D$  is the nominal grain diameter, and  $\nu$  is the kinematic viscosity (see Schlichting, 1979; Wiberg and Smith, 1985). The values of  $c_L$  and  $c_D$  used here are common in the sediment-transport literature.

Rearrangement of equation 2.9 gives the left-hand side of the following equation, which can be equated with the right-hand side by substituting the expressions for the immersed weight of the grain,  $F_{g'}$ , and the drag force,  $F_D$ :

$$\frac{F_D}{F_{g'}} = \frac{\tan \phi_o}{1 + \tan \phi_o (F_L / F_D)} = \frac{\tau_b}{(\rho_s - \rho) g V} \frac{c_D}{2} A_x \langle f^2(z/z_o) \rangle . \quad (2.12)$$

A grain will begin to move from its resting position when an incremental increase in the boundary shear stress  $\tau_b$  just exceeds the value necessary to topple the grain from its pocket; this threshold value is denoted  $\tau_{th}$ . An analogous expression to (2.12) can be written for  $\tau_{th}$ . At the stress  $\tau_b = \tau_{th}$  when the grain begins to move,  $\tau_{th}$  can be found by rearrangement of the left- and right-hand terms in (2.12), which yields:

$$\tau_{th} = [(\rho_s - \rho)gD] \frac{V}{A_x D} \frac{2}{(c_D)_{th}} \frac{1}{\langle f^2(z/z_o) \rangle} \frac{\tan \phi_o}{[1 + (F_L/F_D)_{th} \tan \phi_o]} \quad (2.13)$$

in which the term  $[A_x D/V] = \alpha$  describes the physical properties of the moving grain;  $\alpha = 1.5$  for spheres. The threshold stress can thus be defined in terms of the grain mass and geometric properties, the bed-pocket geometry, the drag coefficient and ratio of the lift to drag forces, and the fluid velocity averaged over the grain cross-section. [See Wiberg and Smith, 1985, 1987b, for a more complete derivation of these expressions, and for a discussion on data analyses performed to derive the lift and drag coefficients. Their method has been used here without modification.]

The flow-velocity equation used in these calculations is given by:

$$u(z) = \frac{u_*^2 z}{\nu} \quad (2.14)$$

where  $z$  denotes the height above the bed. This expression pertains to the vertical profile of velocity within the viscous sublayer draping the bed surface, which has a linear form. Equation 2.14 is appropriate in this instance because the flow velocities used to smooth the bed are negligible, such that the roughness Reynolds number  $R_* = u_* k_s / \nu \leq 3$  (i.e. hydraulically smooth flow). Typical values of  $R_*$  are between 2.5 and 4.0. Grains comprising the sediment bed are totally submerged within the viscous sublayer, which has an average height of  $\delta_v = 11.6\nu/u_*$ . The linear profile of velocity for  $R_* < 3$  is considered valid only in the region  $z > 3k_s$ ; however, given  $\delta_v > k_s$ , the near-bed flow can be approximated by extending the linear velocity profile to the zero-velocity level of the bed.

The value of the bed-roughness parameter  $z_o$ , at which the velocity profile goes through zero, is determined on a grain-by-grain basis. In granular arrangements where the bottom of the almost-

moving grain lies near the average level of the centers of the grains composing the bed surface, then  $z_o$  is taken as the center of the bed particle,  $k_s$ , forming the downwind side of the pocket in which the grain of interest resides (Figure 2.9). In other cases, however, where one or more particles occupy the top of an unstable cluster of grains, the zero level of the bed connects the contact points between adjacent grains supporting the pile, and calculations are performed to determine the stability of the entire mass (see Figure 2.10). These clusters typically contain three to six particles. The reason for this modification in the  $z = 0$  reference is that grains composing the base of a pile might be configured in an unstable array, which would collapse at a given  $\tau_b$ , but they can form a stable bed-pocket geometry for a grain or grains sitting on top of them. These top grains, however, are susceptible to the instability of the underlying cluster, and when  $\tau_b > \tau_{th}$  for the grains at the base, then the whole pile collapses. Each dislocated particle then is moved downwind to the closest available bed pocket for which  $\tau_b < \tau_{th}$ .

The bed-smoothing algorithm applies only within the range of boundary shear stresses below the critical shear stresses for initial motion of individual bed-surface particles. Once the fluid shear is sufficient to roll or entrain particles, momentum exchange between the moving grains, the airflow, and the bed surface begins to alter the fluid forces on grains at or near the bed. Hence, fully posed fluid-mechanical and collisional forces, incorporating the dynamics of momentum exchange between the fluid and solid components, must be included to predict the characteristics of grain trajectories, the vertical dispersal of horizontally accelerating grains that extract momentum from the flow, and the outcome of grains returning to and impacting the bed.

To demonstrate the sensitivity of the bed surface to incremental increases in the local boundary shear stress, Figure 2.11(a-h) shows a sequence of longitudinal cross-sections of a bed segment over the range from no shear to 1.6 times the critical shear stress ( $\tau_{cr}$ ) for initial motion of the  $D_{50}$  surface grains. In this example,  $D_{50} = 0.23\text{mm}$ , and  $(\tau_{cr})_{50} = 9.0 \times 10^{-2} \text{ N/m}^2$  or  $[(\tau^*)_{cr}]_{50} = 1.51 \times 10^{-2}$ , where  $(\tau^*)_{cr} = \left[ \tau_{cr} / (\rho_s - \rho) g D \right]$  is the nondimensional, critical Shields stress. For these and all other calculations, the sediment density  $\rho_s = 2.65 \times 10^3 \text{ kg/m}^3$ , air density =  $1.20 \text{ kg/m}^3$ , and gravitational acceleration  $g = 9.80 \text{ m/s}^2$ . Vertical arrows above surface grains denote particles that will move at the next stress increment (e.g. the next diagram); solid disks specify the



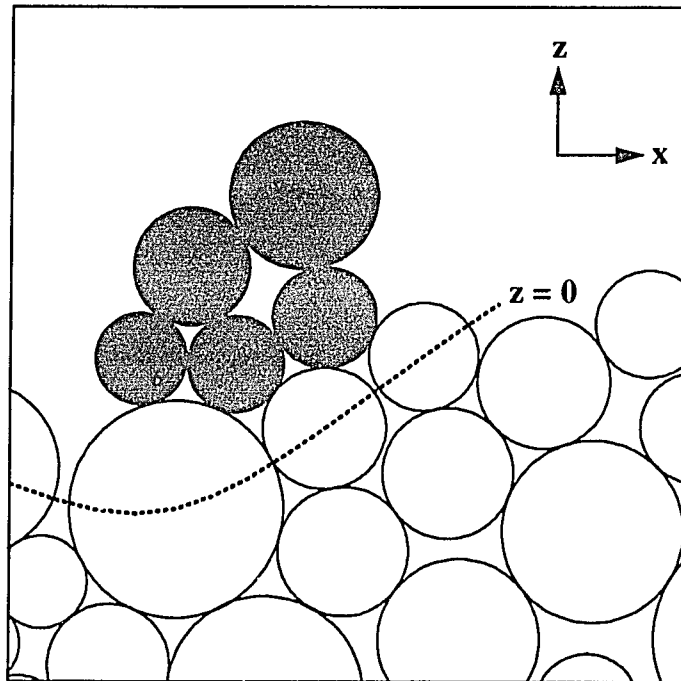


**Figure 2.10** Example of an unstably perched pile of surface grains, denoted as solid disks. These particles are redistributed fluid mechanically prior to subjecting the bed to sediment-transporting flows. The  $z = 0$  reference, at which the fluid velocity goes to zero, is given by the dashed line and connects the contact points between bed grains that support the cluster.

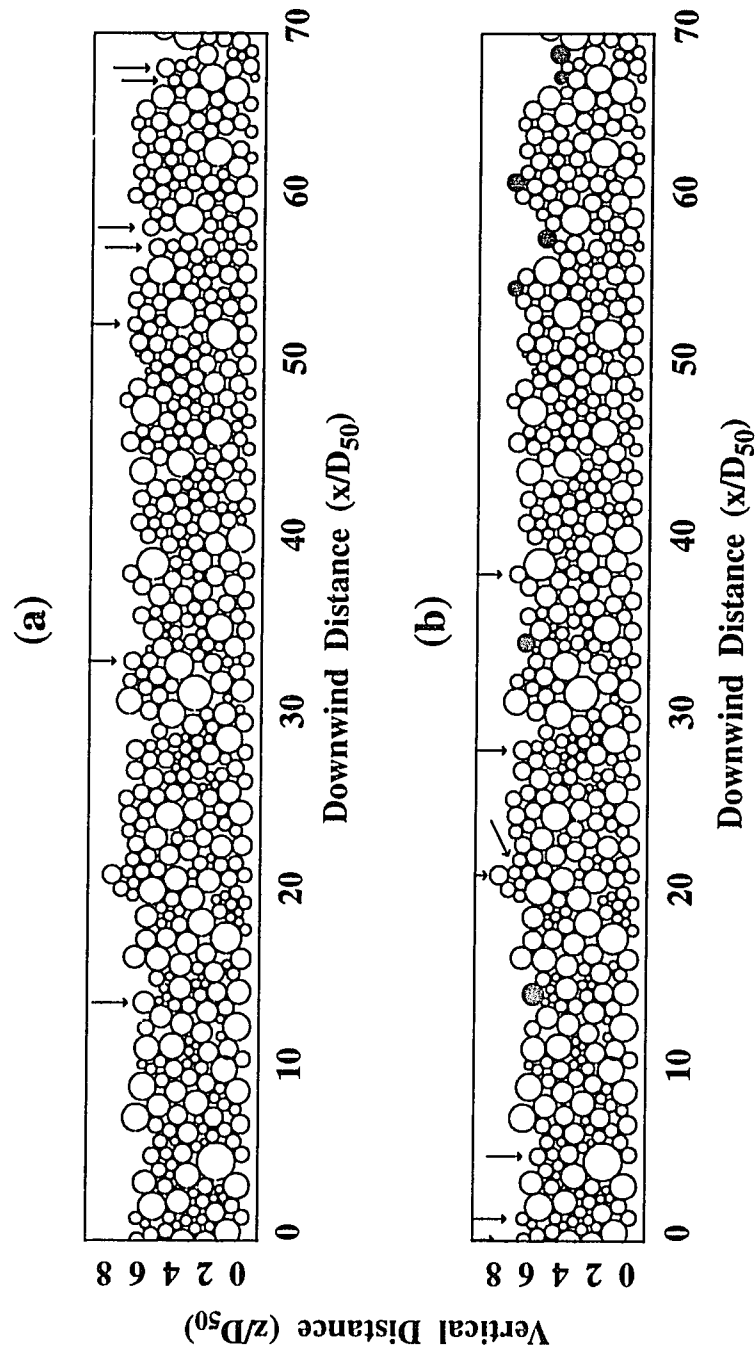


**Figure 2.11** Evolution of the sediment bed surface with increasing fluid shear. Arrows pinpoint grains that will move at the next incremental increase in the Shields stress  $[\tau_*]$  (e.g. in the successive diagram); solid disks represent the new locations of these grains at the given value of  $\tau_*$ . (a) The bed surface at  $\tau_* = 0$ . Grains identified with arrows are shown as solid particles in (b). (b) The bed surface at  $\tau_* = 3.35 \times 10^{-3}$ . The critical Shields stress  $(\tau_{*})_{cr} = 1.51 \times 10^{-2}$  for the  $D_{50} = 0.23\text{mm}$  size fraction.

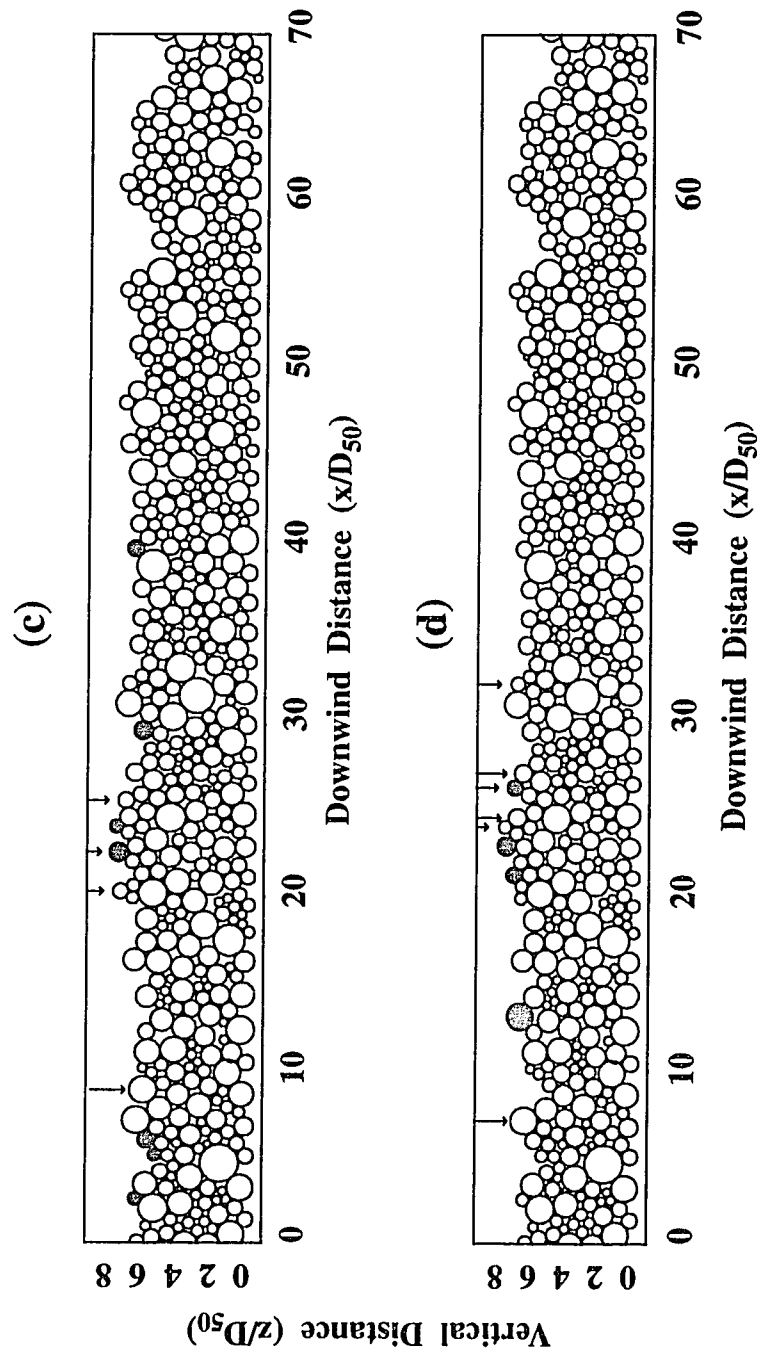


**Figure 2.11 continued.** Evolution of the sediment bed surface with increasing fluid shear. (c) The sediment bed at  $\tau_* = 6.70 \times 10^{-3}$ . (d) The bed surface at  $\tau_* = 1.01 \times 10^{-2}$ . The critical Shields stress  $(\tau_*)_{cr} = 1.51 \times 10^{-2}$  for the  $D_{50} = 0.23\text{mm}$  size fraction.

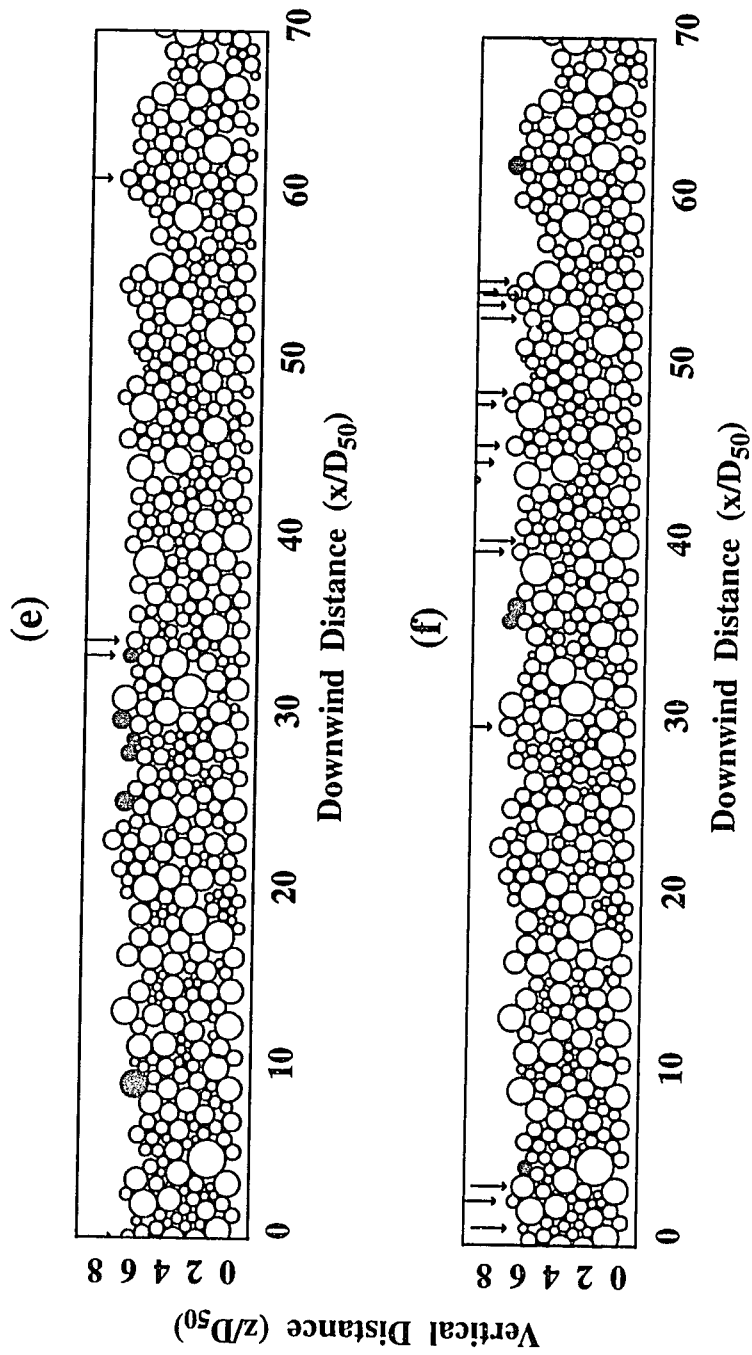


**Figure 2.11 continued.** Evolution of the sediment bed surface with increasing fluid shear. (e) The bed surface at  $\tau_* = [(\tau_*)_{cr}]_{16} = 1.34 \times 10^{-2}$ . The critical Shields stress for the  $D_{50}$  fraction,  $[(\tau_*)_{cr}]_{50} = 1.51 \times 10^{-2}$ , lies between the values of  $\tau_*$  in (e) and (f). This marks the transition between isolated movement of individual grains at the surface, and mobilization of patches of grains that, upon removal, expose the subsurface grains to erosion. (f) The bed surface at  $\tau_* = 1.68 \times 10^{-2}$ . At this value of the stress, some grains are moving as much as  $100D_{50}$  downwind.

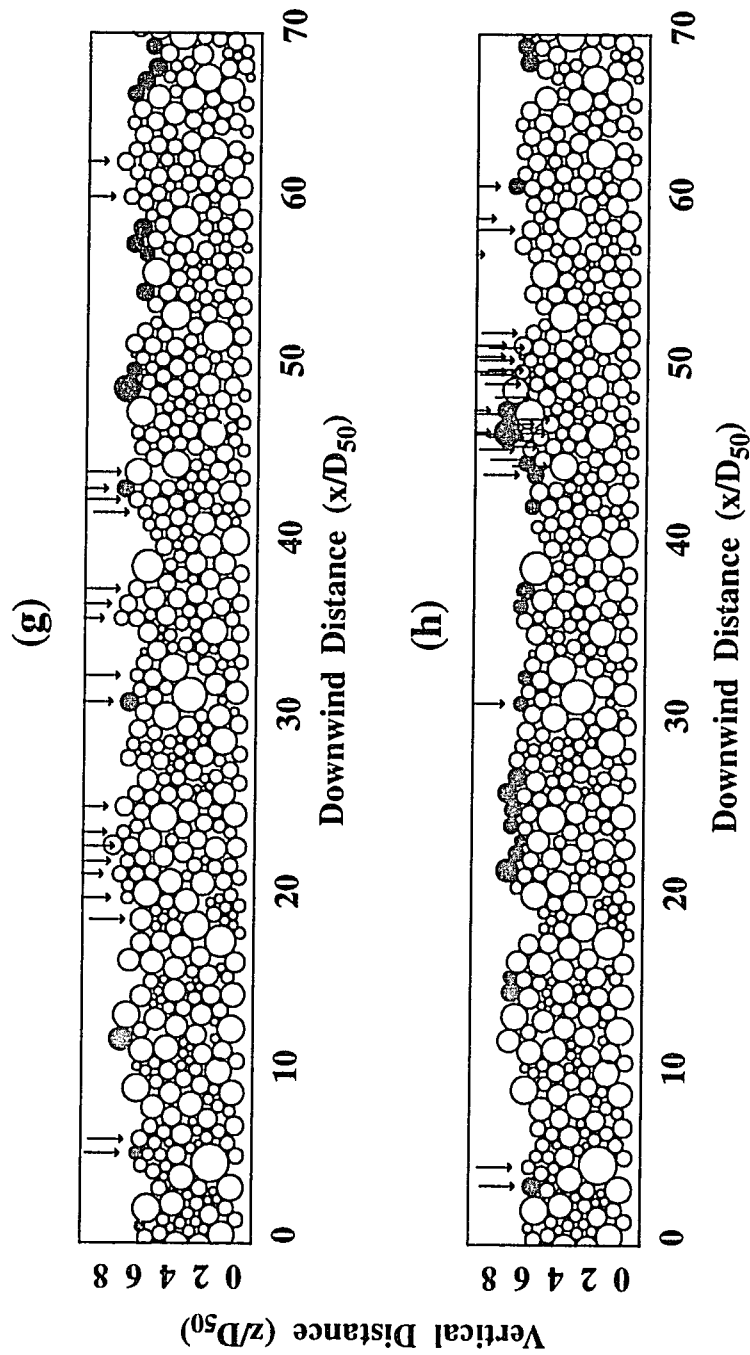


**Figure 2.11 continued.** Evolution of the sediment bed surface with increasing fluid shear. (g) The bed surface at  $\tau_* = 2.01 \times 10^{-2}$ . Grains are beginning to move in discrete surface clusters or patches. (h) The bed surface at  $\tau_* = 2.35 \times 10^{-2}$ . Active erosion of subsurface grains beneath the mobilized grain patches is apparent. The critical Shields stress is  $(\tau_*)_{cr} = 1.51 \times 10^{-2}$  for the  $D_{50} = 0.23\text{mm}$  size fraction and  $(\tau_*)_{cr} = 1.79 \times 10^{-2}$  for the  $D_{84} = 0.30$  size fraction.

new locations of grains removed from unstable, upwind bed-pocket geometries at the specified shear stress. Grains are allowed to move both downwind, onto and off the bed section, as well as upwind in the case where particles on the upward slope of a multi-grain bed depression roll backward into a more stable geometric configuration.

For  $\tau_* = [\tau_b / (\rho_s - \rho)gD_{50}]$  less than the critical Shields stress, the relatively few dislocated grains are toppling from fairly obvious perched geometries. By  $\tau_* = 6.70 \times 10^{-3}$  (Figure 2.11c), the bed has been smoothed of its most noticeable irregular bumps. At  $\tau_* = [(\tau_*)_{cr}]_{D16} = 1.34 \times 10^{-2}$  (Figure 2.11e), the average height of the bed surface is fairly uniform with more regularly arrayed particles, and isolated, dislodged grains are moving, at most, only a couple of bed pockets downwind. This condition persists until slightly above  $\tau_* = [(\tau_*)_{cr}]_{50}$  (e.g. Figure 2.11f), when the sediment surface becomes considerably more mobilized.

For  $\tau_* > [(\tau_*)_{cr}]_{50}$ , the number of grains dislocated downwind increases rapidly. Surface patches of mixed-sized grains begin to develop and move downwind as multi-particle units. Once the several grains forming the surface of a low-amplitude patch are removed from their pockets, the underlying grains also become susceptible to erosion. In many cases, a larger dislodged grain will move downwind and then form a trap for smaller particles travelling behind it, thereby creating another low-amplitude grain cluster that will eventually become destabilized by remobilization of the trapping grain. This grain clustering at near-threshold, fluid-shear velocities might be compared with what has been observed experimentally under marginal-transport conditions in water (Iseya and Ikeda, 1987; Drake *et al.*, 1988), whereby coarser size fractions of the bed surface obstruct the transport of the finer fractions and enhance surface sorting in the downwind direction. Similar observations in wind tunnels have not been reported, largely due to the technical difficulty, even at the lowest measurable transport stages, in tracking an individual particle which is one of hundreds in the field of view. The presence of surface sorting following near-threshold flow experiments (e.g. Bagnold, 1941), however, suggests that grain clustering also develops on mixed-grain eolian beds under marginal flow conditions.

As the fluid shear rises above the critical threshold for  $D_{50}$  grains and approaches that for the  $D_{84}$  fraction,  $[(\tau_*)_{cr}]_{84} = 1.79 \times 10^{-2}$  (see Figure 2.11f), some grains begin to migrate across the

entire bed section without encountering a suitable bed pocket. By  $\tau_* = 2.35 \times 10^{-2}$  (Figure 2.11h), erosion of the surface starts to incorporate subsurface bed particles. These features, including the formation of moving grain clusters, active erosion of the bed surface layer, and movement of grains over distances of  $x \geq 100 D_{50}$ , indicate that grains are interacting dynamically with the fluid and with other particles, and may be entering creep or saltation modes. Hence, their treatment realistically requires a more sophisticated fluid-mechanical model, with which the transitions between marginal and full transport can be explored further.

Multiple runs of the bed-smoothing algorithm with varying grain-size frequency distributions, under both eolian and subaqueous flow conditions, suggest that this technique for preparing a realistic bed surface generally applies in the range of Shields stresses  $\tau_* \leq [(\tau_*)_{cr}]_{50}$ . Below the critical threshold for initial motion of the  $D_{50}$  fraction, no measurable sediment flux has occurred; rather, grain movement results only in rearranging the bed surface to a more stable geometric configuration. With coarser distributions and for poorly sorted beds in subaqueous environments, the threshold for marginal-transport conditions lies closer to  $(\tau_*)_{cr}$  for the  $D_{84}$  fraction. Sediment beds used to perform eolian bedload-transport calculations, therefore, are prepared according to the criterion that true sediment motion occurs at the threshold  $\tau_* = [(\tau_*)_{cr}]_{50}$ .

#### 2.4 Comparison with measured sediment beds

Given the inherent difficulties in observing internal micro-structures of real sediment deposits, quantitative descriptions of granular configurations must rely chiefly on field and laboratory measurements of surface-roughness and bulk-sediment characteristics. Bed-surface morphologies have been analyzed for a limited set of mixed-size bed compositions, primarily through calibrated experimental measurements of bed-pocket geometry angles. Field and laboratory assessments of bulk properties, including bed porosities and permeabilities, yield only an average estimate of grain- to void- ratios (i.e. grain-packing densities) and no specific details concerning the geometric arrangement of constituent bed particles. These measurements, however limited, nevertheless provide some of the only sources of information on natural deposits, with which to evaluate the internal morphologies of beds constructed by the theoretical algorithm

described in this chapter.

Bulk sediment properties relate directly to the probability distribution of particle angles of repose. Grain spacing, a measure of the ratio of grain to interstitial-pore volumes, is governed largely by the  $\phi_o$  vs.  $D/k_s$  relationship, with grain shape and orientation becoming increasingly important in more poorly sorted sediments. Particle angles of repose have been measured for an assortment of bed-surface compositions developed in the absence of fluid flow (Chepil, 1959; Eagleson and Dean, 1961; Miller and Byrne, 1966; Li and Komar, 1986) and under flume conditions (Kirchner *et al.*, 1990). These studies employed similar techniques for measuring angles, in which sediment samples chosen to represent the bed were glued to a rigid plane that could be tilted incrementally, allowing accurate measurement of the plane inclination at which loose test particles, placed on the sediment surface, moved from their respective pockets. Chepil (1959) measured first motion of the bulk sediment sample, analogous to the mass angle-of-repose, rather than that of individual particles. The experiments of Eagleson and Dean (1961) and Miller and Byrne (1966) investigated angles of repose for individually sized particles on a bed of uniform grain diameters, the latter measurements made for both dry and wetted surfaces. Li and Komar (1986) used pebbles of varying roundness to analyze the influence of grain shape on bed-pocket geometries and development of transport-related, bed-particle imbrication. Whereas these studies used laboratory-prepared sediments, Kirchner *et al.* (1990) performed their experiments with naturally sorted coarse-sand to gravel mixtures, documenting substantial variability in particle angle-of-repose distributions between natural grain assortments and uniform materials. They also found a wide range in angle-frequency distributions between water-worked and unworked sediment beds, primarily due to more tightly packed particle arrangements in the fluid-smoothed bed case.

Experimental results appropriate for comparison with computed angle-of-repose distributions for beds constructed in the absence of fluid flow are those of Miller and Byrne (1966) for dry particles and Kirchner *et al.* (1990) for sediments prior to being subjected to flume flow. In the latter study, the authors produced two types of sediment beds, "worked" beds generated by sediment-transporting flume flows, and "unworked" beds initially smoothed of artificial topographic irregularities by a weak flow of water but not exposed to sediment-transporting flows.



In this study, properties of the computer-generated sediment bed are compared to those of the "unworked" flume beds. To effect the conditions under which experiments were performed, grains composing the sediment bed produced in Figure 2.11f (i.e. where  $\tau_* \equiv [(\tau_*)_{cr}]_{50}$ ) were "glued" or held immobile while the loose grains on the surface were permitted to move according to their pocket-geometry characteristics. As shown in Figure 2.12, movable grains (solid disks) occupy the top surface pockets whose constituent particles do not impede their mobility. To obtain sufficient statistics for comparison with measured distributions, an additional 30 bed sections were added in the downwind direction. In each instance, the size of the surface particle  $D_m$ , the size of the bed-pocket grain  $k_m$ , and the magnitude of  $\phi_o$  were recorded.

Results of the model calculations of particle angles of repose are presented in Figure 2.13, for a sample subset of approximately 100 mixed-size grains. The bed roughness length,  $k_s$ , equals the median bed-grain diameter,  $k_{50} = 0.23\text{mm}$  (by weight percentile). The predicted distribution of bed-geometry angles is decomposed by percentile, where  $\phi_n = \phi_{16}, \dots, \phi_{95}$  represents the  $n$ th percentile of the distribution; in keeping with other sediment-bed studies cited previously,  $\phi_{16}$  denotes the 16% of the distribution that is smaller than that value. This graph reveals several important geometric aspects of the theoretically generated sediment beds, which are consistent with experimental observations. First, the mean value of  $\phi_o$  increases as the ratio  $D/k_s$  decreases, a consequence of particle packing geometries that has been well-established in previous experimental studies and theoretical discussions (e.g. Miller and Byrne, 1966; Wiberg and Smith, 1987b; Jiang and Haff, 1993). Second, similar to what was first documented for water-worked mixtures by Kirchner *et al.* (1990), particles on the modelled sediment surface display a wide range of repose angles for a given  $D/k_s$  value. For example, for a particle equal to the median bed-grain size ( $D/k_{50} = 1$ ), the angle  $\phi_o$  may vary by as much as  $30^\circ$ , as illustrated by the range between regression lines for the 16th. and 84th. percentile angles-of-repose. Kirchner *et al.* conclude, on the basis of their experiments with different surface roughnesses and grain properties (e.g. grain roughness and angularity), that this variation in particle angles of repose results from some combination of bed-grain spacing, grain properties, and bed-pocket characteristics. With regard to the latter, for example, grains protrude less from a deeper, wider pocket than a more tightly confined one, such

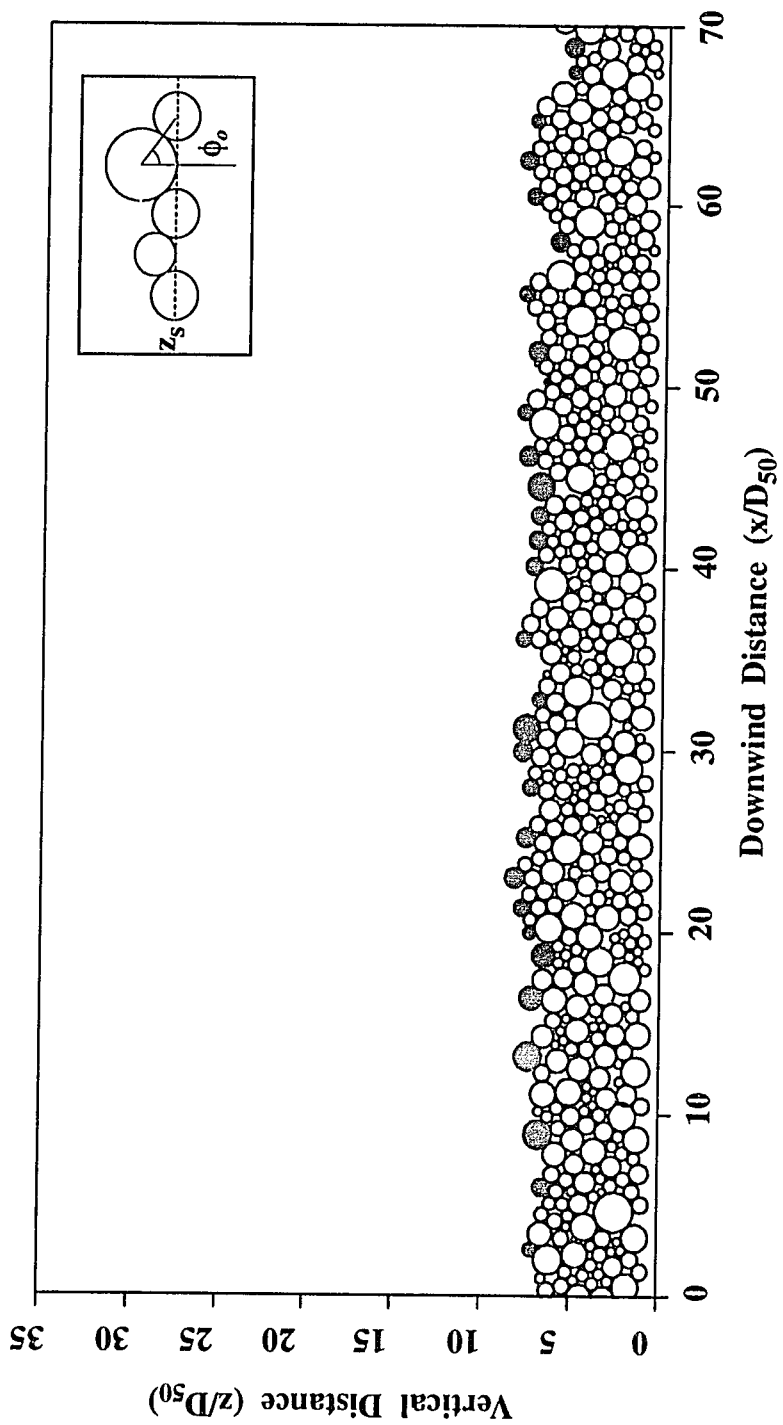
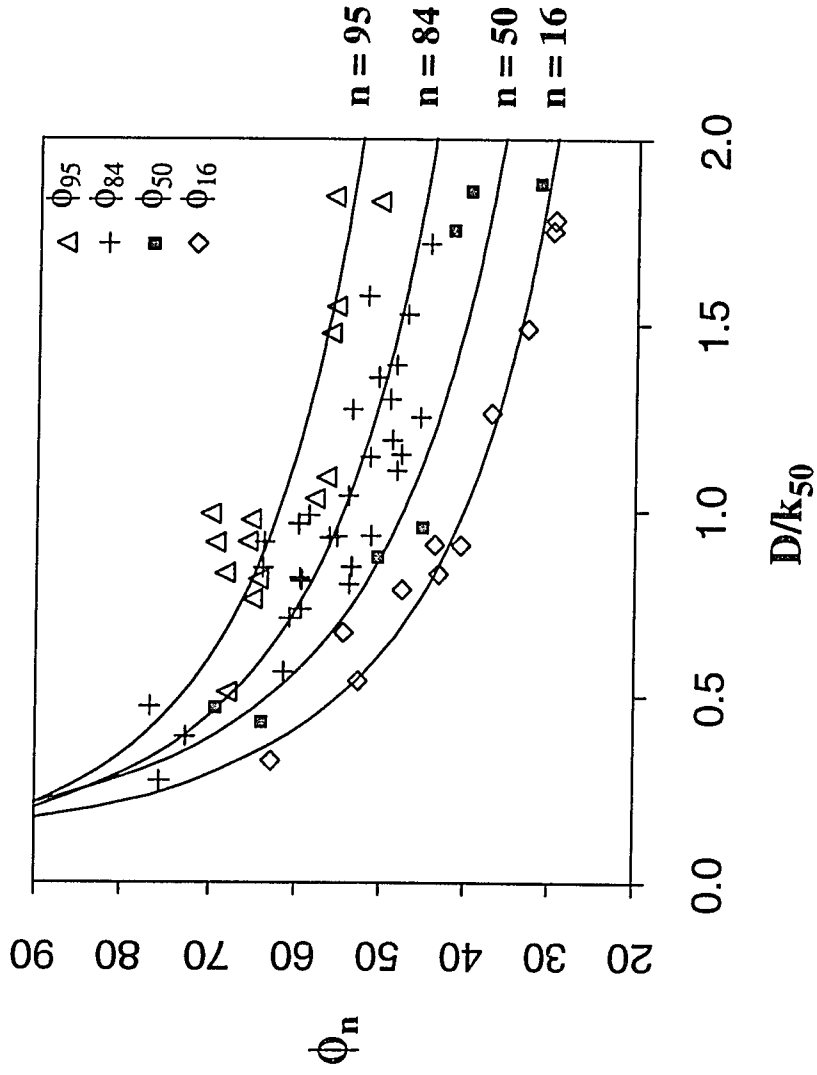


Figure 2.12 Representative bed section showing each surface particle (solid disks) that will move freely from its pocket if the bed were tilted to an angle comparable with its respective particle angle of repose (i.e.  $\phi_o$ ; see inset).



**Figure 2.13** Calculated percentiles of the particle angle of repose, as a function of the ratio of particle size to the median bed-grain diameter ( $k_{50} = 0.23\text{mm}$ ). Regression curves fit to the 16th, 50th, 84th, and 95th percentile model data for about 100 test grains conform to the power-law relationship,  $\phi_n = c_n(D/k_{50})^{\beta_n}$ , where: (1)  $c_{16} = 40.29$  and  $\beta_{16} = 0.449$  ( $r^2=0.97$ ); (2)  $c_{50} = 47.51$  and  $\beta_{50} = 0.411$  ( $r^2=0.93$ ); (3)  $c_{84} = 54.60$  and  $\beta_{84} = 0.311$  ( $r^2=0.76$ ); and (4)  $c_{95} = 62.18$  and  $\beta_{95} = 0.238$  ( $r^2=0.65$ ).

that the relative angle  $\phi_o$  will be larger.

The variation in  $\phi_o$  for a particular  $D/k_s$  ratio has some important implications for mixed-grain sediment transport. As the resistance to movement of a stationary bed grain is proportional to the particle angle of repose (i.e.  $F_R = (F_g - F_L) \tan \phi_o$ ; equation 2.9), the initial motion of that grain may differ considerably depending on the value of  $\phi_o$ . Also, the ability of a saltating grain to eject a particle from the bed depends directly on the morphology of its host bed pocket.

As discussed previously (e.g. equation 2.4), studies of particle angles of repose generally have described  $\phi_o$  in terms of the power-law relationship  $\phi_o = c_o(D/k_s)^\beta$ , where the coefficients  $c_o$  and  $\beta$  are set by sediment conditions of the empirical study. Similar expressions may be obtained for the computed results through curvilinear regression of the 16th, 50th, 84th, and 95th percentiles of the angle-of-repose distribution, respectively. The regression equations subscribe to the general form  $\phi_n = c_n(D/k_{50})^{\beta_n}$ , where: (1)  $c_{16} = 40.29$  and  $\beta_{16} = 0.449$ ; (2)  $c_{50} = 47.51$  and  $\beta_{50} = 0.411$ ; (3)  $c_{84} = 54.60$  and  $\beta_{84} = 0.311$ ; and (4)  $c_{95} = 62.18$  and  $\beta_{95} = 0.238$ . Regression curves are shown in Figure 2.13. These values of  $c_o$  and  $\beta$  fall well within the range of values obtained in other studies. Consistent with the findings of Kirchner *et al.* (1990), however, Figure 2.13 demonstrates that there is no set value for either parameter, as was suggested previously by Miller and Byrne (1966), but rather a range of values that varies, apparently stochastically, with sediment sorting, spatial variability of the particle-scale surface topography, and absence or presence of fluid flow. Although the model results show a systematic increase in the magnitude of  $c_o$  and decrease in  $\beta$ , Kirchner *et al.* caution, on the basis of their reanalysis of previous studies, that such relationships are not consistent across the range of bed grain size, shape, and packing distributions, and that there is no predictive correlation between the two fitted parameters. For example, comparison of  $\phi_{50}$  vs.  $D/k_{50}$  between the model-generated beds and unworked-sediment surfaces of Kirchner *et al.* show a 25% reduction in the value of  $c_{50}$  and a 10% decrease in  $\beta_{50}$ . These variations might be attributed to the relative differences in particle-size distributions and sorting; the median grain diameter of the Kirchner *et al.* flume sediments is  $D_{50} = 4.19\text{mm}$ , with an inclusive graphic standard deviation of 2.94mm (i.e. corresponding to the sedimentological classification of "very poorly sorted"), whereas in the calculations  $D_{50} = 0.23\text{mm}$  with a standard deviation of 0.057mm (i.e. "well-sorted").

Nonetheless, the regression curves displayed in Figure 2.13 are useful for demonstrating the range in probability distributions of angles of repose for individual grains on a mixed-sediment eolian bed.

To compare the generated angle-of-repose statistics with those measured by Miller and Byrne (1966), model results for grains residing in pockets formed by the average grain-size diameter of the bed are plotted with experimental data for dry, rounded sand grains and dry spheres (Figure 2.14). The mean bed-grain diameter of the experimental sediments is  $D_m = \bar{k} = 0.265\text{mm}$ , determined by grain number; hence, model predictions of  $\phi_o$  as a function of  $k_s = 0.265 \pm 0.025\text{mm}$  are shown for comparison. The Miller and Byrne experiments were performed by placing loose, mixed-size grains on a uniform-sized sediment surface. Although the bed-roughness length  $k_s$  is similar, the model results show a wider distribution in bed-pocket geometry angles for comparable values of  $D/\bar{k}$  than the empirical data (e.g. see Figure 2.4). The mean values of  $\phi_o$ , nevertheless, are comparable, as demonstrated by the regression curve for the predicted sample ( $r^2 = 0.98$ ). The values of the regression coefficients compare very well; for the experimental sands, spheres, and computed sample, respectively,  $c_o$  equals 61.5, 50.0, and 58.4, while  $\beta = 0.30$  for the experimental samples and  $\beta = 0.31$  for the theoretical curve. The experimental and theoretically modelled sediment samples have similar sortings (e.g. standard deviations of 0.125mm for the experimental case vs. 0.057mm for the computed sample), which contributes to their highly comparable distributions of mean angles of repose.

As part of their investigation of surface roughness and critical-shear-stress variations in water-sheared bed surfaces, Kirchner *et al.* (1990) experimentally analyzed the differences in bed-pocket geometry angles, or so-called friction angles, between fluid-worked and unworked beds for a poorly sorted mixture ranging from very coarse sand (1 mm) to medium gravel (12 mm). The unworked beds were obtained by removing adhered sections of the flume granular bed prior to running sediment-transporting flows over them. Figure 2.15 compares their probability distributions of friction angle with model-predicted ones for two experimental grain-size classes, a "large" test-grain class with a particle diameter equal to the 82nd percentile of the bed-grain size distribution (i.e.  $D = k_{82}$ ) and a "medium" test grain of  $D = k_{40}$ . The friction-angle frequency distributions for the  $D = k_{84}$  and  $D = k_{40}$  fractions computed from the theoretical sediment bed

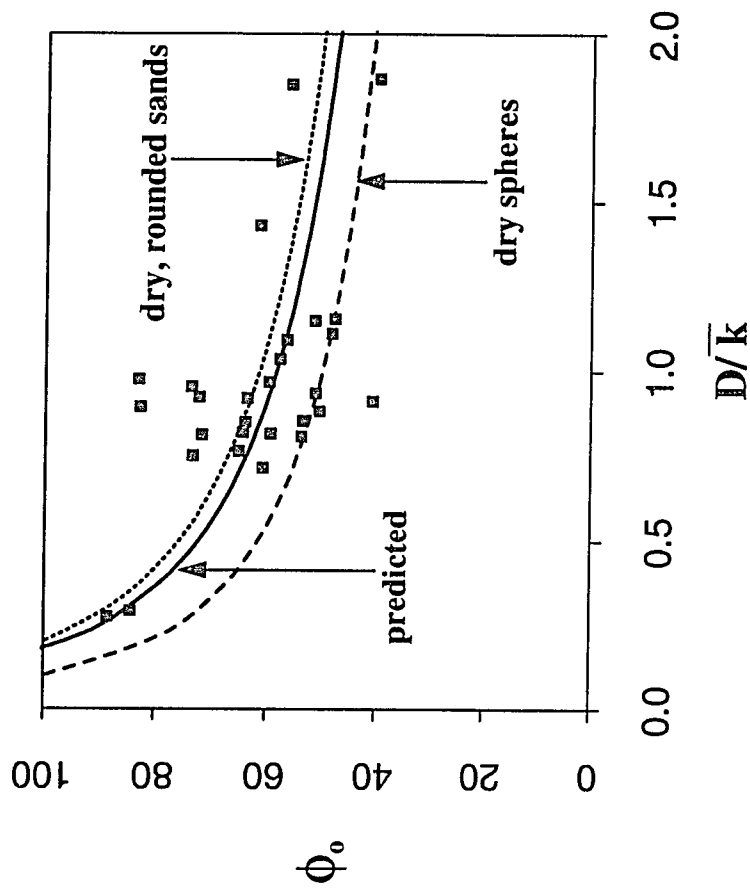


**Figure 2.14** Comparison of model-predicted particle angles of repose with those measured by Miller and Byrne (1966) in the absence of fluid for spheres and rounded nearshore sands (dashed curves), as a function of the test particle diameter ( $D$ ) and the mean bed particle size ( $\bar{k} = 0.265\text{mm}$ ). Predicted values are plotted as points fit by curvilinear regression (solid line;  $r^2 = 0.98$ ) of the form  $\phi_0 = c_0(D/\bar{k})^{-30}$ . The coefficient  $c_0 = 61.5$ ,  $50.0$ , and  $58.4$  for the rounded sands, spheres, and computed sample, respectively.

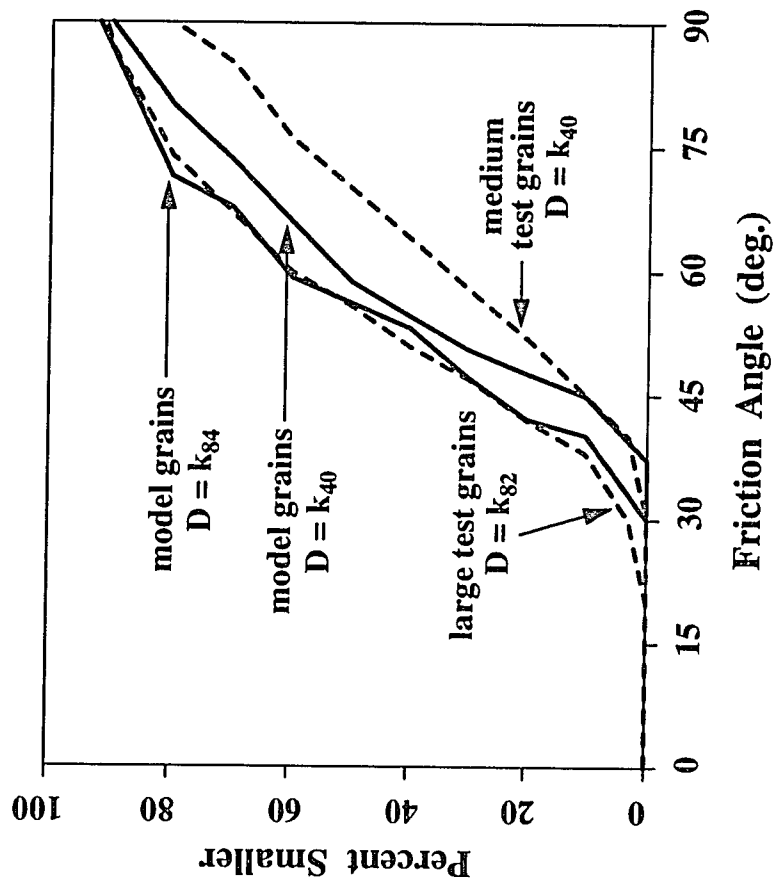


**Figure 2.15** Comparison of particle angle-of-repose distributions for the theoretically modelled granular surface and the sediment beds measured by Kirchner *et al.* (1988); the latter is for the case of flume beds unworked by fluid flow. The two empirical cases (dashed lines) used test grains ( $D$ ) equivalent to the 82nd percentile ("large test grains") and to the 40th percentile ("medium test grains"). For comparison, model test grains ( $D$ ) are equivalent to the 84th and 40th percentiles, respectively.

compare fairly well, despite the noted disparities in grain-size and sorting characteristics. Whereas the  $D = k_{84}$  friction-angle distribution nearly predicts the experimental observations, the  $D = k_{40}$  computed angles are consistently smaller, with the median friction angle varying roughly by  $15^\circ$  between the empirical and predicted cases. These differences may result from the disparity in both absolute grain size and sorting between the experimental and theoretical sediment samples. The small number of measured friction-angle distributions, by which to compare the computed results, unfortunately limits further testing of the relative importance of grain properties versus sorting in controlling the bed-geometry characteristics.

Comparison of bed surface during marginal transport of medium sands versus gravel mixtures suggests that variations in grain-packing geometries between differently sorted sediments may exert relatively more influence on friction-angle distributions than do absolute grain-size differences. For example, analyses of computed bed surfaces under marginal flow conditions show that the larger grains contribute to tighter local packing of the surface, by sheltering adjacent, smaller grains from the flow and by creating large surrounding pore spaces that eventually fill in through entrapment of smaller moving particles. These phenomena occur regardless of whether the large grain is a coarse sand particle on a silt- and sand-sized sediment surface or a pebble in a mixture of sands and granules. Such clustering behavior has also been noted for coarse-sand/gravel mixtures in motion photography of bed-surface generation (e.g. Drake and Shreve, 1987; Drake *et al.*, 1988). Model calculations of friction-angle distributions for differently sorted mixtures (e.g. uniform spheres vs. sand mixtures), however, display much less variability in the very-well-sorted case than in the moderately sorted case. Hence, the consistently smaller friction-angle distributions predicted by the model for the  $D \leq k_{50}$  fractions, compared with those measured by Kirchner *et al.* (1990), may reflect the much better sorting of the eolian sands than the fluvial sand-gravel mixture.

In general, the predicted distributions of bed-surface grain friction angles compare very favorably with experimentally procured data. The range of computed friction angles for the various predicted combinations of surface particles,  $D_m$ , and bed-particle size fractions,  $k_m$ , are well within the range of empirical observations.

With the theoretical bed-construction algorithm, it is possible to measure what cannot be



observed in real deposits, that is, the variations in bed-pocket geometry angles and packing of the bed interior. These statistics provide further insight into the grain-packing geometries of subsurface particles. Using the same bed configuration (e.g. Figure 2.11f) discussed above, pocket-geometry angles for the entire two-dimensional bed were calculated, assuming that the angle  $\phi_o$  is made between the observed particle  $D_m$  and the next grain downwind for which a horizontal line drawn tangentially to its uppermost surface intersects  $D_m$ . In the case where more than one grain fits this criterion, the vertically uppermost grain is chosen as the particle most likely to influence the downwind movement of  $D_m$ . Figure 2.16 shows roughly comparable bed-pocket geometry angles between the bed interior and the bed surface, with the internal, median bed-pocket angle less than that of the bed surface by about  $7^\circ$ . The bed interior, however, displays a considerably greater standard deviation ( $23.29^\circ$  vs.  $15.22^\circ$ ), indicating that the internal bed-particle configurations are more highly variable.

Furthermore, the variability in pocket-geometry angles within the bed interior confirms that the model is not sensitive to the use of semi-empirical  $\phi_o$  vs.  $D/k_s$  expressions to set the grain spacing of the bottom-most grain layer. In fact, setting the grain spacing of the basal layer arbitrarily, by choosing the interstitial length as a random increment of the maximum grain size, produces similar results. Hence, several alternative methods could be employed to construct the bottom layer of the bed without appreciable variation in the bed-pocket-angle distribution.

Another parameter for describing variations in bed-grain packing geometries is the bed porosity, defined as the percentage of the total volume of a bulk sediment sample occupied by voids. The porosity ( $P$ ) of an undisturbed sample typically is estimated from the density of individual sediment grains ( $\rho_s$ ) and the bulk sediment density ( $\gamma_s$ ), where  $P = [1 - (\gamma_s / \rho_s)] * 100$ . The total porosity (%) of a two-dimensional, model-generated sediment bed is calculated by enclosing the granular array with a rectangle of specified length and height (e.g. imposing a rectangle around the perimeter of the bed section shown in Figure 2.17). To obtain an average volume, the rectangle is given a width of one  $D_{50}$ . Conceptually, the sediment bed comprises an infinite number of such rectangles in the cross-stream direction, of which the representative sample gives an average volume estimate. The average porosity is found by subtracting the volume within the rectangle

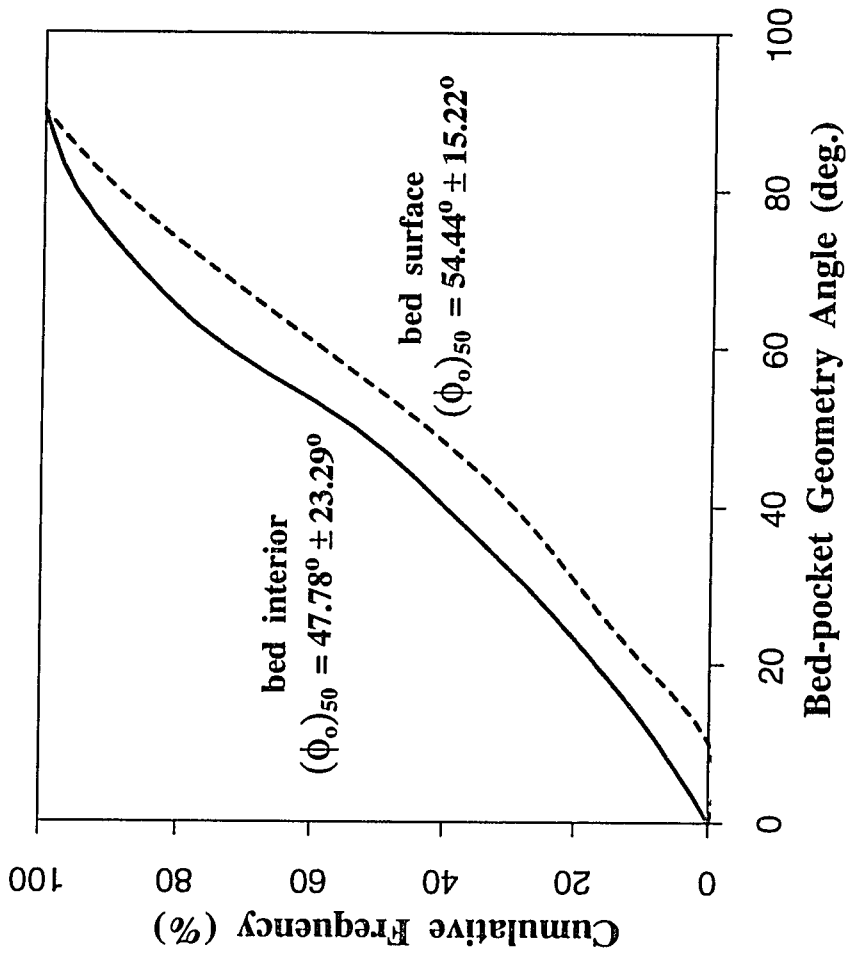


**Figure 2.16** Model predictions of the bed-pocket-geometry angle distribution of the bed surface (dashed curve), compared with the distribution of the bed interior (solid curve). Whereas the median pocket geometry angle  $(\phi_0)_{50}$  is slightly higher in the bed-surface distribution ( $54.44^\circ$  vs.  $47.78^\circ$ ), the subsurface distribution has a greater standard deviation ( $23.29^\circ$  vs.  $15.22^\circ$ ).

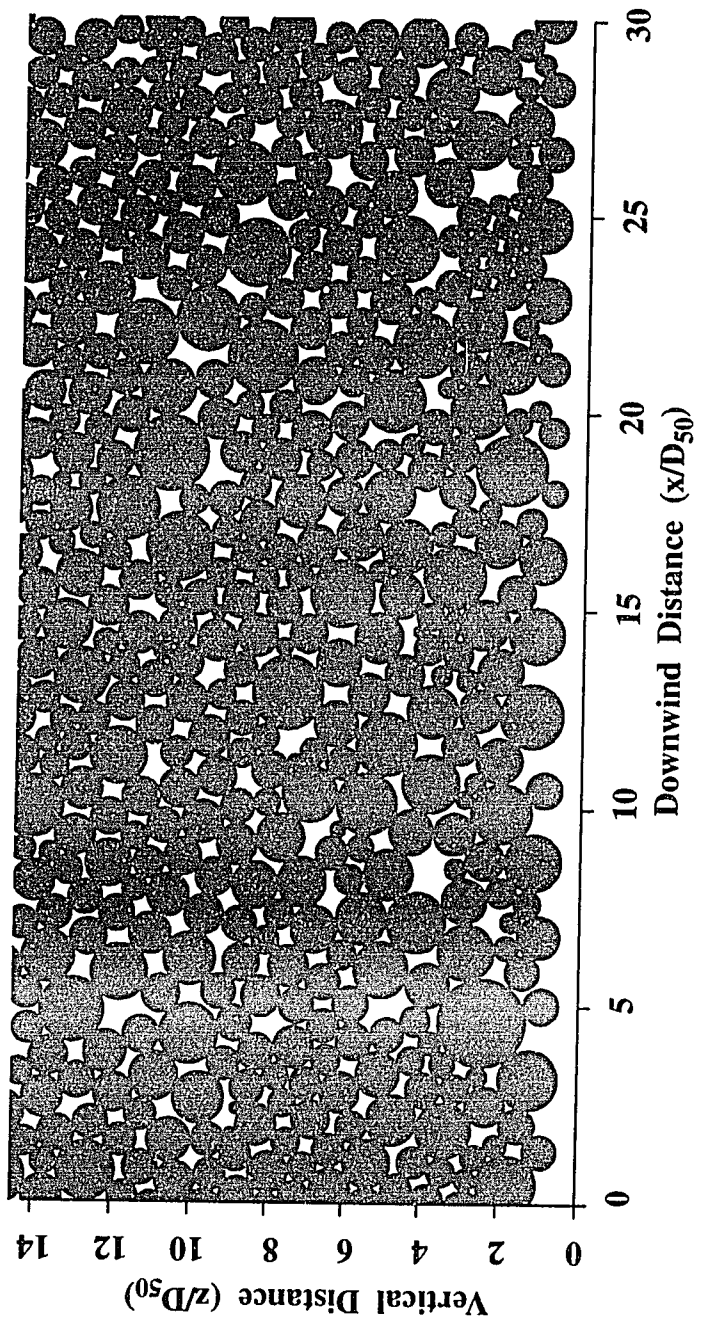


**Figure 2.17** Representative bed section, highlighting the pore spaces (white) between the sediment grains (solid disks). The pore space volume is calculated by subtracting the volume of sediment grains from the total volume of a rectangle drawn around the bed section, assuming the rectangle is one  $D_{50}$  wide and the bed is composed of an infinite number of such rectangles in the cross-stream direction.

occupied by grains from the total interstitial volume, divided by the volume of the rectangle. These calculations exclude the airspace above the surface layer of grains, so that only the subsurface void space is evaluated.

For the bed segment shown in Figure 2.17, the average total porosity is 38.8%. A bed of 40 such sections, with a downwind length of  $1420 D_{50}$ , yields an average porosity of 41.2%. These values compare very well with limited published porosities for natural and experimentally formed, well-sorted, eolian deposits (see Table 2.1), which range from 34% to 55%. Beard and Weyl (1973) found that total porosity can decrease by as much as 15% between extremely well-sorted and very poorly sorted sediments, regardless of grain-size distribution within each sorting class. Pore volume also decreases with fluid working or diagenetic compaction of the bed. Consistent with this observation, the average porosity of the computed initial bed (e.g. prior to wind reworking) is slightly higher than those of the fluid-worked Great Sand Dunes, Sinai dune, and beach-dune sands summarized in Table 2.1. Computed pore volumes compare most favorably with the porosities determined by Schenk (1983) for Great Sand Dunes sands, and Beard and Weyl (1973) for unworked sediment beds composed of moderately to well-sorted sands (e.g. 41.0%). Although grain shape and angularity are considered, based on theoretical analyses, to be of lesser influence on average porosity than are grain sorting and size (e.g. see Beard and Weyl, 1973; Ahlbrandt, 1979), no experimental studies have been performed to verify this observation. Given that the theoretical model yields porosities within the range of empirical values for sands with a variety of shape and roundness characteristics, however, the model's use of smooth spheres does not appear to have any measurable influence on porosities of the computed sediment beds.

## 2.5 Summary

The employment of realistic sediment beds is of great importance in heterogeneous sediment-transport modelling because grain-packing arrangements and densities directly control the small-scale topographic structure of bed surfaces and, thereby, the hydraulic roughness, the relative protrusion of grains into the flow, and the distribution of bed-pocket geometries. In addition, total bedload transport rates may be modified significantly by altering the bed-surface

Table 2.1 Comparison of model-predicted and empirically derived sediment-bed porosities.

environment/ source	mean grain size	sorting (Trask)	grain density ( $\times 10^3$ kg/m <sup>3</sup> )	porosity	author(s)
eolian barrier island dunes, FL.	0.340 mm	well	2.65	44% - 51%	Pryor (1973)
eolian coastal dunes, FL.	0.210 mm	very well	2.65	42% - 55%	Pryor (1973)
dune-crest sands, Sinai Desert	0.210 mm	well	2.65	38% (avg.)	Pye and Tsoar (1990)
dry, unconsolidated beach sands	0.350 mm	moderate	2.65	39.4% (avg.)	Tickell and Hiatt (1938)
dry beach and flu- vial sands	0.700 (D <sub>50</sub> )	moderate	2.65	43% (avg.)	Ludwick (1956)
fluviially reworked, eolian dune sands	0.220 mm	moderate to well	2.6 - 2.7	29.8% - 42% 38.4% (avg.)	Kolbuszewski (1953), <i>et al.</i> (1950)
experimental, unworked eolian beds	0.250 (D <sub>50</sub> )	very poor to extremely well	2.65	38.0% - 45.7%	Beard and Weyl (1973)
experimental, rip- ple stratified sands*	0.234 mm	very well	2.62 - 2.65	39% (avg.)	Schenk (1983)
experimental, grain- fall deposits*	0.234 mm	very well	2.62 - 2.65	43%	Schenk (1983)
model prediction*	0.23 mm	very well	2.65	41.2%	this study

\* dune-crest sands, Great Sand Dunes Nat'l. Monument, Colorado

roughness characteristics, as mass fluxes depend on the ability of protruding particles to be entrained initially by the fluid and subsequently through collisions of saltating particles with stationary bed particles. The degree of relative protrusion is critical, as grains typically are ejected through head-on collisions where the point of contact lies closer toward the equator of the bed grain than the pole of its upper hemisphere. In situations where only the uppermost portion of a bed grain is exposed, as is often the case in more tightly packed granular arrangements, the ballistic force is directed primarily downward into the bed, which might result in rebound of the colliding particle but not ejection of the bed grain. Hence, the accuracy of mixed-grain, sediment-transport modelling depends on using real grain-size frequency distributions and sound geometric arguments for constructing granular arrays to achieve sediment beds with physically realistic grain-packing configurations and densities.

The sediment-bed algorithm described in this work develops granular arrays from measured grain-size frequency distributions, using straightforward trigonometric formulae to position grains chosen at random from this distribution. A fluid-mechanical element serves to smooth the bed surface of any precarious grain clusters created by abruptly terminating the geometric calculations to yield a sediment surface; these topographic artifacts collapse at shear stresses well below those required for initial motion of particles composing the bed. Input parameters to run the model are the grain-size frequency distribution of interest and, for the fluid mechanical component, the grain and fluid densities, the fluid viscosity, and the coefficients of fluid lift and drag. This model differs from others in its use of real particle-size distributions. Employing a natural sorting permits direct comparison of model-predicted bed parameters, such as bed-pocket geometries, with measured values. Founded on simple geometric arguments, the algorithm develops initially unstratified beds that can be used to investigate the mechanical processes by which grain sorting and packing evolve as the wind begins to blow over the surface.

Comparisons of model-derived, sediment-bed properties yield good agreement with available measurements of bed-surface friction angles and bulk sediment characteristics for mixtures with similar size distributions and sorting patterns. At present, relatively little is known quantitatively about the internal morphologies of natural sedimentary deposits; information is

limited to measured profiles and friction angles for a few experimentally produced sediment surfaces, and average porosities and permeabilities of a small number of coastal and inland dune deposits. The utility of this model, therefore, lies in its ability to characterize internal bed morphologies, especially sedimentological properties that are exceedingly difficult to analyze or predict, such as grain packing, bed-pocket distributions, and their control on surface topography. In addition, the bed-generation model has several potential applications to important geological problems, including the hydrodynamics of fluid migration through porous sedimentary deposits.

### Chapter 3: The Fluid Mechanics of Eolian Sediment-Transporting Flows

The complex interactions between moving sand grains and the near-bed wind velocity were described qualitatively, over fifty years ago, by Bagnold (1941). By making detailed wind-tunnel measurements of air blowing over a mobile, unconsolidated bed, he described the feedback mechanism between the wind and moving grains in the sediment-transport layer, whereby as the particles are accelerated by the wind, the grains in turn force the wind to decelerate. This continual adjustment of the vertical structure of the fluid-velocity field to its sediment load, and *vice versa*, influences, among other factors, the near-bed sediment concentration regime and the sediment-flux rates. The momentum-exchange process also governs, to large degree, the downstream distance of particle transport, which ultimately affects the lateral and vertical sorting of bed surface accumulations.

A number of mathematical models, developed within the last several decades, have broadened the general understanding of the physical structure of the wind column and the dynamics of momentum exchange between the stationary bed, moving grains, and the airflow. Anderson *et al.* (1991) summarize the historical evolution of modelling efforts addressing the fluid mechanics of sediment-transporting flows, in addition to recent advances in the understanding of grain-wind interactions over uniform-sized granular beds. Relatively few theoretical investigations of fluid response to multi-grain mixtures have been reported, however, and no dynamical model yet exists for predicting the vertical structure of the fluid flow during transport of heterogeneous mixtures.

Empirical observations of heterogeneous particle transport provide much insight on the complexities of grain-fluid interactions in sediment mixtures. Flume studies of moving granular mixtures (e.g. Wilcock, 1987; Iseya and Ikeda, 1987; Dietrich *et al.*, 1989; Wilcock and Southard, 1989; Kirchner *et al.* 1990; Lisle *et al.*, 1991, 1993) and wind-tunnel experiments (e.g. Gerety, 1984; Yamasaka and Ikeda, 1988) demonstrate that grains comprising a poorly sorted bed are transported at significantly different rates than particles of the same dimension in a uniform-sized material. Other experimental analyses (e.g. Bagnold, 1941; Williams, 1964; Chiu, 1972; Walker,



1981; Gerety and Slingerland, 1983; Gerety, 1985) show that grains within mixtures hop to varying heights depending on size, and that shear velocities at which coarse grain fractions reach their maximum saltation height are greater than for smaller size fractions. These observations suggest that, because grains of disparate size exhibit measurable variability in saltation energetics, each grain-size fraction extracts differing amounts of momentum from the wind column during transport events. The nature of the compounding influence of discrete size fractions on the structure of the fluid-velocity profile, therefore, remains one of the key questions in understanding the aerodynamics of transported, heterogeneous grain mixtures.

The first published theoretical treatment of fluid forces in mixed-grain transporting flows is that of Jiang and Haff (1993), for the case of water. They posed the near-bed fluid layer as a uniform slab moving in the downstream direction, the thickness and bedward extent of which were set using empirical observations. Because it assumes a constant vertical profile of velocity within the slab, their model does not address the height-dependent dynamics of momentum exchange between the flow, the moving grains, and the microtopography of the bed. Currently, no quantitative methods are available for resolving the dynamical interactions between the fluid and solid components of poorly sorted, bedload mixtures.

The mixed-grain eolian model presented here couples the bed-construction algorithm discussed in Chapter 2 with explicit numerical expressions for a fully developed, quasi-exponential, vertical profile of downwind velocity, the bed-roughness parameter ( $z_o$ ) on which it depends, and the momentum-exchange process between the fluid and solid components. Discrete grain-size fractions are treated individually in the calculations, and the total momentum extraction by the moving grains from the fluid is the sum of the momentum extracted by each size fraction. Likewise, the transport rate of the entire mixture obtains from the sum of the fractional transport rates. A sediment bed composed from the grain-size frequency distribution used in transport-rate measurements by Yamasaka and Ikeda (1988) is employed here, to facilitate comparisons between empirical and model-predicted sediment fluxes. Although no fluid-velocity profiles are available from these experiments with which to independently compare model-derived profiles, the fluid-mechanical component of the theoretical formulation can still be evaluated by the ability of the

model to predict the fractional transport rates measured by Yamasaka and Ikeda. The general structure of the model-generated wind profile, as well as the physics of the momentum-extraction process and the saltation properties of discrete size fractions are discussed in this chapter and reviewed in light of available experimental observations for eolian sand mixtures.

### 3.1 Effects of bed roughness

The small-scale topography of a poorly sorted bed surface is of critical importance in a number of sedimentologic and fluid-mechanical problems, as it influences the near-bed flow field, the hydraulic roughness of the bed for the flow in the fluid layer away from the bed (i.e. the flow interior), and the probability distribution of grain angles-of-repose (e.g. Nikuradse, 1933; Owen, 1964; Smith and McLean, 1977; Grant and Madsen, 1982; Dietrich, 1982; Wiberg and Rubin, 1989; Kirchner *et al.*, 1990). The bottom roughness might evolve from some combination of factors, such as sediment moving within the near-bed region, the presence of obstructions or bedforms, and the microtopography of the bed surface. The flow close to the bed is dominated by the grain- and sediment-transport- scale roughness; when present, bedforms also dictate the flow structure in the flow regions away from the bed.

In poorly sorted sedimentary deposits, the vertical profile of downstream fluid velocity can be modified as a result of drag exerted on the flow by the nonmoving part of the bed, especially where large grains or grain clusters protrude into the near-bed flow. Provided that the shear velocities are sufficiently large, a bed element protruding into the flow can create wakes as the flow separates around it. The local flow resistance imposed by bed grains exposed to the fluid stream modifies the velocity distribution and reduces the local boundary shear stress. Under steady, horizontally uniform flow conditions, a velocity profile that varies quasi- or fully logarithmically with flow depth is expected. When a substantial number of obstacles impede the near-bed flow, however, the profile can diverge substantially from a logarithmic form. The magnitude of this effect appears to be directly related to the dimensions and spacing of the roughness elements in relation to the local flow depth. If the bed grains are large relative to the flow depth, for example, the variation from the spatially averaged logarithmic profile might be considerable, as in the case

where boulders emerge above the water surface of a stream. In the eolian environment, it has been hypothesized (e.g. see Bagnold, 1941; Pye and Tsoar, 1990) that the form-drag effects of sand surfaces are minuscule because the depth of the flow relative to the scale of the roughness elements is great. A test of this hypothesis was undertaken here to determine what effects, if any, the particle-scale topographic irregularities exert on the near-bed airstream.

In order to evaluate the effect of bed-surface roughness on the computer-derived sediment bed, an algorithm formulated by Wiberg and Smith (1987a, 1991) was applied, which predicts the modified form of the spatially averaged velocity profile over the bed as a function of the sediment-concentration profile of immobile bed grains. The sediment bed used in these calculations is shown in Figure 3.1. Composed from the grain-size frequency distribution used in the Yamasaka and Ikeda (1988) experiments, this two-dimensional bed averages 1000  $D_{50}$  in length, where  $D_{50}$  is 0.70mm, and contains nearly 11,000 grains. The bed surface has been smoothed by a weak fluid flow, in the manner described in Chapter 2, prior to evaluating its microtopography.

The theoretical approach conforms with that of Wiberg and Smith (1991), although modified in the manner by which concentrations of sediment in the bed are calculated. [See their paper for a full derivation of the mathematical methods.] The total shear stress acting on the fluid in the absence of sediment transport ( $\tau_T$ ) is composed of a fluid stress ( $\tau_F$ ) and a drag stress produced by the flow around each grain exposed at the surface ( $\tau_D$ ):

$$\tau_T(z) = \tau_F(z) + \tau_D(z) \quad (3.1)$$

as a function of height above the bed. The fluid stress is related to the vertical profile of downwind velocity by a one-dimensional, height-dependent, turbulent eddy viscosity [ $K(z)$ ], in which the fluid-velocity scale is a local shear velocity  $(v_*)_f$  associated with the local drag-reduced stress field, and the length scale ( $L$ ) for turbulent mixing is a concentration-weighted average of the bed-region length scale ( $kz$ );  $k$  is von Karman's constant ( $k=0.408$ ). The vertical component of the fluid-velocity gradient is proportional to  $\tau_F$  and inversely proportional to  $K(z)$ , the latter of which may be expressed in terms of the local shear velocity and the length scale on which it acts. Therefore, the fluid stress is given as:

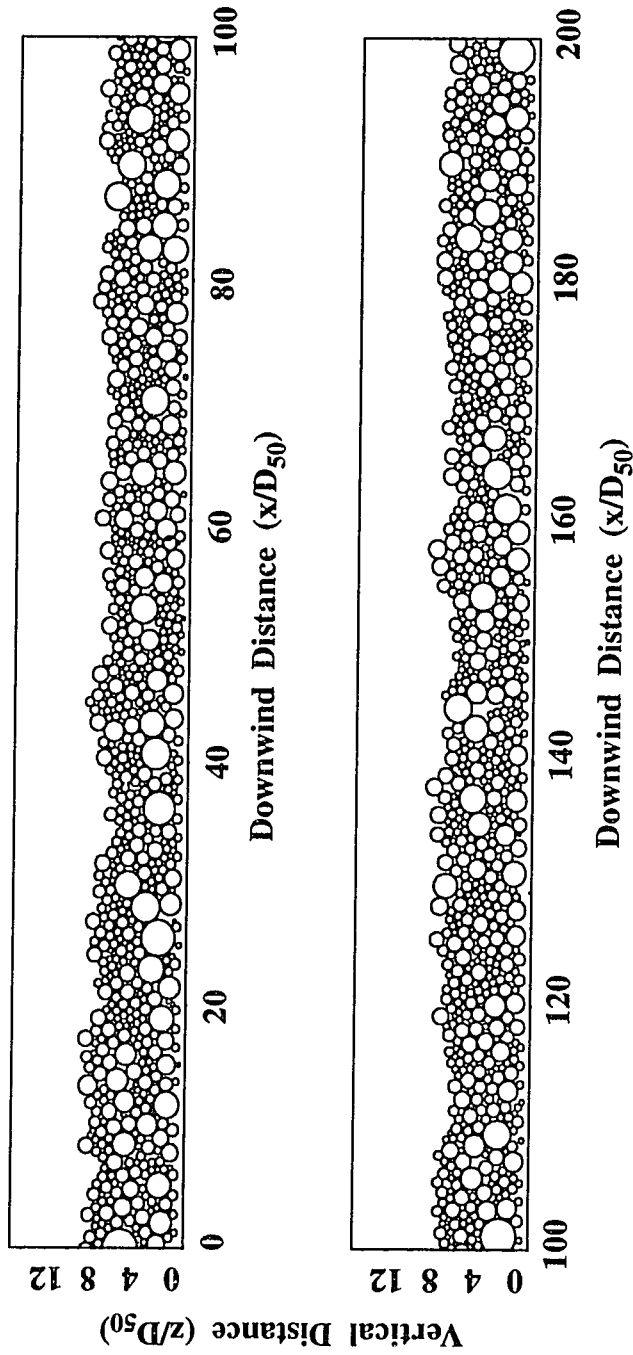


**Figure 3.1** Two-dimensional, computer-generated sediment bed composed from the grain-size frequency distribution used in the experiments of Yamasaka and Ikeda (1988; see Figure 2.3). The horizontal and vertical axes are nondimensionalized by the median grain diameter,  $D_{50} = 0.70\text{mm}$ . The bed extends  $1000D_{50}$  in the downwind direction, averages  $11D_{50}$  in height, and comprises nearly 11,000 grains. Figure continues on the next four pages.

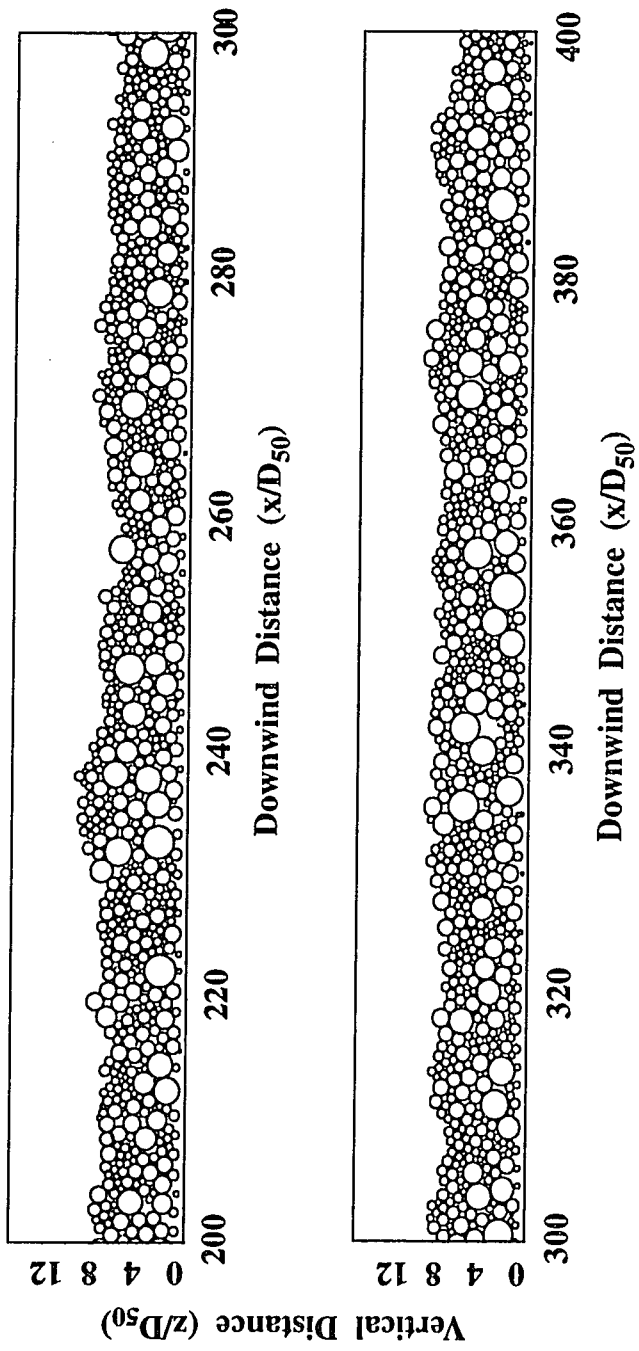


Figure 3.1 continued. Computer-generated sediment bed.

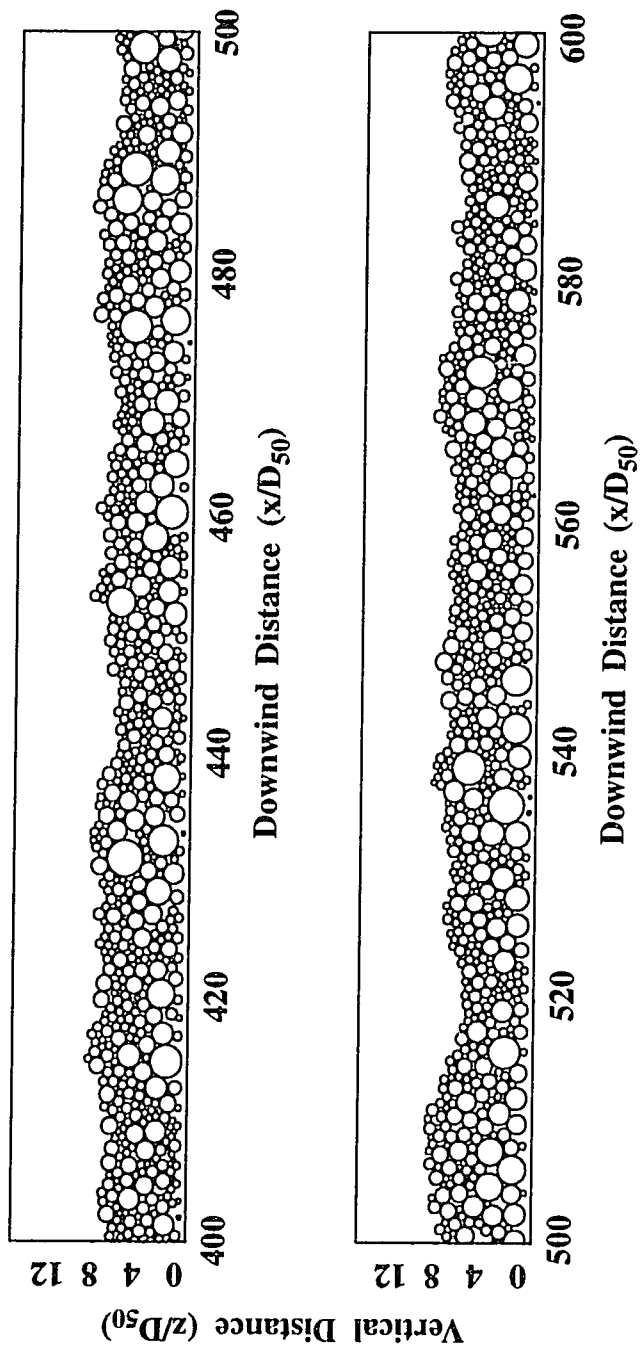


Figure 3.1 continued. Computer-generated sediment bed.

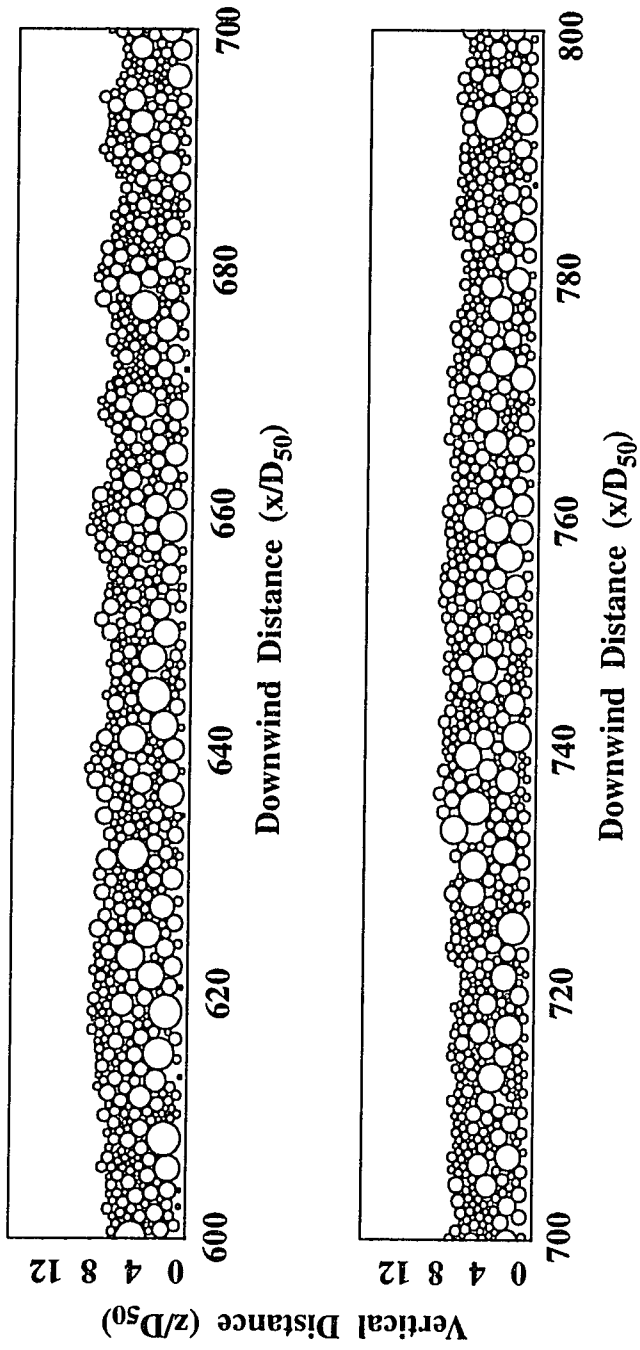


Figure 3.1 continued. Computer-generated sediment bed.

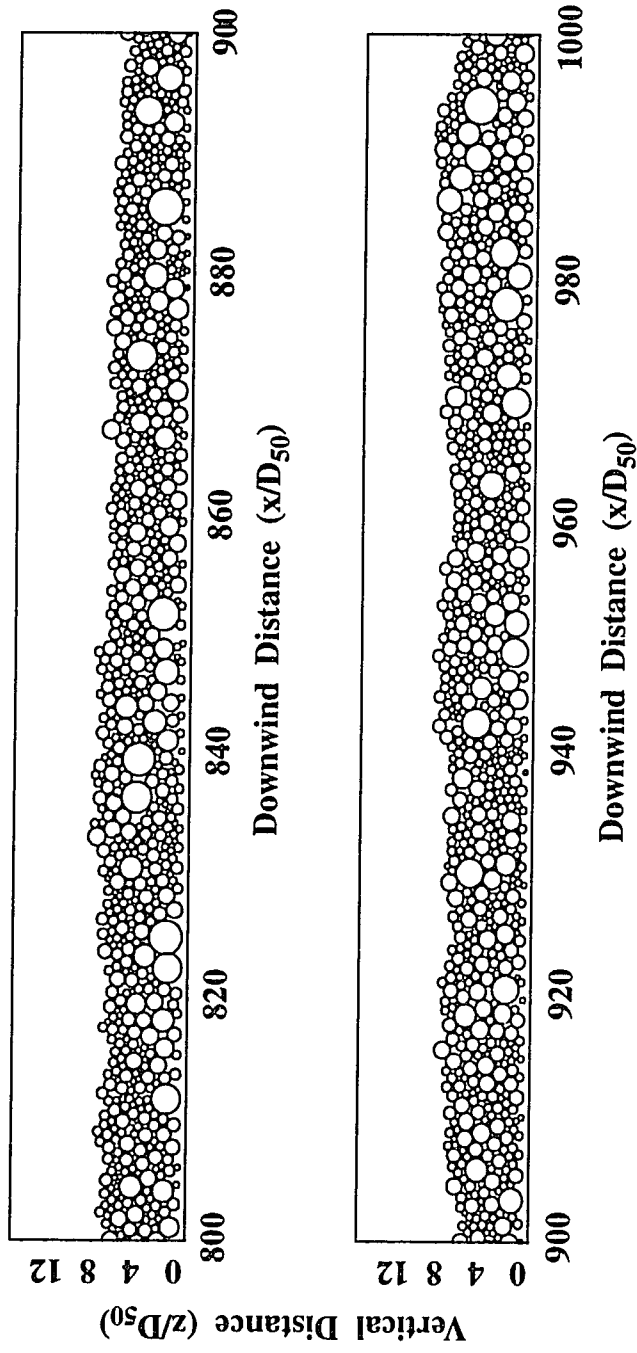


Figure 3.1 continued. Computer-generated sediment bed.



$$\tau_F(z) = \rho K(z) \frac{\partial u}{\partial z} = \rho (v_*)_f L \frac{\partial u}{\partial z} \quad (3.2)$$

where  $\rho$  is the fluid density. The local shear velocity can also be expressed in terms of the total and drag-induced stress, by definition and use of equation (3.1):

$$(v_*)_f = \left[ \frac{\tau_F}{\rho} \right]^{\frac{1}{2}} = \left[ \frac{\tau_T - \tau_D}{\rho} \right]^{\frac{1}{2}}. \quad (3.3)$$

Substituting equation (3.1) into (3.2), and rearranging terms, yields an equation for the vertical velocity gradient in terms of the total and drag-related stresses, as a function of height above the bed:

$$\frac{\partial u}{\partial z} = \frac{1}{L} \left[ \frac{\tau_T - \tau_D}{\rho} \right]^{\frac{1}{2}} = \frac{(u_*)_T}{L} \left[ \left(1 - \frac{z}{h}\right) - \frac{\tau_D}{\tau_b} \right]^{\frac{1}{2}} \quad (3.4)$$

where  $\tau_b$  is the boundary shear stress,  $\tau_b = \rho(u_*)_T^2$ , and  $u_*$  is the fluid shear velocity. This derivation makes use of the fact that the total shear stress  $\tau_T(z) = \tau_b(1 - z/h)$  for steady, horizontally uniform flows, where  $z$  is the height above the bed and  $h$  is the flow depth.

Solution of this equation requires a numerical expression for the length scale for turbulent mixing ( $L$ ) and the drag-induced shear stress  $\tau_D$ . The equation derived by Wiberg and Smith for the length scale is:

$$L = (1 - C_s) \frac{kz}{(1 - z/h)^{1/2}} + \alpha \sum_{m=i}^M C_m D_m. \quad (3.5)$$

The term  $C_s$  is the weighted average of the concentration of each sediment component  $C_m$  represented in the bed, summed over all  $m$  such components:  $C_s = \frac{\sum_{m=i}^M C_m}{\sum_{m=i}^M C_m}$ , where  $M$  represents the largest grain size present in the grain-size frequency distribution and  $i$  the smallest. The coefficient  $\alpha = k = 0.408$  pertains to the case where wakes dominate the zone of vertical momentum mixing.

The drag-induced fluid stress is given by the drag force ( $F_D$ ) per unit area ( $A_T$ ) affected in the downwind, bed-parallel plane by each  $D_m$ , summed over all sediment size fractions  $m$ . This

yields, by definition of the drag force (see equation 2.11), an expression for  $\tau_D(z)$  in terms of the concentration of each sediment component  $C_m$ , a drag coefficient for each component  $(c_d)_m$ , and the square of the fluid velocity, vertically integrated from  $z^- = z_o$  to  $z^+ = z_m$  :

$$\tau_D(z) = \sum_{m=i}^M \left( \frac{F_D}{A\tau} \right)_m = \frac{3}{4} \rho \int_{z^-}^{z^+} u^2 \sum_{m=i}^M \frac{c_d C_m}{D_m} dz . \quad (3.6)$$

At a value of  $z = z_o$ , the fluid velocity approaches zero in the bed (no-slip condition);  $z_m$  is the height of the top of the largest grain sitting on the bed surface. Substitution of  $\tau_D$  into equation (3.4) gives an equation for the vertical velocity gradient that can be solved iteratively, as will be described shortly.

The integration of equation (3.6) requires an algorithm for establishing the  $z = z_o$  level at which  $u \rightarrow 0$  in the bed surface, and for calculating the concentrations of  $D_m$  at successive values of  $z$ . To establish a common reference level for the vertical height scale  $z$ , Wiberg and Smith chose the origin,  $z = 0$ , to be a flat plane such that the bottoms of all grains rest at a common zero level. Given the irregular topographic relief of the sediment beds generated in this study, where the local height of the surface varies by as much as  $6 D_{50}$  between the minima (i.e. bed pockets) and maxima (i.e. tops of grain clusters or coarse grains protruding above the average bed surface), a spatially varying zero-level is employed here. As shown in Figure 3.2, the  $z = 0$  reference curve follows, in general, the points of contact between adjacent grains exposed to the wind at the bed surface. This assumes that the flow over the bed surface cannot penetrate below the solid contact between any two grains. The reference curve has been relaxed in the relatively few cases where the fluid-filled interstice between two grains is less than  $D_i = 0.01\text{mm}$ , the smallest grain diameter of the bed population. This relaxation was introduced primarily to smooth the curve of unrealistic, abrupt changes in  $z = 0$  and does not affect the calculations because these minute interstices are well within the viscous sublayer and they typically lie in the wake of the coarser particle size fractions (e.g.  $D_{50}$  or larger). The vertical height  $z$  is divided into equal increments of  $0.10 D_i$ . Because the  $z = 0$  reference varies spatially, however, so do the  $z=z_m$  increments above; in order to achieve a common level from which to sum  $C_m$  across each level of  $z$  in the downwind direction,

## Fluid Mechanical Surface

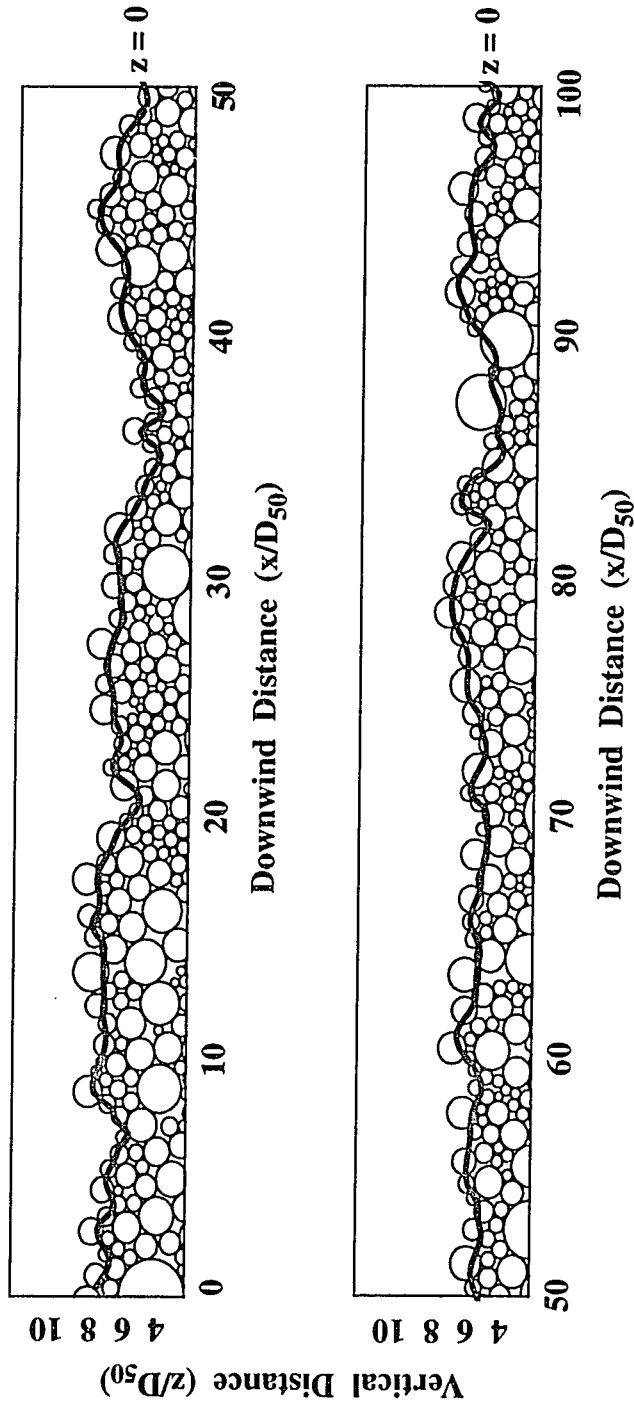


**Figure 3.2** The assumed zero level of the bed ( $z=0$ ) is shown as a solid curve, superimposed on representative longitudinal sections of the computer-generated bed. The position of  $z=0$  varies vertically in relation to the particle-scale topographic irregularities of the bed surface. The curve smoothly connects the grain-grain contacts between adjacent particles exposed to the flow.

therefore, the bed is shifted locally either up or down so that the  $z=0$  reference ultimately represents a flat plane. Only the portion of each grain sitting above the  $z=0$  plane is considered in the computation of grain concentrations.

The concentration of each sediment component  $m$  within each increment of  $z = 0.10D_i$  is the sediment volume per total volume of fluid and sediment,  $C_m = V_m(z)/V_T$ . Because the position of each grain within the sediment bed is known, computation of the sediment concentration can be treated explicitly, rather than using an analytical approach, like that offered by Wiberg and Smith (1991) to approximate the concentration from a frequency distribution of grain sizes. The sediment volume  $V_m(z)$  is found by calculating the fraction of the volume of each sphere belonging to size-fraction  $m$ , at a given level of  $z$ , and summing these values. The concentration of each grain-size fraction present (e.g.  $D_{10}$ ,  $D_{20}$ ,  $D_{30}$  ...) is the ratio of  $V_m(z)$  to the total volume of sediment and fluid in increment  $z$ .

Solving for  $\tau_D$  in equation (3.6) requires a knowledge of the fluid velocity  $u(z)$ , which is unknown at first. Hence, it is necessary to approximate the velocity gradient and iterate several times through equations (3.6) and (3.4) to find the shape of the stable velocity profile. The velocity  $u(z)$  is approximated for the first iteration in equation (3.6) by a form of the "Law of the Wall" equation:  $u(z) = [u_* / k \ln z / (z_o)]$ , where  $u_* = (u_*)_T = [\tau_b / \rho]^{1/2}$ . The value of  $z_o$  is found from the Nikuradse (1933) relationship for  $z_o / k_s$  as a function of the roughness Reynold's number:  $R_* = [(u_*)_T k_s / \nu]$ , in which  $\nu$  is the kinematic viscosity and the bed-roughness length scale,  $k_s$ , is the tenth-percentile grain diameter of the sediment bed,  $D_{10} = 0.23\text{mm}$ . Wiberg and Smith (1991) advocate using a smaller size fraction (e.g.  $D_{10}$ ) as  $k_s$ ; however, the choice of  $k_s \leq D_{50}$  appears to make little difference on the resultant form of the wind-velocity profile, with the grain-size frequency distributions used here. In equation 3.6, the drag coefficient  $(c_d)_m$  must also be approximated because it depends on the nature of the velocity profile through its relationship to the Reynolds number  $Re_m = [\langle u \rangle_m D_m / \nu]$ , where  $\langle u \rangle_m$  is the velocity averaged over the grain of interest. Following Wiberg and Smith, an average value of the drag coefficient is used,  $(c_d)_{avg} = (c_d)_m = 0.45$ , which they found yields a preliminary velocity profile that resembles the final, stable profile in both structure and magnitude. Their calculations show that the form of the velocity

profile appears relatively insensitive to the choice of the drag coefficient; the same is true in the eolian case. In subsequent iterations on the velocity profile, the velocity gradient from  $z = z_o$  to  $z = z_m$  determined from the previous iteration is applied to find the values of  $\tau_D$ ,  $u(z)$ , and the drag coefficient for each sediment component,  $(c_d)_m$ .

The results of these calculations are shown in Figure 3.3, as the fluid velocity ( $u$ ) normalized by the shear velocity ( $u_*$ ), versus the log of height  $z$ . For the sediment bed composed from the size-frequency distributions of the Yamasaka and Ikeda (1988) study, there is little variation of the velocity profile over the nonmoving bed surface from the logarithmic profile for the flow away from the bed (i.e. the velocity profile of the flow interior),  $u(z) = [(u_*)_T/k \ln z / (z_o)_T]$ . This also holds for similar analyses conducted with the beds constructed from the finer sands of the Great Sand Dunes sample (e.g. Figure 2.12). This negligible variation results from the fact that all but the largest grains (i.e.  $D_{95}$ ) are submerged within the viscous sublayer at low to moderate transport stages (e.g.  $T_* = \tau_b/\tau_{cr} \leq 3.0$ ), and the flow within this region is hydraulically smooth:  $R_* = [(u_*)_f k_s / \nu] \leq 3$ . The viscous sublayer comprises a band of laminar flow that has an average height of  $\delta_v = 11.6 \nu/u_*$  and often wraps around bed-surface irregularities on a scale that is large compared to  $k_s$ . The total shear stress  $\tau_T$ , therefore, is equal to the fluid stress  $\tau_F$  because the bed grains exert no drag on the wind (i.e. see equation 3.1). Furthermore, sensitivity tests indicate that because  $D_m \leq \delta_v$ , the velocity profile is fairly insensitive to the grain-by-grain position of the  $z=0$  reference curve, which might vary vertically by  $0.5 D_{50}$  with negligible effect.

These results substantiate hypotheses of Bagnold (1941) and Owen (1964) that the direct influence of particle-scale surface topography on the near-bed velocity profile is negligible and can be ignored in most eolian settings. Both of the sediment bed examples described here consist of fairly well-sorted sands. However, the effects of bed roughness on the local, near-bed wind regime might be more consequential in more poorly sorted mixtures, in which the sediment surface exhibits considerably more microtopographic variability, or for the case where distinct patchiness in grain sorting of the surface layers has developed.

Observations of subaqueous flows over mixed-grain beds and analyses of experimental data (e.g. Leopold *et al.*, 1964; Wiberg and Smith, 1991; Whiting and Dietrich, 1990; Kirchner *et al.*,

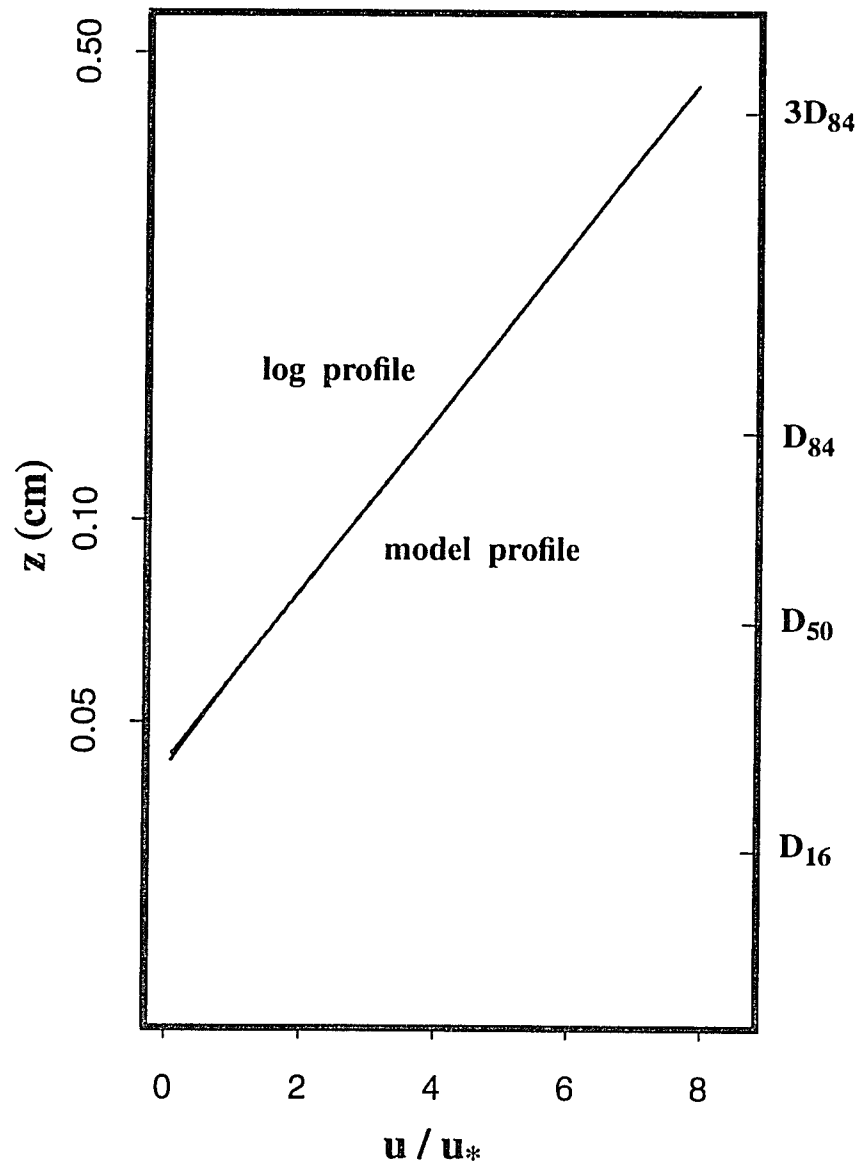


**Figure 3.3** Velocity profile calculated using the algorithm for flow over the nonmoving, poorly sorted bed (“model profile”), compared with the logarithmic profile for the far-field flow in the absence of sediment transport,  $u(z) = [(u_*)_T/k \ln z/(z_0)_T]$ . The fluid velocity ( $u$ ) is normalized by the shear velocity ( $u_*$ ) and the height  $z$ (cm) is logarithmic. The profile is spatially averaged over the nonmoving sediment bed shown in Figure 3.1;  $D_{50} = 0.70\text{mm}$ ,  $k_s = D_{10} = 0.23\text{mm}$ ,  $T_* = [\tau_{cr}/\tau_{cr}] = 3.0$ ,  $R_* = 3.54$ , and  $\delta_v = 0.175\text{mm}$ .

1990) have demonstrated that  $D_{84}$  is the dominant length scale for the hydraulic roughness of water-lain heterogeneous surfaces. Applying this criterion to the mixed-grain eolian beds, for moderate shear velocities (e.g.  $(u_*)_T \leq 2.0$  m/s) in the absence of sediment transport, indicates that the drag-corrected fluid velocity approaches zero in the bed at a value of  $(z_o)_{\text{eff}} = 0.28 D_{84}$  for the Yamasaka and Ikeda size distribution and  $(z_o)_{\text{eff}} = 0.57 D_{84}$  for the Great Sand Dunes size distribution. Little information in the eolian literature can be found with which to evaluate these results for heterogeneous sediment beds, largely because it has proved difficult to measure flow velocities in the absence of sediment motion; even at the critical shear-velocity threshold, the smallest grain size fractions will begin to saltate (e.g. Willetts and Rice, 1985a). Thus far, studies of  $z_o$  in either laboratory or field settings have been conducted in the presence of sediment transport and/or bedforms (e.g. Mulligan, 1988; Greeley *et al.*, 1991, Iversen *et al.*, 1991; Lancaster *et al.*, 1991; Rasmussen and Mikkelsen, 1991; Sherman, 1992). Interestingly, however, the calculated values of  $(z_o)_{\text{eff}}$  compare with ones calculated for beds submerged in water. For example, Whiting and Dietrich (1990) found that the roughness parameter  $(z_o)_{\text{eff}}$  was equal to  $0.1 D_{84}$  for two natural, flat stream beds, one sandy and one gravel-bedded. In an analysis of empirical data from gravel-bedded streams, Wiberg and Smith (1991) determined a value of  $(z_o)_{\text{eff}} = 0.09 D_{84}$ .

While the values of  $(z_o)_{\text{eff}}$  as a function of  $D_{84}$  are roughly similar between water and air, the role of the bed roughness in modifying the velocity profile is quite different. Under moderate shear velocities in water, reduction of fluid momentum is more likely to occur from grain-roughness effects than from grain saltations (e.g. Whiting and Dietrich, 1990), whereas the converse exists in air. Because water and sand are about three orders of magnitude more dense than air, grain-fluid interactions dominate in water and grain saltations at lower flow regimes typically are not very energetic. In air, however, inertial forces dominate and substantially greater numbers of energetic saltations occur, such that momentum extraction from the flow by the moving grains is considerable. The geometry of grain collisions with irregularly arrayed stationary particles on the eolian bed governs the successful ejection of grains into the saltation layer, and it is in this context that the roughness properties of eolian beds exert the greatest control

on modifying the wind profile.

### 3.2 Form of the wind-velocity profile

As described in the preceding section, the viscous sublayer at the bed reduces the near-bed wind velocity substantially more than the bed-surface roughness elements. Below  $\delta_v$ , viscous forces dominate over forces acting to accelerate the fluid, and the vertical profile of fluid velocity is approximately linear. The presence of a viscous sublayer influences the fluid-velocity profile above  $\delta_v$ , where the flow downwind increases logarithmically with distance from the bed. In this near-bed region, fluid shear stresses dominate over viscous shear stresses, and the fluid stress  $\tau_F = (\tau_F)_\eta = \rho(u_\star)_\eta^2$ , where  $\eta$  represents the elevation of the nonmoving portion of the bed (e.g. the fluid-mechanical surface,  $z = 0$ , shown in Figure 3.2). Above  $\delta_v$  but still near the bed, the profile obeys the ‘‘Law of the Wall’’,  $u(z) = [(u_\star)_\eta/k \ln z/(z_o)_N]$ , with  $(z_o)_N \equiv k_s/30$  for hydraulically rough flow and  $(z_o)_N \equiv \nu/(9u_\star)$  for hydraulically smooth flow; between these two flow regimes (i.e. hydraulically transitional flow, where  $3 < R_\star < 100$ ),  $z_o$  is a function of  $R_\star$ , as formulated by Nikuradse (1933; see Smith, 1977). The flow within this logarithmic region is intermittently to fully turbulent, depending on the value of  $R_\star$ , as eddies created in the fully turbulent zone above penetrate the near-bed region. The boundary between the viscous sublayer and the near-bed logarithmic flow is gradational, owing to the effect of passing turbulent eddies (e.g. see Schlichting, 1979; Middleton and Southard, 1984; for a discussion of the viscous - turbulent transition zone). A suitable, well-tested equation that provides a smooth transition between the linear profile for  $z \ll \delta_v$  and the logarithmic profile for  $z \gg \delta_v$  is that of Reichardt (1951; see Schlichting, 1979, p. 601 for comparison with flow measurements):

$$u(z) = u_\star \left[ \left( \frac{1}{k} \ln \left( 1 + k \frac{R_\star z}{k_s} \right) - \frac{1}{k} \left( \ln \frac{R_\star z_o}{k_s} + \ln k \right) \right) \right. \\ \left. \left( 1 - \exp \left( \frac{-z}{k_s} \right) \left( \frac{R_\star}{11.6} \right) - \left( \frac{z}{k_s} \right) \left( \frac{R_\star}{11.6} \right) \exp \left( -0.33 \frac{R_\star z}{k_s} \right) \right) \right], \quad (3.7)$$

where  $u_\star = (u_\star)_\eta$ ,  $z_o = (z_o)_N$ , and  $k_s = D_{50}$ . Wiberg and Smith (1987a) employed this modified



form of the near-bed velocity profile in their numerical algorithm for calculating critical shear stresses for initial motion of heterogeneous sediments in water (see their paper for discussion), and they found that it also provides a good approximation of the velocity profile under hydraulically transitional flow conditions (i.e.  $3 < R_* < 100$ ).

To evaluate the effects of a viscous sublayer on the wind-velocity profile above the computer-generated sediment beds, equation (3.7) was applied in the absence of sediment transport, with  $k_s = D_{10} = 0.23\text{mm}$ ,  $T_* = [\tau_b/\tau_{cr}] = 3.0$ , and  $R_* = 3.54$ . Figure 3.4 demonstrates that accounting for the presence of the viscous sublayer reduces the roughness parameter  $z_o$  (i.e. where  $u \rightarrow 0$  at the bed) by about 40% from that of the profile over the fixed bed with no viscous-sublayer correction.

The fluid layer described by equation (3.7) occupies one of three intergrading but distinctly defined zones comprising the vertical velocity profile (see Figure 3.5). This layer nearest the bed extends vertically to a height of  $\delta_T$ , which is the base of the fully turbulent layer in which the bulk of energetically saltating grains is transported; in this case,  $\delta_T \cong 5.0 \times 10^{-4}$  cm. The top of the saltation layer lies at  $\delta_B$ , above which lies the flow interior described by the logarithmic “Law of the Wall” relationship with  $u_* = (u_*)_T$  and  $z_o = (z_o)_T$ . In this region, the total shear stress  $\tau_T$  is equal to the total fluid stress  $\tau_F$  because there are no saltating grains to exert a drag on the wind. The roughness parameter  $(z_o)_T$  is enhanced by the extraction of momentum by the grains from the fluid below  $\delta_B$ , such that the bed becomes effectively rougher to the flow than is the case when no particles are moving. During saltation,  $(z_o)_T$  is related to the height of the bedload transport layer,  $\delta_B$ .

In the main saltation layer between  $\delta_v$  and  $\delta_B$ , the total stress imposed on the fluid is composed of the stress of the fluid on other fluid particles, plus the stress of the fluid on the sediment particles:  $\tau_F = \tau_{ff} + \tau_{fs}$ . Partitioning of the total stress in this manner was introduced by Bagnold (1954) and subsequently incorporated in sediment-transport models of Owen (1964), Tsuchiya and Kawata (1972), Jensen and Sorensen (1982), Ungar and Haff (1987), Wiberg (1987), Anderson and Haff (1988), and Werner (1990), among others. The shape of the velocity profile in this flow region depends on the magnitude of the shear stress transferred by the fluid to each

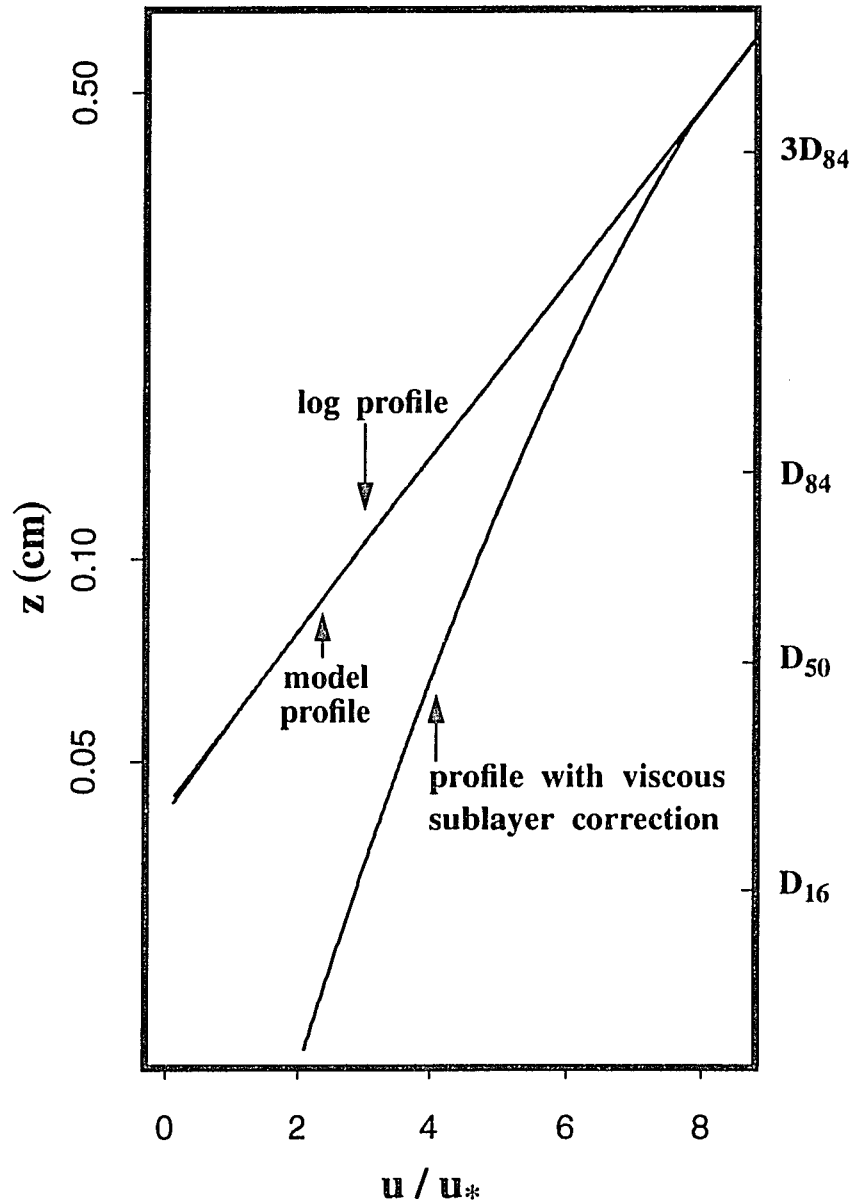


**Figure 3.4** The vertical profile of wind velocity calculated with the Reichardt correction (see equation 3.7) to account for viscous sublayer effects over the nonmoving sediment bed. The modified profile is compared with the log and model profiles shown previously in Figure 3.3. The fluid velocity ( $u$ ) is normalized by the shear velocity ( $u_*$ ) and the height  $z$ (cm) is logarithmic. The profile is spatially averaged over the nonmoving sediment bed shown in Figure 3.1;  $D_{50} = 0.70\text{mm}$ ,  $k_s = D_{10} = 0.23\text{mm}$ ,  $T_* = [\tau_b/\tau_{cr}] = 3.0$ ,  $R_* = 3.54$ , and  $\delta_v = 0.175\text{mm}$ .

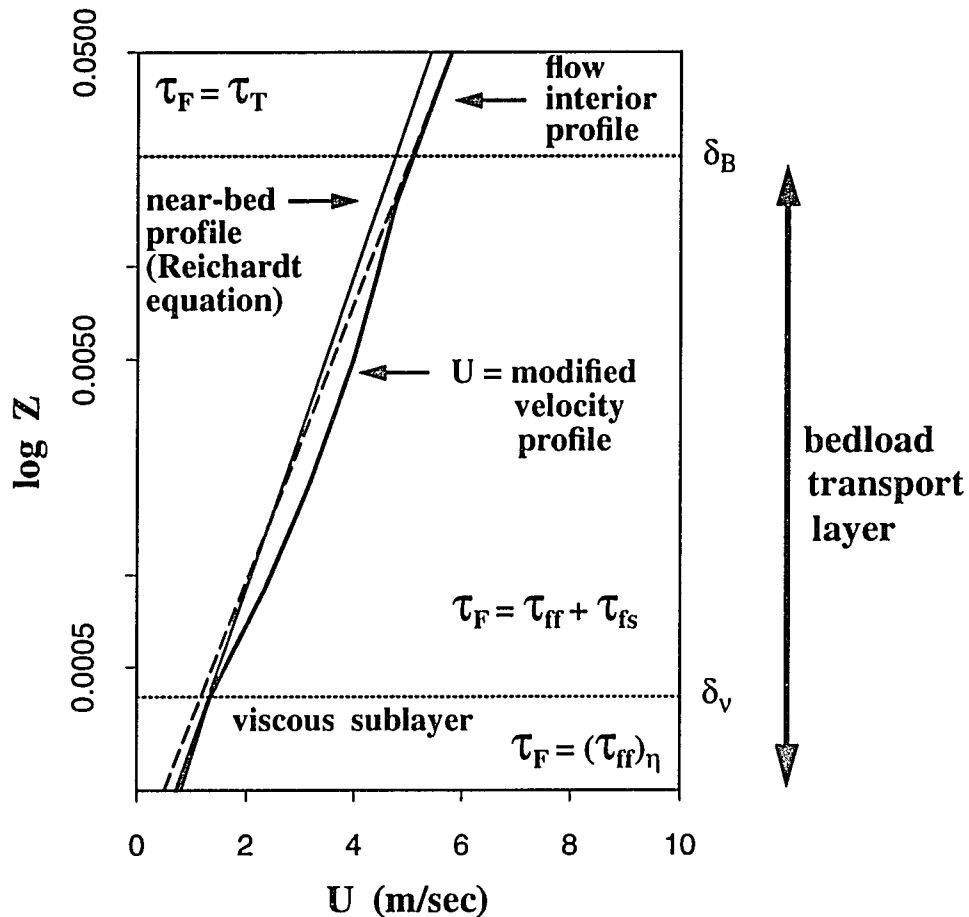


**Figure 3.5** Calculated vertical profiles of wind velocity, plotted as the spatially averaged horizontal velocity ( $u$ ) and the log distance from the bed ( $\log z$ ). The thin solid line is the velocity profile through the viscous sublayer ( $\delta_v$ ) and the overlying logarithmic layer, calculated with the Reichardt correction (equation 3.7); the dashed line is the logarithmic velocity profile above the saltation layer ( $\delta_B$ ), extrapolated toward the sediment bed; and the heavy solid curve represents the actual velocity profile through the bedload-transport layer that accounts for the extraction of momentum by saltating grains. For the case of  $D_{50} = 0.70\text{mm}$ ,  $\tau_T = 8.22 \times 10^{-1} \text{N/m}^2$ , and  $(u_*)_\eta = 6.34 \times 10^{-1} \text{m/s}$ , where  $\eta$  represents the bed surface.

sediment component  $m$  in transit,  $(\tau_{fs})_m$ , which is proportional to the concentration of sediment component  $m$  times the drag force,  $(C_s)_m(F_D)_m$ . Consequently, the velocity profile through the saltation layer is neither linear nor logarithmic, but follows a curve that smoothly connects the near-bed velocity profile with the logarithmic profile of the flow interior.

In Figure 3.5, velocity profiles have been calculated independently for: (1) the near-bed flow region in the absence of sediment transport, using the Reichardt correction (equation 3.7); (2) the flow in the bedload-transport region modified by momentum extraction during grain saltation, using the velocity-profile equation discussed in the following chapter sections; and (3) the interior flow region, using the “Law of the Wall” equation. Calculations were made for a representative case where  $D_{50} = 0.70\text{mm}$ ,  $\tau_T = 8.22 \times 10^{-1} \text{ N/m}^2$ , and  $(u_*)_{\eta} = 6.34 \times 10^{-1} \text{ m/s}$ . This figure illustrates that an extrapolation of the logarithmic profile for the flow interior through the near-bed flow region extracts too much momentum from the saltation layer ( $z < \delta_B$ ). Conversely, an extrapolation of the profile for the near-bed flow into the flow interior overpredicts momentum exchange in the saltation region. The actual velocity profile during sediment transport (heavy solid line) follows the linear profile through the viscous sublayer, the logarithmic profile in the flow interior above  $\delta_B$ , and smoothly connects the two profiles through the saltation layer. Sorensen (1985) has also described the divergence of the profile through the saltation layer from a purely logarithmic form, based on wind-tunnel measurements of velocity profiles during sediment transport which he compared with calculated logarithmic wind profiles for the same shear velocities (e.g. see his Figure 7.3). Hence, the magnitude of the divergence of the velocity profile from a logarithmic form within the saltation layer depends on the amount of momentum exchanged between the moving grains and the transporting fluid.

### 3.3 Momentum extraction from the wind by mixed-size grains

The dominant mechanism for extracting momentum from the wind column over heterogeneous beds of the type described here is that due to grain motion, which includes grain saltation, as well as particle rolling and creep along the bed surface. The dynamics of momentum exchange have been described explicitly in a number of quantitative models for eolian transport of

uniform-sized sand (e.g. Ungar and Haff, 1987; Anderson and Haff, 1988, 1991; Werner, 1990; Sorensen, 1991; McEwan and Willetts, 1991; McEwan, 1993) and characterized experimentally by many workers (e.g. Bagnold, 1941; Chepil, 1945; Horikawa and Shen, 1960; Belly, 1964; Walker, 1981; Gerety and Slingerland, 1983), but have not been treated quantitatively in the case of mixed-size, eolian sediments. The basic mechanics of momentum exchange between the wind and moving grains within a heterogeneous mixture, however, are known conceptually and have been investigated experimentally (e.g. Gerety, 1984). Mixed-grain transporting flows can be described by two general governing equations, one for the sediment components:

$$(\rho_s)_m (C_s)_m \frac{d(\mathbf{u}_s)_m}{dt} = \nabla \cdot (\tilde{\tau}_s)_m - (\rho_s)_m (C_s)_m \mathbf{g} \quad (3.8a)$$

and one for the fluid component:

$$\rho_f C_f \frac{d\mathbf{u}_f}{dt} = \nabla \cdot \tilde{\tau}_F - \rho_f C_f \mathbf{g} \quad (3.8b)$$

where  $\rho_s$  and  $\rho_f$  are the sediment and fluid densities, respectively,  $\mathbf{g}$  is the gravitational acceleration term,  $(C_s)_m$  is the concentration of sediment components, and  $C_f$  is the concentration of fluid parcels. There are  $m$  vector equations for each constituent grain size in a sediment mixture. Each equation for the sediment and fluid phases contains in it a term for the divergence of the stress tensor,  $\nabla \cdot \tilde{\tau}$ . The stress due to the sediment components,  $(\tau_s)_m$ , can be partitioned into two components, as can that for the fluid stress  $\tau_F$ :

$$\tau_s(z) = \tau_{ss}(z) + \tau_{sf}(z) \quad (3.9a)$$

and

$$\tau_F(z) = \tau_{ff}(z) + \tau_{fs}(z) \quad (3.9b)$$

as a function of height above the bed. When a sediment grain leaves the bed and is accelerated by the downwind component of the fluid stress, it exerts a stress on the fluid ( $\tau_{sf}$ ). The grain also exerts stress on other grains through collisions with the stationary grains on the sediment bed ( $\tau_{ss}$ ). If sufficiently energetic, these collisions propel other particles into the flow. The moving grain

extracts momentum from the fluid, which reduces the local shear stress of the fluid parcels on other fluid parcels in the path of the moving grain ( $\tau_{ff}$ ). The fluid also exerts a stress on the moving grain ( $\tau_{fg}$ ), causing it to accelerate in the downwind direction.

In heterogeneous transporting systems, each grain follows a unique trajectory to a given height according to its dynamic interactions with particles comprising the bed and with the wind column, and it extracts a measurable amount of momentum from the airstream at each increment of height it attains. The integrated trajectories of all grains cumulatively act to modify the wind profile, and the thickness of the saltation layer is prescribed by the maximum hop heights achieved by grains within the mixture. Hop heights are dictated by the angle and speed of each grain's lift-off from the bed, which, in turn, depend on the geometries and the momentum transfer of intergranular collisions that result in the rebound of saltating grains and/or the ejections of stationary grains forming the bed surface. Characterizing the momentum-extraction process, therefore, requires quantifying the ballistic and collisional dynamics of the transported grains.

Describing such a system numerically requires an algorithm for accommodating the differential momentum extraction of individual grains or grain-size fractions. The magnitude of the momentum extracted by all grains at each increment of height above the nonmoving portion of the bed then can be calculated as the sum of the momentum extracted by each sediment component. The method presented here builds on a similar model developed previously for uniform grain sizes in air (Calder, 1987) and provides a new technique for quantitatively resolving the form of the modified wind-velocity profile for mixed-grain systems.

### **3.4 Numerical modelling approach. I: Saltation of mixed-sized grains**

To predict the structure of the fluid velocity profile over a mixed-grain sediment bed, this model makes use of four, coupled dynamical components: the computer-generated sediment bed, like that shown in Figure 3.1; a deterministic saltation component that describes the initial motion, ballistic trajectories, and the relative accelerations of the sediment parcels in the moving fluid; a stochastic, collisional component that resolves the geometric arrangements and energetics between moving particles and the grains composing the bed; and a numerical, fluid-mechanical component

that predicts the extraction of momentum from the fluid by the moving grains. Calculations of grain movement proceed forward in time and space, such that the position of each grain along its trajectory, relative to the irregular sediment surface, and the exact geometry of each grain-bed collision are identified precisely. This section discusses the fluid-mechanical elements of the model; the dynamics of grain collisions are discussed in Chapter 4.

The grain-saltation component of the model shares a common approach with several other algorithms available in the literature for air (e.g. Tsuchiya, 1970; Tsuchiya and Kawata, 1972; Reizes, 1978; Jensen and Sorensen, 1982; Hunt and Nalpanis, 1985; Iversen, 1985; Anderson and Hallet, 1986; Ungar and Haff, 1987; Werner, 1990; McEwan and Willetts, 1991), for water (e.g. Tsuchiya, 1969; Wiberg and Smith, 1985), and for snow (e.g. Pomeroy and Gray, 1990), that derive a set of theoretical equations to characterize saltation trajectories based on the forces acting on a particle in a fluid flow. The method used here is that of Wiberg and Smith (1985) for initial motion and saltation of particles in water. Because the mechanisms by which particles begin motion, enter the transporting flow, and trace ballistic-like trajectories within the flow are similar on flat beds in air or water, the mechanical derivation of the algorithm is not critical, providing that the fluid viscosity, densities of the solid and fluid phases, grain sizes, and boundary shear stresses can be stated explicitly. The Wiberg and Smith model was selected for its mechanically based, predictive capability in computing the parameters of full, individual hop trajectories, including their initial and terminal particle velocities and angles.

Numerous studies have addressed the dynamics of fluid forces acting on eolian grains, beginning with experimental work in the 1930's (e.g. Bagnold, 1941; Chepil, 1945; Owen, 1964). In the Wiberg and Smith model, grain motion is initiated from a bed in the absence of bedforms by fluid mechanical forces (i.e. hydrodynamic entrainment) when the downstream- and upward-oriented forces acting on a grain exceed the forces keeping it in contact with the bed. The forces acting on a sediment grain at the bed are those of gravity ( $F_g$ ), lift and drag due to fluid motion over the bed ( $F_L$  and  $F_D$ ), buoyancy ( $F_B$ ), and a balancing force ( $F_R$ ) acting to resist particle motion, all of which have been described previously in Chapter 2 (see Figure 2.9; equations 2.9 - 2.13). When the boundary shear stress ( $\tau_b$ ) overcomes the critical shear stress ( $\tau_{cr}$ ) necessary to

dislodge the sand particle from its pocket, a grain will begin to roll up, or pivot around, the next adjacent grain downstream. As the centrifugal force of the grain exceeds the inward radial component of the gravitational force acting on the particle, it will be ejected into the flow. The critical shear stress for each sediment component  $m$  is given by :

$$(\tau_{cr})_m = [((\rho_s)_m - \rho_f) g D_m] \left[ \frac{V_m}{(A_x)_m D_m} \right] \left[ \frac{2}{(c_d)_m} \right] \left[ \frac{1}{\langle f^2(z/z_o) \rangle} \right] \left[ \frac{\tan \phi_o}{[1 + (\dot{F}_L/F_D)_m \tan \phi_o]} \right] \quad (3.10)$$

where  $\rho_s$  and  $\rho_f$  are the grain and fluid densities, respectively;  $V_s$  is the grain volume and  $A_x$  is the cross-sectional area of the grain [ $V/A_x D = 1.5$  for spheres];  $c_d$  is the drag coefficient;  $\langle f^2(z/z_o) \rangle = \langle u(z)/u_* \rangle$  is the velocity-profile function averaged vertically over the grain cross-section, where  $u_* = [\tau_b/\rho]^{1/2}$ ; and  $\phi_o$  is the bed-pocket geometry angle formed by the pivoting grain and the particle over which it rolls (see Wiberg and Smith, 1985, 1987a, for the physical derivation). The value of  $\phi_o$  is determined directly for each grain resting on the bed, in the manner described in Chapter 2, based on its geometric arrangement with other grains in the computer-generated sediment bed. Wiberg and Smith employ the Reichardt form of the velocity profile (equation 3.7) in their study; here, the velocity profile modified by momentum extraction is used. Critical shear stresses, as well as launch velocities and angles, thereby are calculated theoretically. The number of grains leaving the bed at any time is determined by the bed-geometry arrangement and the fluid-mechanical force balance on each particle as described above.

The numerical solutions for incremental changes in grain position along a trajectory, as functions of time and height above the nonmoving bed, are derived from the equations for turbulent flow near a boundary and for acceleration of a particle in an incompressible flow of moderate- to high- Reynolds number (e.g.  $Re > 1$ ). The forces acting on a grain once it begins to move are the fluid forces of lift, drag, and relative acceleration; the effective grain weight; and the inertial force associated with grain acceleration. Particle spin is neglected. The height of a grain hop, and consequently its acceleration in the downstream direction, is governed primarily by the



forces acting on the grain the instant before it loses contact with the bed. The general form of the governing equation for grain motion in a flow, as derived by Wiberg and Smith (1985), is:

$$\begin{aligned}
 (\rho_s)_m V_m \frac{d\langle \mathbf{u}_s \rangle_m}{dt} &= \rho_f V_m \mathbf{g} + \rho_f V_m \frac{d\langle \mathbf{u}_f \rangle}{dt} + \rho_f \frac{(c_d)_m (A_D)_m}{2} |\mathbf{u}_\Delta| \mathbf{u}_\Delta \\
 + \rho_f V_m (c_m)_m \frac{\partial \langle \mathbf{u}_\Delta \rangle}{\partial t} &+ \rho_f \frac{(c_L)_m (A_L)_m}{2} [ (u_\Delta^2)_T - (u_\Delta^2)_B ] \mathbf{e}_L - (\rho_s)_m V_m \mathbf{g} \quad (3.11)
 \end{aligned}$$

where the vectors  $\mathbf{u}_f$  and  $\mathbf{u}_s$  are the fluid velocity and particle velocity, respectively;  $\mathbf{u}_\Delta$  denotes the difference between the fluid and particle velocities, each averaged over the volume occupied by the grain, [ $\langle \mathbf{u}_f \rangle - \langle \mathbf{u}_s \rangle_m$ ]; the coefficients  $c_L$ ,  $c_d$ , and  $c_m$  are those of lift, drag, and relative acceleration;  $A_L$  and  $A_D$  indicate the cross-sectional area of the grain in the directions of lift and drag;  $V$  is the particle volume;  $\mathbf{e}_L$  is a unit vector in the direction of shear (i.e. normal to the flow); and subscripts T and B refer to the top and bottom of the grain. For spheres,  $c_m = 0.5$  and  $c_L = 0.2$ ; the drag coefficient is calculated as described in Chapter 2. This equation applies to any natural flow of dilute grain and fluid mixtures.

Solutions to the differential equations for each grain trajectory yield a full history of its movement from initial motion, whether aerodynamically entrained or ejected from the bed by grain impact, through all successive hops downwind, to its termination on the bed. An example trajectory is shown in Figure 3.6, where an aerodynamically entrained particle of diameter  $D_m = 0.70\text{mm}$  leaves the bed, travels about  $60D_{50}$  downwind, collides with a stationary grain on the bed surface (dark grain), and rebounds downwind. The position of the grain along its trajectory at equal increments in time is illustrated by a grain image; the distance between successive images indicates the relative acceleration of the particle per unit time. In this figure, for example, the grain is travelling much slower at its outset than toward the end of its trajectory. The Wiberg and Smith (1985) algorithm has been extended here to account for grain position in space, as well as time, so that the saltation trajectories are coupled directly with the sediment bed. The model predicts the angle and speed with which the grain leaves the bed, its maximum hop height and length, and its return speed and angle. Furthermore, because the bed is specified, the dynamics of the grain

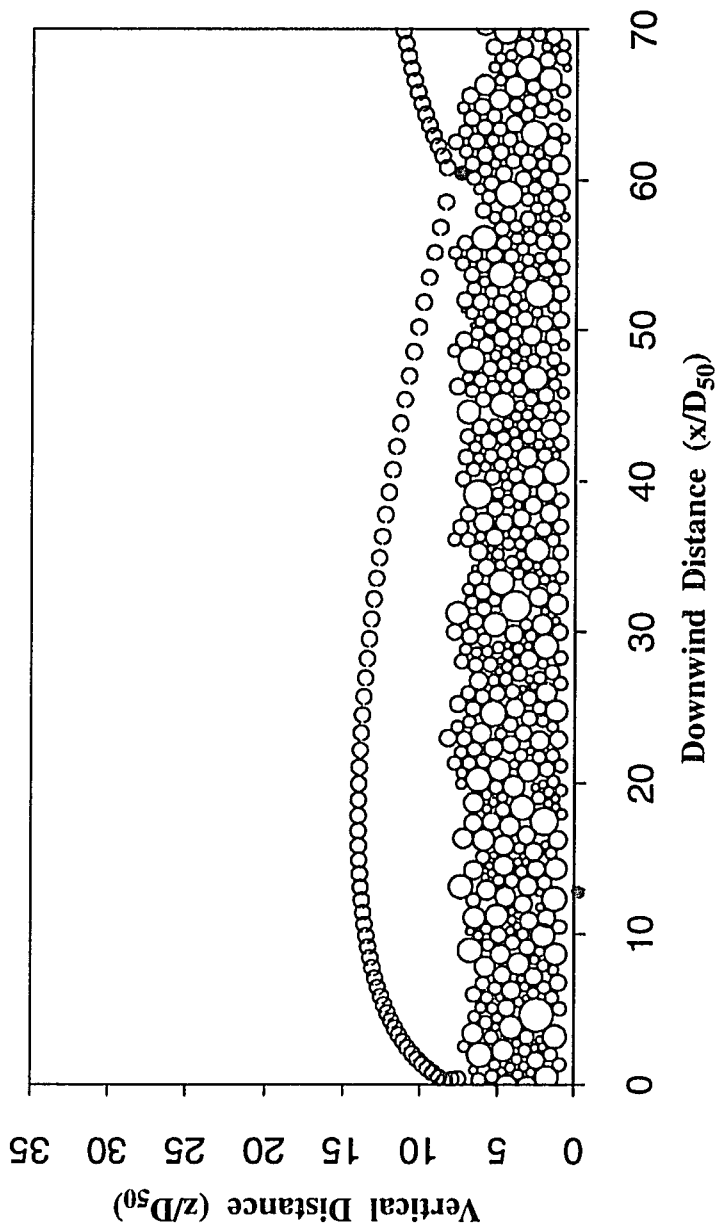


**Figure 3.6** Trajectory of a grain saltating downwind over the sediment bed. The successive positions of the grain relative to the bed, calculated in equal increments of time, are shown from aerodynamic entrainment through collision with a stationary particle on the bed (dark grain) and rebound. The distance between grain positions at each increment in time indicates the relative acceleration of the grain in the downwind direction ( $x/D_{50}$ ), where the grain speed is the greatest an instant before impact with the bed. The diameter of the moving particle  $D_m = D_{50} = 0.70\text{mm}$ ; the transport stage  $(T^*)_{50} = 3.0$ .

impact with a bed-surface element are deterministic and the properties of its rebound or termination are calculable. The model traces multi-hop sequences forward in time and space until the grain is captured by the bed through some geometrically unfavorable collision or is deposited as a result of a drop in the shear velocity below that capable of sustaining its motion.

The method employed here for calculating the parameters of saltation trajectories provides an alternative to other quantitative, eolian-saltation algorithms in the manner by which grain launch and termination angles and velocities are determined, and in its use of a computer-generated, mixed-grain-size sediment bed as an anchor to the calculations. Recent eolian saltation models have departed from the earlier concepts of uniform hop trajectories (e.g. Owen, 1964) by considering a range of hop dimensions with a spectrum of ejection and approach behaviors, as is observed in wind-tunnel experiments (e.g. Willetts and Rice, 1985a, 1989). Ungar and Haff (1986) presented an alternative model that subscribed to one particle trajectory whose vertical lift-off velocity and net acceleration remained constant regardless of changes in the shear velocity acting on the bed. Sorensen (1985) introduced a theoretical approach that calculated a range of trajectory heights, lengths, and lift-off angles, and subsequent modelling efforts, supported by a number of experimental advances in techniques for observing near-bed saltation behavior (e.g. Nalpanis, 1985; Rumpel, 1985; Nickling, 1988; Willetts *et al.*, 1991), have pursued this concept. Many saltation models have made use of wind-tunnel measurements to characterize lift-off behavior directly or to estimate the dislodgment rate and the probability distribution of lift-off velocities and angles from observed transport-rate profiles (e.g. Hunt and Nalpanis, 1985; Iversen, 1985; Sorensen, 1985, 1991; White, 1985; Anderson and Hallet, 1986; Ungar and Haff, 1987; McEwan and Willetts, 1991). In these models, continuous saltation sequences are effected by choosing the number of grain ejecta, the lift-off velocities, and the lift-off angles from probability distributions constructed from empirical observations of the relationship between impact and lift-off velocities (e.g. the “splash function” of, for example, Ungar and Haff, 1987). Inputs to the splash function typically include observed impact angles and speeds, bed slope, and grain mass. Werner (1990) and Anderson and Haff (1988; 1991) broadened the utility of the splash function by combining experimental observations with computer simulations of grains striking a uni-sized

granular bed at chosen angles and speeds known from experiments to be characteristic of airborne grain trajectories, from which lift-off angles and speeds could be derived. Their approaches differed in the way that the test beds were constructed; Werner used a well-packed bed of regularly arrayed grains, while Anderson and Haff developed a less uniform deposit by gravitationally settling grains into a fixed-walled receptacle (i.e. the approach of Jiang and Haff, 1993, and Haff and Anderson, 1993, for grain mixtures of two sizes). These simulations have expanded the understanding of grain-trajectory characteristics past what could be observed experimentally in low or high shear-velocity flows. None of these studies employing splash functions has yet addressed the problem of mixed-grain sediment transport.

The relative importance of aerodynamic entrainment versus impact-driven launch of grains in the total sediment flux remains controversial, largely because of the difficulties in observing this phenomenon experimentally. Employing the splash function derived from computer simulations of grain impacts to a dynamical model of grain saltation, Werner (1990) concluded that impact-propelled grain ejections greatly dominate over fluid entrainment in the steady-state problem. His findings are consistent with wind-tunnel studies of Williams *et al.* (1990). Based on this, and other, studies, some workers (e.g. McEwan and Willetts, 1991; Sorensen, 1991) have neglected fluid entrainment in their models, as have most earlier modelling efforts. Others (e.g. Anderson and Haff, 1988, 1991) account for fluid-mechanical initiation of grains by setting the entrainment rate proportional to the excess shear stress [ $N = \alpha(\tau_b - \tau_{cr})$ ], where the constant of proportionality is assumed such that the grains leave the bed with velocities just sufficient to propel them a distance of one grain diameter from the bed. Others argue for a greater role of fluid-entrainment processes in low and moderate shearing flows on the basis of wind-tunnel experiments (Willetts *et al.*, 1991).

To address the initiation of sediment transport over computer-generated sediment beds, the following methodological algorithm is used. The model is run in such a manner that the first grain to move with increasing shear velocity is entrained aerodynamically. If sufficiently energetic, this grain ejects other grains through collisions with the stationary grains on the bed, which, in turn, eject additional grains. The population of moving grains, then, is composed primarily of grains

initiated by collision, with the exception of the first grain. In the case of very weak flows, several more grains may be initiated by fluid mechanical forces before ejections are produced; in this case, successive, randomly chosen grains are entrained fluid mechanically until one produces grain ejections from the bed. Similar to what has been observed experimentally (e.g. Bagnold, 1941; Iversen, 1985; Nalpanis, 1985), the model predicts that the first few grains to eject from, or roll across, the bed generally promote a cascading effect in the number of grains propelled into motion, such that most low- to moderate- shear velocities readily create an impact-driven saltating population.

In mixed-grain systems in which the microtopographic relief is created by nonuniform arrangements of disparate grain sizes, rather than bedforms, the irregularities of the surface and bed-pocket geometry angles directly govern the ejection angle of bed grains and greatly influence the exchange of momentum between colliding and resting particles. Hence, the ability of the grain to rapidly reach the higher-velocity zones of the windfield are influenced directly by the bed. Knowing the exact geometric configuration of the bed in relation to the particle trajectory parameters, therefore, becomes very important in the momentum-extraction problem for heterogeneous grain mixtures.

### 3.5 Numerical modelling approach. II: Setting the boundary conditions

Owen (1964) first described theoretically how a self-equilibrating system is created between the grains and the wind. As the local wind velocity increases, progressively more grains begin to move. The grain concentration gradient, however, soon reaches a level at which the sediment components extract sufficient momentum that the near-bed flow velocity diminishes. The transport capacity of the wind drops, and the sediment concentration at successive levels above the bed has to adjust to this new transport regime. The concentration of particles in the saltation layer is limited by the condition that the local fluid shear stress ( $\tau_F$ ) progressively decreases, in the direction of the bed, to a critical value just capable of initiating saltation.

To determine the magnitude of  $\tau_F$  at this threshold, and the length scale setting the velocity profile in the saltation layer and above, an appropriate boundary condition must be formulated.

Owen (1964) closed the problem by setting the fluid stress equal to the stress necessary to sustain saltations by impact (e.g. the “impact” stress threshold of Bagnold, 1941, and Chepil, 1945); the magnitude of this stress is smaller than the critical Shield’s stress for initiation of grain movement ( $\tau_F = \tau_{cr}$ ), which forces the boundary shear stress  $\tau_b$  back to the threshold for grain rolling, not for saltation. In the neighborhood of  $\tau_{cr}$  few grains are saltating, and this boundary condition is insufficient for a developed saltation layer. Ungar and Haff (1987), followed by Werner (1990), applied the stress profile for the interior flow [ $\tau_F = \tau_b = \rho(u_*)^2$ ] to the saltation layer, arguing that the energetics of grain saltation are independent of  $\tau_F$  at the bed. Other models (e.g. Sorensen, 1985; Anderson and Hallet, 1986) have employed shear velocities derived from time-averaged velocity measurements to constrain the value of  $\tau_F = \rho(u_*)^2$  at the bed. More recent analyses (e.g. Gerety, 1985; Anderson and Haff, 1991; McEwan, 1993) have questioned the accuracy with which shear velocities can be calculated from measured wind velocities, as well as the validity of assuming a logarithmic profile through the saltation region as a basis for the calculations. Recognizing that the momentum-extraction process results in a wind-velocity profile that can diverge considerably from a purely logarithmic form, others (e.g. Calder, 1987; Anderson and Haff, 1991; McEwan and Willetts, 1991; McEwan, 1993) defined a local fluid shear stress whose profile form is modified by the magnitude of momentum extraction as a function of height above the bed. A common modelling approach (e.g. Anderson and Haff, 1991; McEwan and Willetts, 1991) has been to set the local fluid-shear velocity in the near-bed region initially by a value corresponding to the logarithmic wind profile [ $\tau_b = \rho(u_*)^2$ ] of the flow interior, and then to iterate on a modified velocity-gradient expression to find a stable solution for the wind profile in the saltation layer.

The theory for determining the local shear-stress threshold in mixed-grain transporting systems departs from that of the uniform-grained models above in that not one value of  $\tau_F$ , but a range of values for each grain-size fraction present, must be found. Following an approach developed for eolian transport of uniform sizes (Calder, 1987; Calder and Smith, 1989), the critical threshold at which the local fluid shear stress reaches a minimum during sediment transport is given by a shear stress that relates to the initiation of grain saltation ( $\tau_{ff}$ ) <sub>$\eta$</sub> , rather than initiation of

grain rolling. Hereafter, this term is denoted simply as  $\tau_\eta$ , where  $\eta$  denotes the nonmoving part of the bed. For each sediment component  $m$  in a granular mixture,  $(\tau_\eta)_m > (\tau_{cr})_m$ ; however, the value of  $(\tau_\eta)_m$  differs considerably between grain sizes because of the particle-force dependence on grain volume  $V_m$  and bed-pocket angle geometry  $\phi_o$  (i.e. in the force resisting particle motion:  $F_R = [(\rho_s - \rho)gV_m \tan \phi_o]$ ). In heterogeneous sediments, therefore, setting the boundary condition for the local, effective fluid shear stress associated with the saltation layer requires treating each grain-size fraction separately, as will be discussed shortly.

The boundary condition for the fluid-velocity profile modified by the presence of grains of different sizes at the bed and in the bedload layer is that the velocity approaches zero at a height equal to the bed-roughness scale ( $z_o$ ). In the near-bed flow region,  $z_o$  as a function of the local sediment-bed topography and thickness of the viscous sublayer is set initially by the Nikuradse (1933) relationship for flow over a fixed, non-sediment-transporting bed. The Nikuradse length scale  $(z_o)_N$  for the flow before sediment transport occurs is a function of the shear velocity  $(u^*)_\eta$ , the characteristic bed-length scale  $k_s$ , and the fluid viscosity  $\nu$ ; for hydraulically transitional flows ( $3 \leq R_* \leq 100$ ),  $(z_o)_N = f\{R_* = [(u^*)_\eta k_s / \nu]\}$ , and for hydraulically rough flows ( $R_* > 100$ ),  $(z_o)_N = k_s/30$ . Nikuradse derived these relationships for a planar surface of spheres with uniform sizes and packing, and others (e.g. see Sherman, 1992) have suggested that  $z_o = 2D_{50}/30$  is more representative of irregular, mixed-grain bed surfaces. It was demonstrated previously (i.e. section 3.1) that the particle-scale topographic irregularities of the computer-generated sediment beds used here have little effect on the form of the vertical velocity profile in the absence of sediment transport and that at low- to moderate- transport stages, most grains likely are submerged within the viscous sublayer. Because the relationship between grain size and roughness length generally is unclear, however, a further test of the effect of varying the characteristic length scale  $k_s$  on the form of the near-bed velocity profile was conducted. In three different scenarios, using the Reichardt equation for the near-bed, vertical velocity profile (equation 3.7) and  $(u^*)_\eta = 7.58 \times 10^{-2}$  m/s,  $k_s$  was taken to be the median grain diameter ( $D_{50}$ ); twice the median grain diameter ( $2D_{50}$ ), which is approximately equivalent to  $D_{84}$  of this size-frequency distribution; and the average diameter of the bed-surface grain ( $D_m$ ) lying at each increment of distance  $x = 10D_{50}$  downwind,

which corresponds to the average wavelength of microtopographic bed irregularities (e.g. bumps formed by grain clusters; see Figure 3.1). In the latter case, the vertical velocity profile was calculated at increments of  $(x/D_{50})$  and spatially averaged over the length of the sediment bed. In each case,  $z_o$  was positioned spatially above the elevationally varying  $z=0$  reference line shown in Figure 3.2. There was negligible variation among the three calculated profiles and the Reichardt-modified velocity profile shown in Figure 3.4. Hence,  $z_o$  for the near-bed flow is taken as originally posed by Nikuradse with  $k_s = D_{50}$  and is spatially anchored to the  $z=0$  reference line at successive points in the downwind direction.

As sediment motion ensues, however, the effective bed roughness  $z_o$  is enhanced by moving sediment above the fluid-solid interface. Owen (1964) postulated that the particles travelling within the saltation layer create a roughness to the non-sediment-transporting flow above by shedding wakes that introduce local turbulences in the flow. He also hypothesized that the magnitude of the bed-roughness parameter is proportional to the height of the bedload layer ( $\delta_B$ ), which he estimated by balancing the kinetic energy of a grain leaving the bed with an initial vertical velocity comparable to the shear velocity ( $u_*$ ), against the potential energy of the particle at the top of its trajectory. Owen showed this dependence of the roughness parameter on the shear velocity in his formulation of  $(z_o)_{st} = \alpha(u_*^2/2g)$ , where  $\alpha = 2.07 \times 10^{-2}$ . Some have followed this approach (e.g. Anderson and Hallet, 1986; Rasmussen and Mikkelsen, 1991). Others (e.g. Anderson and Haff, 1988, 1991; McEwan and Willetts, 1991) have set the initial sediment-transport roughness,  $(z_o)_{st}$ , equivalent to the Nikuradse value for hydraulically rough flow (i.e.  $z_o = D/30$ ) and iterated on the velocity profile as it gradually adjusts to the momentum-exchange regime of the steady-state, sediment-transporting flow, thereby deriving a new value of  $(z_o)_{st}$  as the height above the bed where  $u = 0$ . Anderson and Haff (1991) further refined the initial Nikuradse-type roughness parameter by setting  $z_o \approx 2D/30$  [i.e.  $2D \approx 0.1\text{mm}$  is about the mean height of impact craters developed by saltating grains impacting the surface and driving other grains from the local impact locus; this concept originates from experimental observations of Bagnold (1941)]. Ungar and Haff (1987) set  $z_o = D/30$  for each iteration and then adjusted the magnitude of the velocity at this height until the velocity profile was consistent with the impact velocity of the



representative saltation trajectory used in their calculations. Werner (1990) assumed  $u = 0$  at  $z_o = D/30$  above the tops of grains ejected from the bed, arguing that a variation in the roughness parameter, on the order of a fraction of a grain diameter, had little effect on the saltation trajectories and, hence, on the mean vertical profile of wind velocity. Sorensen (1991) set  $z_o$  corresponding to a value calculated for flow over small sand ripples, also suggesting that the roughness parameter exerts little influence on the wind profile.

This model employs an iterative technique to resolve the form of the wind profile modified by grain-induced momentum extraction and to obtain a correct value of  $(z_o)_{st}$ . In the mixed-grain problem, this calculation must be carried out for each sediment component until the momentum distribution between the fluid and all moving grains equalizes for a given local shear stress. The iteration scheme, described more fully later on, incorporates a numerical expression for  $z_o$  that depends on the concentration of grains moving as bedload, the thickness of the saltation layer  $\delta_B$ , and the shear velocity. The form of this equation is derived at the end of this chapter section. The numerically derived values of  $(z_o)_{st}$  for mixed-size sediments correspond most closely to those calculated with the analytical expression developed by Sherman (1992), who re-parameterized Owen's expression specifically to describe roughness resulting from saltation. He argued that Owen's relationship did not isolate the sediment-transport roughness from skin-friction roughness and that, to do so, the shear velocity ( $u_*$ ) in Owen's equation should be replaced by the excess shear velocity required to initiate sediment transport [ $u_* - (u_*)_{cr}$ ], and the skin-friction roughness ( $2D_{50}/30$ ) should be subtracted from the equation. The resulting equation of Sherman is  $(z_o)_{st} = \left\{ [\alpha(u_* - (u_*)_{cr})^2]/g - 2D_{50}/30 \right\}$ , where  $\alpha = 2.52 \times 10^{-2}$ . This equation gives roughness-parameter values within a factor of 2 of those predicted by the model, whereas Owen's relationship yields values that in some cases are an order of magnitude higher.

The method derived here for calculating the local fluid shear stress differs from published eolian models for uniform grain sizes in that  $\tau_{ff}$  is calculated explicitly for each grain size within a mixture. The value of the critical shear stress (or shear velocity) for grain saltation for each grain size in a mixture is determined by initiating the motion of grains fluid mechanically, allowing them to hop continuously downwind, recording their trajectory sequences, and determining their mode

of transport at incremental increases in  $\tau_b > (\tau_{cr})_m$ . Transport modes can be determined directly from the model both visually, by graphing the position of each grain as it moves along its trajectory (e.g. Figure 3.6), and quantitatively, by calculating the distance between the centers of the moving grain and every grain that it passes over on the bed surface. Grain “rolling” is defined here as grain motion in which the particle never loses contact with stationary particles on the bed. Grain “saltation” refers to any particle that physically clears the next grain downwind without touching it; typically, once a grain is airborne, it will travel at least over the next several grains downwind. For the purposes of this shear-stress analysis, the definition of saltation includes creep, reptation, full saltation, and the rest of the class of terms (e.g. see discussion in Pye and Tsoar, 1990) used to describe grain motion other than rolling. This distinction is made to differentiate between particles that enter the airstream and exchange momentum with the near-bed flow above the viscous sublayer, versus those grains that are wholly to partially submerged in the viscous sublayer and whose forward momentum is complicated by continual contact with the bed-surface irregularities. For each grain-size fraction (e.g.  $D_{10}$ ,  $D_{20}$ , ...) present in the computer-generated sediment bed plotted in Figure 3.1, the transport mode of each grain moving at a particular value of the boundary shear stress is evaluated. At least 300 grain trajectories are analyzed at each increment of  $\tau_b$ . Grains are allowed to hop or roll continuously downwind until some unfavorable collision geometry terminates their movement. It is also possible to determine which grains absorb momentum transferred by the incoming particle but are not ejected from the bed; these particles vibrate in their bed pockets without being launched.

The ratio of the number of grains rolling to that saltating is calculated at increments of the transport stage  $[(T^*)_m = \tau_b/(\tau_{cr})_m]$  equal to  $0.10T^*$ . Results of the analysis are shown in Figure 3.7 as a function of the transport stage and the percent of rolling versus saltating grains, for seven grain-size fractions within the mixture. Figure 3.7 demonstrates that the range of transport stages between when only 50% of the grains are saltating and when 100% of the grains are saltating is small in the finer size fractions (e.g.  $D \leq D_{40}$ , where  $D_{40} = 0.50\text{mm}$ ). For the median and coarser size fractions ( $D \geq D_{50}$ ), however, the transport stage at which 100% of the grains saltate is about 15% greater than for the case where 50% of the particles saltate. In order to define  $(\tau_\eta)_m$ ,

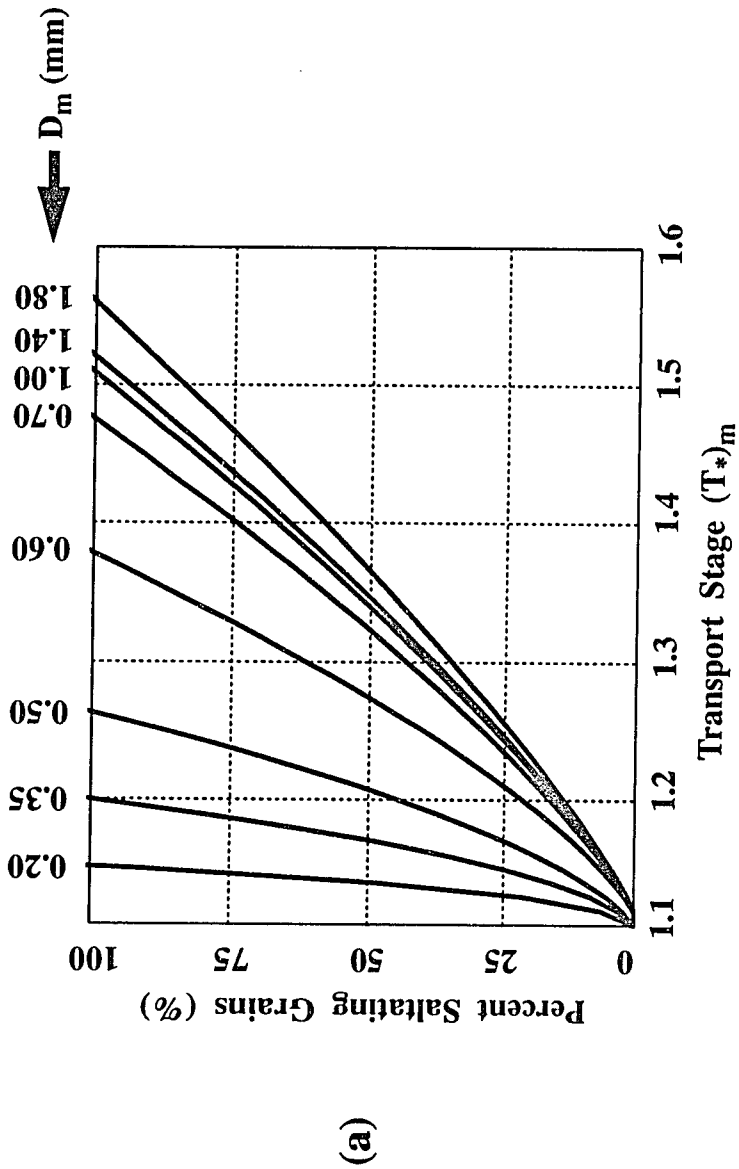


Figure 3.7 Model predictions of the critical shear stress for initiation of saltation for grain-size fractions of the sediment mixture. (a) Calculated percentages of each grain-size fraction ( $m$ ) entering the saltating mode as the transport stage [ $(T^*)_m = \tau_b/(\tau_{cr})_m$ ] increases. The transition from 0% to 100% grains saltating within any discrete grain-size fraction occurs almost instantaneously for the finer fractions (e.g.  $D_5 = 0.2\text{mm}$ ,  $D_{18} = 0.35\text{mm}$ , and  $D_{40} = 0.50\text{mm}$ ) and over an increasingly large range for the median ( $D_{50} = 0.70\text{mm}$ ) and coarser fractions (e.g.  $D_{70} = 1.0\text{mm}$ ,  $D_{86} = 1.4\text{mm}$ ,  $D_{95} = 1.8\text{mm}$ ).

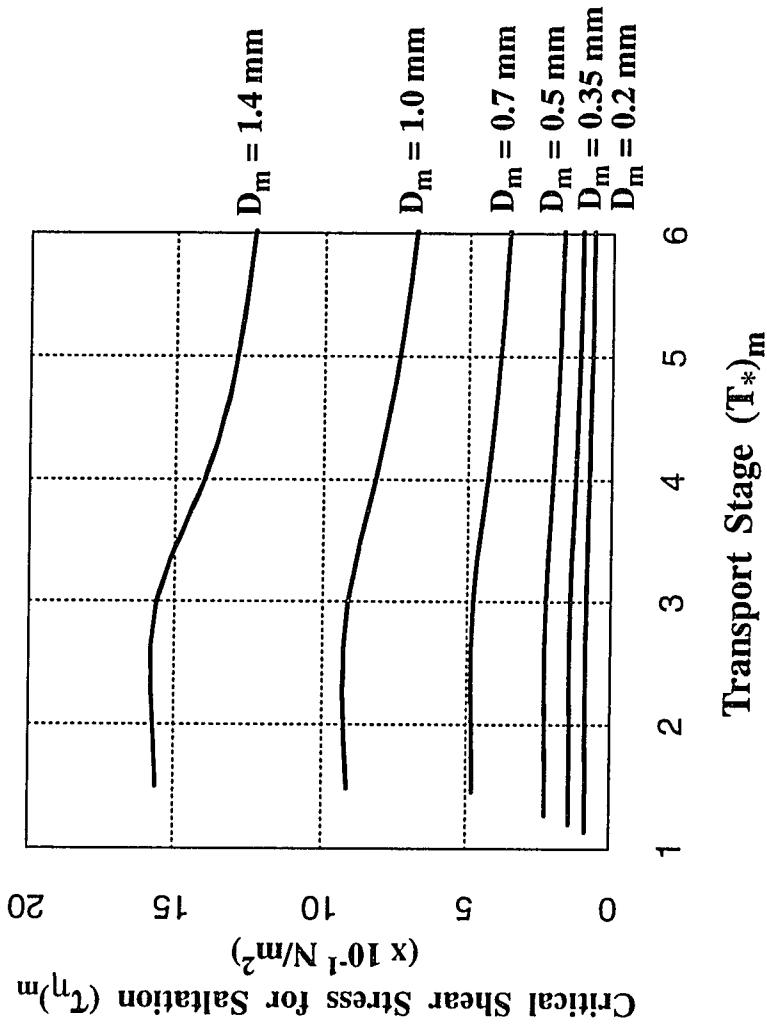


Figure 3.7 continued. Model predictions of the critical shear stress for initiation of saltation for grain-size fractions of the sediment mixture. (b) Calculated variation in the critical stress,  $(\tau_{\eta})_m$ , with increasing transport stage,  $[(T^*)_m = \tau_b/(\tau_{cr})_m]$ , for each grain-size fraction in the mixture. The magnitude of  $(\tau_{\eta})_m$  must be reduced at the higher transport stages (i.e.  $(T^*)_m > 3.0$ ) in order for the steady-state saltation criterion to apply.

consequently, it is necessary to determine what constitutes a “significant” percentage of each grain size saltating into the airstream, for the local fluid stress field to be appreciably altered by the moving sediment.

The solution to the question of significant saltation requires testing each value of  $(\tau_{\eta})_m$  with the model to evaluate which criterion (e.g. 50% vs. 100% saltation) leads to a stable, steady-state saltation regime for each sediment component. Steady-state saltation is achieved when the population of moving grains is self-replicating, that is, when each terminated hop sequence is replaced, on average, by a newly initiated one. The conceptual theory of self-regulation within the saltation layer has been reviewed by others (e.g. Pye and Tsoar, 1990; Anderson and Haff, 1991). Self-replication does not imply that only one grain will be ejected per hop sequence; many hop sequences result in no replacement ejections, while others might eject numerous grains into the moving sediment load. For the bed to be neither eroded nor aggraded over time requires that this condition hold.

The appropriate value of  $(\tau_{\eta})_m$  for each of the sediment components  $m$  was evaluated by selecting a particular grain-size fraction (e.g.  $D_{10}$ ,  $D_{20}$  ...), initiating hop trajectories of grains from that size class from random positions on the bed surface, allowing them to proceed downwind until they terminated, and determining whether each size fraction maintained an average equivalent of grain ejections and terminations over time (i.e. self-replication of the saltating population). Only grains of the selected size class were allowed to hop down the bed, so that the momentum exchange between that size fraction and the wind-velocity profile could be evaluated. The fluid shear stress was raised incrementally over a range of low to moderate transport stages (e.g.  $1 \leq (T^*)_m \leq 6$ ), and  $(\tau_{\eta})_m$  varied until self-replication was achieved at each increment of the transport stage. This test was conducted with at least 300 hop sequences for each grain-size fraction. These analyses employed the fully posed bedload-transport model, including the collisional and momentum-extraction algorithms yet to be discussed. In addition to achieving self-replication, the calculations required stabilization of the wind-velocity profile and the momentum exchange between moving grains of the given size class and the fluid. Simultaneous solutions for the unknown value of  $(\tau_{\eta})_m$ , the effective bed roughness ( $z_o$ ) enhanced by grain-fluid interactions

during sediment transport, and the structure of the velocity profile modified in response to the moving concentration of sediment components  $(C_s)_m$  were obtained by iteration. This test was repeated for each grain-size fraction individually, such that an appropriate value of the critical shear stress for saltation  $(\tau_\eta)_m$  was found for each size fraction in the mixture. Results of this analysis are shown in Figure 3.7b for six grain-size fractions.

Figures 3.7a and 3.7b demonstrate that the critical shear stress necessary for saltation of each size fraction  $(\tau_\eta)_m$  depends strongly on the transport stage. Furthermore, the manner in which  $(\tau_\eta)_m$  varies systematically with transport stage appears to be independent of grain size. At lower transport stages [e.g.  $(T^*)_m \leq 3$ ], the appropriate value of  $(\tau_\eta)_m$  for each sediment component corresponds to the 100% saltation criterion. At higher transport stages [e.g.  $(T^*)_m \geq 3$ ],  $(\tau_\eta)_m$  decreases, such that at a transport stage of  $(T^*)_m = 6$ , the critical shear stress for grain saltation  $(\tau_\eta)_m$  is reduced to a value corresponding to when only 75% of the particles saltate. This predicted relationship is shown in Figure 3.8a, in which the logarithm of the transport stage [ $\ln(T^*)_m$ ] is plotted against the percentage of saltating grains, for any grain-size fraction ( $D_m$ ). A reduction in  $\tau_\eta$  with increasing transport stage was predicted in the case of uniform-grain sizes also, although the decrease in the fluid stress with increasing transport stage occurred more rapidly (e.g. at a stress corresponding to 50% of the grains saltating at  $(T^*)_m = 6$ , versus 75% for the mixed-grain case). One explanation for this behavior is that as the boundary shear stress rises, grains become increasingly energetic and collide rigorously with the bed, some ejecting many more than one particle during the course of their multiple-hop path downwind. For self-replication to be maintained, however, the fluid flow must adjust to the increasing concentration of energetically moving grains such that they extract relatively less momentum from the flow, lose forward acceleration, and impart less momentum to stationary grains during collision with the bed. This is achieved through decreases in the fluid shear stress acting on the bed  $(\tau_\eta)$ . Therefore, as the transport stage increases above  $(T^*)_m = 3$ , the critical shear stress for saltation of each size fraction drops proportionately.

This reduction in  $\tau_\eta$  agrees, in general, with wind-tunnel observations that the fluid velocity in the bed region, as a function of the sediment-transport  $z_o$  and  $(u^*)_\eta$ , drops with incremental

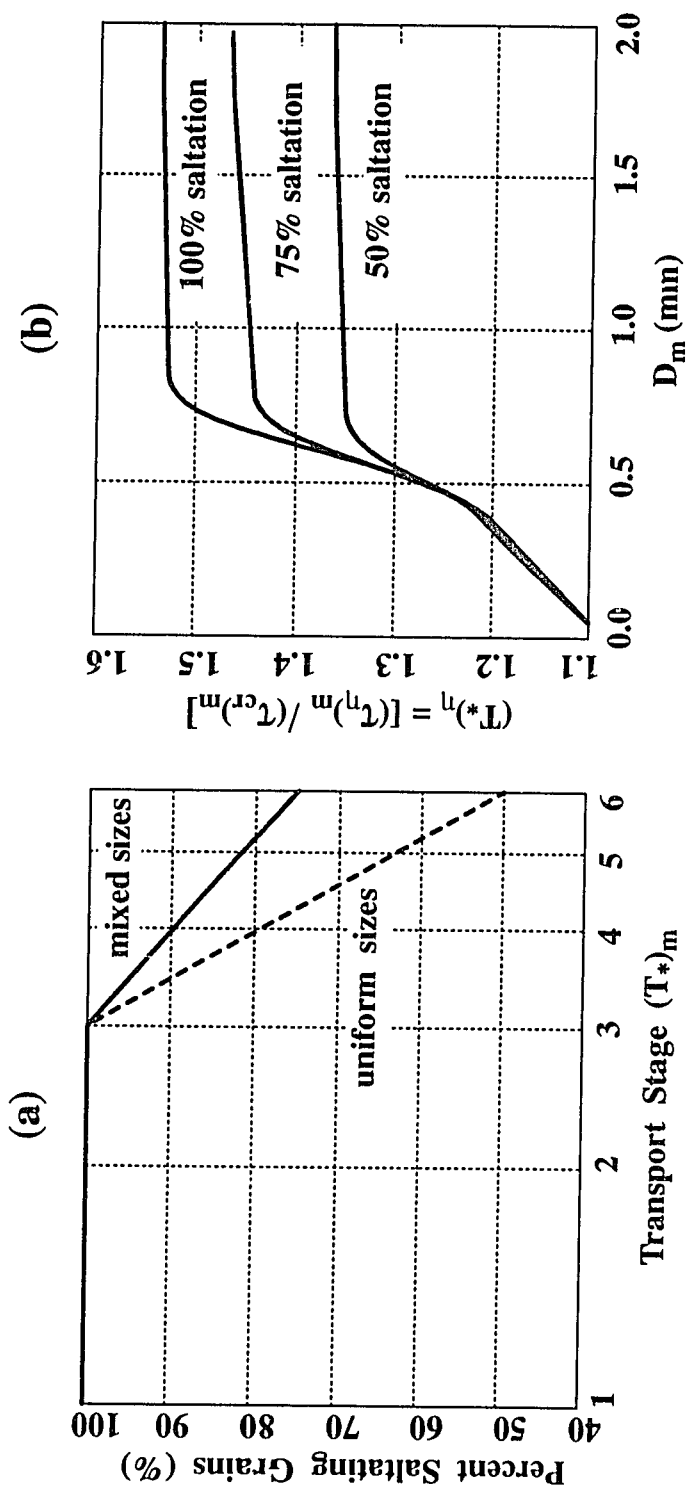


**Figure 3.8** Dependency of the critical fluid shear stress for initiation of saltation ( $\tau_\eta$ ) on grain-size fraction ( $D_m$ ) and transport stage ( $T^*_m = [\tau_\eta / (\tau_{cr})_m]$ ). **(a)** The predicted relationship between increasing transport stage ( $T^*_m$ ) and the percentage of salting grains. The curves apply to any grain-size fraction in the poorly sorted mixtures used herein. The decrease in numbers of salting grains with increasing transport stage, necessary for maintaining steady-state saltation, varies similarly for all grain sizes; however, the decrease is less rapid for grains travelling over a mixed-grain bed than over a uniform-sized bed. **(b)** Calculated critical transport stages for initiation of grain saltation  $[(T^*)_\eta = (\tau_\eta)_m / (\tau_{cr})_m]$  as a function of grain-size fraction ( $D_m$ ), for the 50%, 75%, and 100% saltation thresholds. The appropriate value of the critical stress  $(\tau_\eta)_m$  at a particular transport stage,  $1 \leq (T^*)_m \leq 6$ , can be found by determining the correct percentage of salting grains in **(a)** and applying that value to **(b)**, which then gives  $(\tau_\eta)_m$  as a function of  $(T^*)_\eta$ .

increases in the boundary shear stress  $\tau_b$  (e.g. Bagnold, 1941; Chepil and Woodruff, 1963). The results shown in Figure 3.8, however, differ from those obtained from published uniform-grain-size models. For example, some authors (e.g. Werner, 1990, Anderson and Haff, 1991; Sorensen, 1991) concluded that the steady-state fluid shear stress at the base of the saltation layer falls below the threshold required for aerodynamic entrainment (i.e.  $\tau_\eta < \tau_{cr}$ ) irrespective of transport stage, consistent with Bagnold's (1941, 1973) theory of an impact threshold below the fluid-entrainment threshold, whereas others (e.g. McEwan and Willetts, 1991) have argued that the shear stress at the bed is approximately equal to that required for sustaining aerodynamic entrainment ( $\tau_\eta = \tau_{cr}$ ), at all values of the transport stage. The variance in results might be due to the manner in which grain saltations and sediment concentrations were calculated in the various models, which drives the momentum-extraction computation and, hence, the determination of the local fluid shear stress associated with sediment transport. Anderson and Haff (1991) confined their calculations to a subset of grains with ten distinct impact velocities and their associated probability distributions of grain-ejection frequencies and lift-off velocities, while McEwan and Willetts (1991) employed a splash function based on wind-tunnel measurements of observable grain-saltation properties and grain-ejection frequencies. Sorensen (1991) and McEwan (1993) developed analytical expressions for the shear-stress and fluid-velocity profiles, which essentially yielded results similar to those obtained numerically; this is consistent with the fact that both authors based their analytical approximations on the splash functions of Anderson and Haff (1988; e.g. in the case of Sorensen) and McEwan and Willetts (1991; e.g. in the case of McEwan). Gerety and Slingerland (1983), however, speculate on the basis of wind-tunnel experiments with heterogeneous sands that threshold shear velocities deviate according to grain size from those given by Bagnold's impact law for uniform materials. The threshold stresses necessary to maintain saltation of coarse grains are higher than predicted by the impact-threshold theory, whereas those of smaller grains would be expected to be lower than the impact threshold. This variation arises from the unequal probability of various grain sizes being mobilized through collision on an irregularly arrayed, heterogeneous bed, whereby exposure of the bed particles to bombardment by moving grains differs substantially. Model predictions of a variation in  $\tau_\eta$  with grain size and transport stage are most consistent with



those of the empirical study, although the drop in the entrainment thresholds of the smaller size-fractions below their corresponding impact thresholds was not predicted. Model results establish that, for the sediment mixtures used, the fluid shear stress at a transport stage of  $(T^*)_m = 6$  still exceeds the threshold for fluid-mechanical initiation of grain motion  $[(\tau_\eta)_m > (\tau_{cr})_m]$  by as much as 1.5 times. At transport stages much greater than  $(T^*)_m = 6$ , outside the realm of those studied here, however, the fluid shear stresses for saltation of each grain-size fraction might well fall into or below the range of those necessary for sustaining aerodynamic entrainment.

Figure 3.8 summarizes the predicted values of the fluid shear stress for each grain-size fraction during sediment transport, necessary to set the boundary conditions for the fluid-velocity profile at the bed as a function of grain size and transport stage. Figure 3.8a gives the appropriate grain-saltation criteria as a function of transport stage  $(\tau_b/\tau_{cr})$ , which is independent of grain size. Based on the selected criteria (e.g. 75% vs. 100% grain saltation), a correct value of the grain-modified, fluid-shear stress can be obtained from Figure 3.8b, which shows the relationship between grain size ( $D_m$ ) and the critical shear stress for saltation of that grain size  $[(T^*)_m = (\tau_\eta)_m / (\tau_{cr})_m]$ , or the ratio of the critical shear stress for grain saltation and that for initial grain motion]. For  $D_m \geq D_{50} = 0.7\text{mm}$ , these curves approach asymptotes, as the magnitude of the shear stress required to initiate grain saltation, over that for initiation of grain rolling, becomes proportionately higher.

While the computational methods described here apply to any mixed-grain sediment bed, the values of the local fluid shear stress given in Figures 3.7 and 3.8 pertain to the sediment mixture of this study, as well as to others with a similar grain-size frequency distribution. For substantially different grain-size frequency distributions, it would be desirable to carry out a complementary set of calculations to verify the relationship between grain size, transport stage, and transport mode. Comparisons of the fluid shear stress for each size fraction in the mixed-grain case with those predicted for each grain size over a like-sized sediment bed indicate that the local fluid shear stress must be reduced significantly more in the latter case. This suggests that grains hopping over a mixed-grain bed are relatively less energetic and extract less momentum from the flow on average than in uni-sized deposits at the same transport stage. As hop heights are

governed in part by the magnitude and direction of grain lift-off angles and velocities in relation to the bed, which are, in turn, influenced by the topographic irregularities of the sediment deposit, the effects of the mixed-grain bed on the structure of the momentum-extraction profile are indirect but critically important.

### 3.6 Numerical modelling approach. III: Quantifying momentum extraction

The momentum exchange between the fluid and sediment, resulting in particle acceleration downwind, is accomplished primarily through the horizontal component of the drag force  $[(F_D)_m]_x$  acting on each sediment component  $m$ . Owing to the rapid decrease in concentration of moving grains with distance from the bed, which has been documented experimentally and theoretically (e.g. see summary by Pye and Tsoar, 1990), the momentum-extraction process is most sensitive to the concentration field nearest the bed. The magnitude of the stress exerted by the fluid on the moving particles at successive heights above the bed, therefore, becomes a function of  $[(F_D)_m]_x$  multiplied by the sediment concentration at each level. This relationship has been made use of in several models addressing uniform grain-size materials (e.g. Sorensen, 1985, 1991; Ungar and Haff, 1987; Werner, 1990; Anderson and Haff, 1991, McEwan and Willetts, 1991; McEwan, 1993). These authors described the dynamics of the momentum-exchange process through applying a body force per unit volume acting in the upwind direction; the vertical profile of the cumulative drag force acting within the saltation layer was then calculated by summing the magnitude of the body forces on all particles present at each level above the bed. In their models, the concentration of moving grains was set by the number of grains permitted by a splash function to leave a given bed area per unit time.

Momentum extraction is calculated similarly in the mixed-grain case by quantifying the product of the drag force per unit sediment volume and the concentration of each sediment component ( $C_m$ ) at successive heights above the bed. In this model, the concentration of moving grains is predicted by the saltation model. The product  $(F_D)_m C_m$  is summed over all such components at each level, from which the momentum extracted by each size fraction at each level can be determined. The total momentum reduction of the fluid by the grains at each increment of

height above the nonmoving part of the bed is the sum of the momentum extracted by each sediment component:  $(F_D C_s)_{tot} = \sum_{m=1}^M (F_D)_m C_m$ .

The stress of fluid-solid interactions,  $(\tau_{fs})$ , can be expressed as a force per unit area. The unit area over which the drag force on each grain acts is represented as the downwind distance between any two like-sized grains ( $L$ ) times the grain diameter ( $D_m$ ). The two grains can appear at any height in the fluid. The distance ( $L$ ) obtains from the definition of sediment concentration, which is the ratio of the sediment volume to the total volume of fluid and sediment combined  $[C_m = (\pi D_m^3/6)(LD_m^2)^{-1}]$ . Rearranging this expression,  $LD_m = [\pi D_m^2]/[6C_m] = [V_m/C_m]D_m$ , where  $V_m$  is the volume of the sediment grain. This technique has also been applied to uniform grain-size transport in air (Calder, 1987) and in water (Wiberg, 1987; Wiberg and Smith, 1989).

The stress of the fluid acting on a sediment component  $m$ , therefore, is the horizontal component of the drag force  $[(F_D)_m]_x$  per unit area ( $LD_m$ ), which can be rewritten as a function of the grain concentration  $C_m$  based on the geometric argument above:

$$(\tau_{fs})_m = \frac{[(F_D)_m]_x}{LD_m} = \left[ \frac{(F_D)_m}{V_m} \right]_x C_m D_m \quad (3.12)$$

where  $F_D = (\rho/2) c_d A_D |\mathbf{u}_\Delta| u_\Delta$ ;  $\mathbf{u}_\Delta$  is the difference between the air and grain velocity,  $A_D$  is the cross-sectional area of the grain normal to the drag force, and  $c_d$  is the drag coefficient. The total stress of the fluid in the saltation region,  $\tau_T = \tau_F$ , acting on any sediment component  $m$  is partitioned into the stress of the fluid acting on each sediment component  $(\tau_{fs})_m$  and the fluid-borne stress in the path of each moving particle  $\tau_{ff}$ , which for clarification is denoted here as  $(\tau_{ff})_m$ . Hence,  $(\tau_T)_m = (\tau_{ff})_m + (\tau_{fs})_m$ , following this notation. Substituting equation 3.12 into this expression yields:

$$(\tau_T)_m = (\tau_{ff})_m + \left[ \frac{(F_D)_m}{V_m} \right]_x C_m D_m \quad (3.13)$$

where  $(\tau_T)_m$  is the total local shear stress affected by sediment component  $m$ . There are  $m$  such equations representing each grain-size fraction within the mixture.

Manipulation of equation 3.13 yields explicit expressions for both the local fluid stress and

the concentration of each grain-size fraction at the bed. At the local bed surface ( $\eta$ ), the local fluid shear stress is equal to the critical shear stress for initiation of grain saltation [ $\tau_{ff} = (\tau_{ff})_\eta$ ], as discussed in the previous section (3.5). Evaluating equation 3.13 at the bed and rearranging gives an expression for the total fluid stress at the bed in terms of the momentum exchange between the fluid and any given grain-size fraction:

$$(\tau_T)_m - [(\tau_{ff})_\eta]_m = \left[ \left( \frac{(F_D)_m}{V_m} \right)_x C_m D_m \right]_\eta . \quad (3.14)$$

An expression for the concentration of moving sediment components  $m$  at the bed also derives from rearrangement of equation 3.14, written for each grain-size fraction in terms of the total shear stress, the critical shear stress for the initiation of saltation [ $[(\tau_{ff})_\eta]_m = (\tau_\eta)_m$  by convention], the drag force per unit volume on a sediment grain just above the nonmoving portion of the bed, and the grain diameter:

$$(C_m)_\eta = \frac{(\tau_T)_m - (\tau_\eta)_m}{[(F_D)_m / V_m]_\eta D_m} . \quad (3.15)$$

The sediment concentration of component  $m$  at any level within the saltation layer may be expressed as its magnitude relative to that at the bed; consequently,  $(C_*)_m$  is defined here as the concentration of component  $m$  normalized by the concentration of component  $m$  at the bed:  $C_m = (C_m)_\eta (C_*)_m$ . Likewise,  $(F_*)_m$  represents the drag force per unit volume of component  $m$ , normalized by its value at the bed:  $[(F_D)_m / V_m] = [(F_D)_m / V_m]_\eta (F_*)_m$ . These nondimensional parameters  $(F_*)_m$  and  $(C_*)_m$  both go to unity at the nonmoving bed surface.

An expression for the local fluid stress on each sediment component can now be written in terms of these nondimensional parameters in a rearrangement of equation 3.13:

$$(\tau_{ff})_m = (\tau_T)_m - (F_* C_*)_m [(F_D)_m / V_m]_\eta C_m D_m \quad (3.16a)$$

$$= (\tau_T)_m - [(\tau_T)_m - (\tau_\eta)_m] (F_* C_*)_m , \quad (3.16b)$$

which is solved for each sediment component  $m$  at a level  $z$  above the bed, in terms of the known critical shear stress for initiation of saltation  $\tau_{\eta}$ , the total local shear stress  $(\tau_T)_m$  affected by sediment component  $m$ , and the momentum reduction associated with the moving grains  $(F_*C_*)_m$ .

A numerical expression for the fluid velocity gradient as a function of height above the bed is derived by applying the turbulent mixing-length hypothesis to equation 3.16b above. Within the saltation layer, the local fluid stress  $\tau_{ff}$  is proportional to the vertical variation in fluid velocity and the height-dependent, turbulent eddy viscosity, approximated as  $K = k(u_*)_f z$ :

$$\tau_{ff} = \rho k (u_*)_T z \frac{\partial u}{\partial z} \quad (3.17)$$

where  $k = 0.408$  is von Karman's constant,  $(u_*)_T$  is the total local shear velocity, and  $\rho$  is the fluid density. The use of a mixing-length model to close the governing equation (i.e. equation 3.8b) is in common with numerous uniform-grain-size, sediment-transport theories (e.g. Sorensen, 1985; Calder, 1987; Wiberg, 1987; Ungar and Haff, 1987; Werner, 1990; Anderson and Haff, 1991; McEwan and Willetts, 1991; Raupach, 1991; Sorensen, 1991; McEwan, 1993). Rewriting equation 3.16b in terms of the local shear velocity  $(u_*)_f$  gives:

$$[(u_*)_f]_m = \left[ \frac{(\tau_{ff})_m}{\rho} \right]^{\frac{1}{2}} = [(u_*)_T]_m \left[ 1 - \left( \frac{(\tau_T)_m - (\tau_{\eta})_m}{(\tau_T)_m} \right) (F_*C_*)_m \right]^{\frac{1}{2}} \quad (3.18)$$

and substituting into equation 3.17 yields an equation for the velocity gradient as a function of momentum reduction associated with each sediment component  $m$ :

$$\left[ \frac{\partial u}{\partial z} \right]_m = \frac{[(u_*)_T]_m}{kz} \left[ 1 - \left( \frac{(\tau_T)_m - (\tau_{\eta})_m}{(\tau_T)_m} \right) (F_*C_*)_m \right]^{\frac{1}{2}}. \quad (3.19)$$

Integration of equation 3.19 produces a numerical expression for the vertical profile of fluid velocity for each sediment component  $m$  over the region extending from the  $z=0$  reference line in the sediment bed to any level within the saltation layer ( $z < \delta_B$ ):

$$u(m) = \frac{[(u_*)_T]_m}{k} \int_{(z_o)_N}^z \left[ 1 - \left( \frac{(\tau_T)_m - (\tau_\eta)_m}{(\tau_T)_m} \right) (F_* C_*)_m \right]^{\frac{1}{2}} \left[ \frac{1}{z} \right] dz, \quad (3.20)$$

where  $(z_o)_N$  is the effective roughness of the surface before sand transport, spatially adjusted to the  $z=0$  reference line of Figure 3.2. Hence, for any value of the transport stage  $[(T_*)_m = \tau_T/(\tau_{cr})_m]$ , the fluid velocity at height  $z$  above the bed, modified by transport of a given sediment component  $m$  at that level, depends on the excess total local fluid stress  $[S_T = (\tau_T - \tau_\eta)/\tau_T]$  and the magnitude of the momentum extracted from the flow by the moving grains  $(F_* C_*)_m$ . This equation poses the velocity profile for any sediment component  $m$  as a function of height  $z$  above the bed, in terms calculable with the sediment-transport model described herein. The values of the critical shear stress for initiation of saltation for each sediment component  $(\tau_\eta)_m$  are derived with the numerical theory presented in section 3.5. The remaining unsolved term, therefore, is  $(F_* C_*)_m$ ; a method for calculating the momentum-extraction parameter is now discussed.

Similar to methods introduced by others for uniform-sized sediments (e.g. Sorensen, 1985; Anderson, 1986; Ungar and Haff, 1987; Wiberg, 1987; Werner, 1990; Anderson and Haff, 1991; McEwan and Willetts, 1991), the horizontal component of the drag force  $(F_D)_x$  for each sediment component  $m$  is calculated by the saltation model for successive increments of height  $z$  above the bed, along its entire trajectory. Quantifying the sediment concentration follows Wiberg (1987; see Wiberg and Smith, 1989) and Calder (1987); this approach differs from the uniform-grain eolian models cited above, which derive the number of grains ejected per unit area of the bed per unit time from simulations involving experimental observations and which assume either identical grain trajectories (e.g. Ungar and Haff, 1987) or employ a selected subset of trajectory possibilities (e.g. Sorensen, 1985; Anderson, 1986; Werner, 1987, 1990; Anderson and Haff, 1991; McEwan and Willetts, 1991).

In this model, a large number of continuous particle-hop sequences (e.g. 200) are computed via the saltation algorithm described in section 3.4, coupled with the predictive collisional component (Chapter 4). Each grain rebounds in a series of unique trajectories whose lift-off angles and velocities depend on the predicted dynamical and geometric properties of its random

collision with stationary particles on the mixed-grain bed. The sediment concentration is equivalent to the probability of each particle occupying a spot in the flow at a given instant in time; hence,  $C_m$  is proportional to the time ( $\Delta t$ ) that each component particle spends in an increment  $z_i = \alpha D_m$ , where  $\alpha = 0.10$  (i.e.  $\Delta z = z_{i+1} - z_i$ ). For a single grain  $s$ ,  $C_s(z) \sim (\Delta t / \Delta z)$ . The magnitudes of the drag force  $[(F_D)_s]_x$ , the flight time per increment  $(\Delta t / \Delta z)$ , and the product  $[(F_D)_s]_x (\Delta t / \Delta z)$ , on both the upgoing- and downgoing- limbs of individual trajectories are summed. The product of the drag force times sediment concentration is determined by grain-size fraction (e.g.  $D_{10}$ ,  $D_{20}$ , ...), such that its value for any component  $m$  at a particular flow height  $z$  is the sum for all grains within that grain-size class; therefore,  $[(F_D)_m]_x (\Delta t / \Delta z)_m = \sum_{s=m}^{m+1} [(F_D)_s]_x (\Delta t / \Delta z)$ . The true value of the sediment concentration for each component  $C_m(z)$  is obtained from the previously described relationship:  $C_m(z) = [(C_m)_\eta (C^*)_m](z)$ , where  $(C_m)_\eta$  is found from equation 3.15. Because the probability distribution of like-sized grains in motion is dictated by the frequency distribution of that particle size in the bed surface, the number of grain trajectories summed to yield any component product  $[(F_D)_m]_x C_m$  may vary from 100 for the tail members of the distribution to 1000 for the median class. The momentum-extraction profile for each component is normalized by dividing  $(F_D)_m C_m$  at each level of  $z$  by its respective value at the bed:  $(F \cdot C^*)_m = [(F_D)_m C_m] / [(F_D)_m C_m]_\eta$ .

Figure 3.9 shows representative normalized profiles for the sediment concentration, horizontal component of the drag force, and the product  $(F \cdot C^*)_m$  for the case of  $D_{50} = 0.70\text{mm}$ ,  $(T^*)_{50} = 3.0$ , and  $n = 1276$  hop trajectories. As expected, the concentration profile (Figure 3.9a) displays a quasi-exponential decrease in the mass of moving particles with distance from the bed, similar to profiles constructed from wind-tunnel measurements of sediment discharge (e.g. Williams, 1964; Sorensen, 1985). The drag-force profile (Figure 3.9b) confirms that the greatest cumulative, instantaneous force acting on particles of a given size fraction occurs near the bed at the outset of particle trajectories, where the relative velocities between the moving fluid and the slower-moving particles are the greatest. The curve drops back in the vicinity of the origin because many particles are moving faster than the wind and, therefore, the horizontal component of the drag force acting on these grains becomes negative shortly before collision with the bed. As

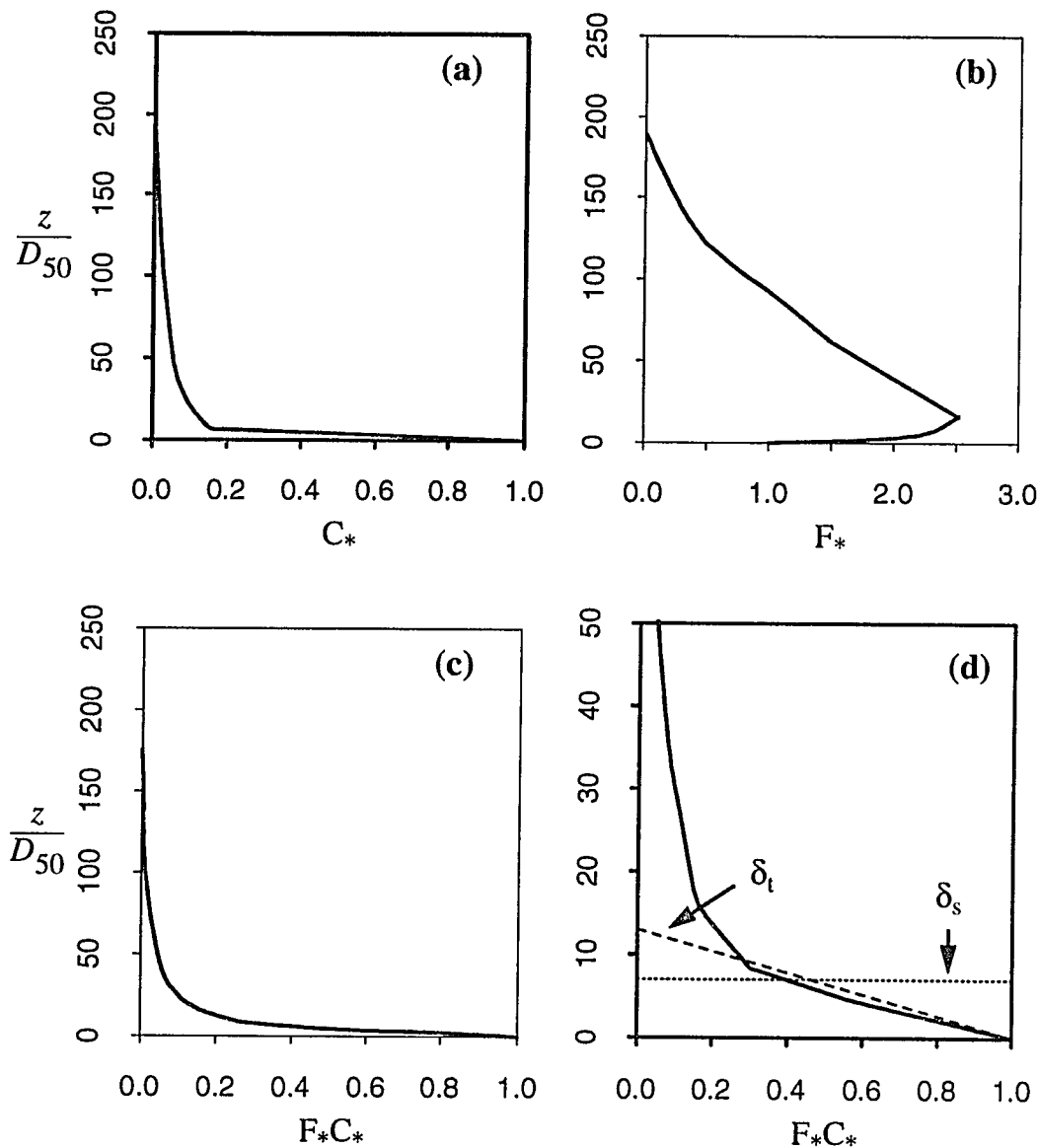


**Figure 3.9** Smoothed vertical profiles of the sediment concentration, horizontal component of the drag force, and product of the drag force times concentration, as functions of height above the bed ( $z$ ) nondimensionalized by the median grain diameter ( $D_{50}$ ). (a) sediment concentration nondimensionalized by its value at the bed,  $C_*$ . (b) drag force normalized by the value at the bed,  $F_*$ . (c) product of the drag force times sediment concentration ( $F_*C_*$ ) normalized by its value at the bed. (d) analytical solution to the near-bed profile,  $(F_*C_*)_m = [1 - z/(\delta_t)_m]$ , valid to a height of  $\delta_s = 7D_{50}$ . For the steady-state case in which the flow is in equilibrium with moving grains from all represented size fractions;  $D_{50} = 0.70\text{mm}$ ,  $(T_*)_{50} = 3.0$ , and  $n = 1276$ . The height of the saltation layer ( $\delta_B$ ) is  $222.4 D_{50}$ , set by the maximum hop height of the  $D_{18}$  size fraction.



demonstrated in Figure 3.9c, the shape of the momentum-extraction curve  $(F_*C_*)_m$  is dominated by the form of the concentration profile. The structure of this curve remains the same regardless of the grain size ( $D_m$ ) or the transport stage  $(T_*)_m$ . The curve shifts laterally for each grain-size fraction, depending on the relative numbers of grains extracting momentum from the flow and the energetics of the saltation trajectories, which define the thickness of the bedload layer. A stabilized curve, however, reproduces itself because the population of moving grains equilibrates with the wind profile, such that the distribution of hop heights and lengths remains uniform and the thickness of the saltation layer becomes constant. The momentum-extraction curve retains its shape but shifts vertically depending on the grain-size fraction; this derives from the fact that the smaller fractions tend to hop higher and more energetically than the coarser fractions at a given transport stage, an observation that has been verified experimentally (e.g. Gerety and Slingerland, 1983; Barndorff-Nielsen *et al.*, 1985b).

Through the flow-transition region between the viscous sublayer near the bed surface and a level in the saltation layer corresponding to  $14D_m$ , the momentum-extraction profile for each grain-size fraction is linearly decreasing (e.g. Figure 3.9d). This observation applies to all grain-size fractions within a mixture and at all transport stages studied. Consequently, the  $(F_*C_*)_m$  curve for each sediment component  $m$  in this flow region may be approximated linearly. This approximation facilitates an analytical solution to the modified velocity profile in the flow-transition region (i.e.  $z \ll \delta_T$ , as indicated in Figure 3.5). Hence, below the level of  $\delta_t = 14D_m$ , the momentum-extraction profile is defined as:

$$(F_*C_*)_m = \frac{(\delta_t)_m - z}{(\delta_t)_m} = \left[ 1 - \frac{z}{(\delta_t)_m} \right] = 1 - \xi_m . \quad (3.21)$$

This approximation applies only to the near-bed region. Above some height  $(\delta_s)_m$  (see Figure 3.9d), which is less than  $(\delta_t)_m$  [e.g.  $(\delta_s)_m \approx 7D_m$ ], the  $(F_*C_*)_m$  curve is calculated numerically through equation 3.20.

The equation for the modified fluid-velocity gradient (3.19) can now be rewritten by substituting the analytical expression for  $(F_*C_*)_m$  (equation 3.21) as it pertains to the near-bed

region,  $z < (\delta_s)_m$ :

$$\left[ \frac{\partial u}{\partial z} \right]_m = \frac{[(u_*)_T]_m}{kz} \left[ 1 - \left( \frac{(\tau_T)_m - (\tau_\eta)_m}{(\tau_T)_m} \right) (1 - \xi_m) \right]^{\frac{1}{2}} \quad (3.22a)$$

$$= \frac{[(u_*)_\eta]_m}{kz} [1 + (S_\eta)_m \xi_m]^{1/2} \quad (3.22b)$$

where  $[(u_*)_\eta]_m = [(\tau_\eta)_m / \rho]^{1/2}$ , and  $(S_\eta)_m = \{ [(\tau_T)_m - (\tau_\eta)_m] / (\tau_\eta)_m \}$  is the nondimensional excess shear stress defined in terms of the critical shear stress for initiation of motion of each sediment component  $m$ . The integral form of equation 3.22b, from  $(z_o)_N$  where  $\xi = (\xi_\eta)_N$ , to any height  $z$  above the bed, is:

$$u(m) = \frac{[(u_*)_\eta]_m}{k} \int_{(\xi_\eta)_N}^{\xi} \frac{[1 + (S_\eta)_m \xi_m]^{1/2}}{\xi_m} d\xi \quad (3.23a)$$

$$= \frac{[(u_*)_\eta]_m}{k} \left[ 2 [1 + (S_\eta)_m \xi_m]^{1/2} + \ln \frac{[1 + (S_\eta)_m \xi_m]^{1/2} - 1}{[1 + (S_\eta)_m \xi_m]^{1/2} + 1} \right] \Bigg|_{(\xi_\eta)_N}^{\xi} \quad (3.23b)$$

by integral definition. Integration yields the analytical form of the modified fluid-velocity profile for the lower part of the saltation layer, appropriate for each sediment component  $m$ , as a function of height above the bed surface, the critical shear velocity for initiation of saltation  $[(u_*)_\eta]_m$ , and the excess shear stress related to the saltation threshold:

$$u(m) = \frac{[(u_*)_\eta]_m}{k} \left[ 2 [1 + (S_\eta)_m \xi_m]^{1/2} - 2 [1 + (S_\eta)_m (\xi_\eta)_m]^{1/2} \right. \\ \left. \ln \left[ \frac{[1 + (S_\eta)_m \xi_m]^{1/2} - 1}{[1 + (S_\eta)_m \xi_m]^{1/2} + 1} \right] \left( \frac{[1 + (S_\eta)_m (\xi_\eta)_m]^{1/2} + 1}{[1 + (S_\eta)_m (\xi_\eta)_m]^{1/2} - 1} \right) \right] \quad (3.24)$$

where  $\xi_m = [z/(\delta_v)_m]$ ,  $(\xi_\eta)_m = [(z_o)_N/(\delta_v)_m]$ , and  $(\delta_v)_m = 14D_m$ . This expression collapses to the familiar ‘‘Law of the Wall’’ equation for  $|(S_\eta)_m \xi_m| \ll 1$ .

Equation 3.24 may be modified further to account explicitly for viscous effects in the region of the bed. As discussed earlier in this chapter, the presence of a viscous sublayer draping the granular surface has a measurable effect on the bed-roughness parameter  $(z_o)$  under weak flow regimes. Incorporating the Reichardt correction described in section 3.2 (equation 3.7) yields smooth transitions between the linear velocity profile within the viscous sublayer,  $\delta_v \equiv 11.6\nu/(u^*)_\eta$ , the near-bed flow region whose profile is approximated linearly,  $\delta_v < z < \delta_s$ , and the quasi-logarithmic profile of the transition zone between the viscous and fully turbulent layers  $\delta_T$ , which lies somewhere between  $\delta_v$  and  $\delta_t = 14D_m$  for low- to moderate- transport regimes. Combining equations 3.7 and 3.24 yields the following:

$$\begin{aligned}
 u(m) = & \\
 & \frac{[(u^*)_\eta]_m}{k} \left\{ \ln \left[ 1 + \frac{R_* z_o}{2.5k_s} \left( \frac{[1 + (S_\eta)_m \xi_m]^{1/2} - 1}{[1 + (S_\eta)_m \xi_m]^{1/2} + 1} \left[ \frac{[1 + (S_\eta)_m (\xi_\eta)_m]^{1/2} + 1}{[1 + (S_\eta)_m (\xi_\eta)_m]^{1/2} - 1} \right] \right) \right] \right. \\
 & + \left[ -\ln \frac{R_* z_o}{k_s} + 2.3 \right] \left[ 1 - \exp\left(-\frac{z}{k_s}\right) \left(\frac{R_*}{11.6}\right) - \left(\frac{z}{k_s}\right) \left(\frac{R_*}{11.6}\right) \exp\left(-0.33\frac{R_* z}{k_s}\right) \right] \\
 & \left. + 5 \left[ [1 + (S_\eta)_m \xi_m]^{1/2} - [1 + (S_\eta)_m (\xi_\eta)_m]^{1/2} \right] \right\} \quad (3.25)
 \end{aligned}$$

where  $R_* = [(u^*)_\eta]_m k_s / \nu$ ,  $k_s = D_{50}$ , and  $z_o = (z_o)_N$ .

Above the saltation layer ( $z > \delta_B$ ), the fluid-velocity profile is given by:

$$u = \frac{(u^*)_T}{k} \ln \frac{z}{(z_o)_T} \quad (3.26)$$

As described earlier, the bed-roughness parameter  $(z_o)_T = (z_o)_{st}$  is governed by the extraction of

momentum within the saltation layer. The magnitude of  $(z_o)_T$  for the wind profile modified by each airborne sediment component  $m$  is found by first integrating equation 3.19 for the velocity gradient through the saltation layer above  $(\delta_s)_m$ . The magnitude of the fluid velocity at  $(\delta_s)_m$  is obtained through equation 3.25, which can also be applied at  $(\delta_B)_m$  to calculate the velocity difference between  $(\delta_s)_m$  and  $(\delta_B)_m$ . The velocity difference is then added to the magnitude of the velocity at  $(\delta_s)_m$ , to obtain the wind velocity at the top of the saltation layer  $u[(\delta_B)_m]$ . Substituting  $u[(\delta_B)_m]$  and  $z = (\delta_B)_m$  into equation 3.26 gives:

$$[(z_o)_T]_m = \delta_B \exp \left[ -k \frac{u[(\delta_B)_m]}{[(u_*)_T]_m} \right]. \quad (3.27)$$

The shape of the velocity curve above  $(\delta_s)_m$  and the value of  $(z_o)_T$  must be found iteratively for each grain-size fraction in the saltation layer, because the velocity profile depends on  $(F \cdot C_*)_m$ , but  $(F \cdot C_*)_m$  depends on the velocity profile through the drag-force term.

The vertical profile of fluid flow during sediment transport over heterogeneous beds, thus, comprises three separate layers whose velocities are matched at the boundaries of each zone. The near-bed velocity profile between  $z = 0$  and  $z = \delta_s$  corresponds to equation 3.25, in which the linear profile within the viscous sublayer smoothly connects with the profile in the transition zone [ $\delta_s \approx O(\delta_T)$ ] between the viscous sublayer below and the turbulent flow above. Within the main saltation layer,  $\delta_s < z < \delta_B$ , the velocity-profile equation is given by equation 3.20, in which the magnitude of momentum extraction is calculated as the horizontal component of the drag force on grains times the concentration of moving particles. Above the saltation layer,  $z > \delta_B$ , the velocity profile is calculated by the "Law of the Wall" equation (3.27), where the magnitude of the sediment-transport-enhanced, bed-roughness parameter  $(z_o)_T$  depends on the momentum-modified velocity profile through the saltation region and must, consequently, be found through iteration. The convergence of the unified velocity profile with each subsequent iteration is oscillatory in nature, as extraction of too much momentum in one step generates a population of moving grains that is too energetic in the next step. These fluctuations occur systematically, though, and their magnitudes are predictable, such that the curves can be weighted as a function of  $z$  by the fraction

of  $F_*C_*$  under- or over- predicted. A stable solution typically results after three to five iterations. Because the velocity profile depends on  $F_*C_*$ , which, in turn, depends on the volume of each sediment size in motion, the response of the velocity profile to each airborne grain-size fraction must be calculated separately. Hence, the total momentum defect at each level in the flow comprises the sum of the momentum extracted by each sediment component, resulting in a unique relationship of each grain size to the velocity profile of the windstream.

### 3.7 Calculated momentum-extraction profiles

Mixed-grain sediment-transport theory is complicated by the existence of three, interrelated unknown quantities: the magnitude of momentum extracted by each sediment component from the flow, the relative influence of the momentum exchanged by each size fraction on the net momentum-extraction profile, and the form of the vertical profile of downwind fluid velocity. Hence, the numerical scheme developed to quantify the momentum deficit in the vertical profile of wind velocity comprises a series of iterative steps. The following two paragraphs summarize this procedure.

The first iteration requires an initial velocity profile which, in turn requires an initial momentum-extraction profile. The latter may be characterized by a set of curves, one for each fraction of the grain-size frequency distribution that, when summed, yield the profile of momentum extracted by all grains of the sediment mixture. Because the relative proportion of the momentum transferred between the fluid and the various grain sizes is unknown, a suitable hypothesis for their relationship must be established. This is achieved by calculating the momentum-extraction curve generated when only grains of a particular size class are in motion. This calculation is repeated not only for each grain-size fraction present, but also for each incremental increase in the boundary shear stress. There are several mechanisms for deriving the initial profile of fluid velocity, including guesswork. The method chosen here was to impose the previously calculated velocity profile, for the same relative grain diameter, from the uniform-sized sediment case (Calder, 1987). Iterations are performed to find the stable forms of the velocity and momentum-extraction profiles for each grain size.

The second series of iterations uses these initial momentum-extraction and fluid-velocity profiles as input to calculate the full sediment-transport problem, in which grains of all sizes are permitted to move from the bed. For the flux of the mixture to be self-replicating under steady-state conditions, the momentum exchange between the wind and each size fraction should equilibrate with time. Iterations are required to stabilize the velocity and fractional momentum-extraction profiles. A stable solution for the wind profile during transport of a granular mixture yields a total bedload flux in which each grain deposited on the bed is replaced on average by an ejected grain of any size.

No empirical data yet exist with which to test the ability of this fluid-mechanical algorithm to quantify the momentum exchange between the fluid and each sediment component during heterogeneous bedload transport; in fact, measurements of the fluid velocity as it responds discretely to each grain-size concentration in a moving mixture would be very difficult to procure. Measured mass-flux profiles, however, provide an avenue for back-calculating many important dynamical properties of transporting systems, including the mean local shear velocities and the concentration gradients of moving grains as a function of height. Empirical bedload-transport rates also have been used extensively by others to verify theoretical predictions of the magnitude of the wind-grain momentum feedback. Typically, mass-flux measurements of sediment mixtures have been presented as one curve representing total bedload discharge, rather than as a suite of constituent curves for the range of grain-size fractions present. Whereas the magnitude of momentum extraction in uniform-sized sediments can be evaluated, in an average sense, against such a curve, the mixed-grain problem requires the fractional mass-flux profiles to verify that the momentum exchange between the fluid and each size class has been accounted for adequately. Consequently, the grain mixture of the Yamasaka and Ikeda (1988) experiments is employed here, so that a comparison between measured and experimental fractional-transport rates can be made.

Calculating the initial form of the momentum-extraction profile for each grain-size fraction proceeds by aerodynamically initiating a grain from a given size class into motion, at the specified boundary shear stress, and allowing it to travel downwind until it lodges in the bed surface. Grains hop or roll, depending on their kinetic energy, and execute one to many (e.g. 100) rebounding

trajectories until some geometric grain configuration of the bed surface, or particle momentum insufficient to propel them over a bed element, terminates forward movement. The latter typically occurs when the bulk of grain-borne momentum is transferred to stationary grains of disparate size on the bed surface. Depending on the geometry of a collision, particles also rebound in the upwind direction and collide with the bed before resuming hop sequences downwind (i.e. trajectories in the negative x-direction), as has been observed experimentally (e.g. Willetts; see comments in Anderson and Haff, 1991). The sediment bed shown in Figure 3.1 is assigned periodic boundaries, so that any grains travelling farther than  $1000 D_{50}$  downwind are re-entered at the upwind boundary with the same particle velocity and ballistic characteristics that propelled them from the downwind edge. Following aerodynamic entrainment of the first particle, all other grains are ejected by impact. Only those ejected particles belonging to the specified size class are permitted to move from the bed. An average of 300 grain trajectories are computed for each grain-size fraction. The momentum-extraction and fluid-velocity profiles generated from the first iteration are employed in the second iteration, and so on, until the profiles from successive iterations converge on a single, stable form. The vertical profile of downwind velocity for each subsequent iteration is calculated as described in section 3.6 (equations 3.25, 3.20, and 3.26), with the appropriate local fluid shear stress associated with the grain-saltation threshold (Figure 3.8). Consistent with the format of the Yamasaka and Ikeda (1988) data, the grain-size frequency distribution is divided into seven size fractions:  $D_5 = 0.20\text{mm}$ ,  $D_{18} = 0.35\text{mm}$ ,  $D_{40} = 0.50\text{mm}$ ,  $D_{50} = 0.70\text{mm}$ ,  $D_{70} = 1.0\text{mm}$ ,  $D_{86} = 1.4\text{mm}$ , and  $D_{95} = 1.8\text{mm}$ . For each of these size fractions, a stable momentum-extraction profile is derived at a specified transport stage. These calculations are repeated for five transport stages in the low to moderate range, i.e.  $1 \leq (T^*)_m \leq 6$ . This procedure yields a suite of momentum-extraction curves that then can be used as input to the full transport model (i.e. the realistic case where all grains of all sizes are permitted to move into the airstream).

The momentum-extraction term  $(F^*C^*)_m$  is computed as described in the previous section (3.6), whereby the magnitude at each level above the bed, in increments of  $z = 0.10D_{50}$ , is the sum of the up- and down- going limbs of any of the trajectories crossing that bin level. Because the  $z=0$

reference is non-planar (e.g. Figure 3.2), the initiation point of every trajectory is shifted either up or down from a common plane, so that each increment in height  $z$  is horizontally uniform in the downwind direction and all values of  $(F_*C_*)_m$  as a function of  $z$  are binned appropriately. This calibration is analogous to taking all the grains forming the bed surface and positioning them with their bottoms along a flat plane. Whereas the initiation points of all trajectories now coincide at a common origin, the termination points of some trajectories might lie above or below the origin, by a fraction of the difference between the largest and smallest grain diameter present (e.g.  $1.5 \text{ mm} = 2D_{50}$ ). This disparity proves to be insignificant in that the dominant momentum extractors in the saltation layer are those highly energetic grains moving faster than the wind within  $2D_{50}$  of the bed; consequently, they are not extracting momentum from the flow and their trajectory tails, a fraction above or below the origin, can be neglected. For the few less-energetic grains still being accelerated by the wind near their termini, and whose trajectory tails lie above the calibrated origin (e.g. usually  $< 5\%$  of the moving sand population), the magnitude of  $(F_*C_*)_m$  in the last bin is applied to all remaining bins between it and the origin, so that an artificial decay in the momentum-extraction profile at the bed is not created through missing data points.

Figure 3.10 shows a representative momentum-extraction curve for the case of  $D_m = 0.20\text{mm}$  and transport stage  $(T_*)_m = [\tau_b/(\tau_{cr})_m] = 3.0$ , plotted as  $F_*C_*$  for that size fraction versus the height above the bed, nondimensionalized by  $D_m$ . The actual profile exhibits the expected monotonic decay with increasing height, although with numerous positive momentum spikes. These spikes signify the tops of individual trajectories, or multiple trajectories with uniform heights, and exist because there were an insufficient number of trajectories in the sample to mask the effects of singular trajectories. The momentum maxima typically correspond to grains that spent a relatively long period of time near the tops of their trajectories. With fewer statistics than used here ( $n = 380$ ), the frequency of the spikes increases; the converse holds for a greater number of data points (e.g. 2000-5000). The number of statistics gathered here is sufficient, however, for delineating the trend of the curve for the first iteration, and greater numbers provide no appreciably different net result. When iterating, these excursions from the average trend can exacerbate the oscillatory nature of the final profile convergence. A smoothing routine, therefore, is used to



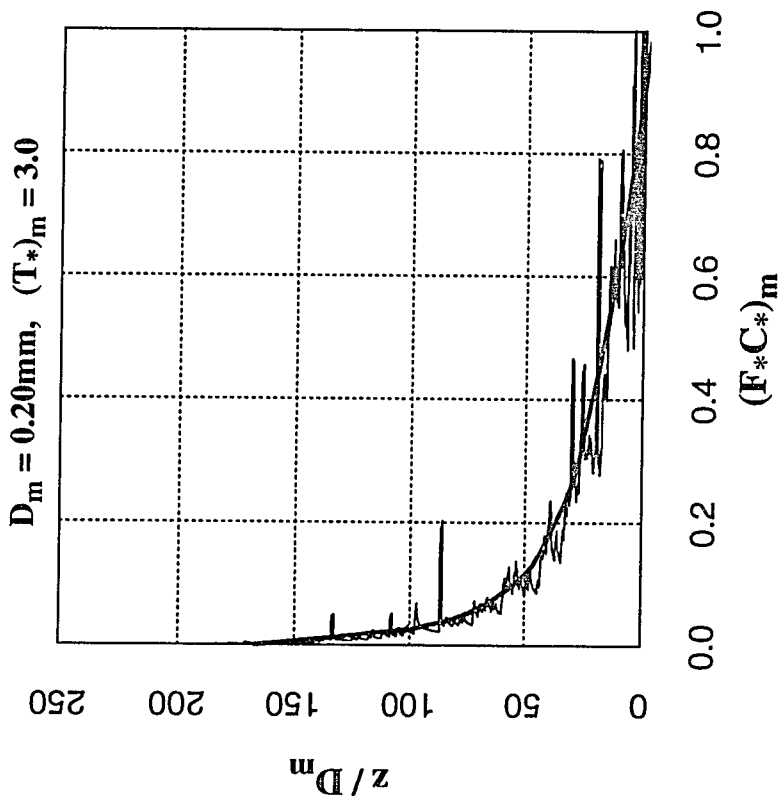


**Figure 3.10** Calculated momentum-extraction profile for grains of one size fraction,  $D_m = D_5 = 0.20\text{mm}$ , moving over the mixed-grain bed at a transport stage of  $(T^*)_m = [\tau_b/(\tau_{cr})_5] = 3.0$ . Momentum extracted grains of this size fraction,  $(F \cdot C^*)_5$ , is plotted as a function of the height above the bed ( $z$ ) normalized by the fractional grain diameter  $D_5$ . The computed profile (fluctuating curve) is fit with a smooth curve by weighted least-squares regression.

dampen the influence of individual trajectory spikes. The uniform, solid curve in Figure 3.10 is the smoothed profile for this case. Curve smoothing is performed using a robust, locally weighted regression (e.g. see Cleveland, 1979), in which the fitted value at  $(F_*C_*)_m$  is the value of a polynomial fit to the calculated curve using weighted least squares. The weight for  $[(F_*C_*)_m, (z/D_m)]$  is large if  $(F_*C_*)_m$  is close to the fitted value and small if it lies farther away. This method is used for smoothing all other momentum-extraction curves presented here.

The results of iterating to find stable momentum-extraction curves, as input to the full bedload-transport calculations, are plotted in Figure 3.11 for a transport stage of  $(T_*)_m = 3.0$ . The curves for four representative grain-size classes, spanning the frequency distribution of the sediment mixture, are graphed as a function of the nondimensional momentum exchange for each component  $m$ ,  $(F_*C_*)_m$ , and nondimensionalized height above the bed,  $z/D_m$ , where  $D_m = 0.20\text{mm}$ ,  $0.35\text{mm}$ ,  $0.7\text{mm}$ , and  $1.4\text{mm}$ , respectively. Each profile, as a function of grain size and height above the bed, represents an initial hypothesis as to the relative magnitude of momentum extracted from the flow by grains of a given size fraction, independent of the compounding influences of other simultaneously moving size fractions. When the vertical axis is normalized by a factor of  $(D_m/D_{50})$ , these four profiles collapse to essentially the same curve, as indicated by Figure 3.12. The suite of curves may now be represented by one  $F_*C_*$  profile, that for the  $D_{50}$  case, as a function of  $(z/D_m)(D_m/D_{50}) = (z/D_{50})$ . Normalization demonstrates that the constituent momentum-extraction curves for a range of grain sizes possess the same curvature and vary straightforwardly in magnitude by the ratio of the selected grain size  $D_m$  to the median grain size for the distribution  $D_{50}$ . This functional relationship can now be introduced in the full transport calculations for the sediment mixture. Subsequent iterations on the momentum-extraction profiles during simultaneous transport of all sizes prove that while the absolute magnitude of momentum extraction for each constituent might vary from that of the initial iteration, the relative proportion between size fractions remains the same. The relationship between size fractions, embodied in Figure 3.12, thus holds for the range of grain sizes and transport stages investigated here.

With a mechanism for generalizing the momentum-extraction relationship between size fractions, the bedload transport of the grain mixture now can be addressed. Because the  $F_*C_*$

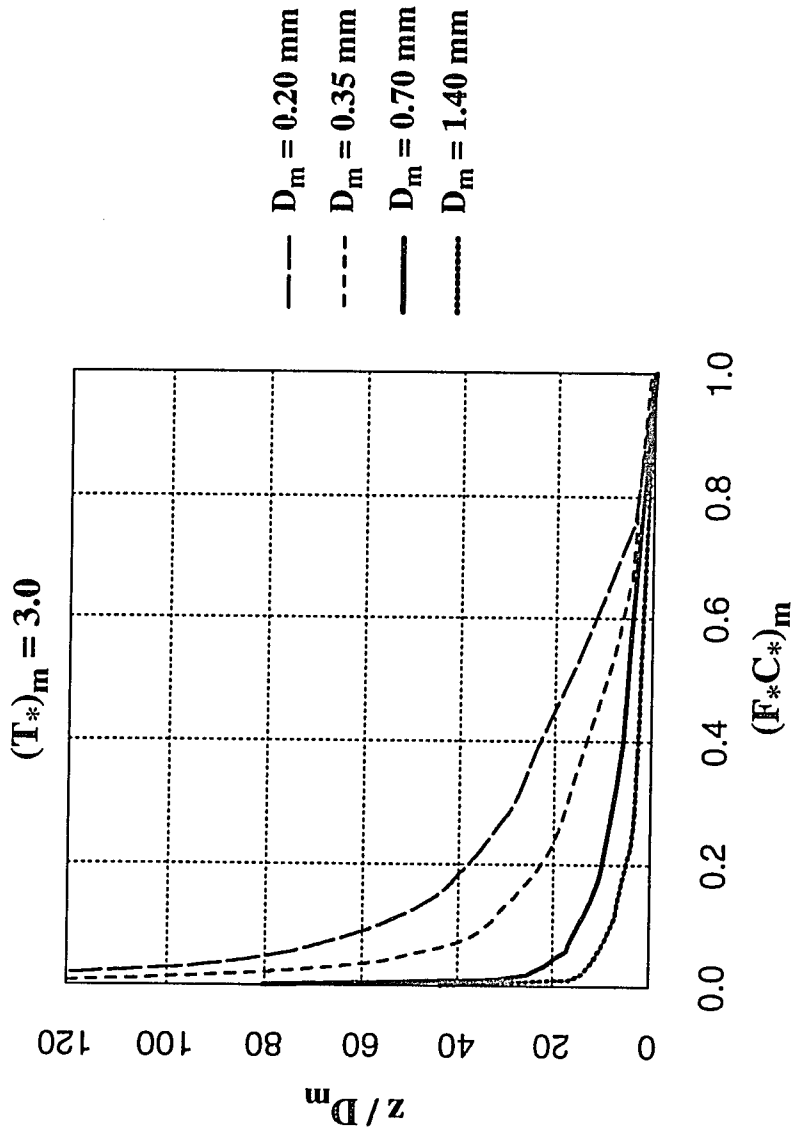


**Figure 3.11** Momentum-extraction profiles for four grain-size fractions within the sand mixture, plotted as  $F^*C^*$  for each fraction normalized by its respective value at the bed,  $(F^*C^*)_m$ . Height ( $z$ ) above the bed is normalized in each case by the respective grain diameter of the fraction ( $D_m$ ). These curves were obtained in separate runs of the model, at  $(T^*)_m = 3.0$ , in which only the specified size fraction was allowed to eject from the bed.

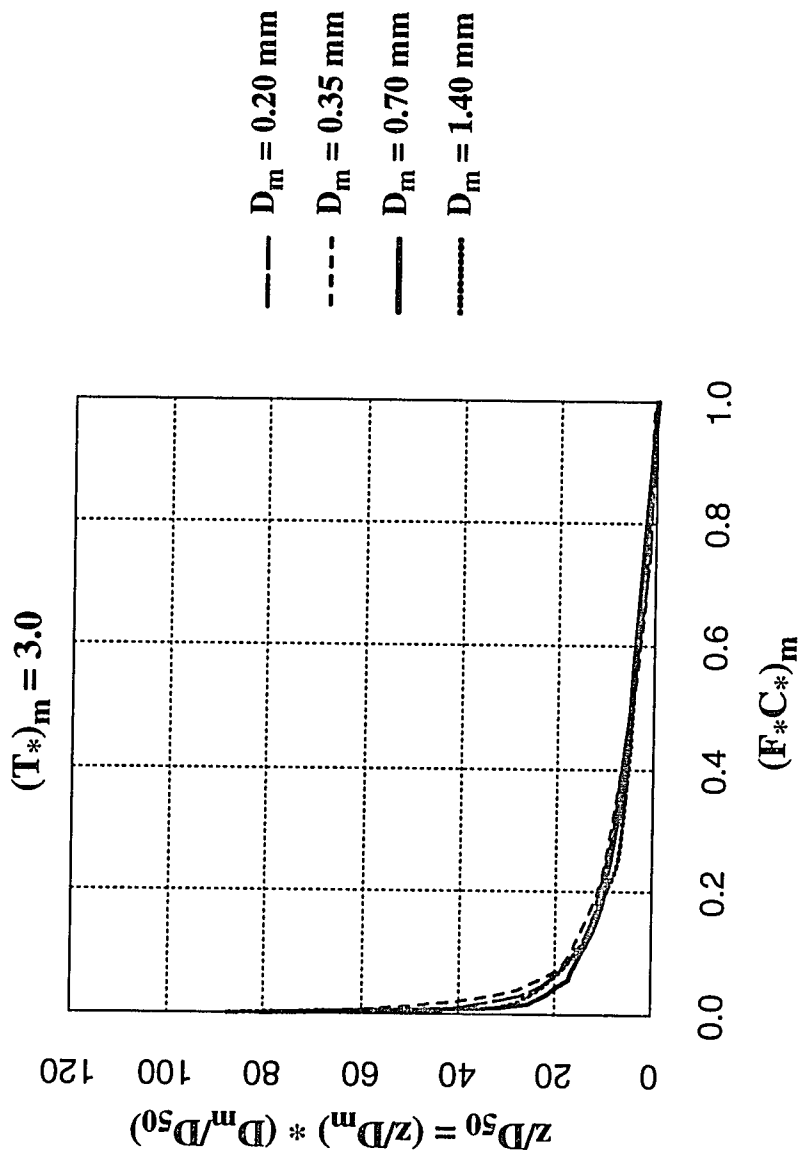


**Figure 3.12** The four momentum-extraction curves shown in Figure 3.11, with the vertical axis  $(z/D_m)$  normalized by  $(D_m/D_{50})$  such that the curves are represented by the same height scale  $(z/D_{50})$ . The momentum-extraction curve for the  $D_{50}$  component approximates the average curve for the four grain-size fractions.

profile for the median grain size adequately represents each sediment component ( $D_m$ ) when multiplied by  $(D_{50}/D_m)$ , an initial velocity profile for the saltation layer during full transport can be derived through equations 3.20 and 3.25, with  $(F_*C_*)_m = (F_*C_*)_{50}$ . This fluid-velocity profile is called by the computer program; then, for any grain at any level in the flow, the appropriate value of the forward fluid velocity as it responds to that grain may be found by multiplying by a factor of  $(D_{50}/D_m)$ , yielding a suite of curves for the grain-size fractions like those shown in Figure 3.11. This result is useful for two reasons. First, it simplifies the technical method, such that one velocity-profile equation, with  $(F_*C_*)_m = (F_*C_*)_{50}$ , input to the model can be reconstituted within the program through the scaling factor  $(D_{50}/D_m)$  thereby reducing the number of necessary equations. More importantly, because the component momentum-extraction curve for the  $D_{50}$  fraction represents an average of the curves for all fractions within the mixture, it appears that the appropriate length scale for momentum exchange between sediment grains and the transporting fluid is  $D_{50}$ .

As described previously, bedload-transport calculations proceed by aerodynamically initiating the first grain and generating a population of moving grains from any particles it ejects through subsequent collisions with the bed surface, and so on. For the full bedload-transport case, any grains ejected from the bed are allowed to move. All ejecta are accounted for, to determine what mode of transport (e.g. rolling, creep, saltation) they exhibit, how many grains of any particular size they eject, what trajectory characteristics (e.g. lift-off and impact behaviors) they display, how they interact dynamically with the flow (e.g. the magnitude of momentum transfer as a function of height above the bed), and what causes their termination.

The total momentum extracted by grains of all size classes moving at a particular height in the airflow is determined by summing the magnitudes of momentum extracted by each size fraction:  $F_*C_*(z) = \sum_{m=1}^M (F_*C_*)_m(z)$ . Figure 3.13 shows the momentum-extraction profiles for four grain-size fractions obtained through iteration of the initial velocity profile. The vertical axis  $z$  is normalized by  $D_{50}$  to provide a common reference for all curves. Summing these curves produces a new momentum-extraction profile for the sediment mixture from which the modified form of the wind-velocity profile may be calculated for the subsequent iteration.

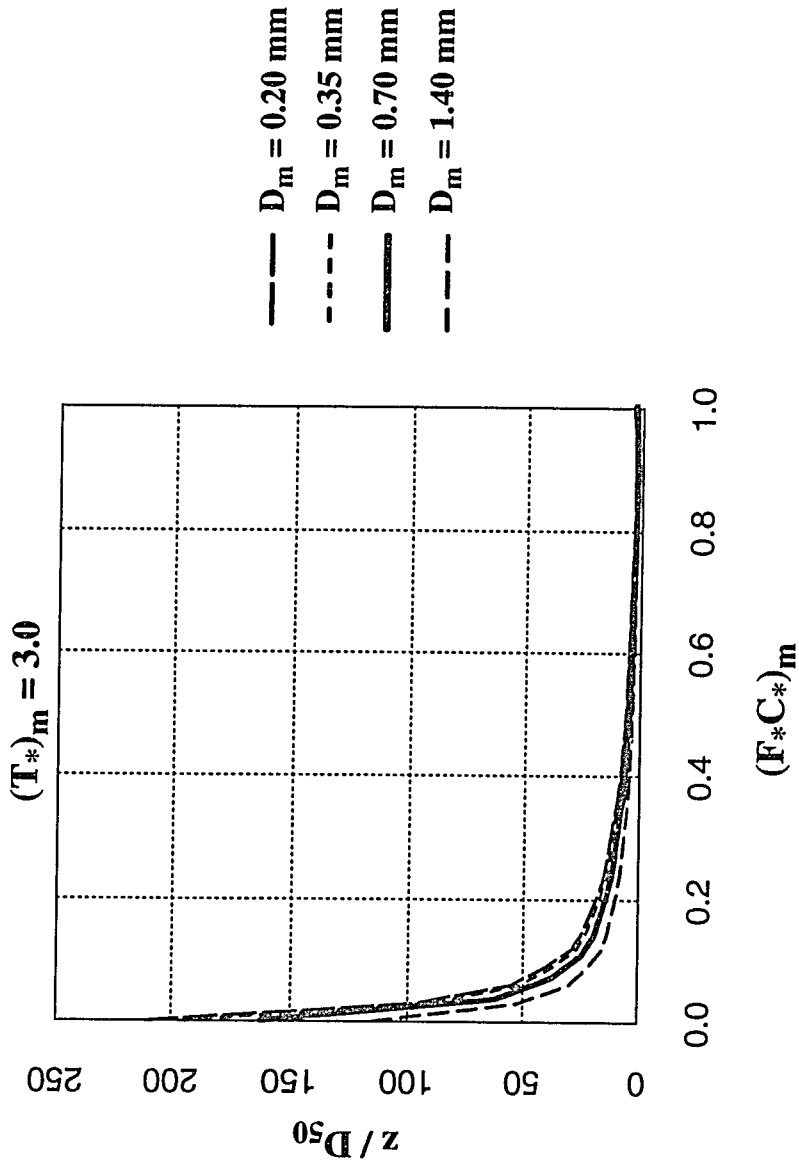


**Figure 3.13** The total momentum extracted by all grains at a transport stage of  $(T^*)_m = 3.0$  is the sum of the component momentum-extraction curves for the grain-size fractions. Profiles of four size fractions of the sediment mixture are shown here, normalized to the same height scale ( $z/D_{50}$ ):  $D_5 = 0.20\text{mm}$ ,  $D_{18} = 0.35\text{mm}$ ,  $D_{50} = 0.70\text{mm}$ , and  $D_{86} = 1.4\text{mm}$ . The  $D_{50}$  curve represents the average curve in shape and magnitude, with the finer fractions extracting proportionately more momentum from the flow and the coarser fractions extracting relatively less.

Figure 3.13 again demonstrates that the average momentum extracted by all grain sizes at a given height ( $z/D_{50}$ ) is represented by the component momentum-extraction profile for the  $D_{50}$  fraction. This figure also shows that the coarser size-fraction,  $D_{86} = 1.40\text{mm}$ , extracts relatively less momentum from the fluid-grain mixture than the finer size fractions,  $D_5 = 0.20\text{mm}$  and  $D_{18} = 0.35\text{mm}$ . Experimental analyses (e.g. Williams, 1964; Gerety and Slingerland, 1983) and field studies (e.g. De Ploey, 1980; Draga, 1983) of sand transport have concluded that particles from the smaller size fractions in a mixture generally tend to hop higher on average than coarser grains; consequently, the thickness of the saltation layer is defined by the maximum hop heights of the smaller particles. Model results are consistent with these observations. In the case of  $(T^*)_m = 3.0$ , the maximum trajectory height achieved by the smallest size fraction ( $D_5 = 0.20\text{mm}$ ) is 60% higher than that for the coarser size fraction ( $D_{86} = 1.4\text{mm}$ ). The differences in inertial mass between the two size fractions largely are responsible for this variation; the critical shear stress required to initiate saltation is an order of magnitude higher for the  $D_{86}$  fraction than for the  $D_5$  class (e.g.  $9.14 \times 10^{-1} \text{ N/m}^2$  compared with  $8.64 \times 10^{-2} \text{ N/m}^2$ ). Consequently, at a given shear velocity, the smaller grains are accelerating more rapidly relative to the fluid near the bed than are the larger ones. They possess comparatively more kinetic energy, which propels them higher into the flow than the coarser particles. The faster-moving, smaller grains, therefore, extract proportionately more momentum from the flow than do the coarser particles on average, leading to the range of momentum-extraction profiles observed here.

The condition of steady-state bedload transport requires that the sediment bed is neither eroding nor aggrading through time. Hence, self-replication of the moving sand population must be achieved, such that every grain terminating motion at the bed is replaced, on average, by an ejected grain of any size. The sediment-transport calculation thereby is constrained in the model by the criterion of self-replication. Momentum-extraction and fluid-velocity profiles thus are considered to be converged on a final form when the moving population is in equilibrium with the wind, and successive iterations yield no change in the structure of the fluid-velocity profile.

Examination of the converged momentum-extraction profiles for a series of transport-stage conditions yields an unexpected result. The proportion of each grain-size fraction composing the

sediment bed is similar to that in the sediment-transport layer. Therefore, not only is each terminated grain replaced, on average, by another grain of any size, but the mean replacement of terminated grains of a given size class is by grains from the same class. For example, 4% of the sediment bed is composed of the finest size fraction. For the range of transport stages investigated, the finest fraction averages 4% of the size-frequency distribution of grains transported by the flow. The grain-size probability distributions of the sediment bed and bedload layer are not identical in all cases, but typically correspond to within 5%. It is not entirely clear why this should be the case, although the size frequency distribution of the bedload-transport layer ultimately is controlled by the number of grains of each size fraction available in the surface layers of the bed. Hence, stable forms of the momentum-transfer and fluid-velocity profiles for sand mixtures appear to be achieved only when the grain-size frequency distribution of the bedload comes to equilibrium with the distribution of grain sizes residing in the bed.

Stabilized momentum-extraction profiles for the entire frequency distribution of moving particles ( $F_*C_*$ ) are shown in Figure 3.14 for two transport stages,  $(T_*)_{50} = [\tau_b/(\tau_{cr})_{50}] = 3.0$  and  $(T_*)_{50} = 6.0$ , as a function of height  $z$  nondimensionalized by the median grain diameter  $D_{50} = 0.70\text{mm}$ . These graphs demonstrate the oscillatory behavior of the iterative process. Five iterations were required to achieve convergence for the lower transport stage [ $(T_*)_{50} = 3.0$ ]; the final form of the momentum-extraction profile, yielding an equilibrated wind-velocity profile, is graphed as a heavy, solid line and overlies two curves of the same shape and magnitude (i.e. the two preceding iterations) that, consequently, are not visible in the figure. In the case of  $(T_*)_{50} = 6.0$ , four iterations were required to find a stable solution. The iterative process appears to be more stable at the higher transport stages, resulting in lower-amplitude oscillations in the iterative process than observed in the lower transport-stage cases; possible reasons for the greater stability of the momentum-extraction profile at higher shear velocities are described later in this chapter.

In a similar manner, the profiles of momentum transfer between all grains and the fluid at successive heights above the bed,  $F_*C_*(z)$ , may be calculated for a number of transport stages. Figure 3.15 illustrates the variation in magnitude of momentum extraction as a function of height  $z/D_{50}$ , for a range of transport stages in the low- to moderate- transport regime ( $1.0 < (T_*)_{50} < 6.0$ ).



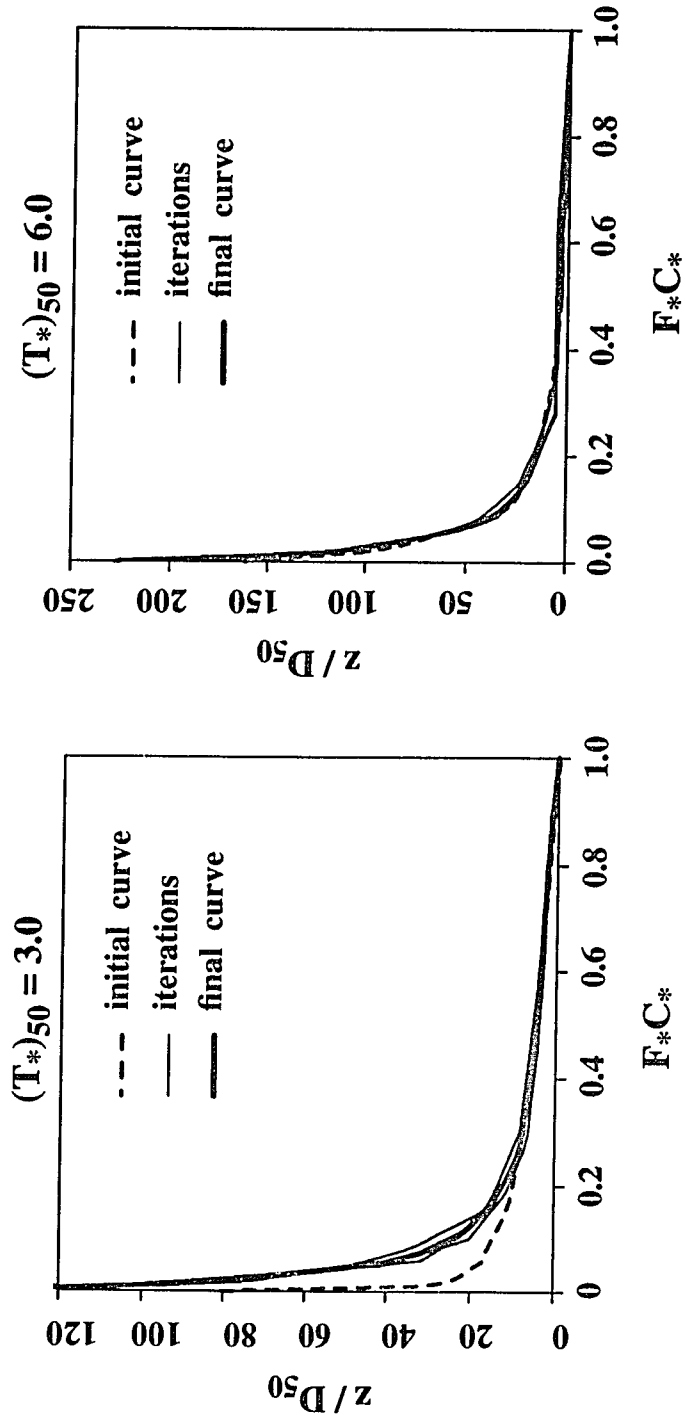
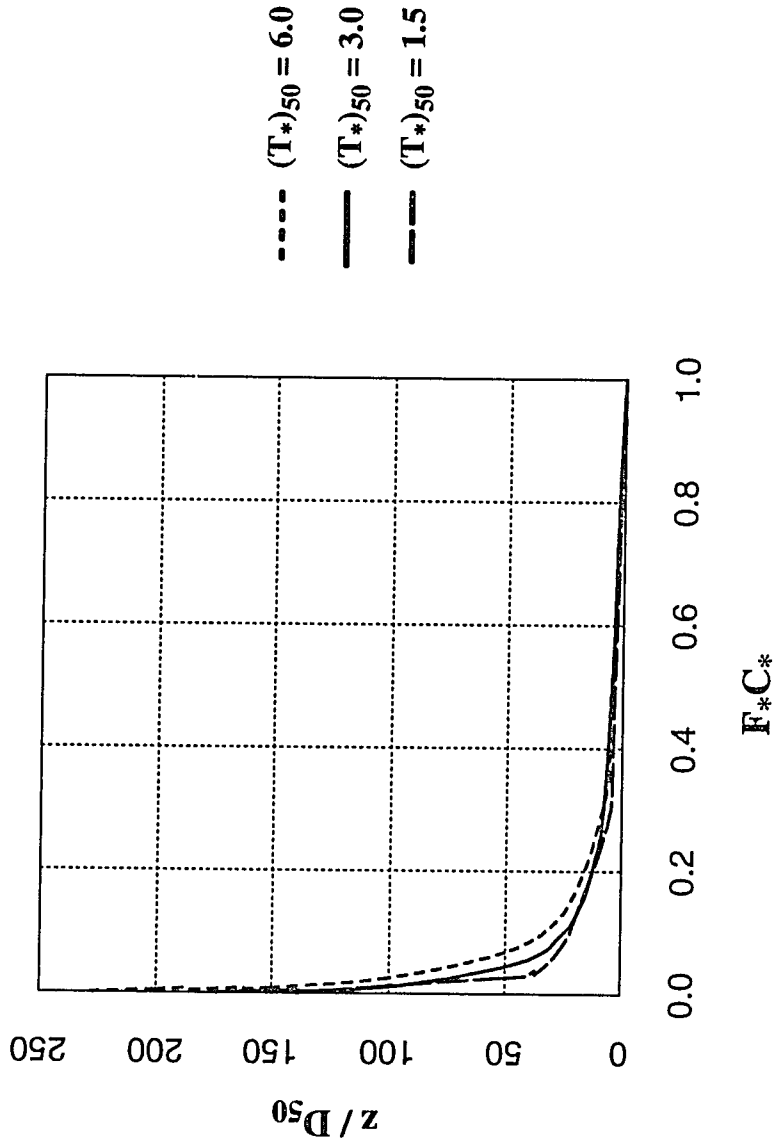


Figure 3.14 Examples of converged momentum-extraction profiles, for transport stages  $(T^*)_{50} = 3.0$  and  $(T^*)_{50} = 6.0$ , as a function of non-dimensional height ( $z/D_{50}$ ). The stable form of the profile (heavy solid line) represents the total momentum extracted by all moving grains,  $(F^*C^*)_m$ , which is the sum of the momentum extracted by each sediment grain. Convergence of the momentum-extraction curves with successive iterations is oscillatory, and the final curve is achieved after 5 iterations for the  $(T^*)_{50} = 3.0$  case and 4 iterations for the  $(T^*)_{50} = 6.0$  case. The initial curve for the first iteration is derived by a process described in the text and illustrated in Figure 3.12.



**Figure 3.15** Momentum-extraction profiles for the mixture of moving grains, calculated for a range of transport stages ( $1.0 < (T^*)_{50} < 6.0$ ) as a function of nondimensional height above the bed ( $z/D_{50}$ ). These results show that the sediment load extracts relatively less momentum at the lower transport stage [ $(T^*)_{50} = 1.5$ ] and relatively more at the higher transport stage [ $(T^*)_{50} = 6.0$ ]. The maximum height of the salta-tion layer varies between  $\delta_B = 153D_{50}$  for the  $(T^*)_{50} = 1.5$  case and  $\delta_B = 232D_{50}$  for the  $(T^*)_{50} = 6.0$  case.

As expected, the higher shear-velocity flows transfer proportionately more momentum to the higher-energy saltating populations. The maximum height of the saltation layer varies between  $\delta_B = 153D_{50}$  for  $(T^*)_{50} = 1.5$  and  $\delta_B = 232D_{50}$  for  $(T^*)_{50} = 6.0$ , as grains of all sizes become increasingly energetic through momentum exchange with the fluid and with other grains during collisions with the bed surface.

Momentum-extraction profiles for the range of transport stages ( $1.0 < (T^*)_{50} < 6.0$ ) collapse to roughly one curve of the same shape and magnitude, when the vertical axis ( $z/D_{50}$ ) in Figure 3.15 is normalized by the height of the bedload layer ( $\delta_B/D_{50}$ ), such that  $(z/\delta_B) = [(z/D_{50})(D_{50}/\delta_B)]$ . The normalized  $F^*C^*$  profiles, as a function of  $z/\delta_B$ , are shown in Figure 3.16a for the three representative transport stages of the previous figure. These results support the theory, first stated by Owen (1964) for uniform-grain eolian transport, that the magnitude of momentum exchange between mixed-size grains and the airflow during heterogeneous bedload transport is scaled by the height of the saltation layer, and *vice versa*. Furthermore,  $(F^*C^*)$  versus  $\delta_B$  varies in a predictable manner with increasing transport stage. Gerety and Slingerland (1983) similarly remarked that small grains tended to hop higher than larger grains in their experiments, but that the difference between average jump heights for the fine and coarse size fractions decreased with increasing boundary shear stress.

Consistent with empirical observations, the mixed-grain model predicts, as shown in Figure 3.16b, that  $\delta_B$  increases linearly with transport stage, to a value of  $(T^*)_{50} = 3.0$ , at which  $\delta_B$  varies minimally with increasing transport stage. The predicted values of  $\delta_B$  for five transport stages were used to construct this graph. The plateau in the curve coincides with that shown for the variation in the grain-size-dependent, critical shear stress for initiation of saltation  $(\tau_{\eta})_m$  as a function of transport stage (e.g. Figure 3.8a), in which the values of  $(\tau_{\eta})_m$  reach their maximum at  $(T^*)_m = 3.0$ , followed by a rapid decline toward the higher transport regimes. Together, these results suggest that the fluid flow reaches a threshold around  $T^* = 3.0$ , at which the saltation layer is saturated with energetically saltating grains that are extracting proportionately the maximum amount of momentum from the flow, at the maximum values of  $(\tau_{\eta})_m$ , that the fluid can sustain. As flow velocities increase, the wind regime must adjust to the greater surficial roughness created

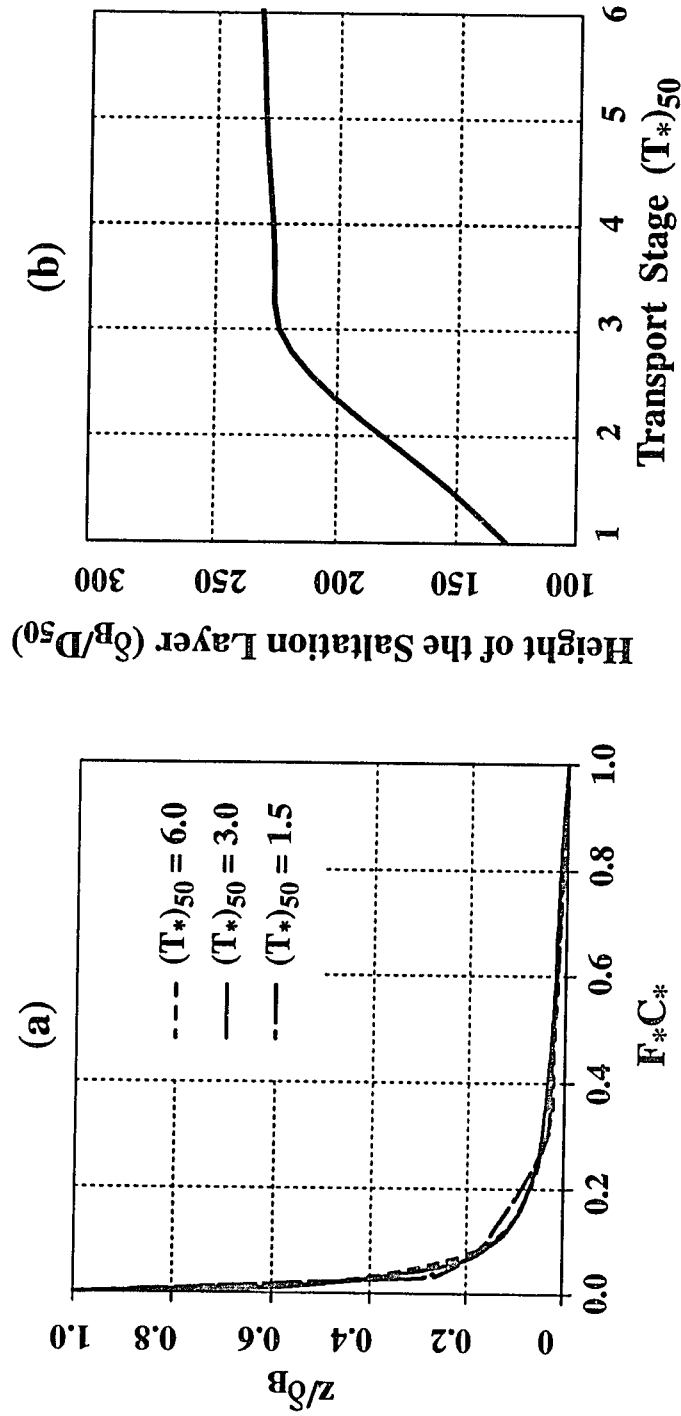


**Figure 3.16** Calculated momentum-extraction profiles for the sediment mixture ( $F_*C_*$ ) at three values of the transport stage  $(T^*)_{50}$ , plotted as a function of height ( $z$ ) normalized by the height of the saltation layer ( $\delta_B$ ). (a) The momentum-extraction curves for the three transport stages shown in Figure 3.15 collapse to one curve that is essentially uniform in shape and magnitude, when the vertical axis ( $z/D_{50}$ ) is normalized by  $(\delta_B/D_{50})$ , such that the new vertical height scale is  $(z/\delta_B)$ . (b) For the sediment mixture, the predicted relationship between the height of the saltation layer ( $\delta_B$ ), nondimensionalized by the median grain diameter ( $D_{50}$ ), and increasing transport stage. For each transport stage, the thickness of the saltation layer is prescribed by the maximum jump height of grains within the mixture (e.g. generally particles from the finer size fraction).

by the increasing concentration of moving grains at all levels in the flow. To moderate the stress exerted on the flow by the grains that would tend to reduce fluid momentum within the saltation layer, the local fluid shear stress diminishes by an amount necessary to keep each grain-size fraction saltating but sufficient to maintain flow velocities. A balance is achieved between incremental increases in the flow velocity with transport stage and corresponding decreases in the local fluid shear velocities necessary to sustain saltations. As Bagnold (1941) found from wind-tunnel measurements, the mean flow velocities of the saltation layer actually decrease as the velocities of the flow interior increase. The near-bed decrease in flow velocities corresponds to a reduction of  $(\tau_\eta)_m$ , which causes the grains to be accelerated less by the fluid. This, in turn, decreases their potential energy for ejecting other grains into the saltation layer, which meters the concentration of moving grains, as well as the energetics of rebounding grains. As the height of the saltation layer depends on the kinetics of moving grains, which rely on both the momentum-exchange process and dynamics of collisions with the bed, its magnitude varies in proportion to the magnitude of momentum transfer to grains with increasing transport stage.

The normalization in Figure 3.16 provides a strong computational advantage because it can be used to predict the stable form of the momentum-extraction profile ( $F_*C_*$ ) without having to go through the lengthy iterative process. For any transport stage  $(T_*)_{50} \leq 6$ , the height of the saltation layer ( $\delta_B$ ) may be obtained from Figure 3.16b. The momentum-extraction profile for that transport stage then is found by scaling the average  $F_*C_*$  profile in Figure 3.16a (e.g. the profile corresponding to  $(T_*)_{50} = 3.0$ ) by  $z/\delta_B$ .

Comparison of the total momentum-extraction profiles for heterogeneous sediment transport ( $F_*C_*$ ) with those predicted for uniform-grain bedload transport yields another interesting trend. Figure 3.17 shows the correlative profiles for three transport stages, for the case where the uniform grain diameters are equivalent to the median of the grain mixture (i.e.  $D = D_{50} = 0.70\text{mm}$ ). At the lowest transport stage shown [ $(T_*)_{50} = 1.5$ ], the magnitude of momentum transfer between grains and the fluid is considerably lower for the mixed-grain than the uniform case, whereas the magnitudes are virtually identical at the higher transport stage [ $(T_*)_{50} = 6.0$ ]. The reason for this convergence at higher transport stages lies primarily in the nature of grain

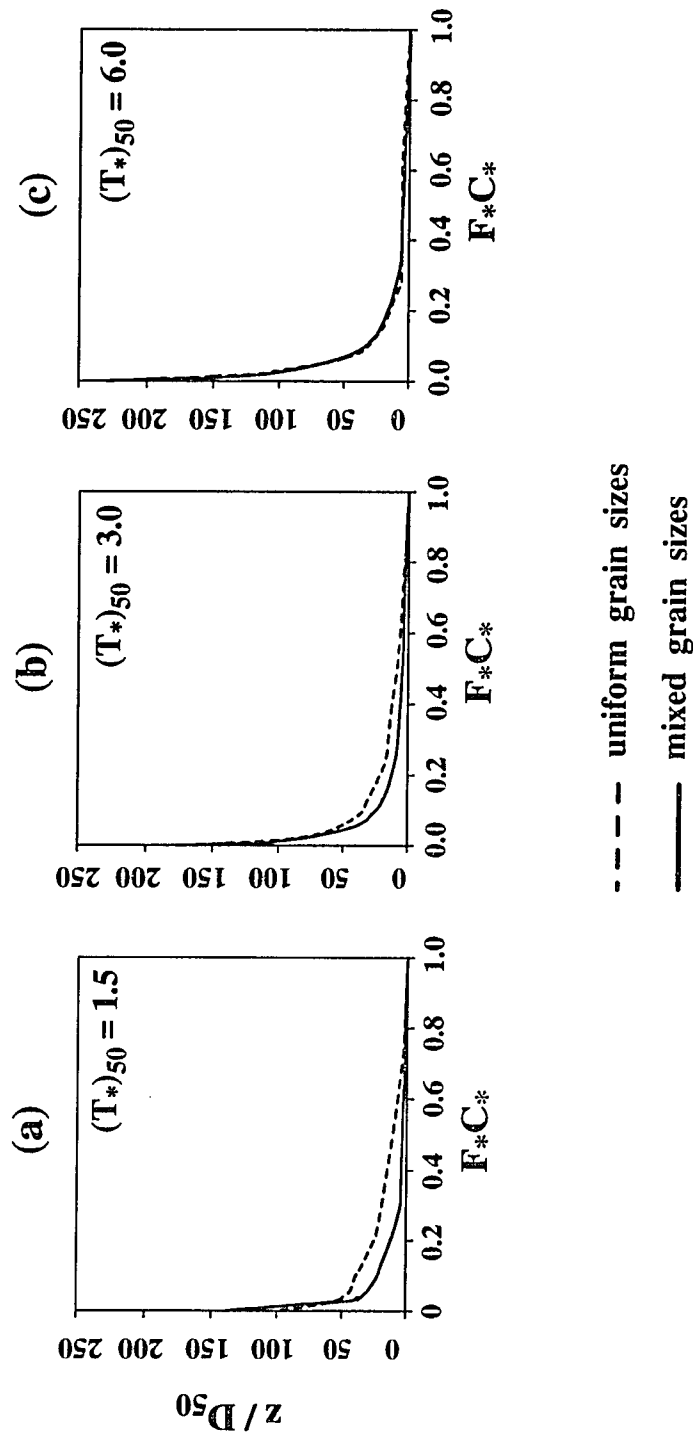
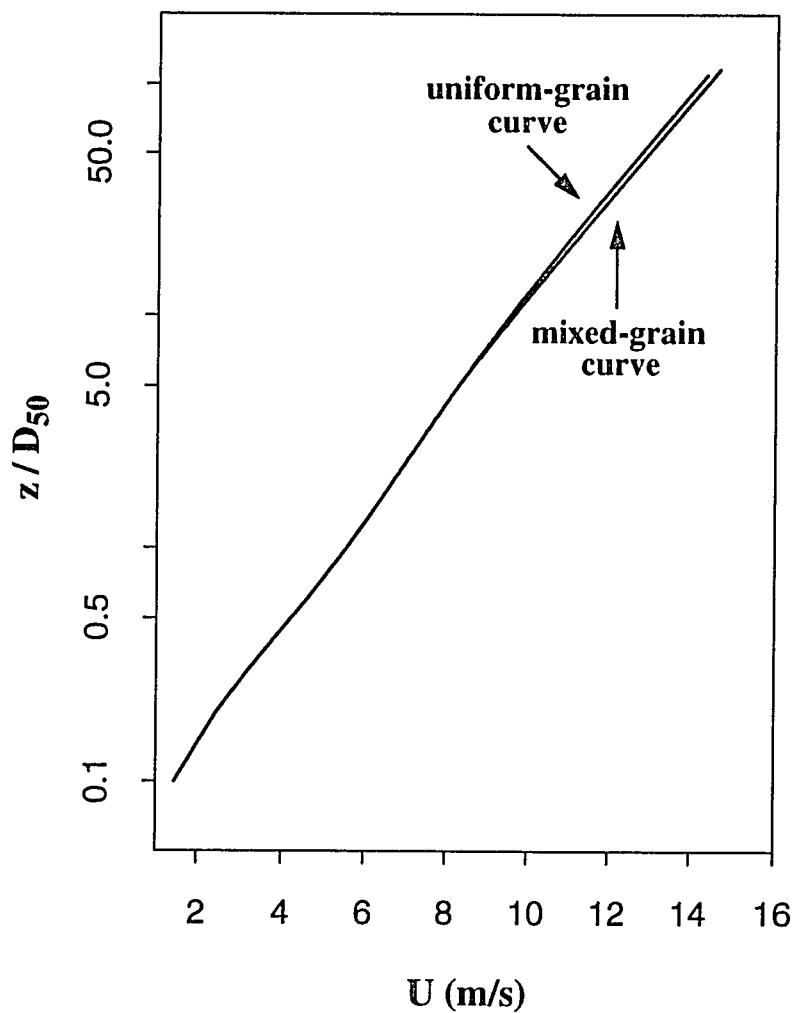


Figure 3.17 Comparison of calculated momentum-extraction profiles ( $F \cdot C^*$ ) for uniform-grain-size bedload versus mixed-grain-size bedload, at three values of the transport stage [ $(T^*)_{50} = 1.5$ ,  $(T^*)_{50} = 3.0$ , and  $(T^*)_{50} = 6.0$ ]. The diameter of the uniform grains,  $D = 0.70\text{mm}$ , is equivalent to the median grain size of the heterogeneous mixture,  $D_{50} = 0.70\text{mm}$ , and the vertical height scale ( $z$ ) is nondimensionalized by  $D = D_{50}$ .

collisions with the bed. At lower transport stages, when the majority of grains that dominate the momentum-transfer process above the mixed-grain bed surface comprise the finer fractions of the size distribution, characteristics of the bed surface play a strong role in dictating grain motion. In heterogeneous sedimentary deposits, the smaller grains have a lesser probability of being exposed to either fluid- or impact- generated entrainments because they often occupy pockets between larger grains. In addition, their frequency distributions of lift-off velocities and angles display a greater range, depending on the diameter of the grain that they must pivot over to launch from the bed. In contrast, the probability and behavior of grain lift-off are more uniform in like-sized deposits. Therefore, relatively more grains enter the higher-velocity regions of the flow. At a transport stage of  $(T^*)_{50} = 1.5$  (e.g. Figure 3.17a), fewer grains of the heterogeneous mixture are achieving the heights of particles ejected from the uniform-sized bed; the thickness of the saltation layer is  $110D_{50}$  for the former and  $149D_{50}$  for the latter case. At higher transport stages, however, the larger grains are mobilized energetically and smaller grains in the grain interstices at the surface are exposed to the flow through removal of the coarser grains. All particles are comparatively more energetic and are able to rebound from the type of collisions that would have caused them to lose momentum at lower transport stages (e.g. small grains colliding with large grain pockets). Hence, the rebounding grains become less susceptible to the topographic irregularities of the bed surface. In both the uniform and mixed-size cases at higher transport stages (e.g. Figure 3.17c), grain energetics become progressively metered by the reduction in the local fluid shear stress  $(\tau_{\eta})_m$ , such that the wind-velocity profile seems to react less sensitively to the material characteristics of the bed surface.

Sensitivity analyses of the model to the choice in the momentum-extraction profile indicate that the form of the wind-velocity profile is not very sensitive to  $F_*C_*$ . For example, the momentum-extraction profile for the uniform-grain case in Figure 3.17b was used with the mixed-grain frequency distribution and sediment bed to calculate the form of the velocity profile during bedload transport. Approximately 300 grain trajectories were tabulated. Similarly, the momentum-extraction curve for the grain-size fraction  $D_{86} = 1.40\text{mm}$  and for the grain-size fraction  $D_{18} = 0.35\text{mm}$  (e.g. Figure 3.14) were tested. In each case, the component momentum-



**Figure 3.18** Calculated vertical profiles of velocity ( $U$ ) through the saltation layer ( $z \leq \delta_B$ ) at a transport stage of  $(T^*)_{50} = 3.0$ , employing different momentum-extraction profiles to test the sensitivity of the model to the form of the  $F_*C_*$  curve. The vertical axis is the log of the nondimensional height ( $z/D_{50}$ ). The mixed-grain curve is predicted by the model as the stable profile for the mixed-grain case (i.e. Figure 3.15). The uniform-grain curve is calculated by imposing the momentum-extraction profile for the uniform-grain population (Figure 3.17b) on the velocity-profile equations for the mixed-grain case. The curves parallel one another above  $\delta_B$  (i.e. in the flow interior).



extraction profiles were calculated in the manner previously described (i.e. multiplying the height factor by  $D_{50}/D_m$  to derive the appropriate curves for each component as a function of  $z/D_m$ ). Results of the tests are shown in Figure 3.18, plotted as the vertical profile of fluid velocity ( $U$ ) versus height above the bed ( $\ln z/D_{50}$ ). The velocity profiles calculated with the momentum-extraction profiles corresponding to  $D_{18}$ ,  $D_{50}$ , and  $D_{86}$  map a tight cluster around the “mixed-grain” curve on the graph. There appears to be negligible variation below heights of about  $10D_{50} \approx \delta_s$ ; within the main saltation layer above, the curves diverge by only 7% at the tops of their respective bedload layers ( $\delta_B/D_{50}$ ). However, substantial variations occur in the mode of transport and the bedload-flux rates between the various test scenarios. For the cases where the uniform-grain and the  $D_{18}$  curves were used, too much momentum extraction resulted in a population of less energetic grains, in which the bedload-flux rates for all size-fractions dropped by almost an order of magnitude from those calculated using the  $D_{50}$  momentum-extraction curve as input. Conversely, the  $D_{86}$  curve extracted insufficient momentum; the coarse grain fractions showed an increase in discharge rates of about 1.5 times that of the  $D_{50}$  case, and the finer fractions yielded fractional transport rates about 2 times greater. None of the test cases produced self-replicating populations. Imposing the average momentum-extraction profile from Figure 3.16a, on the other hand, yields a stable, self-replicating grain population in one iteration. This suggests that small adjustments in the magnitude of the fluid velocity with distance from the bed exact a measurable change in the momentum transfer between the wind and the moving grains, significantly altering the concentration and energetics of grains within the saltation layer, upon which the bedload-flux rates and the dynamics of equilibrium saltation depend.

### 3.8 Summary

This chapter addresses the modification of the near-bed profile of wind velocity as a result of momentum exchange between the fluid and moving sand grains. Methods for computing the velocity profile have not been formulated previously for poorly sorted sediments. The model presented here contains numerical expressions for calculating the shape of the wind profile iteratively, including the parameters on which it depends (e.g. the local fluid shear velocities, the

extraction of momentum from the flow by each grain-size fraction, and the roughness parameter associated with sediment transport).

Numerical calculations of the effects of bed roughness on the flow, created by grains of disproportionate size and by small grain clusters forming bed protuberances, indicate that the major influence of the bed surface on the vertical profile of fluid velocity lies in controlling the grain-size probability distribution of particles leaving the surface, the nature of grain collisions, and the lift-off characteristics of ejected grains. The number, mass, and energetics of grains entering the flow per unit area per unit time, through either fluid- or impact- driven entrainment, dictates the magnitude of momentum extracted from the flow and, consequently, the local fluid-velocity profile. The model predicts that grains composing the nonmoving sediment surface in the absence of bedforms create negligible form drag on the near-bed velocity profile, and that the viscous sublayer draping the bed surface exerts a measurable, but small, effect on the near-bed airstream under weak flow conditions in the absence of sediment transport.

Stating the sediment bed explicitly permits calculating the height at which the fluid velocity approaches zero in the bed (e.g.  $z = z_o$ ), as it varies in the downwind direction due to particle-scale topographic irregularities of the surface. The vertical profile of velocity and the force balance on moving grains also can be computed as a function of time and geographic position, so that the trajectory of each grain is anchored to the bed, and the interactions between the grain and the moving fluid are evaluated as a function of height above the topographically varying surface. Coupling the sediment-bed component with grain-trajectory and grain-bed collision algorithms permits calculation of individual trajectories, including the angle and speed of grain impacts with the bed, the lift-off angles and speeds of ejected and rebounding particles, the path of moving grains through the bedload layer, and the particle drag-force and grain- concentration terms necessary to compute the extraction of momentum by each moving grain.

A local fluid shear stress is identified as the appropriate stress for the near-bed flow during sediment transport, rather than the total fluid stress of the flow interior. Unlike that described in uniform-grain models (e.g. Anderson and Haff, 1991; McEwan and Willetts, 1991; McEwan, 1993), the local shear stress is defined as that necessary to initiate particle saltation ( $\tau_{ff} = \tau_{\eta}$ ) and

is shown to be dependent not only on grain size ( $D_m$ ) but also on transport stage [ $(T^*)_m = \tau_b / (\tau_{cr})_m$ ]. For  $(T^*)_m \leq 3.0$ , the stress increases almost exponentially with transport stage. For  $(T^*)_m > 3.0$ , this term varies semi-logarithmically with increasing transport stage and reduces uniformly for all grain sizes. At a transport stage of  $(T^*)_m = 6.0$  (i.e. the highest transport stage analyzed in this study), the critical shear stress for initiating saltation is still higher than that required to initiate grain motion (i.e. the critical Shield's stress). These results are fairly consistent with observations of Gerety and Slingerland (1983) for wind-tunnel transport of heterogeneous sands.

A set of equations is derived to quantify numerically the vertical profile of downwind velocity during sediment transport, as a function of the critical shear stress for initiating saltation  $(\tau_\eta)_m$  and a nondimensional term  $(F^*C^*)_m$  representing the momentum exchange between each grain-size fraction and the transporting fluid. Because the form of the wind-velocity profile is dependent on the magnitude of momentum extracted by each sediment component  $m$ , there are  $m$  such component equations that must be summed to yield the momentum-extraction curve of the entire sediment mixture. The fluid-velocity profile is calculated in the viscous sublayer and transition zone between the viscous and turbulent fluid layers above by an analytical expression that accounts for the effects of the viscous sublayer and the extraction of momentum by grains moving nearest the bed. The profile transitions smoothly to a numerical expression that applies in the bedload transport layer (i.e.  $z < \delta_B$ ), in which the magnitude of momentum extracted by each particle within each mobilized grain-size fraction is calculated. The value of the momentum deficit at each height above the bed  $(F^*C^*)_m(z)$  is the sum of the momentum extracted by each sediment component. The "Law of the Wall" equation is employed for the flow interior above the saltation layer, with a numerically solved expression for the bed-roughness parameter  $(z_o)_T$  enhanced by sediment transport. Because the structure of the wind-velocity and momentum-extraction profiles must be solved simultaneously, calculations are iterative.

Predicted momentum-extraction profiles for the grain-size fractions composing the sediment mixture scale by the median grain size  $D_{50}$ . For each transport stage considered, the momentum-extraction curve for the  $D_{50}$  fraction represents an average of the momentum extracted by all grains from the flow, with the coarser grain-size fractions extracting relatively less

momentum and the finer fractions extracting relatively more. The component profiles, therefore, can be normalized in the vertical axis by  $z/D_{50}$ , such that they collapse to a single profile. This yields a straightforward mechanism for computing the vertical profile of wind velocity; the profile in response to each moving grain can be calculated by scaling the  $F_*C_*$  term in the velocity equation by a factor of  $D_m/D_{50}$ . For each successive iteration required to converge the velocity profile, the component momentum-extraction profiles can be treated similarly. The iterations are oscillatory and generally converge in less than six iterations.

The vertical profile of wind velocity generally stabilizes when the conditions of self-replication are achieved. Model results show that not only is each terminated grain replaced, on average, by an ejected one, but that the grain-size frequency distributions of grains in the bedload-transport layer match those of the sediment bed. Hence, each grain-size fraction within the sand mixture is self-regulating.

The profiles of momentum extracted by all grains  $F_*C_*$  as a function of height above the bed, for a range of transport stages, collapse to roughly the same curve when the height term  $z$  is nondimensionalized by the height of the bedload layer  $\delta_B$ . The interdependence of the momentum-exchange process and the maximum height to which grains hop, therefore, can be quantified at incremental increases in the transport stage. The fluid-mechanical algorithm predicts a linear increase in  $\delta_B$  with transport stage  $T_* \leq 3.0$ ; thereafter, the saltation-layer thickness increases minimally with increasing transport stage, for the range of transport stages investigated here (e.g.  $T_* \leq 6.0$ ). Hence, it appears that the fluid-velocity profile reaches a threshold in the neighborhood of  $T_* = 3.0$ , at which the flow increasingly begins to moderate grain ballistics by progressively lowering the value of  $(\tau_\eta)_m$  for each size fraction.

The height of the bedload layer is a sensitive indicator of changes in the grain-fluid interactions within the near-bed flow region. The critical stress  $(\tau_\eta)_m$  depends on the probability distribution of grain ejections, which, in turn, depends on the sizes of grains and the topographic irregularities forming the bed surface. The critical link between the properties of the sediment bed and the momentum-extraction process, therefore, is the mechanics of grain collisions with the granular surface. This is the subject of the next chapter.

## Chapter 4: Grain Collisions with the Bed

The principal influence of the sediment bed on the wind-velocity profile in mixed-grain, eolian systems like that represented here lies in controlling the mechanics of grain collisions with particles comprising the deposit. Model investigations of aerodynamic roughness, described in the previous chapter, have shown that the airstream above the bed is relatively immune to form drag associated with individual surface-roughness elements and to minor variations in skin friction. In the absence of bedforms, the energetics, ballistic properties, and numbers of grains entering the flow are governed largely by the size, sorting, and geometric arrangement of particles within the bed. The ability of a grain to reach the higher-velocity regions of the wind column, and thereby extract measurable momentum from the flow, depends on the angle and speed with which it launches from the bed. The ballistic properties of grain lift-off, in turn, are dictated by its bed-pocket angle geometry and relative protrusion into the flow, which are factors of the packing and sorting characteristics of the grain-size frequency distribution of the deposit. Bed-pocket angle geometries also govern the pathway by which energy and momentum are transferred to stationary bed grains when impacted by particles saltating across the bed surface. A critical link in understanding bedload-transport dynamics of heterogeneous mixtures, therefore, involves the process of grain-grain interactions at the bed.

Grain-bed collisions have been investigated extensively over the past several decades, both experimentally and theoretically. Increasingly sophisticated equipment deployed in wind tunnels has opened the near-bed region to analysis, including high-speed motion photography (e.g. White and Schulz, 1977; White, 1982; Willetts, 1983; Nalpanis, 1985; Willetts and Rice, 1985a, 1986a, 1986b, 1988, 1989; Mitha *et al.*, 1986; Willetts *et al.*, 1991; Willetts and McEwan, 1993) and laser-monitoring devices (Nickling, 1988). These studies have contributed the bulk of trajectory statistics on which many theoretical models of the collision process rely. Theoretical algorithms have enhanced the physical interpretation of grain-impact dynamics considerably by addressing bedload-transport conditions under which experimental observations of the bed region are difficult to procure (e.g. high transport-stage, high particle-concentration flows and marginal transport-

stage flows).

Numerical models of intergranular-collision phenomena have dealt almost exclusively with materials of uniform size, primarily for computational tractability. In addition, the relative sizes of particles ejected during wind-tunnel experiments are indistinguishable photographically, and numerical algorithms employing “splash functions” that treat the collision process statistically (e.g. Jensen and Sorensen, 1986; Ungar and Haff, 1987; Werner and Haff, 1988; Werner, 1990; Anderson and Haff, 1991; McEwan and Willetts, 1991; McEwan *et al.*, 1992; Willetts and McEwan, 1993) do not include the effects of mixed-size grains. Analytical models that possess a collisional component (e.g. Sorensen, 1991; McEwan, 1993) employ uniform-sized materials for the same reason, in that splash-function results are used to tailor the derivation of analytical expressions for particle-ejection velocities, angles, and rates.

Recently, Haff and Anderson (1993) introduced mixed-size grains to the arena of eolian grain-collision studies. They extended their splash function numerically to incorporate the effects of mixtures of two grain sizes in an investigation of the interparticle forces created between grains during collisions. Because their model focuses on particle-particle dynamics, they include no ballistic or fluid-mechanical component in their calculations. A primary conclusion of their work is that grain-ejection behavior appears to be governed largely by the particle-scale microtopographic irregularities of the mixed-size sediment surface in the absence of bedforms, a finding that is supported by the results of this study.

The numerical algorithm presented here expands the collisional component of a uniform-grain model formulated previously (Calder, 1987), to quantify the interactions between grains in a heterogeneous sand mixture. Coupled with the ballistic and fluid-mechanical elements introduced earlier, this model traces each particle in space and time as it approaches the sediment bed with a speed and angle predicted by the saltation trajectory and the dynamical interactions of the particle with the wind. Unlike its predecessor model, which contained a random element to predict the exact location of the stochastic collision between uniform-sized grains, this collisional algorithm quantifies the mechanics of collisions deterministically by calculating each point along the grain trajectory relative to the horizontal bed distance, such that the locus of impact on the computer-

generated bed can be predicted exactly. The stochastic nature of real grain-bed collisions is preserved by the model, in that the exact site of the collision is not known *a priori* but, rather, is encountered by the grain as it completes its ballistic trajectory. Collisions between the incoming grain and the stationary bed particle it strikes are partially elastic, and the vector of momentum transfer to the bed is prescribed by the geometry of the collision and the relative masses of the involved grains. The grain rebounds and ejects its target particle depending on the magnitude of momentum exchanged, their respective inertial masses, and the topographic characteristics of the adjacent bed surface. The bed-pocket angle geometry constrains motion of the potentially ejected grain, while the success of the rebound depends on the geometry of the collision, the local bed slope, and the presence of bed pockets or protruding grains that could obstruct its launch route. All of these factors determine the initial conditions for the subsequent grain hop. Grain motion ceases when the particle is captured by a pocket in the surface of the sediment bed.

Although no statistics on collisional parameters are available for the grain-size frequency distributions used here, the results of model-predicted impact behavior can be evaluated in a general sense with data on mixed-grain populations collected by others (e.g. Willetts and Rice, 1985a, 1989). The mixed-grain collisional algorithm provides an opportunity to quantify the dynamics of grain-bed interactions between simultaneously transported, grain-size fractions in a mixture, which has not been possible yet under experimental conditions. Additionally, comparisons between the predicted collisional statistics of uniform and heterogeneous mixtures display considerable variation in the behavior and outcome of grain-grain impacts, resulting from the differences in bed roughness, which lead to large-scale variations in bedload discharge rates. A discussion of collision statistics follows the derivation of a general algorithm for grain-bed interactions in mixed-size sedimentary deposits.

#### **4.1 Numerical model of mixed-grain collisions**

The collisional algorithm comprises two components. The first characterizes the geometric relationships between the position of the incoming grain relative to the first particle it strikes on the bed surface, the position of the impacted grain relative to other grains composing the bed (e.g. the

bed-pocket angle geometry), which governs the pathway of momentum exchange between the colliding grain and the granular bed, and the positions of both rebounding and ejected grains relative to local bed irregularities that potentially obstruct their departure from the surface. The second component partitions the impact momentum of the incoming grain among the disparate-sized particles comprising the bed in the vicinity of the collision site.

An example grain-bed collision is shown in Figure 4.1, for a particle of diameter  $D_m = 0.83\text{mm}$  (stippled disk) striking a stationary grain ( $D_m = 0.86\text{mm}$ ) on the computer-generated sediment bed. Collisions occur in two dimensions (i.e. in a vertical plane parallel to the flow direction), a conceptual approach shared with most uniform-size eolian models. Although the possibility of grains striking more than one stationary particle in the down- and cross- stream directions has been noted (e.g. Rumpel, 1985; McEwan *et al.*, 1992), grain-rebound statistics produced by computer simulations in which the incoming grain strikes only a single bed grain have been shown to agree with empirical observations. For example, McEwan *et al.* (1992) tested the single or “target” grain hypothesis by comparing the results of a simple collisional model with high-speed film images of grain-bed contacts procured by Willetts and Rice (1985a). The actual grain-bed collisions were not observable on film because the grains disappeared from view into bed pockets, or splash craters created by one to several grain collisions, before rebounding. Hence, McEwan *et al.* compared the average time between observed grain disappearance and rebound re-emergence with an algorithm predicting the duration of collisions between uniform spheres on the basis of known impact and rebound velocities, and the distance travelled by a grain between its exit from and return to the field of view. In their model, the impact momentum could be partitioned between numerous bed particles. They found, however, that the best agreement between observed and calculated collision durations obtained from the single-grain impact hypothesis. It might be concluded from these numerical experiments, as well as from observations of the range of bed-pocket geometry angles, that the probability of an incoming grain hitting one grain squarely is greater than it striking two or more grains with comparable force. Hence, the grain's forward momentum probably is transmitted principally to one grain and then redistributed among other grains composing the subsurface layers of the bed.



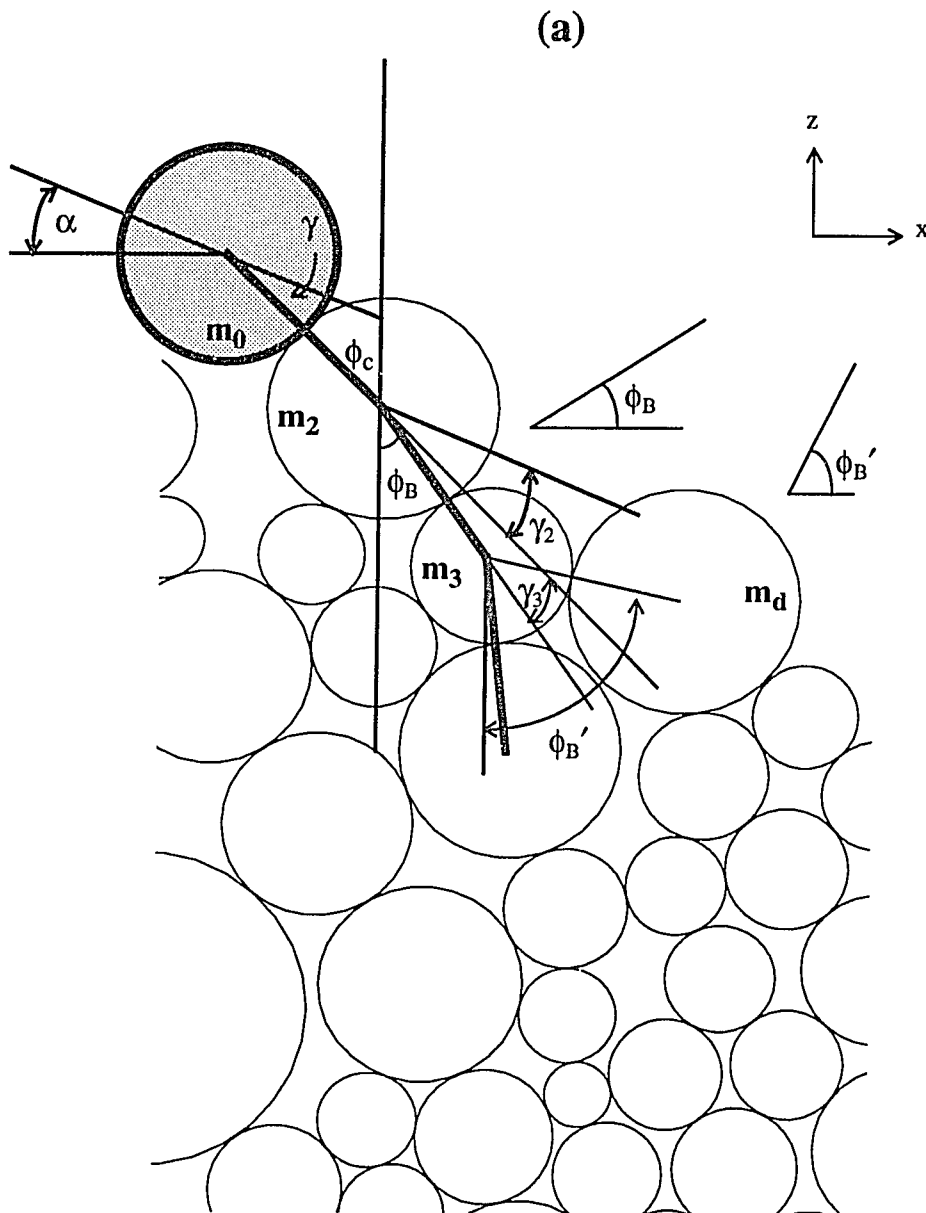


**Figure 4.1** Collision geometry between an incoming grain (stippled) and mixed-size grains composing the sediment bed. (a) angles:  $\alpha$  is the impact angle of the colliding grain of mass  $m_0$ ;  $\phi_c$  is the critical angle of particle rebound;  $\phi_B$  and  $\phi_B'$  are the angles of lift-off for the ejected grains of mass  $m_2$  and  $m_3$ , providing, in the latter case, that the next downwind particle ( $m_d$ ) is removed; and  $\gamma$ ,  $\gamma_2$ , and  $\gamma_3$  are angles used in the coordinate-axis rotations to calculate the velocity-vector components for each grain.

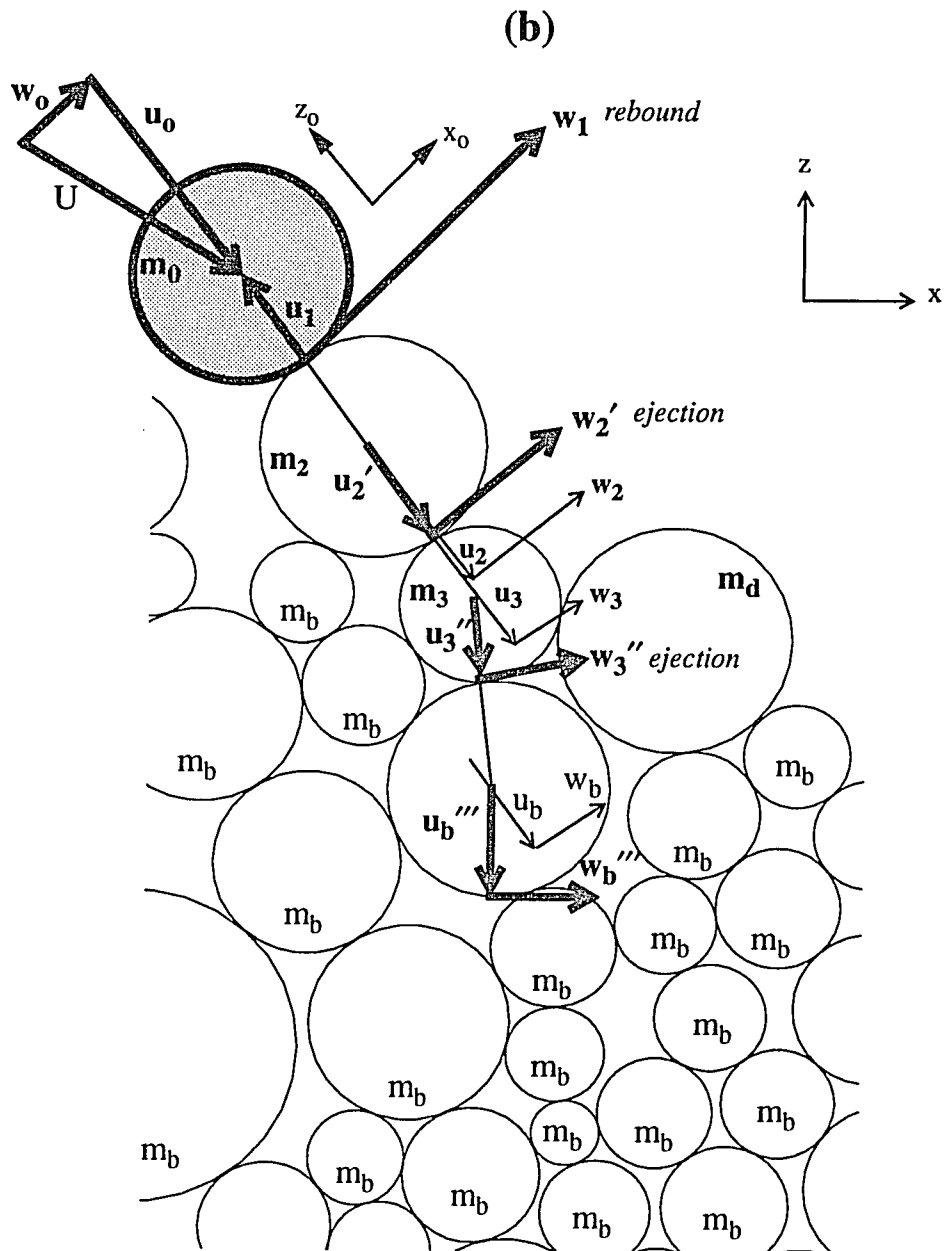


**Figure 4.1 continued.** Collision geometry of an incoming grain (stippled) and mixed-size grains composing the sediment bed. (b) components of grain velocity: the impact velocity ( $\bar{U}$ ) has components  $u_0$  and  $w_0$ , from which can be calculated the rebound velocity components of grain of mass  $m_0$  ( $u_1$  and  $w_1$ ), the ejection velocity components of grain mass  $m_2$  ( $u_2'$  and  $w_2'$ ) and grain mass  $m_3$  ( $u_3''$  and  $w_3''$ ). Grains of mass  $m_b$  represent the immobile portion of the sediment bed. Velocity components  $u_2$ ,  $w_2$ ,  $u_3$ , and  $w_3$  are used in the coordinate-axis rotations about  $x_0$  and  $z_0$  to calculate the velocity-vector components for each grain.

The mixed-grain collision model presented here assumes that one to several grains conceivably may be ejected from the bed surface. In Figure 4.1, for example, two grains of mass  $m_2$  and mass  $m_3$  potentially are dislodged, and the remainder of the sedimentary deposit is treated as a rigid bed of infinite mass ( $m_b$ ). Exactly how many grains are propelled from the bed during a single impact, and how the so-called “mean replacement capacity” (Anderson *et al.*, 1991) depends on the microtopographic characteristics of natural sediment beds and the local shear velocities, are topics of ongoing experimentation and numerical investigation.

Early quantitative analyses of uniform sediments (e.g. Owen, 1964; Tsuchiya, 1972; Reizes, 1978; Rumpel, 1985) disregarded grain ejections altogether, and later work has followed two approaches. The first involves developing probability distributions of the number of ejecta per impact event based on wind-tunnel observations (e.g. Anderson and Hallet, 1986; Sorensen, 1985; Werner, 1990). Others (e.g. McEwan and Willetts, 1991; McEwan *et al.* 1992; McEwan, 1993) have calculated the number of ejecta based on the experimentally measured differences in magnitude between a particle’s incoming and rebounding velocities, and the number of partitions among bed grains necessary to achieve the observed level of momentum dissipation. Experimental accounts of particle-ejection numbers have ranged from 1-3 particles (e.g. Willetts and Rice, 1985a, 1986a) for well-sorted grain mixtures at moderate shear velocities to on the order of 10 particles (e.g. Mitha *et al.*, 1986) for uniform spheres (BB’s) at high shear velocities. The second approach derives ejection statistics by computer simulation of the impact process. Ungar and Haff (1987) introduced the concept of a “splash function”, in which the number of ejections was taken to be proportional to the square of the impact velocity. Later workers (e.g. Werner, 1990) pointed out that their function did not account for the coexistence of a high-energy rebounding population and a lower-energy group of ejected particles. Subsequently, Werner and Haff (1986, 1988) investigated grain-impact behavior by applying the particle-dynamics method (i.e. analyzing all body and contact forces acting on grains within the bed) to simulated, regularly arrayed, densely packed beds of uniform-sized particles. They calculated an average of 6 ejections per impact, which could be high given the fact that closely packed, aligned particles respond differently to local disturbances than irregularly arrayed deposits with packing more typical of eolian sand beds. Anderson

and Haff (1988, 1991) relaxed the packing in their uniform-size, computer-generated beds and produced large numbers of grain-impact statistics to extend the splash function into the range of flow conditions in which wind-tunnel measurements are difficult to procure, such as when the sediment bed is obscured to view by dense concentrations of moving particles. Their results are consistent with the conclusions of Willetts and Rice (1985a, 1989) and Werner (1990) that the number of ejecta increases approximately linearly with the impact speed of the incoming grain. They predict on the order of 5 ejecta at lower impact velocities (e.g. 1 m/s) and in the neighborhood of 20 ejections at higher impact velocities (e.g. 8 m/s). McEwan and Willetts (1991), on the other hand, record many fewer ejections at comparable impact velocities in their numerical simulations of uniform-size grains (e.g. an average of 5 grains). In numerical experiments with their two-grain-size beds, Haff and Anderson (1993) found that coarse grains (0.32mm) striking a bed of finer grains (0.23mm) at 8 m/s released as many as 50 ejecta, while fine grains impacting a bed of coarse particles at comparable speeds ejected only 5 grains. They attribute the tenfold decrease in ejecta numbers to the differences in particle mass.

A resolution to the problem of characterizing the ejection frequency distribution with respect to impact velocities could be facilitated by further examination of the outcome of multiple ejections. Of greater importance than the absolute numbers of grain ejecta per impact is the percentage of dislodged grains that actually produce viable hop trajectories. The grains that modify the saltation regime most effectively are those that reach higher levels in the flow where the wind-grain momentum exchange becomes significant. As shown earlier, the population of grains of any size moving at low energies along the bed surface have relatively less impact on the structure of the wind-velocity profile. The ability of a saltating grain to propel more than a few grains energetically into the flow is limited, and empirical studies have shown that energetic collisions producing multiple ejections typically result in a few energetic ejections and relatively more low-energy particle displacements (e.g. Willetts and Rice, 1985a, Mitha *et al.*, 1986). In the case of mixed-grain sizes, the dynamics of grain collisions are complicated further by the particle-mass frequency distribution of the bed surface, as well as the substantial variability in surface roughness leading to increased exposure of some grains on topographic highs and decreased exposure of others in bed

pockets. It is interesting that the lowest numbers of ejecta were recorded from the mixed-grain experimental studies of Willetts and Rice (1985a, 1989) using natural sands with a size-frequency distribution comparable to the Great Sand Dunes sample described in Chapter 2 (e.g. Figure 2.1). Willetts and McEwan (1993) and Williams *et al.* (1990) attribute the considerable disparity (e.g. factor of 3) between dislodgment rates calculated from empirical observations of mixed-size sediments (e.g. Willetts and Rice, 1989) and those derived experimentally or theoretically for uniform sediments (e.g. Williams *et al.*, 1990; Anderson and Haff, 1991; McEwan and Willetts, 1991) to the surface irregularities of the heterogeneous sediment bed.

The approach chosen here is to allow a maximum of two ejections per impact, the exact number and physical behavior (e.g. kinetic energy) of which depend on the magnitude of momentum transfer and the bed-pocket characteristics of the collision site. This formulation most closely approximates the results of the Willetts and Rice studies. Furthermore, this same approach was taken in the previous study of uniform sizes (Calder, 1987) and, because the calculated particle-transport rates compared very well with wind-tunnel measurements, it is considered a viable hypothesis for the mixed-grain case. The underlying assumption is that if multiple ejections occur, only a few grains potentially will gain sufficient momentum through impact to leave the bed surface energetically. As a test of this hypothesis, the model was modified in such a manner that many grains in the bed were free to move; at moderate Shields stresses [e.g.  $(\tau_*)_{50} = 4.52 \times 10^{-2}$ ;  $(T^*)_{50} = 3.0$ ], multiple ejections in which more than one particle instigated a new hop sequence were found to be rare, regardless of the relative masses of the impacting and stationary particles. This assumption undoubtedly breaks down in the case of large grains striking a bed of smaller particles at high Shields stresses; energetic coarse grains are known to drive smaller grains from the collision site when they collide with sufficient force to form craters in the bed surface (e.g. Bagnold, 1941; this has also been observed for uniform materials by Mitha *et al.*, 1986). These high Shield's stress environments, however, are not treated in this work. Also the effects of a three-dimensional bed on the nature of mixed-grain collisions might shed a different light on this working hypothesis. For now, though, the more tractable case involving collisions on a two-dimensional bed is pursued.

The numerical model predicts that, at moderate Shields stresses, grain collisions commonly occur between the incoming grain and a pocket formed between two bed grains. In this situation, the potential for mobilizing both grains is greatest when a coarse grain collides with finer grains. Conversely, a fine grain typically is not able to dislocate either particle forming the pocket. In the former case, it was found that allowing both grains to move results in energetic ejection of the grain on the downwind side of the pocket and more feeble motion of the upwind grain (i.e. they generally did not move more than  $1D_{50}$  upwind). This observation is consistent with the fact that the momentum vector of the incoming grain is oriented principally in the forward, rather than the upwind, direction.

As depicted in Figure 4.1a, the primary momentum transfer between the incoming grain and the particles on the bed occurs along a curve defined by the lines-of-centers of subjacent grains. This approach has been used previously for uniform-sized materials (e.g. Rumpel, 1985; Calder, 1987; McEwan *et al.*, 1992). Incoming grains may strike a bed grain at any position along its exposed surface, both in the upwind and downwind quadrants of its upper hemisphere. The impulsive force transmitted by the colliding grain drives bed grains downward, primarily along this vector, and particles several layers below the surface are inhibited from appreciable horizontal motion because, in order to do so, they would have to displace layers of grains at depth within the bed. The results of model-derived collisions suggest that motion of the bed grains is inhibited even in the near-surface layers in mixed-size deposits. For example, grain of mass ( $m_d$ ) in the diagram would have to be displaced by mass ( $m_3$ ) in order for the latter to be ejected from the bed. Such a displacement would require that mass ( $m_3$ ) receive sufficient momentum through the collision to move a grain three times its mass from a stable bed-pocket geometry. In the range of transport stages investigated (i.e.  $1 \leq (T^*)_m \leq 6$ ), this does not happen. At greater depths in the bed, disturbed grains must push other grains ahead of them along trajectories through the bed. As this is physically plausible only at high transport stages when all grains in successively deeper layers within the bed are mobilized (e.g. during bed erosion; see Bagnold, 1941), momentum is transferred back in the direction of the surface along these same momentum vectors. The dissipation of collisional energy increases with the number of contacts along this pathway. Such energy damping

might result in grains being jostled on the surface adjacent to the point of collision, as has been observed experimentally (e.g. Mitha *et al.*, 1986), but the magnitude of momentum exchange must be considerable to pop these grains from the surface into the airstream.

The lines-of-centers connecting the incoming grain with bed grains in the collision site (e.g. heavy solid lines in Figure 4.1a) represents the primary reference line for calculating the impact geometry because it is defined on the basis of known variables: the impact angle ( $\alpha$ ), relative to the horizontal plane of the bed surface, and the vector velocity ( $\vec{U}_s$ ) of the colliding grain. The lift-off angles of the rebounding grain (mass  $m_0$ ) and the ejected particles (masses  $m_2$  and  $m_3$ ) are calculated as a function of the trigonometric relationships between the colliding grain and the first grain it contacts on the bed (mass  $m_0$ ), and the bed-pocket angle geometries of the bed particles. The incoming grain rebounds at an angle  $\phi_c = (90^\circ - \alpha - \gamma)$ , where  $\gamma$  is a function of the impact angle and the geometry of the collision. Mass  $m_2$  is ejected into the flow at an angle  $\phi_B$  prescribed by its bed-pocket angle geometry (see Chapter 2 for discussion). Likewise, mass  $m_3$  is launched at an angle  $\phi_B'$  based on its bed-pocket angle geometry defined by its relationship with the downwind grain of mass  $m_d$ . Angles  $\gamma_2$  and  $\gamma_3$  pertain to the coordinate-axis rotations necessary to calculate the velocity components of the potentially ejected grains.

Factors governing the velocity with which a grain rebounds from the bed include its linear momentum at the instant before impact and the degree of elasticity of its collision with a stationary grain on the bed surface. Only a small fraction of the internal energy of a saltating system is rotational; therefore, the effects associated with particle spin can be neglected. Linear momentum just prior to impact is determined by the speed and angle of the incoming grain. It is assumed that under steady, horizontally uniform flow conditions, the small perturbations in the particle trajectory associated with turbulent fluctuations as it nears the bed negligibly affect particle forward momentum and, hence, the exact location of grain contact with the bed.

The degree of elasticity of a collision between spherical particles commonly has been characterized by a coefficient of restitution ( $\beta$ ) (e.g. Tsuchiya, 1972; Reizes, 1978; Werner and Haff, 1986, 1988), which represents the average percent of kinetic energy or linear momentum transferred during impact to the bed in the absence of interstitial fluid. Models employing splash func-

tions or experimental observations of collisions between uniform-sized grains have incorporated an analogous term to describe the efficiency of the collision; this term appears as the constant of proportionality in the linear relationship of grain impact velocity to rebound velocity (e.g. McEwan and Willetts, 1991; McEwan *et al.*, 1992).

As applied here, the coefficient of restitution signifies the average percent of kinetic energy ( $\beta_E$ ) or linear momentum ( $\beta_M$ ) that would be transferred in a vacuum during a collision between two similar-density sand grains of natural sphericity and angularity, and unequal size. Restitution coefficients are lower for natural sediment particles than for spheres of the same material properties because irregularities of the grain surface create local stresses, producing substantially greater inelastic deformation. Limited information exists on the magnitude of  $\beta$  for natural sand grains; typically, coefficients of restitution are given as constants derived from analysis of numerical collision data and are usually on the order of 0.40 - 0.85. The restitution coefficient in this model is a function of impact-grain momentum and increases as the velocity of the impacting grain approaches zero (e.g. Goldsmith, 1960; Tataru and Moriwaki, 1982; Lun and Savage, 1986); at low impact speed, the collision is purely elastic and  $\beta_E = 1$ . As  $\beta$  is independent of the properties of the interstitial medium, the form of the restitution coefficient employed by Wiberg and Smith (1985) is used:  $\beta = [0.87 - 0.083(\ln(\rho_s \vec{U}_s))]$ , where  $\vec{U}_s$  is the grain impact speed,  $\rho_s$  is the sediment density, and the constants are set by empirical data. The term  $\beta$  is multiplied in the equations of particle momentum and velocity by the ratio of grain masses, so that the differences in mass between the colliding grain and the particle it impacts are taken into account. This formulation of the restitution coefficient differs from that employed by Haff and Anderson (1993) in their two-grain-size collision algorithm, in that it describes momentum transfer during impact of one grain with one other grain rather than momentum exchange between all grains in the continuum.

Collisions are treated in a momentum- and energy- conserving manner, with momentum and energy transfer to the bed through particle-particle interaction accounted for by the coefficient of restitution. Momentum and energy are conserved about coordinate axes normal and tangential to the point of contact between the incoming grain of mass  $m_0$  and the first grain (mass  $m_2$ ) it strikes on the bed (i.e. axes  $x_0$  and  $z_0$  in Figure 4.1b). At the instant before collision, the momentum of



the colliding grain equals the product of its mass times velocity ( $m_0 \vec{U}_s$ ). Following the collision, this momentum is reduced by the inelasticity of the impact and redistributed, as shown in Figure 4.1b, among: (1) the grain as it rebounds, (2) the one to several ejected grains ( $m_2$  and  $m_3$ ), and, (3) the population of grains comprising the remainder of the sediment bed ( $m_b$ ). For mixed-size grains in a two-dimensional perspective, the scalar equations for conservation of linear momentum are:

$$\beta_M m_0 u_0 = m_0 u_1 + m_2 u_2 + m_3 u_3 + \dots + m_b u_b \quad (4.1a)$$

and

$$\beta_M m_0 w_0 = m_0 w_1 + m_2 w_2 + m_3 w_3 + \dots + m_b w_b \quad (4.1b)$$

where the mass ( $m$ ) of the incoming grain is assumed to remain constant during the collision (i.e.  $m_0 = m_1$ );  $u$  and  $w$  are the components of velocity along, and perpendicular to, the lines-of-centers connecting the grains; and  $\beta_M$  denotes the coefficient of restitution for linear momentum. Additional free grains ( $m_n, \dots, m_b$ ) can be added to the problem, if desired.

The energy balance between the rebounding grain and all sediment grains within the bed is given by:

$$\beta_E^2 (u_0^2 + w_0^2) = u_1^2 + w_1^2 + \frac{m_2}{m_0} (u_2^2 + w_2^2) + \frac{m_3}{m_0} (u_3^2 + w_3^2) + \dots + \frac{m_b}{m_0} (u_b^2 + w_b^2) \quad (4.2)$$

where  $\beta_E^2$  is the square of the restitution coefficient for kinetic energy. For two isotropic, non-rotating spheres subjected to a head-on collision,  $\beta_E^2 = \beta_M^2 = \beta^2$  (Symon, 1971), which is assumed to be valid for rounded sand grains as well.

The system of equations represented by (4.1) and (4.2) are simplified by noting that the cumulative mass of the many grains composing the rigid bed at depth is very large compared to the mass of each grain in the deforming layer above this level; therefore,  $m_1 = m_2$  is of the same order as  $m_0$ , but  $m_b \gg m_0$ . At the instant of impact, the bed grains all must have the same velocity components along the lines-of-centers as impact momentum is transferred downward from the collision site, and the corresponding velocity components for each of the potentially ejected grains must be of the same order of magnitude. Each velocity component is determined through a coordi-

nate axis rotation about  $x_0$  and  $z_0$ ; for example,  $u_2$  in the pre-impact coordinate system becomes  $u_2'$  through axis rotation into the reference frame of  $m_2$  and  $u_3$  becomes  $u_3''$  (see Figure 4.1b). In addition, the curvature of the lines-of-centers, and thereby the angle for each of the (n-1) coordinate rotations, is relatively small. Consequently, all of the center-to-center velocity components, except  $u_0$  and  $u_1$ , are the same order of magnitude, for the range of grain sizes investigated here. As a result,  $|m_2u_2|$ ,  $|m_3u_3|$ , ...,  $|m_nu_n|$  are all much less than  $|\beta m_0u_0|$ , and  $|m_bu_b|$  is on the order of  $|\beta m_0u_0|$ . Therefore,  $u_b \ll u_0$ . With these constraints, equation 4.1a simplifies to:

$$\beta m_0 u_0 = m_0 u_1 + m_b u_b \quad (4.3)$$

Moreover, as long as the rotation angles are small,  $|m_2w_2|$ ,  $|m_3w_3|$ , ...,  $|m_nu_n| \ll |\beta m_0w_0|$ , and:

$$\beta m_0 w_0 = m_0 w_1 + m_b w_b \quad (4.4)$$

Equations (4.2), (4.3), and (4.4) combine to give:

$$\left(\frac{m_b}{m_0}\right)^2 (u_b^2 + w_b^2) = 2\beta u_0 \left(\frac{m_b}{m_0} u_b\right) + 2\beta w_0 \left(\frac{m_b}{m_0} w_b\right) \quad (4.5)$$

Rearrangement of equation 4.5 leads to an expression for the velocity component parallel to the lines-of-centers of the incoming and impacted grains at the instant of collision. It is:

$$u_b = 2\beta u_0 \frac{\left(1 + \frac{w_0 w_b}{u_0 u_b}\right)}{\left(1 + \frac{w_b^2}{u_b^2}\right) \left(\frac{m_b}{m_0}\right)} \quad (4.6)$$

The unknown velocity components for the moving grains can now be computed in terms of  $u_0$ ,  $w_0$ , and  $u_b$ . Momentum transfer between grains in the bed follows a curved path, so the unknown velocity components can be related to these known velocities only if a series of coordinate-axis rotations is performed about angles that can be defined on the basis of the known impact position  $\phi_c$  and impact angle  $\alpha$ . The launch of grain with mass  $m_2$  is accomplished through the velocity component  $w_2'$  and is determined by a coordinate axis rotation of  $u_2$  and  $w_2$  about angle  $\gamma_2$ :

$$u_2' = u_2 \cos \gamma_2 - w_2 \sin \gamma_2 \quad (4.7a)$$

$$w_2' = w_2 \cos \gamma_2 + u_2 \sin \gamma_2. \quad (4.7b)$$

Likewise, the velocity component  $w_3'$  governs the ejection of grain with mass  $m_3$ :

$$u_3' = u_3 \cos \gamma_2 - w_3 \sin \gamma_2 \quad (4.8a)$$

$$w_3' = w_3 \cos \gamma_2 + u_3 \sin \gamma_2. \quad (4.8b)$$

With four unknown velocity components, equations (4.8) and (4.9) must be solved simultaneously. Consequently, another coordinate-axis rotation is invoked, which redefines  $u_3$  and  $w_3$  in terms of the vector between  $m_2$  and  $m_3$ , and  $u_b$  and  $w_b$  in terms of the vector between  $m_3$  and the first grain mass  $m_b$  beneath it. This permits applying the boundary condition that  $m_b$  has no component of vertical velocity. Rotating the velocity components of  $m_3$  and  $m_b$  through  $\gamma_3$  gives:

$$u_3'' = u_3 \cos \gamma_3 - w_3 \sin \gamma_3 \quad (4.9a)$$

$$w_3'' = w_3 \cos \gamma_3 + u_3 \sin \gamma_3 \quad (4.9b)$$

$$u_b'' = u_b \cos \gamma_3 - w_b \sin \gamma_3 \quad (4.9c)$$

$$w_b'' = w_b \cos \gamma_3 + u_b \sin \gamma_3. \quad (4.9d)$$

At the instant of impact: (1)  $w_2' = w_3'$ , (2)  $u_2' = u_3'$ , (3)  $w_3'' = w_b''$ , and (4)  $u_3'' = u_b''$ . By incorporating these constraints in equations (4.9a-d) above, solutions are obtained for each velocity component involved in these rotations. Applying the boundary condition to equation (4.9d) that the bed is immobile and the vertical component of bed velocity ( $w_b'''$ ) is zero, yields an equation for  $w_b$ :

$$w_b = -u_b (\tan \gamma_3) . \quad (4.10)$$

Component  $u_3$  derives from substitution in equation (4.9a) of  $u_3'' = u_b''$  and rearrangement:

$$u_3 = u_b (1 + \tan^2 \gamma_3) + w_3 \tan \gamma_3 . \quad (4.11)$$

Substitution in equation (4.8a) of  $u_2' = u_3'$  and substitution of  $u_3$  from equation (4.11) gives:

$$u_2 = u_b (1 + \tan^2 \gamma_3) + w_3 \tan \gamma_3 - \tan \gamma_2 (w_3 - w_2) , \quad (4.12a)$$

which can be simplified further for the case where  $\gamma_3 \neq 0$  and  $[m_b/m_0] \gg 1$ , to:

$$u_2 \approx w_3 (\tan \gamma_3 - \tan \gamma_2) + w_2 \tan \gamma_2 \quad (4.12b)$$

since the term containing  $u_b$  becomes negligible compared with the other terms in (4.12a).

In order to close the problem, an assumption must be made regarding the magnitude of the

vertical velocity component of the rebounding grain,  $w_1$ . If linear momentum is conserved in a collision, then the incoming grain likely behaves the same at impact as it does in rebound; that is, if the impact is 30% elastic, then the grain will retain 30% of its momentum on rebound. Therefore,  $w_1 = \beta w_0$ . Equation (4.1b) can then be rewritten as:

$$\frac{m_b}{m_0} w_b = \left[ \frac{m_2}{m_0} w_2 + \frac{m_3}{m_0} w_3 + \dots + \frac{m_{b-1}}{m_0} w_{b-1} \right] \quad (4.13)$$

At the instant of collision, the momentum of mass  $m_2$  equals that of  $m_3$ , such that  $\frac{m_2}{m_0} w_2 = \frac{m_3}{m_0} w_3$ . Therefore,

$$w_2 = \frac{m_3}{m_2} w_3 . \quad (4.14)$$

Finally, substituting equation (4.14) into (4.13) yields:

$$w_3 = \frac{1}{2} u_b \frac{m_b}{m_3} \tan \gamma_3 . \quad (4.15)$$

With some further substitution and rearrangement, the general equations for all velocity components of the rebounding mass ( $m_0$ ) and two potentially ejected grains ( $m_2$  and  $m_3$ ) are derived. The components of lift-off velocity of each grain now are posed in terms of known quantities: the velocity components of the incoming grain,  $u_0$  and  $w_0$ , predicted by the saltation-trajectory algorithm described earlier, and the angles of impact ( $\alpha$ ), rebound ( $\phi_c$ ), ejection ( $\phi_B$  of mass  $m_2$  and  $\phi_B'$  of mass  $m_3$ ), and the coordinate-axis rotations ( $\gamma_2$  and  $\gamma_3$ ). These equations apply to all collision geometries between moving grains and the heterogeneous sediment bed, and the number of equations may be increased by similar arguments to include a greater number of ejecta. They are:

$$u_1 = -\beta u_0 \left[ \left( 2 \left( \frac{1 - \frac{w_0}{u_0} \tan \gamma_3}{1 + \tan^2 \gamma_3} \right) - 1 \right) + \frac{m_2}{m_3} \left( \frac{1 - \frac{w_0}{u_0} \tan \gamma_3}{1 + \tan^2 \gamma_3} \right) \tan \gamma_3 (\tan \gamma_3 - \tan \gamma_2) \right]$$

$$+ \left[ \frac{1 - \frac{w_0}{u_0} \tan \gamma_3}{1 + \tan^2 \gamma_3} \tan \gamma_3 \tan \gamma_2 + \frac{1 - \frac{w_0}{u_0} \tan \gamma_3}{1 + \tan^2 \gamma_3} \tan^2 \gamma_3 \right] \quad (4.16a)$$

$$w_1 = \beta w_0 \quad (4.16b)$$

$$u_2 = \beta u_0 \left[ \frac{m_0}{m_3} \left( \frac{1 - \frac{w_0}{u_0} \tan \gamma_3}{1 + \tan^2 \gamma_3} \right) \tan \gamma_3 (\tan \gamma_3 - \tan \gamma_2) \right.$$

$$\left. + \frac{m_0}{m_2} \left( \frac{1 - \frac{w_0}{u_0} \tan \gamma_3}{1 + \tan^2 \gamma_3} \right) \tan \gamma_3 \tan \gamma_2 \right] \quad (4.16c)$$

$$w_2 = \beta u_0 \frac{m_0}{m_2} \left[ \frac{1 - \frac{w_0}{u_0} \tan \gamma_3}{1 + \tan^2 \gamma_3} \right] \tan \gamma_3 \quad (4.16d)$$

$$u_3 = \beta u_0 \frac{m_0}{m_3} \left[ \frac{1 - \frac{w_0}{u_0} \tan \gamma_3}{1 + \tan^2 \gamma_3} \right] \tan^2 \gamma_3 \quad (4.16e)$$

$$w_3 = \beta u_0 \frac{m_0}{m_3} \left[ \frac{1 - \frac{w_0}{u_0} \tan \gamma_3}{1 + \tan^2 \gamma_3} \right] \tan \gamma_3 \quad (4.16f)$$

$$w_2' = w_2 \cos \gamma_2 + u_2 \sin \gamma_2 \quad (4.16g)$$

$$w_3'' = w_3 \cos \gamma_3 + u_3 \sin \gamma_3 \quad (4.16h)$$

The angles  $\gamma_2$  and  $\gamma_3$  are found trigonometrically. For  $\phi_B \geq \phi_c$ ,  $\gamma_2 = (\phi_c - \phi_B)$  and for  $\phi_B < \phi_c$ ,  $\gamma_2 = (90 - \alpha - \phi_c)$ . For  $\phi_B' \leq \phi_c$ ,  $\gamma_3 = (\phi_c - \phi_B')$  and for  $\phi_B' > \phi_c$ ,  $\gamma_3 = (\phi_c - \phi_B)$ . The launch velocity of mass  $m_2$  is given by the magnitude and direction of vector  $w_2' e_2'$ , and the potential launch velocity of mass  $m_3$  by  $w_3'' e_3''$ . In the particular collision scenario illustrated in Figure 4.1(a,b), however, the model predicts that the second mass  $m_3$  does not eject because mass  $m_d$  obstructs its lift off from the bed. Hence, the ability of  $m_3$  to leave the bed subsurface depends directly on the relative mass of  $m_d$  and the bed-pocket angle geometry formed by  $m_3$  and  $m_d$ .

#### 4.2 Model predictions of collisional dynamics

Results of coupling the collisional algorithm with the previously described sediment-bed and saltation-trajectory model elements yield some intriguing views of the bed region during transport events. The model possesses some advantages over wind-tunnel experiments, in that it is possible to follow each moving grain forward in time and space across a sediment bed whose physical characteristics are known in great detail. This permits calculation of the dynamical interaction of the grain with the fluid flow and the exact nature of each particle collision with the sediment bed. In addition, the relative masses of the moving and impacted grains are known, making it possible to evaluate the collision mechanics of mixed-size particles with a heterogenous and topographically varying sediment surface. The model also predicts the cause of grain termination and the characteristics of the bed depression in which the grain temporarily or ultimately comes to rest.

For the purposes of the collisional analysis described here, the model permits only one grain to be ejected per collision, in addition to the impacting (rebounding) grain. This is the simplest working hypothesis, as discussed earlier, that grain-bed collisions yield a single ejection more energetic than any others from one collision site. Because these secondary ejecta from a single collision contribute relatively little to bedload transport rates and to modification of the vertical profile of wind velocity, it is assumed that their effect can be neglected in the flat bed, mixed-grain problem. To produce collision statistics, the outcome of each impact is noted and any grain that is ejected from the bed is pursued to record its flight and collision histories. Grains that hop off the downwind side of the sediment bed (Figure 3.1) are recirculated to the upwind side, to effect a bed

of infinite length.

The purpose of these calculations is to quantify the collisional and fluid-dynamical properties of mixed-grain sediment transport, rather than the sedimentological details of bed evolution during transport events. Hence, the geometric configuration of the bed surface is held uniform. Sites vacated by ejected grains are filled with particles of comparable size, such that no net erosion of the surface occurs. Although the bed model is designed to accommodate the addition and removal of grains, so that the evolution of the bed surface over time can be examined, this feature is omitted from these calculations to reduce the level of bookkeeping required to run the model for the bedload-transport problem. Additionally, posing the model in this manner facilitates analysis of the fundamental behavior of particles over unsorted, mixed-grain sediment beds without the complicating effects of sorting and surface armoring.

Of interest in the study of eolian surface processes is the mode of grain transport, e.g. what percentages of the moving grain population energetically saltate and what percentages travel in weakly energetic trajectories near the bed surface. Saltating grains typically travel many grain-diameters' distance above the bed for much of their flight time, extracting significant amounts of momentum from the flow. Because the weakly energetic grains relocate in short, low-energy jumps across the bed, they contribute relatively little to the modification of the near-bed flow regime over flat beds in the range of transport stages considered here. However, these low-energy ejecta, variously termed "creep" (e.g. Bagnold, 1941; Greeley and Iversen, 1985), "splash" (e.g. Mitha *et al.*, 1986), and "reptations" (e.g. Ungar and Haff, 1987), play a considerably greater role in the formation of eolian ripples and other small-scale bedforms (e.g. Sharp, 1963; Ellwood *et al.*, 1975; Walker, 1981; Anderson, 1987), and for this reason many have perceived a need for distinguishing between classes of grain motion. As yet, numerical models based on the splash-function approach have not been able to differentiate classes of grain ejecta because the relationships between particle dislodgment rates, lift-off velocities, rebound probabilities, and the properties of the sediment bed that limit grain motion are not understood fully and have proven difficult to measure experimentally (e.g. see discussion in Anderson *et al.*, 1991; Willetts and McEwan, 1993). For example, of the photographed grain ejections used as an observational base for constructing

splash functions (e.g. Willetts and Rice, 1985a), little is known about how many ejecta successfully rebounded downwind to dislodge other particles, what their trajectory heights and lengths were, and for what values of the lift-off velocity particles did not rebound.

The model presented here offers some additional insight to these problems. As described previously, grains ejected from the computer-generated sediment bed have lift-off velocities and angles predicted by the geometric configuration of the local bed surface and the collision-induced transfer of momentum between grains of unequal size. Thus, the probability of grain rebound or ejection can be quantified for each grain. Any particle disturbed by collision is analyzed by the model, to determine whether its motion is confined to the bed pocket in which it resides or whether the grain is propelled some distance in the upwind or downwind direction. A comparison of computer-generated hop trajectories for the suite of rebounding and ejected particles suggests that the moving population may be separated into three transport modes, as shown in Figure 4.2, based on particle dynamics and statistical arguments.

Three classes of grain transport are identified: high-energy saltations, impact-induced grain rolling, and low-energy saltations, the latter including creep, splash, reptations, and the host of terms (e.g. see Pye and Tsaoar, 1990; Anderson *et al.*, 1991) used to describe grains that lose contact with the sediment bed only for fleeting intervals but are not capable of ejecting other particles. An example of a highly energetic saltation sequence is shown in Figure 4.2a, wherein the grain travels tens of grain diameters above the bed and hundreds of grain diameters downwind in successive trajectories, and is capable of ejecting other grains that will enter the saltation layer successfully. In Figure 4.2a, a grain ( $D_m = 0.44\text{mm}$ ) finer than the median bed size ( $D_{50} = 0.70\text{mm}$ ) approaches the bed at a low impact angle ( $6.2^\circ$ ) and with a high impact velocity ( $11.7\text{ m/s}$ ) relative to wind speed ( $4.69\text{ m/s}$ ). The low angle of approach relative to the horizontal, the relative protrusion of the bed grain it strikes, and the similar mass of the impacted grain, allow the incoming grain to collide directly with the exposed upwind side of the bed particle and propel it from its bed pocket. Because the pocket is unobstructed by other protruding bed grains, the ejected grain enters the free stream (shown as an arrow). Although the colliding grain loses almost 85% of its terminal velocity via impact, the collision orientation is such that the grain rebounds with sufficient kinetic



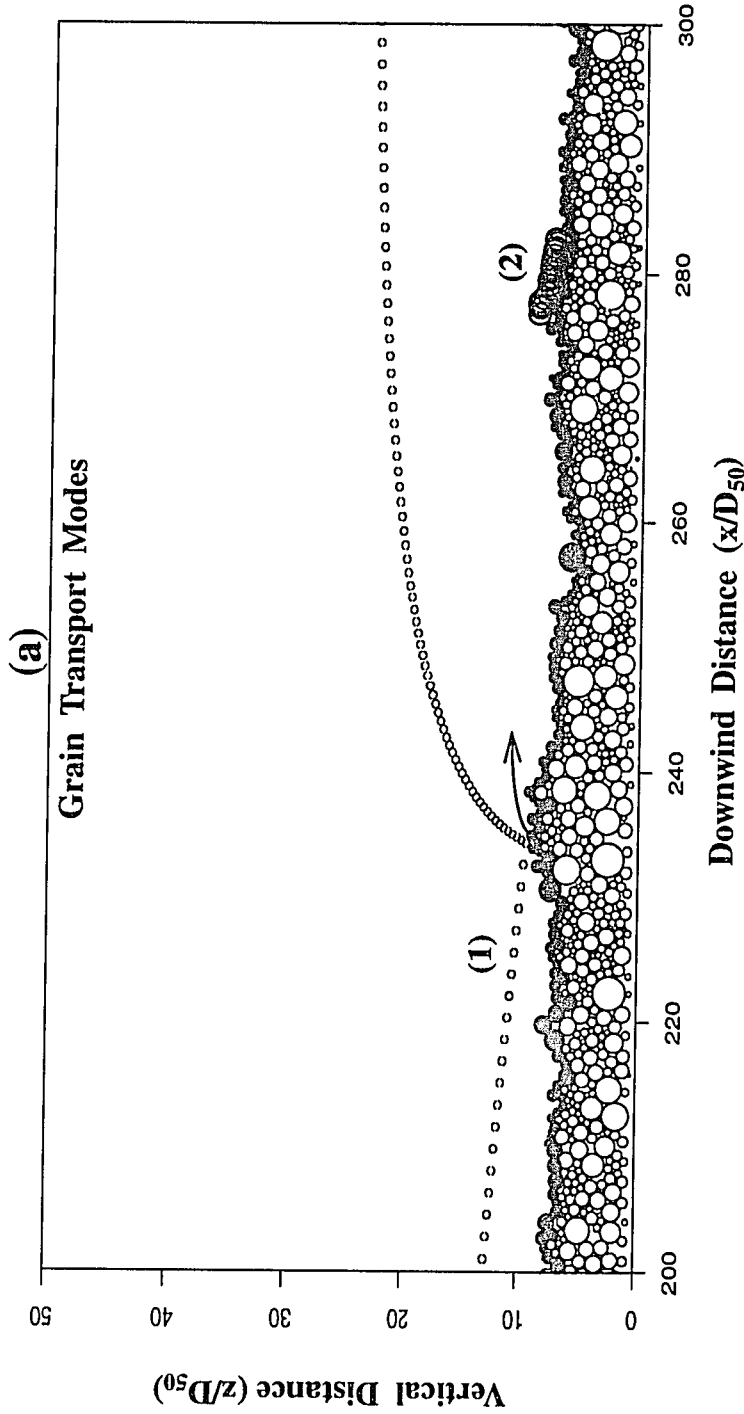


**Figure 4.2** Transport modes of moving grains across the mixed grain bed ( $D_{50} = 0.70\text{mm}$ ), at a transport stage of  $(T^*)_m = 3.0$ . (a) End members of the grain-motion spectrum. Computed trajectory (1) demonstrates an energetic collision between a saltating grain ( $D_m = 0.44\text{mm}$ ) and a slightly larger stationary particle on the bed surface ( $D_m = 0.63\text{mm}$ ), resulting in the rebound of the incoming grain and ejection of the bed grain (ejection trajectory shown as arrow). The grain strikes along the exposed upper hemisphere of the bed grain at a relatively low impact angle ( $6.2^\circ$ ) and high impact velocity ( $11.7\text{ m/s}$ ) relative to wind speed ( $4.69\text{ m/s}$ ), rebounding with 17% of its pre-collision velocity. The grain rebounds high into the flow because of the favorable collision site and a vertical component of ejection velocity that is twice the horizontal velocity component. Trajectory (2) shows a grain ( $D_m = 1.22\text{mm}$ ) rolling across the bed surface. Initiated by a colliding grain of comparable size (not shown), this particle rolls about  $8D_{50}$  downwind, without losing contact with the bed, before settling in a bed depression.

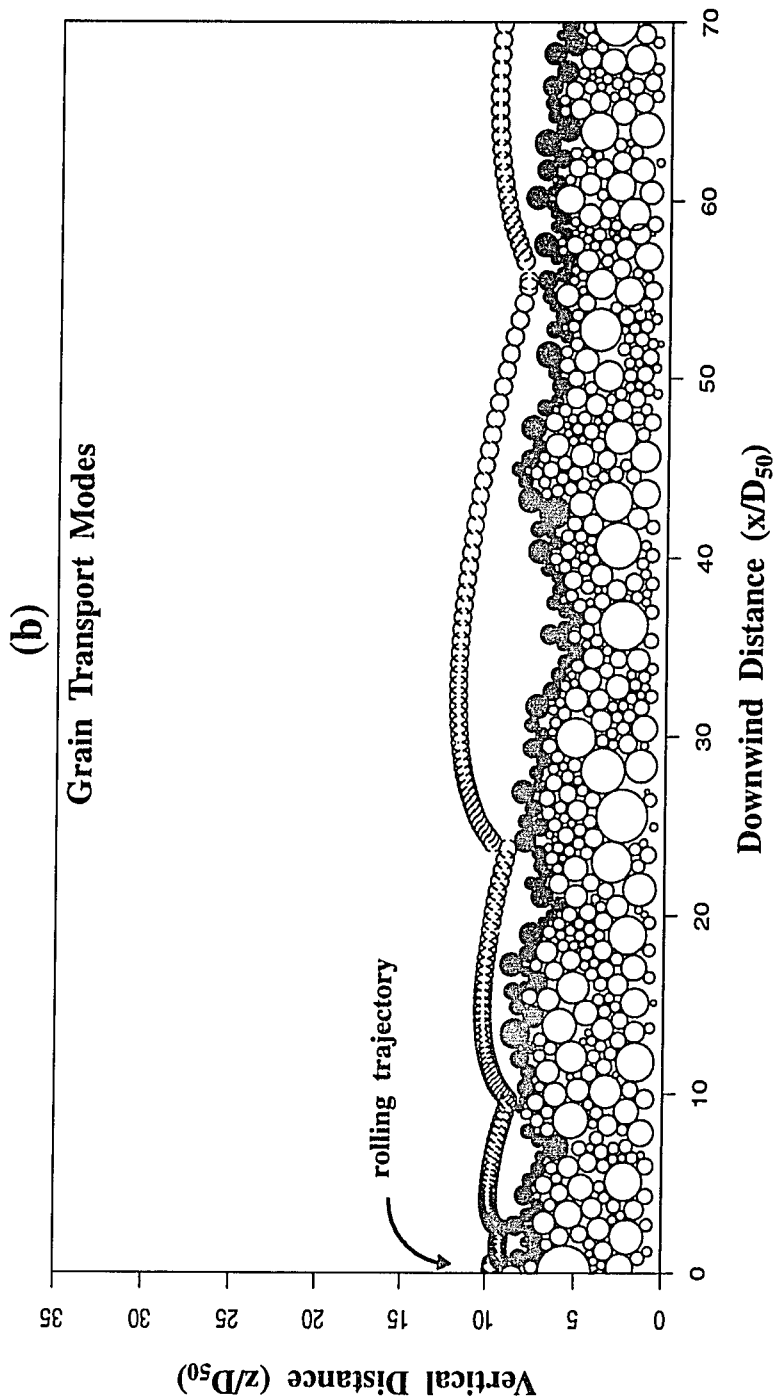


**Figure 4.2 continued. (b)** Downwind series of low-energy trajectories of a rebounding grain ( $D_{50} = 0.70\text{mm}$ ). The grain rolls into view at  $x = 0D_{50}$  and executes four rebounding hops before terminating just beyond the right-hand margin of the graph, by colliding with a bed pocket on the upwind side of an immobile particle twice its size. Typical of model-predicted, low-energy rebounds, the forward lift-off velocity component of each rebound of the moving grain exceeds the vertical velocity component by an average factor of two; consequently, the grain travels forward close to the bed in glancing collisions with the tops of grains that protrude into the flow. Grazing collisions result in low lift-off angles (e.g.  $14.9^\circ$  average) and low lift-off velocities ( $0.17\text{ m/s}$  average), which, in turn, results in low impact speeds ( $0.45\text{ m/s}$  average) and few ejections.

energy to propel it away from the bed. Its component of vertical velocity is twice that of its horizontal velocity the instant following the collision, which is typical of rebounds from energetic collisions of this geometric arrangement.

At the opposite end of the energy spectrum is grain rolling, in which the grain moves downwind without losing contact with the bed. Rolling may be induced either aerodynamically or by grain-grain collision. In Figure 4.2a, a large grain ( $D_m = 1.22\text{mm}$ ) is driven from its exposed bed pocket by a moving grain of comparable size (not shown) and rolls across other grain surfaces before reaching a bed pocket whose orientation impedes its downwind progress. The grain continuously loses momentum to stationary particles it rolls over, although an insufficient amount to eject other bed particles. Large grains, under low and moderate flow conditions, are observed to roll several tens of grain diameters' distance downwind over locally smooth bed sections (e.g. where finer grains have collected preferentially), similar to what has been observed in flume experiments (e.g. Iseya and Ikeda, 1987; Whiting *et al.*, 1988). These grains possess insufficient forward momentum to rebound from the bed surface into the flow; in addition, the absence of bed-grain protrusions comparable to the size of the rolling particle reduces its potential for ejecting bed particles.

The class of particles moving between energetic saltation and rolling occupy a terminologically grey zone, in which the lowest energy trajectories might be classified as grain rolling and the higher energy particles might be included with the energetic saltations. Figure 4.2b illustrates such a series of low-energy saltations, in which the grain varies between rolling and short, low hops. The distinction between these and higher-energy saltations is that no grains are ejected by the moving particle and that the grains are influenced more by mechanical forces of frequent contact with the topographic irregularities of the bed than by fluid-mechanical forces. This is a function of the weak momentum transfer and the geometry of each grain collision. As the particle travels in short hops, it impinges the bed at angles closer to  $20^\circ$ , such that it impacts the uppermost surfaces of exposed bed grains in glancing collisions, rather than head-on impacts. Consequently, the grain proceeds downwind in a series of glancing collisions with the tops of exposed bed particles. This collision orientation is unfavorable for ejecting grains, since the pathway of momentum transfer

along the lines-of-centers of the colliding grains is directed more vertically into the bed than laterally or away from the bed, as is the case with head-on collisions. Grazing collisions result in low lift-off angles and particle rebound speeds with higher components of horizontal velocity than vertical velocity. In this example, grain impact velocities of the hop series average 0.45 m/s and lift-off velocities average 0.17 m/s, with an average 38% reduction in particle velocity between impact and rebound.

Some workers have differentiated grain saltations as belonging to the rebound population or to the low-energy group of ejecta that splash from the bed via impact but do not rebound after landing (e.g. Ungar and Haff, 1987; Sorensen, 1991). Anderson *et al.* (1991) have further decomposed the low-energy saltation spectrum into a surface-creep component, which conceptually refers to those ejected grains that rearrange the sediment surface primarily through contact forces between surface grains. These distinctions become even more difficult to quantify in grain mixtures because the irregularities of the bed surface ultimately control the progress of all particles downwind. For example, the mixed-grain model shows that energetically ejected particles may execute a long, high jump but then become trapped on the first rebound by striking the bed unfavorably. Unfavorable collisions, which often do not produce additional ejections, include striking a bed pocket or a larger grain close to its equator, such that the colliding grain rebounds horizontally upwind and terminates within the confines of the bed depression. Also, ejecta might execute a low-energy, non-rebounding hop only a few grain diameters' distance downwind but knock another precariously perched grain from a bed pocket with negligible momentum loss. Furthermore, the pattern of hop sequences varies from grain to grain, due to the microtopographic variations of the bed surface. Model results show that sequences of downwind trajectories executed by one grain can fluctuate between the three modes of transport, depending on the outcome of each collision. This behavior has been photographed in wind-tunnel experiments with sand mixtures (e.g. Barndorff-Nielsen *et al.*, 1985b; Willetts and Rice, 1985b). Therefore, a grain might energetically rebound from several downwind collisions, then lose momentum through collision with bed irregularities or larger grains and execute a series of low-energy hops. Thus, the grain might be contributing to several aspects of bed dynamics and bedform construction during its travel, and

defining its mode of transport becomes arbitrary.

A statistical distinction between high-energy and low-energy saltations can be made by plotting the model-predicted, particle impact speeds against their lift-off speeds. This relationship has been used by others (e.g. Anderson and Haff, 1988, 1991; McEwan and Willetts, 1991; McEwan *et al.*, 1992) to predict lift-off speeds for uniform-sized grains from numerical collision data, where the magnitudes of particle lift-off velocities are linearly related to the magnitudes of impact velocities through a collision coefficient:  $U_{\text{rebound}} = \epsilon U_{\text{impact}}$ , with  $\epsilon$  ranging from 0.50 to 0.80. In Figure 4.3a, the relationship between impact and lift-off velocities for the mixed-grain saltating population is given for two transport stages,  $(T^*)_m = 3.0$  and  $(T^*)_m = 6.0$ ; both the lift-off velocities of the rebounding and ejected grains are included in the graph. A linear least-squares fit of the point scatter in the  $(T^*)_m = 3.0$  case demonstrates that the predicted collision outcomes can be decomposed into two groups represented by fit lines of different slope and intercept (dashed lines); they are the dense cluster of points representing low-impact-speed, low-launch-speed grains, and the diffuse scatter of grains with higher impact and launch velocities. The same trend is seen for the transport stage of  $(T^*)_m = 6.0$ . A non-linear weighted regression of all points demonstrates that the best fit for the population of moving grains is curvilinear, as indicated by the heavy, solid curves in both graphs, which smoothly connect the regression lines fit to low-velocity and higher-velocity grains.

These results show that particles of all sizes with impact speeds less than about 1.0 m/s and rebound speeds less than 0.3 m/s form a fairly distinct subset of the moving-grain population, both statistically and mechanically. These are the grains that travel one to several short, low hops from the collision site, rarely ejecting particles into the windstream, and whose downwind progress ultimately is influenced more by the topographic features of the bed than by fluid forces. They contrast with the subset of higher-velocity particles, which are sufficiently energetic to dislodge other particles from the bed during impact and whose contact with the bed is fleeting. These low-velocity grains comprise about 28% to 30% of the moving population (198 of 690 observations at  $(T^*)_m = 3.0$  and 152 of 507 observations at  $(T^*)_m = 6.0$ ), which compares with the observations of Bagnold (1941), Willetts and Rice (1985b), and others that the low-energy group of moving grains rep-

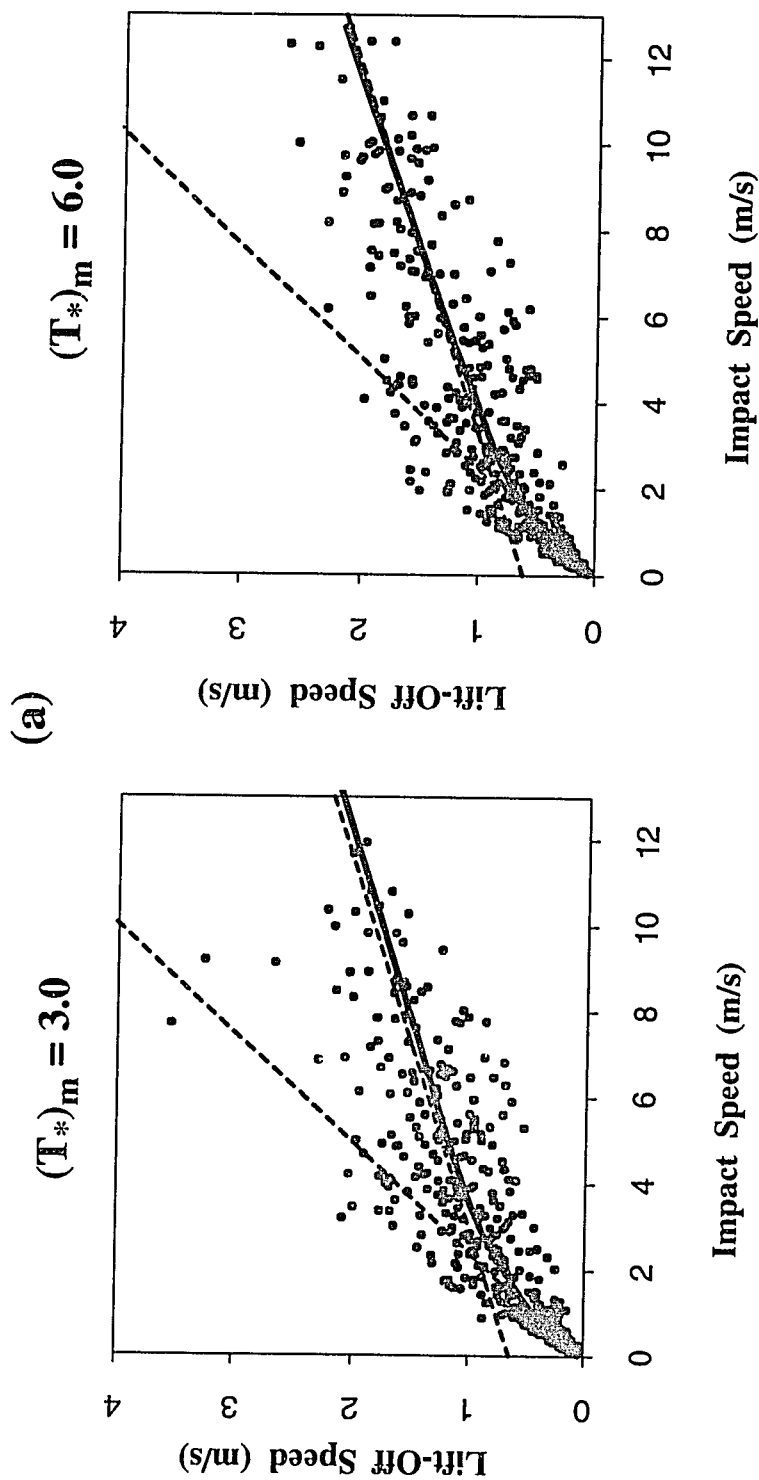


Figure 4.3 Comparison of model-predicted grain impact speeds and lift-off speeds for all particles in the sediment mixture, at two transport stages,  $(T^*)_m = 3.0$  and  $(T^*)_m = 6.0$ . (a) Linear least-squares regression (dashed lines) demonstrates that grains with low impacting and low rebounding speeds (i.e. impact speeds less than 1.0 m/s and lift-off speeds less than about 0.3 m/s) are best fit by a line with differing slope and intercept than the population of grains with higher velocities. The solid line in each graph is the non-linear weighted regression curve that best describes the populations of both low-velocity and higher-velocity grains. Little difference is observed between the two transport stages. For  $(T^*)_m = 3.0$ , the number of grain collisions  $n = 690$ ; for  $(T^*)_m = 6.0$ ,  $n = 507$ .

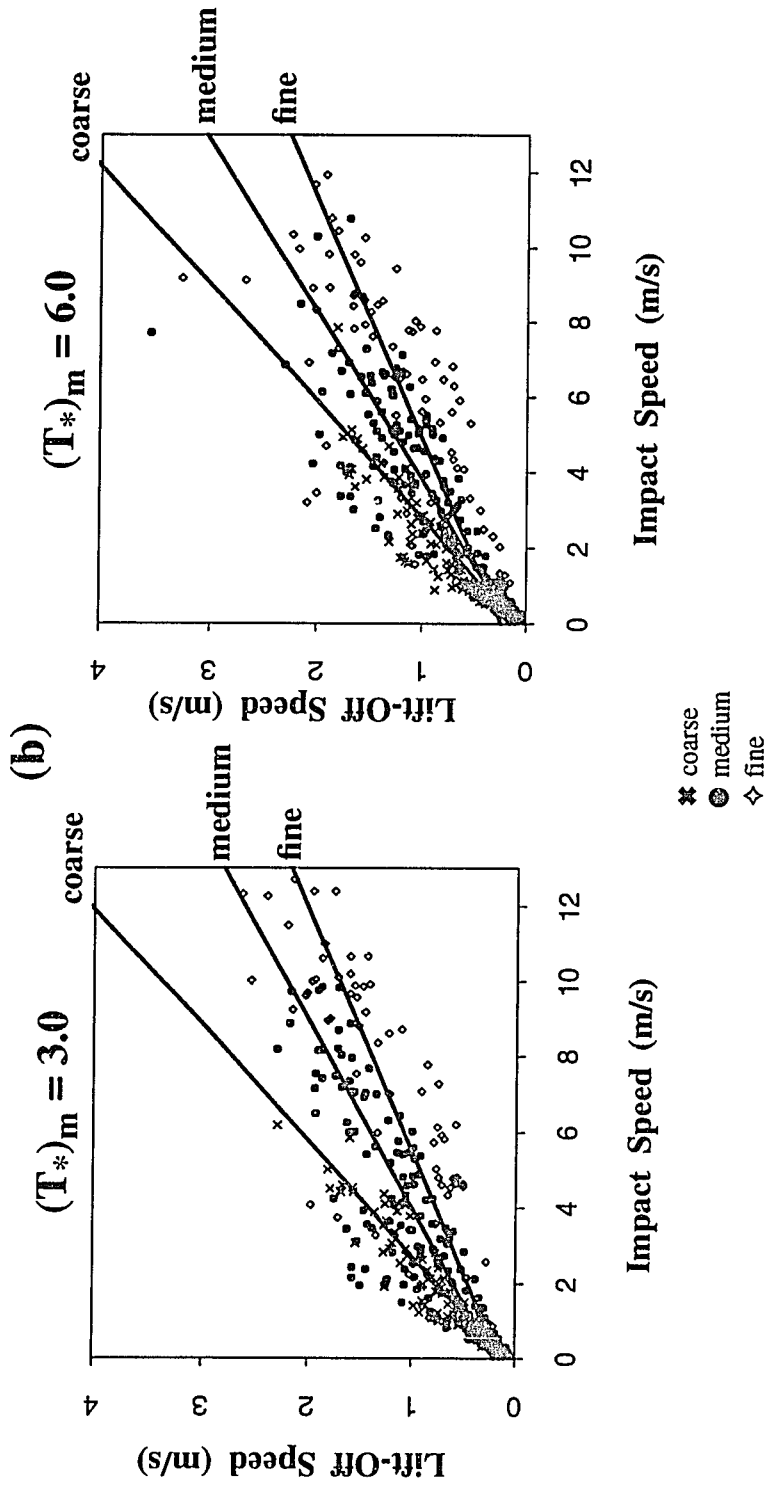


Figure 4.3 continued. Comparison of model-predicted grain impact speeds and lift-off speeds for all particles in a sediment mixture, at two transport stages,  $(T^*)_m = 3.0$  and  $(T^*)_m = 6.0$ . (b) For each transport stage, a linear least-squares fit to the model results for three grain-size fractions in the mixture: coarse ( $D_m \geq 1.0\text{mm}$ ), medium ( $0.5\text{mm} < D_m < 1.0\text{mm}$ ), and fine ( $D_m \leq 0.50\text{mm}$ ). Correlation coefficients for  $(T^*)_m = 3.0$  [and  $(T^*)_m = 6.0$ ] are 0.33 [0.34] for the coarse size fraction, 0.25 [0.23] for the medium size fraction, and 0.20 [0.18] for the fine size fraction.

resents about 25% of the total bedload.

Further decomposition of the point scatter in Figure 4.3a by grain-size fraction shows that the larger grains retain a higher percentage of their impact speed than do the smaller grains. Figure 4.3b plots impact speed versus lift-off speed of the rebounding and ejected grains, for the fine fraction ( $D_m \leq 0.5\text{mm}$ ), medium fraction ( $0.5\text{mm} < D_m < 1.0\text{mm}$ ), and coarse fraction ( $D_m \geq 1.0\text{mm}$ ). Willetts and Rice (1989) conclude, from their collisional experiments with a finer, more well-sorted sand mixture ( $D_{50} \cong 0.35\text{mm}$ ), that rebounding grains, regardless of size, retain about 60% of their impact speed on average. These model results suggest that grains colliding with the mixed-grain bed retain even less than 60% of their pre-collision speed, with values generally ranging from 55% to 15% depending on the geometric characteristics of the collision and the ratio of grain masses involved in the impact. The lift-off velocities of the ejected grains average 15% of the impacting-grain velocities, which compares with the value of 10% obtained from the Willetts and Rice experiments. Correlation coefficients for the size fractions at  $(T^*)_m = 3.0$  are: (1) 0.33 for the coarse fraction [0.34 at  $(T^*)_m = 6.0$ ]; (2) 0.25 for the medium fraction [0.23 at  $(T^*)_m = 6.0$ ]; and 0.20 for the fine fraction [0.18 at  $(T^*)_m = 6.0$ ]. The difference between the empirical and theoretical results for saltating and ejected grains might be due, in part, to the absence in the measured data of low-energy grains which could not be observed clearly in the experiments. Graphs of the empirical results (e.g. McEwan *et al.*, 1992, Fig. 7) indicate that the subset of low-energy grains predicted by the model are missing from the empirical observations. The measured and calculated ratios of impact to lift-off velocities are comparable if the subset of low-energy particles is removed from the latter results.

There appears to be little dependency of the results on transport stage. This might reflect the fact that the momentum extraction by the saltating grains from the airflow scales with transport stage (e.g. Figure 3.8); between the transport stages of  $(T^*)_m = 3.0$  and  $(T^*)_m = 6.0$ , the moving grains must compensate for the near-bed reduction in fluid-shear velocities, so that the maximum grain speeds for each size fraction approach an asymptote at the higher transport stages. This was seen previously with respect to saltation heights (e.g. Figure 3.16).

Model results for continuous saltation sequences across the mixed-size bed demonstrate that



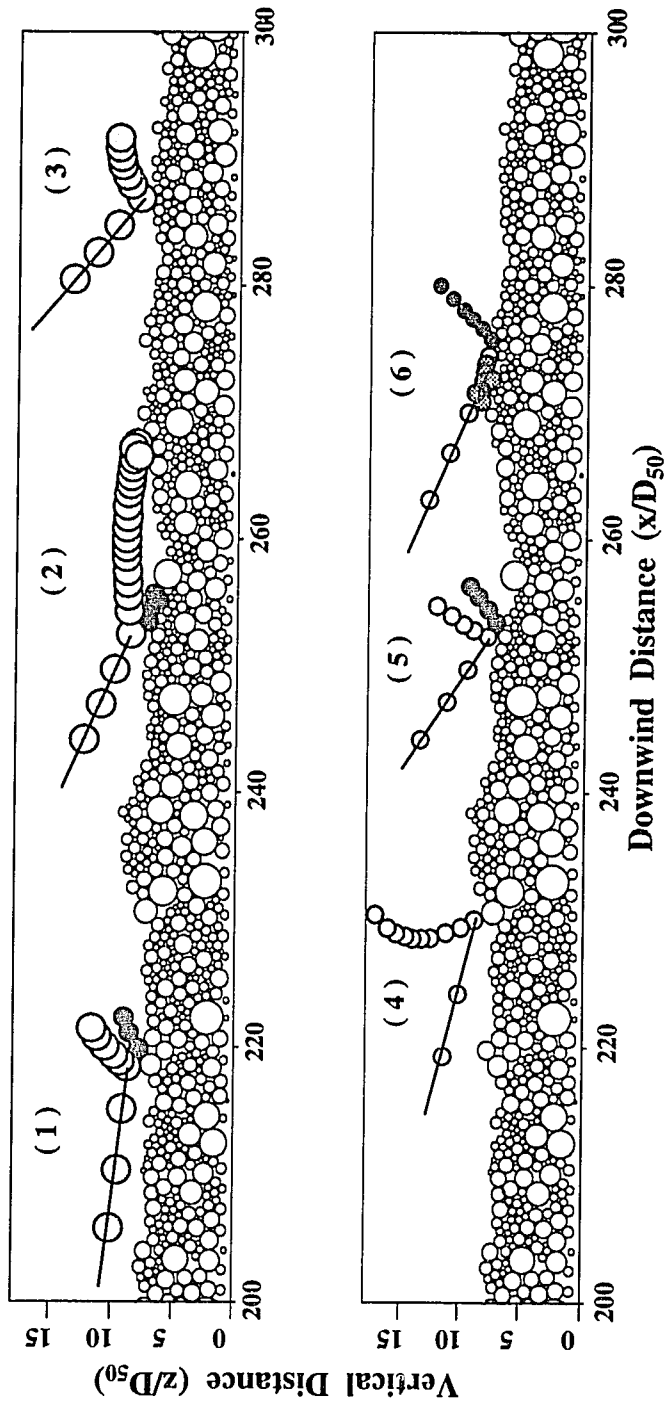


**Figure 4.4** Examples of grain collisions with the mixed-grain-size bed. The upper panel illustrates collision outcomes between a coarse grain ( $D_{90} = 1.5\text{mm}$ ) and particles on a representative bed section. The lower panel shows collisions between a smaller grain ( $D_{40} = 0.50\text{mm}$ ) and particles in the same bed section. Stippled disks are the colliding grains; solid disks are the ejected grains. (1) energetic collision produces grain rebound and ejection of a smaller particle ( $D_m = 0.65\text{mm}$ ). (2) glancing collision with a smaller particle ( $D_m = 0.50\text{mm}$ ) knocks it from its exposed pocket, and it rolls into the downwind bed depression; the colliding grain terminates downwind. (3) collision with the top of small grain drives it further into the bed; the colliding grain rebounds with low velocity. (4) energetic collision with a larger particle results in energetic rebound with no ejection. (5) collision between like-sized particle results in energetic rebound and ejection. (6) collision close to the bed particle's equator ( $D_m = 0.45\text{mm}$ ) sends the impacting grain upwind and the ejected particle downwind; the colliding particle jostles within an upwind depression before terminating (particle movement shown by hatched disks).

particles tend to eject others of their own relative size. Figure 4.4 illustrates some of the more common collision scenarios predicted by the mixed-grain model. The upper diagram in the figure shows three types of collisions between a coarse grain ( $D_{90} = 1.5\text{mm}$ ) and grains of unequal size on the sediment bed at a transport stage of  $(T^*)_m = 3.0$ . The lower diagram contrasts collisions between a small grain ( $D_{40} = 0.50\text{mm}$ ) and particles on the same bed surface. For reference, the saltating grains are represented as stippled disks and the grains they eject as solid disks. Only the portions of the continuous grain trajectories near the bed surface are shown; the direction of the incoming trajectory is given by a curve connecting grain positions computed as a function of time, whereas, the outgoing trajectories are shown by grain position only. Variations in impact angle and speed of the incoming grain, the relative masses of the involved grains, the position of collision across the upper surface of the impacted grain, and the geometry of the bed pocket in which the impacted particle sits create a different collision outcome in each case. In the first case, labelled (1) in Figure 4.4, the coarse grain approaches the bed from upwind at an angle of  $7.2^\circ$  and speed of  $1.74\text{ m/s}$ . It collides with a particle about half its size ( $D_m = 0.65\text{mm}$ ) along its upwind, exposed surface, driving it from the bed. The colliding particle rebounds with approximately a third of its velocity an instant before impact. In the second case (2), the  $D_m = 1.5\text{mm}$  particle strikes a  $D_{40} = 0.50\text{mm}$  close to its upper pole. Perched on the edge of a bed depression, this grain is driven forward and down into the depression. With insufficient momentum necessary to drive it over the coarse, stationary bed particle in its path, the ejected grain jostles in the depression before coming to rest. The glancing collision imparts relatively greater forward velocity to the saltating particle than vertical velocity, so that it rebounds parallel to the bed in the downwind direction and strikes another grain. Having gained little forward momentum in this short hop, the particle loses momentum further through the collision and settles upwind into an adjacent bed pocket. Collision (3) demonstrates the situation in which a large grain strikes one or several fine grains ( $D_{18} = 0.35\text{mm}$ ). Given that very little surface area of a small grain is exposed to the flow, by virtue of its packing configuration with other grains, the top of this bed grain is the only feasible point of collision with the saltating particle. The line connecting the centers of the colliding and impacted grains, hence, is oriented downward from the sediment surface, and the collision drives the smaller

particle into the bed surface, such that it cannot eject into the airstream. Striking the bed with a relatively high impact angle ( $36^\circ$ ) and low impact speed (0.78 m/s), the particle rebounds with low velocity into the flow and executes one more hop before coming to rest. Although coarse grains are more likely to eject grains with a range of masses than are smaller grains, their potential for ejecting grains and rebounding energetically into the flow is greatest when they collide with grains of their own relative mass.

In the second diagram of Figure 4.4, three types of collisions are shown for a grain from the finer tail of the size-frequency distribution ( $D_{40} = 0.50\text{mm}$ ). In collision (4), the grain collides with the upwind surface of a stationary particle twice its size (i.e. the ratio of their masses is  $m_0/m_2 = 0.15$ ) and rebounds in a high trajectory that initially curves upwind before the grain is accelerated downwind by the flow. The relative masses of the grains and the nature of the bed pocket in which the larger grain resides (i.e. partially buried by other surface grains) inhibits motion of the impacted grain. Collision (5) illustrates the energetic collision between the particle and one of identical mass. This is the same particle dislodged by the coarser grain in collision (2); however, in this instance, the point of collision occurs closer to the upwind equator of the bed grain than near its top, so that the momentum impulse transmitted by the incoming grain is oriented more laterally than downward. Therefore, the bed particle launches at a fairly high angle ( $41^\circ$ ) and saltates downwind, as does the rebounding particle. Collision (6) illustrates a frequent outcome, in which the incoming grain strikes near the equator on the upwind side of a stationary particle and rebounds upwind. In this instance, the rebounding grain (i.e. movement shown by hatched disks) collides with another grain forming the lip of an upwind bed depression and ricochets back into the depression before coming to rest. The collision orientation is favorable for ejection of the initially struck grain, which replaces the incoming grain in the saltation layer.

Table 4.1 summarizes the outcomes of 1275 grain collisions at a transport stage of  $(T^*)_m = 3.0$ . The results are given in terms of the percent of grains of a particular size fraction  $D_m$  (rows) ejecting grains from each of six size fractions in the mixture (columns). The statistics include any grain that moves from its bed pocket via collision, regardless of its mode of transport (e.g. rolling vs. saltating). Grains eject other grains their own size in approximately 50% of their collisions

**Table 4.1** Relationship of the size of the saltating grain to the size of the grain it ejects during a collision with the bed surface. For each saltating size fraction (rows), the percentage of grains of each size fraction ejected (columns) is given. Roughly half of the grains ejected by colliding particles of a particular size fraction are of the same relative size (e.g. shaded boxes). For the case of  $D_{50} = 0.70\text{mm}$  and  $(T^*)_m = 3.0$ .

		Size of Ejected Grain (mm)					
Size of Saltating Grain (mm)	$\leq 0.35$	0.35-0.5	0.5 - 0.7	0.7 - 1.0	1.0 - 1.4	$\geq 1.4$	
$\leq 0.35$	50%	45%	5%				
0.35 - 0.5	18%	57%	17%	8%			
0.5 - 0.7		0%	46%	35%	19%		
0.7 - 1.0		10%	15%	55%	10%	10%	
1.0 - 1.4		9%	14%	23%	47%	7%	
$\geq 1.4$		5%	15%	10%	15%	55%	

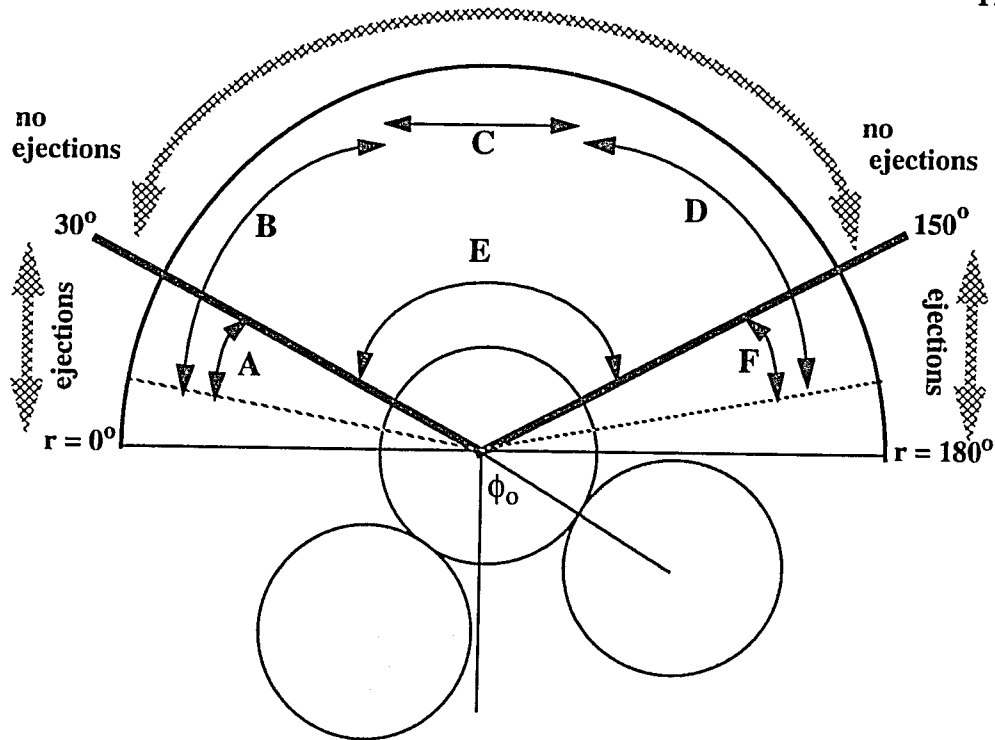
with the bed. The finest fraction ( $D_m \leq 0.35\text{mm}$ ) primarily ejects grains of only the smallest mass but, with a favorable collision geometry, will dislodge particles twice their mass by glancing impacts with a perched bed particle that can be knocked readily from its pocket (e.g. the mass of a 0.35mm grain is  $1.0 \times 10^{-4}$  gm, compared with  $2.0 \times 10^{-4}$  gm for a 0.50mm particle). As the size of the saltating grain increases, the range of ejectable particle sizes spreads, although particles as large as the median grain diameter ( $D_{50} = 0.70\text{mm}$ ) infrequently dislodge particles more than twice their mass. The coarsest fractions (e.g.  $D_m \geq 1.0\text{mm}$ ) dislodge the broadest range of particle sizes. These results reflect the dependency of the components of particle lift-off velocity (e.g. equations 4.16) on the ratio of the incoming mass to the mass of the impacted grain ( $m_0/m_2$ ). The probability of small grains ejecting grains much larger than themselves is reduced by the fact that the mass ratio is much less than unity, whereas the ratio is greater than or equal to unity for the coarsest grain sizes in the mixture. Collisions in which an incoming grain ejects a bed particle more than twice its mass (e.g. the 10% of grains greater than 1.4mm ejected by the  $D_m = 0.7\text{mm}$  fraction) are facilitated greatly by the geometry of the impact; these collisions typically involve grazing collisions with large grains prominently perched in small bed pockets, in which the momentum transfer required to prod the bed particle from its pocket is minimal. On the other hand, the probability of coarse particles dislodging more than a small percentage of the finer grains (e.g. 5% in Table 4.1) is greatly reduced by the fact that the small particles are protected in the interstices between larger grains. Bagnold (1941) witnessed that as the transport stage rises, the likelihood of grains moving others of more disparate size increases, particularly in the case of grains being knocked from exposed positions. The results for a transport stage of  $(T^*)_m = 6.0$  are not appreciably different from those presented for  $(T^*)_m = 3.0$ , however, which suggests that if such events occur, they must happen at higher transport stages than studied here.

Heterogenous sand mixtures affect the mechanics of grain-grain collisions, therefore, in two principal ways. One is by modifying the energetics and momentum of particle lift-off, resulting to large degree from differences in the masses of particles involved in the collision. This observation is not a new one, as it has been discussed conceptually in the literature since Bagnold's (1941) earliest experiments and surmised from transport studies of mixed-size sediments (e.g. Williams,

1964; Gerety and Slingerland, 1983). The other important influence of the particle-size distribution is that it governs the bed-pocket geometries and relative protrusions of the stationary grains and, therefore, the ability of the incoming particle to dislodge bed grains in the direction of the fluid flow. As can be seen in Figure 4.4, the grains most likely to be ejected are those whose upwind surfaces, between their equators and upper poles, are exposed to the flow. On the flat bed, this precludes a fair number of grains from being ejected, until their upwind surfaces are exhumed by the removal of adjacent grains. This observation only applies to moderate flow conditions in which bed cratering does not occur.

Inspection of the geometries of collisions summarized in Table 4.1 suggests that the position of impact most favorable for ejecting a bed particle of roughly the same size as the incoming grain is along the lower portion of the upwind, exposed surface of the grain. This was also observed for model-predicted collisions in uniform-sized sediments. In the latter case, a series of 300 collisions were calculated at three different transport stages  $[(T^*)_m = 3.0, 4.0, 6.0]$ , in which the impact angles, impact speeds, and points of grain contact were allowed to vary between collisions. The outcomes of these grain-grain impacts were analyzed with respect to the position of grain contact. Figure 4.5 describes the range of collisional outcomes for an equidimensional-grain configuration in which the particle angle of repose is  $60^\circ$ , typical of well-sorted, natural sediments. The diagram shows two bed-pocket grains supporting the impacted grain (i.e. "target" grain; colliding grain not shown). Positions of impact ( $r$ ) across the upper hemisphere of the stationary grain range in the downwind direction from  $0^\circ \leq r \leq 180^\circ$ . If sufficiently energetic, impacts occurring in the arc of contact positions  $r \leq 30^\circ$  will eject the target grain (i.e. below the line-of-centers between bed grains formed by the bed-pocket geometry angle  $\phi_o$ ). Similarly, saltating grains that rebound upwind and impact the stationary grain on its downwind side at symmetrically identical positions ( $r \geq 150^\circ$ ), may also eject the target grain. If the point of collision occurs within the range  $30^\circ < r < 150^\circ$ , however, the target particle will not eject. Figure 4.5 also summarizes the ranges of possible outcomes for the colliding (rebounding) grain in terms of the position of contact ( $r$ ) with the bed grain.

In the mixed-grain case, the variability in bed-pocket geometry angles created by the juxta-



- A** Upwind rebound following ejection
- B** Upwind terminations
- C** Downwind terminations (no ejections)
- D** Terminations of upwind-rebounding grains
- E** Rebounds (no ejections)
- F** Terminations of upwind-rebounding grains following ejection of bed particle

**Figure 4.5** Diagram of possible outcomes following a collision between an incoming grain and the equidimensional particles composing the sediment bed. In this two-dimensional configuration, the particle angle of repose  $\phi_0$  is  $60^\circ$ ; impact positions ( $r$ ) between the moving particle and bed grain range in the downwind direction from  $0^\circ \leq r \leq 180^\circ$ . Model calculations show that the incoming grain rarely ejects the bed particle if it strikes anywhere across the grain surface from  $30^\circ \leq r \leq 150^\circ$  (i.e. above the line of centers formed by  $\phi_0$ ). In the range  $0^\circ \leq r \leq 30^\circ$  and  $150^\circ \leq r \leq 180^\circ$ , the bed grain may be ejected by a downwind-saltating grain or upwind-rebounding grain, respectively. Outcomes (labelled A - F) are identified above and occur over the regions of the grain surface as shown.

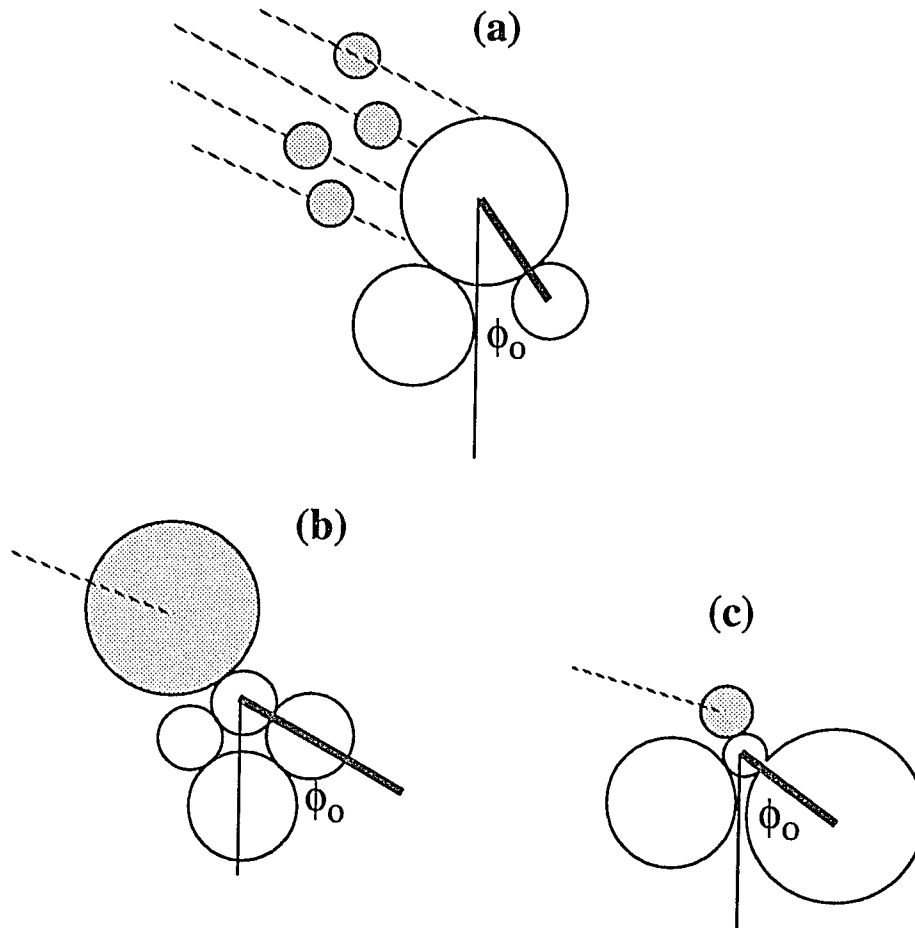


**Figure 4.6** Range of collision possibilities for grains of unequal size. Compared with the range of contact points between equidimensional grains, disparate-sized particles have relatively more opportunity (a), or less potential (b, c), for contacting the surface of a given bed particle. The wider the bed-pocket geometry angle ( $\phi_0$ ), the less surface area of the bed grain is exposed to the incoming particle (stippled) and the lower the potential for a collision to eject the particle. In collision (a), the ejection potential is low, due to the disparity in grain masses, but the range of rebound possibilities is large.



position of grains of disparate size leads to a substantially wider range of collisional outcomes. As shown in Figure 4.6a, the surface area of a bed grain with which an incoming grain may collide is relatively greater for the finer fractions than for the coarser fractions, resulting in a wider array of rebound possibilities. The disparity in particle masses, however, prevents the bed particle from being ejected. Collisions occurring below the equator of the bed grain generally lead to particle terminations in the upwind direction. For coarse grains colliding with smaller particles (Figure 4.6b), the point of collision is narrowed to a small fraction of the upwind surface of the bed grain. As the bed-pocket geometry angle increases, the amount of surface area exposed to the incoming grain decreases, and the potential for ejecting grains decreases (Figure 4.6 c).

Comparisons of collision statistics between the uniform-grain population and the grain mixture demonstrate the degree of variability resulting from the nonuniformity of particle mass and topographic inhomogeneities of the sediment bed in the mixed-grain case. Figures 4.7 through 4.12 plot the predicted impact speeds and angles, lift-off speeds and angles, and hop heights and lengths for a uniform population of  $D = 0.35\text{mm}$  grains saltating over a similar-sized bed, contrasted with statistics for the  $D_{18} = 0.35\text{mm}$  fraction over a mixed-grain bed, in which  $D_{50} = 0.70\text{mm}$ , at a transport stage of  $(T^*)_m = 3.0$ . The same comparison is made for  $D = 0.70\text{mm}$  uniform grains and the  $D_{50} = 0.70\text{mm}$  fraction of the mixture. Statistics were computed in the same manner for the uniform and mixed-grain cases; grains were allowed to hop down a sediment bed until they terminated through unfavorable collision with a bed particle. Results are graphed as the statistical parameter (e.g. impact speed in Figure 4.7) versus the cumulative percent of the number of grains, where 50% signifies the median observation.

These results show that, in general, the  $D_{18} = 0.35\text{mm}$  fraction of the mixture collides more energetically and travels greater distances downwind than similar-sized particles ( $D = 0.35\text{mm}$ ) over a uniform bed. Conversely, the median ( $D_{50} = 0.70\text{mm}$ ) and coarse ( $D_{50} > 0.70\text{mm}$ ) fractions, in general, travel less far and possess lower pre- and post- collision velocities than do their unidimensional counterparts. In Figure 4.7, the  $D_{18} = 0.35\text{mm}$  fraction averages 60% greater maximum impact speeds than the  $D = 0.35\text{mm}$  uniform grains. In contrast, the  $D_{50} = 0.70\text{mm}$  fraction averages about 50% lower maximum impact speeds than the  $D = 0.70\text{mm}$  uniform grains. The

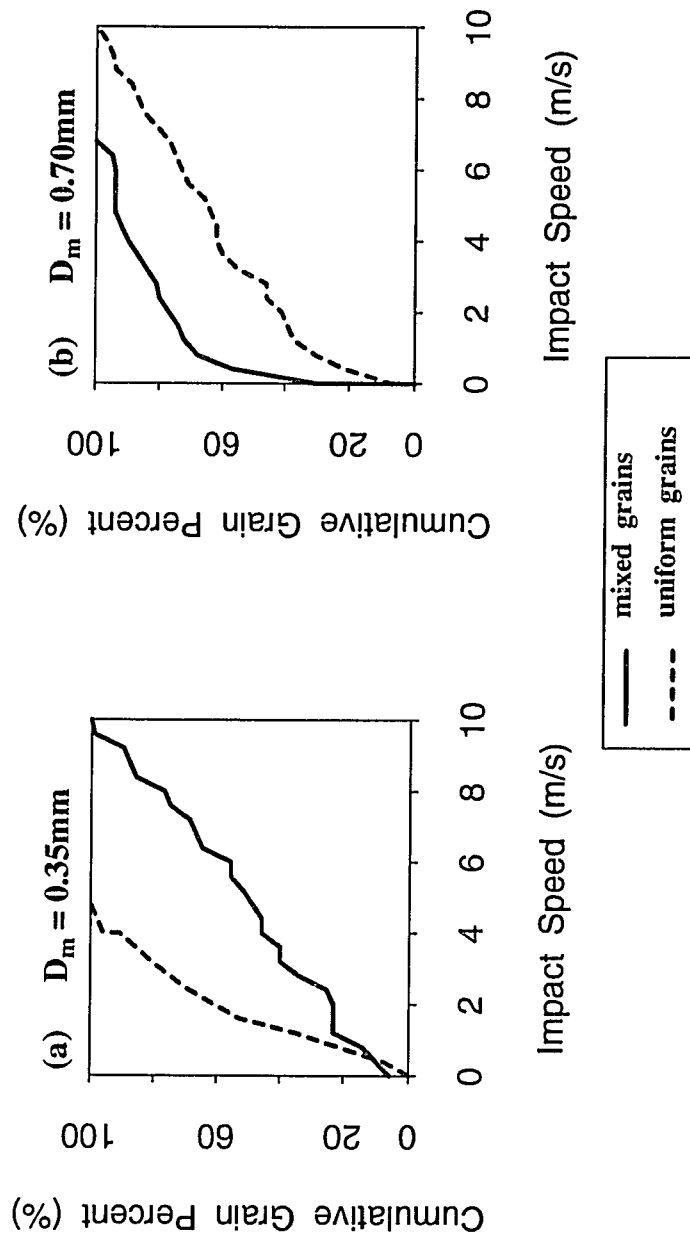


**Figure 4.7** Comparison of impact speeds for grains of size  $D_m$  colliding with a mixed-grain sediment bed ( $D_{50} = 0.70\text{mm}$ ) and with a bed of uniform grain size  $D_m$ . Impact speed (m/s) is plotted against the cumulative percent of grain number. (a) for the case where  $D_m = 0.35\text{mm}$ ,  $(T^*)_m = 3.0$ . (b) for the case where  $D_m = 0.70\text{mm}$ ,  $(T^*)_m = 3.0$ .

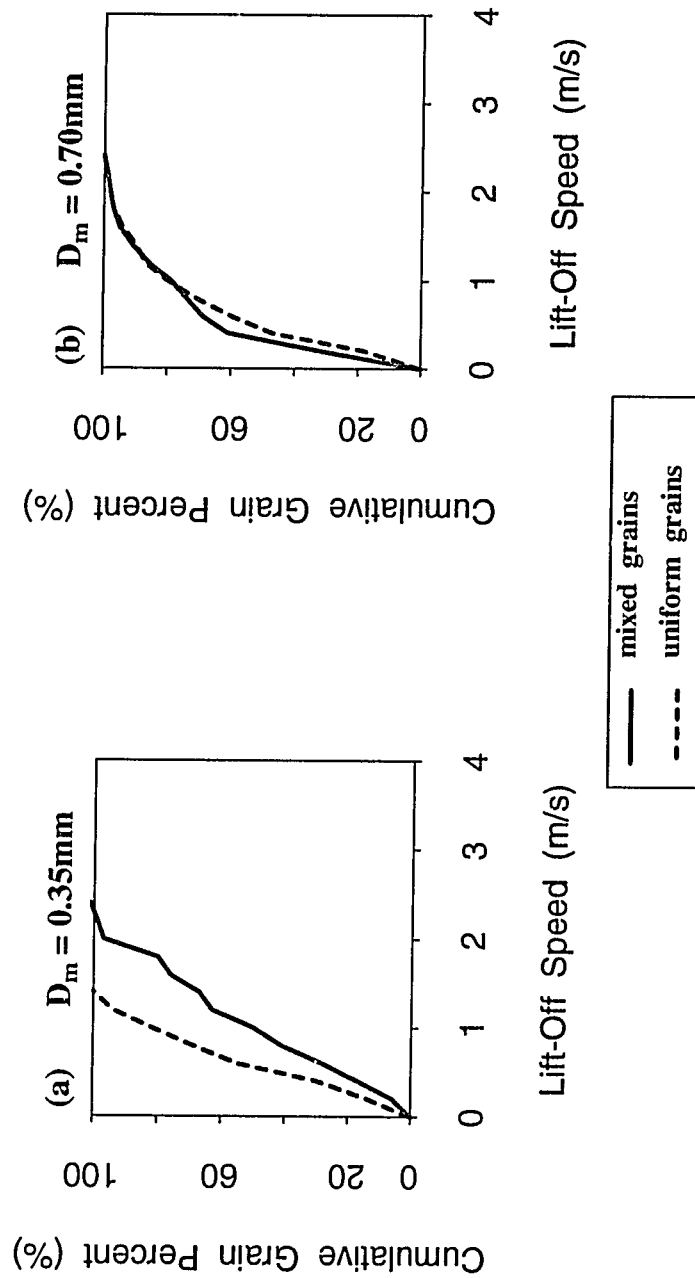


**Figure 4.8** Comparison of lift-off speeds for grains of size  $D_m$  colliding with a mixed-grain sediment bed ( $D_{50} = 0.70\text{mm}$ ) and with a bed of uniform grain size  $D_m$ . Lift-off speed (m/s) is plotted against the cumulative percent of grain number, and includes both rebounding and ejected grains. (a) for the case where  $D_m = 0.35\text{mm}$ ,  $(T^*)_m = 3.0$ . (b) for the case where  $D_m = 0.70\text{mm}$ ,  $(T^*)_m = 3.0$ .

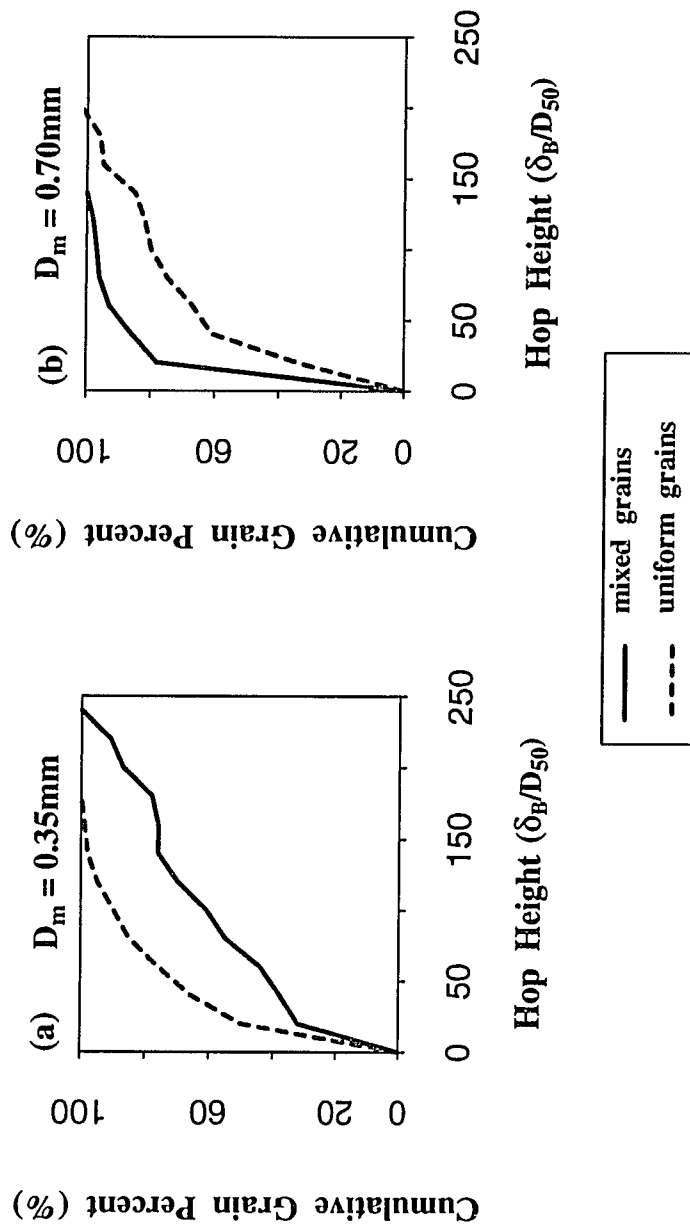


Figure 4.9 Comparison of hop heights for grains of size  $D_m$  colliding with a mixed-grain sediment bed ( $D_{50} = 0.70\text{mm}$ ) and with a bed of uniform grain size  $D_m$ . Trajectory height ( $\delta_B$ ), nondimensionalized by the grain diameter  $D_{50}$ , is plotted against the cumulative percent of grain number. (a) for the case where  $D_m = 0.35\text{mm}$ ,  $(T^*)_m = 3.0$ . (b) for the case where  $D_m = 0.70\text{mm}$ ,  $(T^*)_m = 3.0$ .

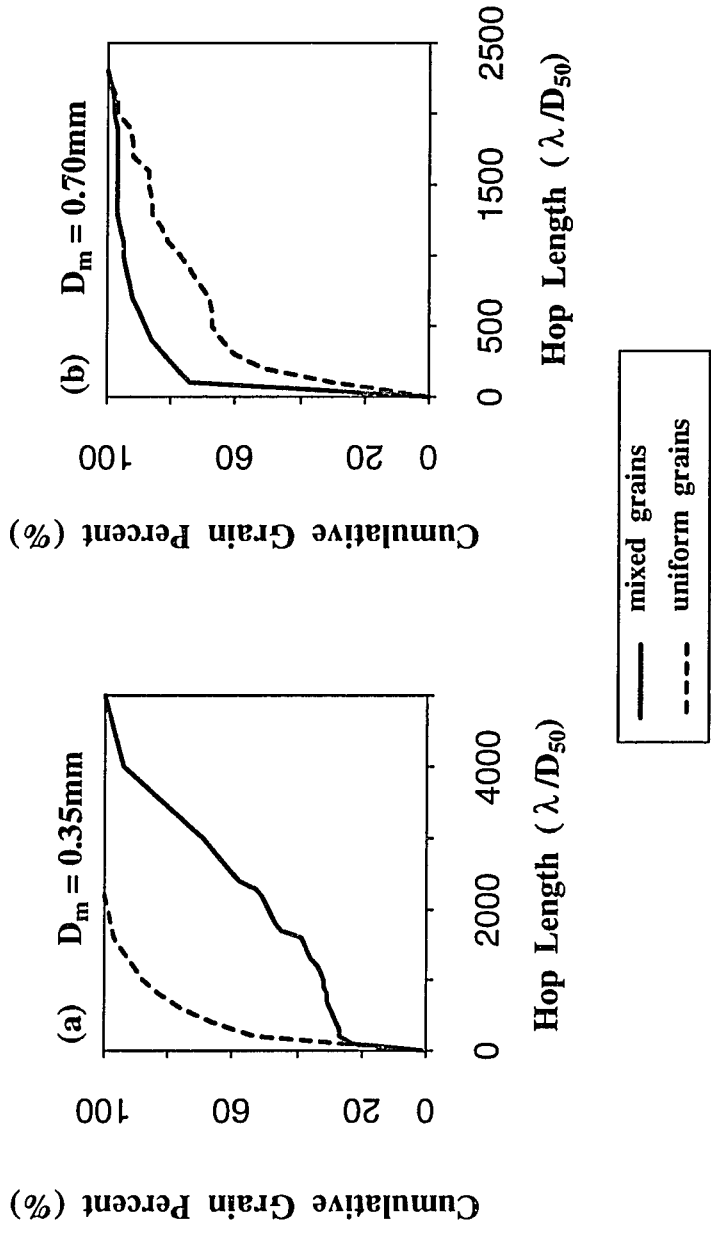
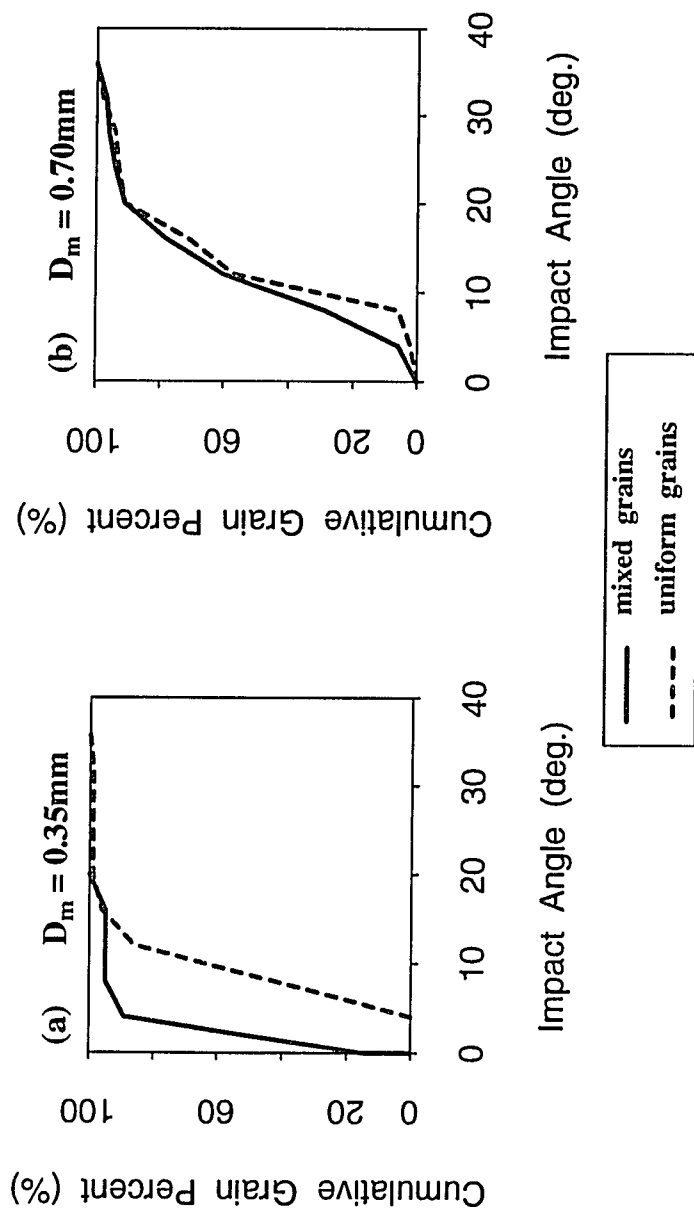
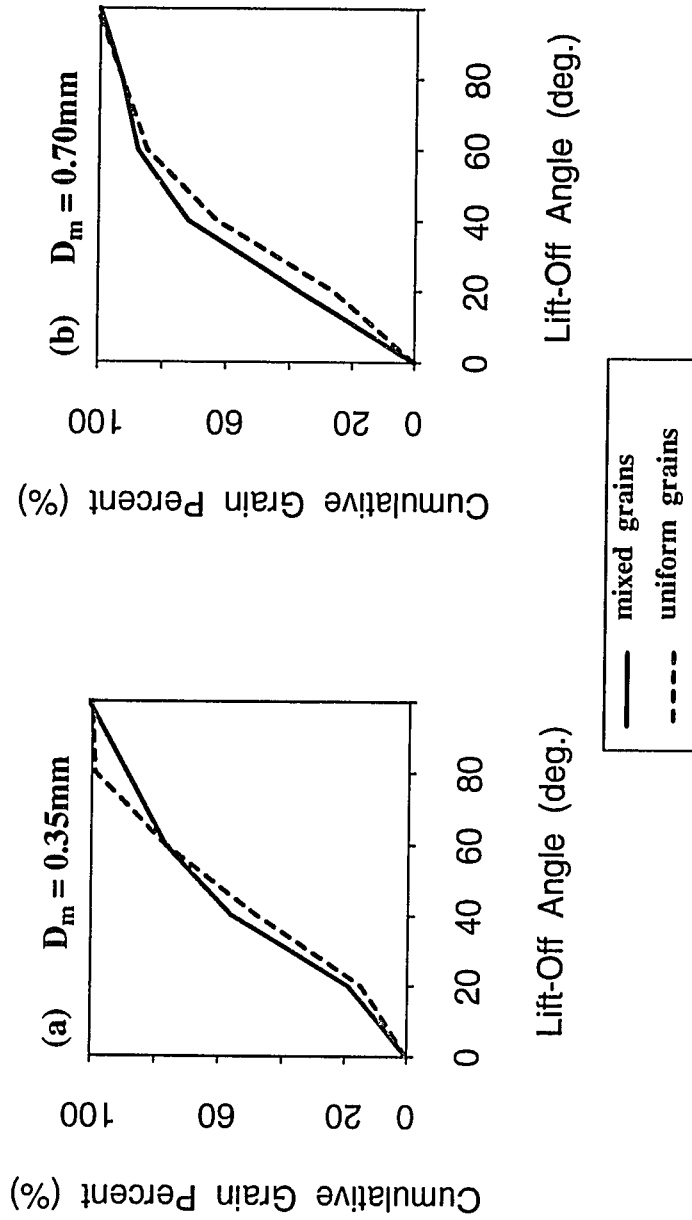


Figure 4.10 Comparison of hop lengths for grains of size  $D_m$  colliding with a mixed-grain sediment bed ( $D_{50} = 0.70\text{mm}$ ) and with a bed of uniform grain size  $D_m$ . Trajectory length ( $\lambda = x$ ), nondimensionalized by the grain diameter  $D_{50}$ , is plotted against the cumulative percent of grain number. (a) for the case where  $D_m = 0.35\text{mm}$ ,  $(T^*)_m = 3.0$ . (b) for the case where  $D_m = 0.70\text{mm}$ ,  $(T^*)_m = 3.0$ .



**Figure 4.11** Comparison of impact angles for grains of size  $D_m$  colliding with a mixed-grain sediment bed ( $D_{50} = 0.70\text{mm}$ ) and with a bed of uniform grain size  $D_m$ . Impact angle (degrees) is plotted against the cumulative percent of grain number. (a) for the case where  $D_m = 0.35\text{mm}$ ,  $(T^*)_m = 3.0$ . (b) for the case where  $D_m = 0.70\text{mm}$ ,  $(T^*)_m = 3.0$ .



**Figure 4.12** Comparison of lift-off angles for grains of size  $D_m$  colliding with a mixed-grain sediment bed ( $D_{50} = 0.70\text{mm}$ ) and with a bed of uniform grain size  $D_m$ . Lift-off angle (degrees) is plotted against the cumulative percent of grain number, and includes both rebounding and ejected grains. (a) for the case where  $D_m = 0.35\text{mm}$ ,  $(T^*)_m = 3.0$ . (b) for the case where  $D_m = 0.70\text{mm}$ ,  $(T^*)_m = 3.0$ .

same trend is seen in the particle lift-off speeds, although the variance is less great (Figure 4.8). Maximum particle hop heights are a factor of two greater for the  $D_{18} = 0.35\text{mm}$  fraction than the  $D = 0.35\text{mm}$  uniform grains, whereas the  $D_{50} = 0.70\text{mm}$  particles in the mixture tend, as a whole, to hop half as high as the uniform-sized grain population (Figure 4.9). As particle trajectory lengths are a function of hop height, the results for hop length are comparable with trajectory height, although for the  $D = D_{50} = 0.70\text{mm}$  grains, the maximum grain-trajectory length appears to be similar between the two cases (Figure 4.10). The model predicts that the long trajectories of the energetically saltating grains tend to have lower angles of approach to the bed than do shorter saltations in which the grain rises from the bed and returns abruptly without being accelerated appreciably in the downwind direction. Higher jumps lead to greater particle acceleration away from the bed, which promotes greater particle speeds, longer trajectories, and lower angles of approach with the bed. Hence, the  $D_{18} = 0.35\text{mm}$  particles in the mixture average lower impact angles than do the uniform grains because approximately 50% of the grains are travelling greater distances downwind (Figure 4.10). Figure 4.11 demonstrates that the difference in particle impact angles is relatively greater for the  $D_{18} = 0.35\text{mm}$  fraction compared with the  $D = 0.35\text{mm}$  uniform grains, than for the  $D_{50} = 0.70\text{mm}$  fraction compared with the  $D = 0.70\text{mm}$  uniform grains. In the latter case, the impact angles are nearly comparable between the mixed and uniform grains, because the hop lengths of the particles are more identical. Finally, the grain lift-off angles of the mixed-size and uniform grains (Figure 4.12) demonstrate the same range of values, although for the  $D_{18} = 0.35\text{mm}$  grains within the mixture, a smaller percentage of the grains achieve high launch angles above about  $60^\circ$ . Lift-off angles of the  $D_{50} = 0.70\text{mm}$  fraction are more nearly identical to the  $D = 0.70\text{mm}$  uniform grains, as were the lift-off speeds. Similar analyses conducted with coarser particles (e.g.  $D_{86} = D = 1.4\text{mm}$ ) suggest that the grains of the mixture are even less energetic by comparison than observed in the  $D = D_{50} = 0.70\text{mm}$  case.

Particles saltating over a mixed-grain bed, therefore, exhibit considerably different collisional histories than is the case for grains saltating over a uniform-sized bed. The variance increases as the ratio of the particle size to the characteristic bed-particle size (i.e.  $D_m/D_{50}$ ) drops below about 0.75 or rises above about 1.25 for the sediment mixtures used in this analysis. The



$D_{18} = 0.35\text{mm}$  grains in the mixture may achieve higher saltation trajectories, and hence greater impact speeds, than  $D = 0.35\text{mm}$  grains on a uniform bed because of their access to a greater range of collision sites along the exposed surfaces of the bed grains than is possible for a similar-sized grain colliding with an irregular array of uniform particles. Also, fine grains primarily collide with particles larger than themselves, which they are incapable of ejecting, whereas particles of the same diameter on a uniform bed are more likely to expend energy ejecting particles from the surface. The median fraction of the mixture behaves more similarly to the uniform-size population, because the bed surface is dominated by particles of that fraction, and the collisional geometries are more comparable to that of uniform granular arrays. The coarsest particles of the mixture, on the other hand, primarily collide with particles smaller than themselves. The potential for head-on collisions of a coarse grain with the upwind side of bed particles, which are the most favorable for returning saltating grains at high lift-off angles into the flow, are greatly reduced and glancing collisions with the uppermost surfaces of bed grains are the more common occurrence (e.g. Figure 4.6b) with energetically saltating coarse grains.

Bedload-transport experiments with grain mixtures have shown that particle trajectory heights are a function of grain size (e.g. Williams, 1964; Gerety and Slingerland, 1983) and that fine fractions contain the most energetic grains within a mixture (e.g. Willetts and Rice, 1985a). Model predictions of particle behavior for discrete size fractions within the mixture are consistent with these findings and, furthermore, permit quantitative analysis of the differences in collision mechanics between size fractions. Figures 4.13 through 4.15 show the range of variation in model-derived impact speeds and angles, lift-off speeds and angles, and hop trajectories between three size fractions,  $D_{18} = 0.35\text{mm}$ ,  $D_{50} = 0.70\text{mm}$ , and  $D_{86} = 1.4\text{mm}$ , at a transport stage of  $(T^*)_m = 3.0$ . Grains of the coarsest fraction approach the bed with a maximum of 25% less impact velocity than the median fraction and 75% less velocity than the finest fraction (Figure 4.13a). Because saltating coarse grains are less energetic on average than fine grains, due to inertial forces and the nature of their collisions with the bed, they tend to travel closer to the sediment surface, where they are accelerated relatively less by the fluid. The decreasing trend in mean particle velocity with increasing grain mass also has been measured in radioactive-tracer experiments with grains of dif-

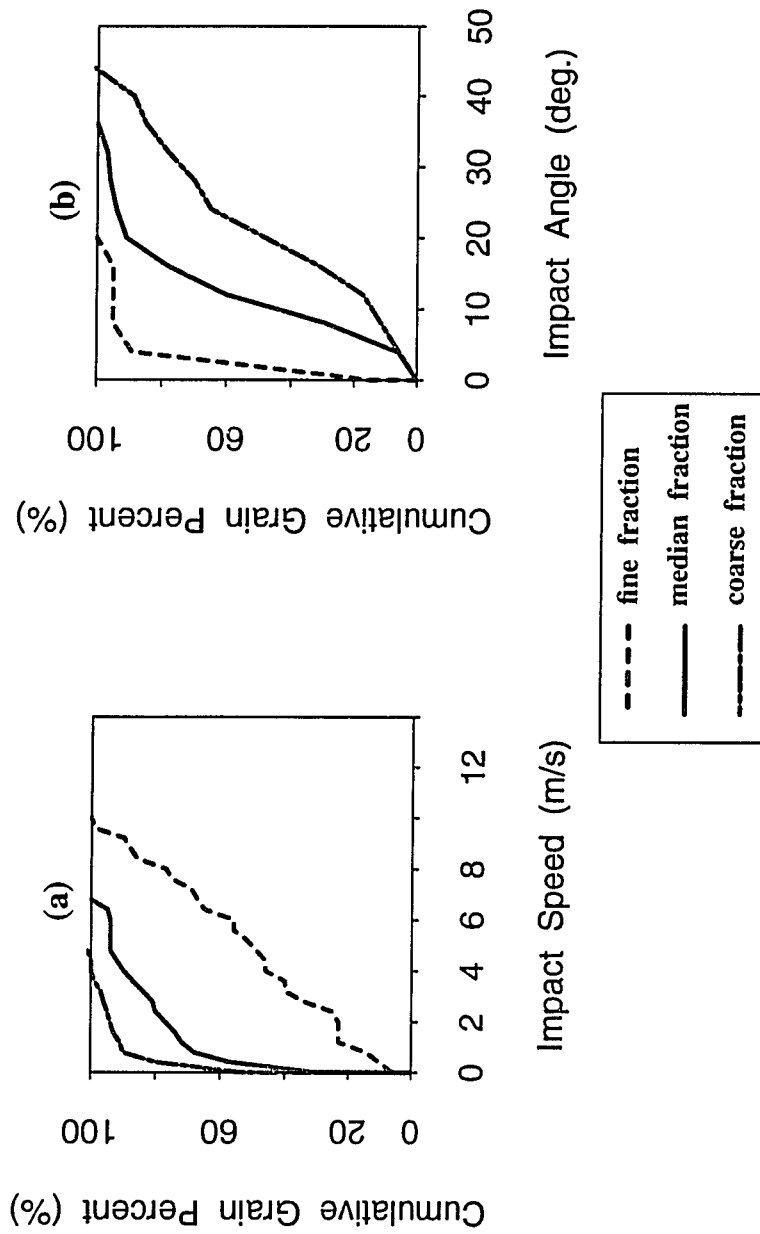


**Figure 4.13** Comparison of impact speeds and angles for three size fractions in the sediment mixture: fine fraction ( $D_{18} = 0.35\text{mm}$ ), median fraction ( $D_{50} = 0.70\text{mm}$ ), and coarse fraction ( $D_{86} = 1.4\text{mm}$ ). (a) impact speed (m/s) versus cumulative percent of grain number. (b) impact angle (degrees) versus cumulative percent of grain number. Transport stage  $(T^*)_m = 3.0$ .

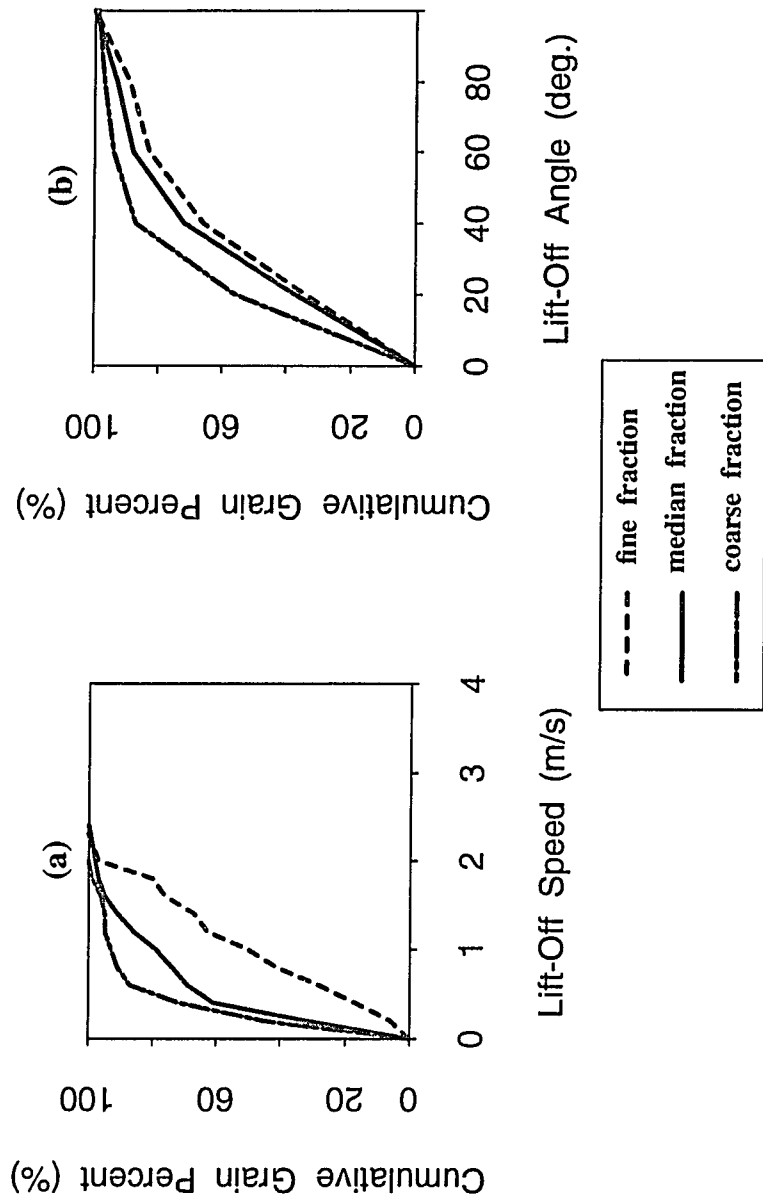


**Figure 4.14** Comparison of lift-off speeds and angles for three size fractions in the sediment mixture: fine fraction ( $D_{18} = 0.35\text{mm}$ ), median fraction ( $D_{50} = 0.70\text{mm}$ ), and coarse fraction ( $D_{86} = 1.4\text{mm}$ ). (a) lift-off speed (m/s) versus cumulative percent of grain number. (b) lift-off angle (degrees) versus cumulative percent of grain number; includes both rebounding and ejected grains. Transport stage  $(T^*)_m = 3.0$ .

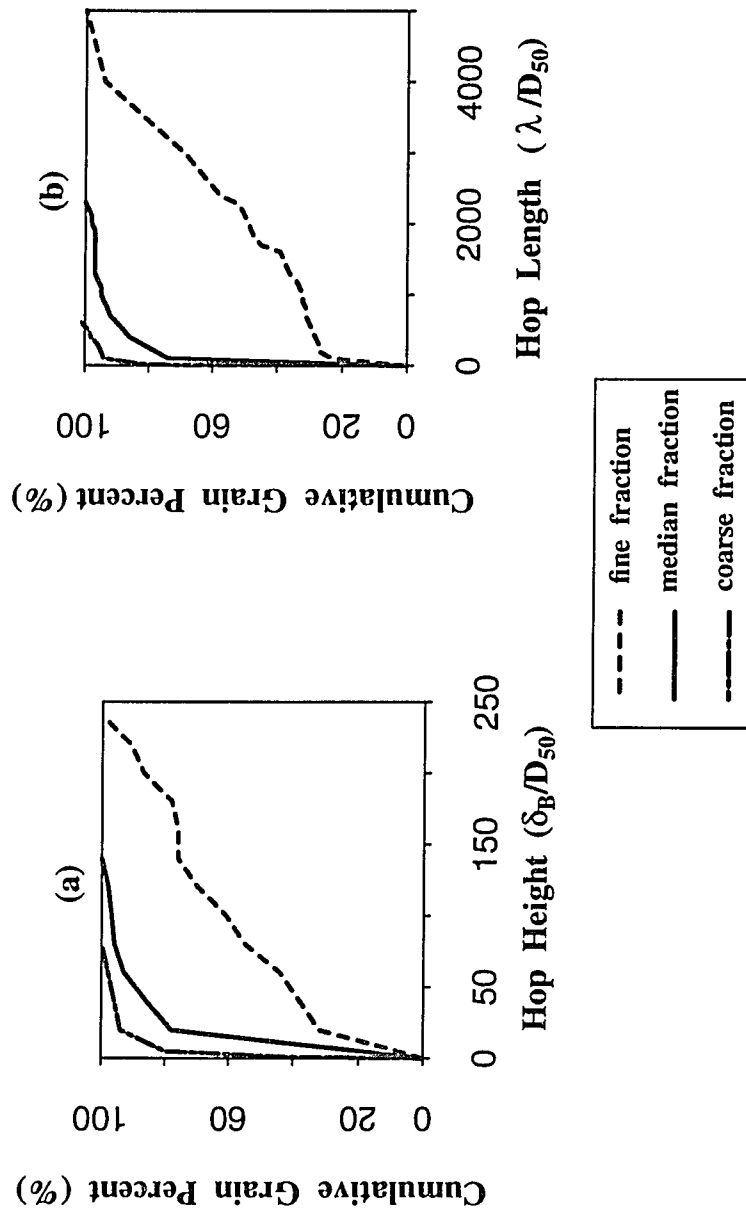


**Figure 4.15** Comparison of grain hop heights and lengths for three size fractions in the sediment mixture: fine fraction ( $D_{18} = 0.35\text{mm}$ ), median fraction ( $D_{50} = 0.70\text{mm}$ ), and coarse fraction ( $D_{86} = 1.4\text{mm}$ ). (a) hop height ( $\delta_B$ ), nondimensionalized by  $D_{50}$ , versus cumulative percent of grain number. (b) hop length ( $\lambda$ ), nondimensionalized by  $D_{50}$ , versus cumulative percent of grain number. Transport stage  $(T^*)_{in} = 3.0$ .

ferent mass by Barndorff-Nielsen *et al.* (1985b). Consequently, coarse grains follow shorter trajectories whose approach angles are steeper than those of the high-energy, long-trajectory saltations (e.g. Figure 4.2b, compared with Figure 4.2a). Thus, the range of impact angles for the coarse fraction is substantially greater than those of the median and fine fractions (Figure 4.13b). The average decrease in impact angle with decreasing grain size similarly has been observed from photographs of the trajectories of natural sands and experimental spheres (e.g. Bagnold, 1941; Chepil, 1961; Sharp, 1963; White and Schulz, 1977; Nalpanis, 1985; Willetts and Rice, 1985a).

As the impact angle decreases, the incoming grain is more likely to collide with the upwind surface of an exposed bed grain and rebound at a higher angle from the horizontal into the flow. As the smaller grains on average possess smaller impact angles, access relatively more of the bed surface area, and arrive with higher impact velocities than the coarse grains, a greater percentage rebound with high lift-off velocities (Figure 4.14a). Given the variability in collision outcomes with the mixed-grain bed, however, the range of lift-off speeds is not nearly as great as that of the impact speeds. A greater percentage of the coarse grains lift off with lower velocity than the other fractions. Because coarse grains primarily strike grains of similar or smaller mass, however, they tend to retain a greater percentage of their impact velocity (e.g. Figure 4.3b) than do fine grains hitting larger particles, such that the sediment bed moderates, to a degree, the differences in mean particle lift-off velocity between grain sizes. The three fractions each have a few stray grains achieving the same maximum lift-off speed; in each instance, they resulted from an energetic particle colliding with a grain of approximately the same mass. The lift-off angles (Figure 4.14b) reflect the same trend, in which a smaller percentage of the  $D_{86} = 1.40\text{mm}$  grains achieve the higher lift-off angles, with the exception of the few energetic rebounds between like-sized grains. In addition, as the coarse grains tend to exhibit more glancing collisions than the other fractions, their lift-off angles are expected to be skewed toward the lower values.

The larger moving particles travel less far, on average, into the airstream because of their lower mean lift-off velocities and angles, and their greater mass. Consequently, maximum hop heights are approximately half those of the median fraction and three times less than trajectory heights of the fine fraction (Figure 4.15a). An even greater range in hop lengths between the

coarse and fine fractions is predicted (Figure 4.15b), with the fine grains averaging longer hops. Calculated saltation trajectories are consistent with wind-tunnel and field observations of saltation trajectories in mixed-size sediments (e.g. White and Schulz, 1977; De Ploey, 1980; Draga, 1983).

An analysis of the number of hops made by each grain transported downwind (Figure 4.16) shows that finer grains average about 30% fewer hops per sequence than the median fraction and 60% fewer hops than coarse grains; the majority of fine grains execute less than five hops before terminating on the bed surface, whereas coarse grains tend to make closer to twenty hops per sequence. The difference relates to the morphology of the bed surface. Just as small grains can rebound more readily than coarse ones from collisions with particles situated in bed depressions, they may also become trapped by these depressions. The most common method of grain trapping predicted by the model is for particles to strike at a low position on the upwind side of a grain bordering a bed depression, rebound upwind at an almost horizontal angle, strike the upwind side of the hollow, and jostle within its confines for some time until all particle momentum is dissipated (e.g. collision (6) in Figure 4.4). Conversely, a coarse grain is less likely to be captured by particle-scale bed depressions due to its relative size, and it will continue to hop or roll, if sufficiently energetic, until it lodges against a particle or cluster of particles in a stable bed-geometry arrangement. The deposition of coarse grains on the surface creates local obstructions on the bed surface, which trap additional particles. If allowed to run forward in time, the model shows that these coarse grains begin to trap other coarse grains, creating local patches of coarsened bed surface, while the bed interstices fill with the finer grains. This mechanical trapping of particles by bed irregularities may lead to the development of bed coarsening, local surface armoring, and bedform instabilities, as has been described from field and wind-tunnel investigations of bed evolution (e.g. Sharp, 1963; Ellwood *et al.*, 1975; Schenk, 1983).

Model predictions of the total distance travelled per hop sequence by the fine ( $D_m \leq 0.50\text{mm}$ ), medium ( $0.50\text{mm} < D_m < 1.0\text{mm}$ ), and coarse ( $D_m \geq 1.0\text{mm}$ ) fractions of the mixture indicate that the majority of fine particles travel farther than grains from the coarser size fractions. Figure 4.17 shows the total distance travelled ( $x/D_{50}$ ) versus cumulative percent of grain number for each fraction, for transport stages  $(T^*)_m = 3.0$  and  $(T^*)_m = 6.0$ . Although the small grains aver-

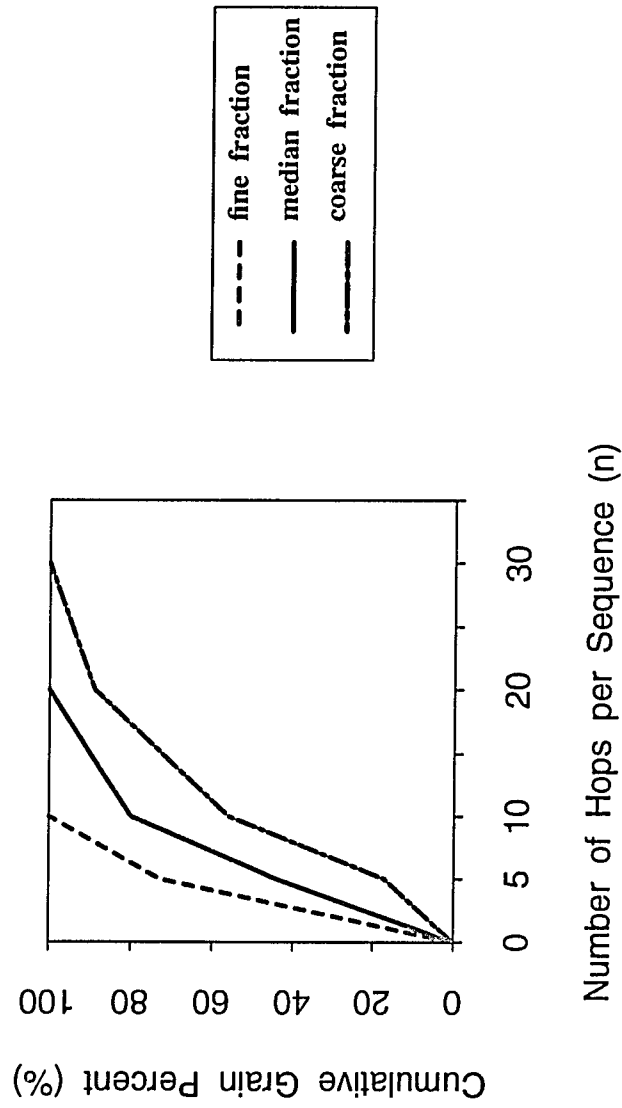


**Figure 4.16** Comparison of the number of continuous trajectories per hop sequence, for three size fractions in the sediment mixture: fine fraction ( $D_{18} = 0.35\text{mm}$ ), median fraction ( $D_{50} = 0.70\text{mm}$ ), and coarse fraction ( $D_{86} = 1.4\text{mm}$ ). A grain that comes to rest temporarily, before being remobilized downwind through another collision, is considered to execute several hop sequences. Transport stage  $(T^*)_m = 3.0$ .

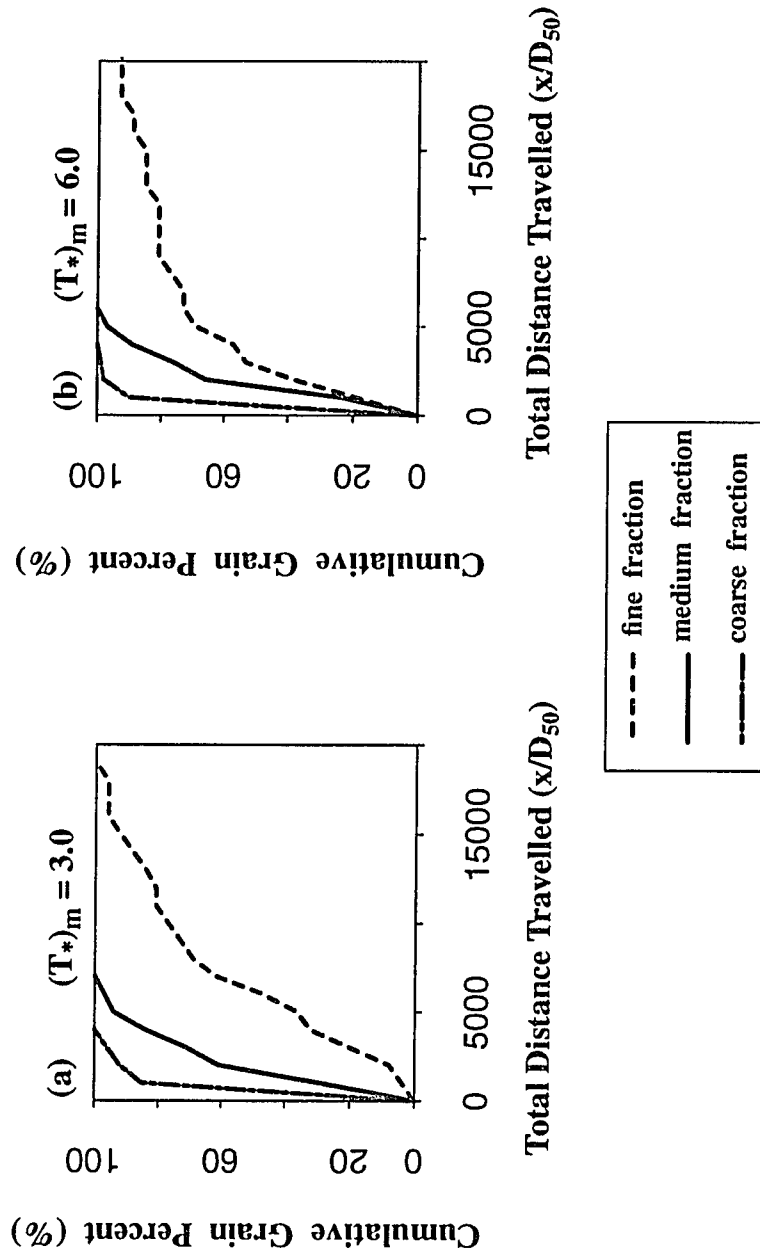


Figure 4.17 Comparison of the total distance travelled by each grain, for three size fractions in the sediment mixture: fine fraction ( $D_m \leq 0.50\text{mm}$ ), medium fraction ( $0.50\text{mm} < D_m < 1.0\text{mm}$ ), and coarse fraction ( $D_m \geq 1.0\text{mm}$ ). Plotted as the total downwind distance ( $x$ ) travelled, nondimensionalized by the median grain diameter ( $D_{50}$ ). (a) for a transport stage of  $(T^*)_m = 3.0$ . (b) for a transport stage of  $(T^*)_m = 6.0$ .



age less than five hops per sequence, their very long saltation trajectories relative to those of the coarser fractions place them almost five times farther downwind, on average, than coarse grains saltating from the same origin. The maximum distance travelled by the 100th percentile of the fine fraction is almost an order of magnitude greater than the coarse fraction. These results have some backing in the literature. In wind-tunnel tracer experiments using dyed sand, Willetts and Rice (1985b) found that particles collected in an end trap tended toward the finer size fractions, although they expressed some reservations concerning their experimental design, largely related to the length of their wind tunnel and the ability to produce a steady-state saltating condition.

Analysis of the variation in collision statistics for individual size fractions as a function of increasing transport stage yields no clear trends, although it appears that the maximum impact and rebound speeds, and maximum hop heights and lengths, increase with rising transport stage. Figure 4.18 shows, for the  $D_{50} = 0.70\text{mm}$  fraction, the impact speeds and lift-off speeds, as a function of the cumulative percent of grain number, for the transport stages of  $(T^*)_m = 1.5, 3.0, \text{ and } 6.0$ . It appears that the 80th percentile of grains average roughly comparable particle speeds at impact and take-off, and that the primary variation in collisional dynamics occurs for the remaining 20% of particles which become relatively more energetic with increasing boundary shear stresses.

### 4.3 Comparison with measured statistics

The high-precision, detailed experiments of Willetts and Rice (1985a, 1986, 1989) provide one of the only published data sets of collision statistics for grain mixtures, in which the observations were recorded by size fraction. Given that the numerical collision algorithm predicts measurable variations in the collision behavior of different grain sizes within a mixture, it is important to test the model results by size fraction.

Willetts and Rice (1985a) obtained collision data in a wind tunnel by filming the grain-bed interactions between particles of a particular size fraction and a sediment bed composed of all sizes in the mixture. Sands introduced from each of three size fractions were allowed to saltate once or twice across an immobile, roughened surface before colliding with a tray of sand; the grains were introduced a few at a time so that high-speed photographs could be made of collisions in the sand

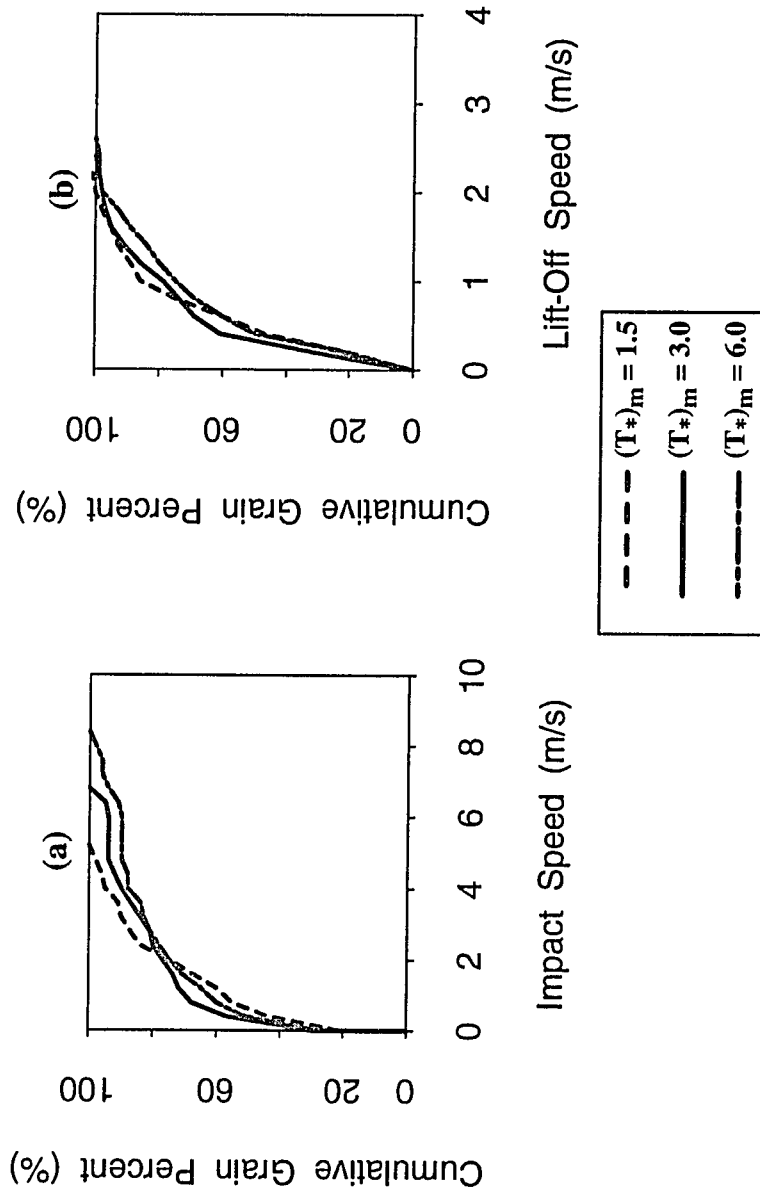


**Figure 4.18** Comparison of impact speeds and lift-off speeds for the  $D_{50}$  size fraction of the mixture, at three transport stages:  $(T^*)_m = 1.5$ ,  $(T^*)_m = 3.0$ , and  $(T^*)_m = 6.0$ . (a) impact speed (m/s) versus cumulative percent of grain number. (b) lift-off speed (m/s) versus cumulative percent of grain number; includes both rebounding and ejected grains.

tray without a dense concentration of saltating grains obscuring the field of view. Their experimental sands were segregated into three fractions: coarse ( $0.35\text{mm} < D_m < 0.60\text{mm}$ ), medium ( $0.25\text{mm} < D_m < 0.35\text{mm}$ ), and fine ( $0.15\text{mm} < D_m < 0.25\text{mm}$ ). Information obtained for each size fraction from these experiments included particle impact speed and angle, rebound speed and angle, and the lift-off angles and speeds of initially stationary particles ejected from the bed by impact. Willetts and Rice define a dimensionless rebound velocity, which is the ratio of the grain impact velocity to its rebound velocity, and a dimensionless ejection velocity, which is the ratio of the grain impact velocity to the lift-off velocities of grains ejected by the collision. Their experiments were conducted at an approximate transport stage of  $(T^*)_m = 1.5$  (i.e.  $u_* = 3.96 \times 10^{-1} \text{ m/s}$ ).

For the comparison, sediment-transport calculations were made at the same transport stage with a sediment mixture of approximately the same grain-size frequency distribution. A computer-generated sediment bed composed of the Great Sand Dunes mixture (e.g. Figure 2.1) was employed, and a steady-state population of moving grains was achieved in the manner described in Chapter 3. To compile the model-derived statistics, the collision predictions are divided, similar to the experiments, into a coarse fraction ( $0.30\text{mm} < D_m < 0.50\text{mm}$ ), medium fraction ( $0.23\text{mm} < D_m < 0.30\text{mm}$ ), and fine fraction ( $0.17\text{mm} < D_m < 0.23\text{mm}$ ), where  $D_{16} = 0.17\text{mm}$ ,  $D_{50} = 0.23\text{mm}$ , and  $D_{84} = 0.30\text{mm}$ .

Table 4.2 compares the experimental and predicted values for the collision variables by the mean and standard deviation of the sample. Values for the two cases are of similar order of magnitude (i.e. within a factor of two) and show the same relative trends with decreasing grain size, i.e. a slight increase in the mean grain impact speed, decreases in the impact angle and the dimensionless rebound velocity, and increase in the rebound angle. In addition, predicted mean ejection angles are greatest for the medium fraction, and the dimensionless ejection velocity appears not to vary substantially between fractions in either the measured or numerically derived samples. The model predicts mean impact velocities, for all three fractions, that are about 30% lower than the empirical values, mean dimensionless rebound velocities that are about 35% lower, and mean dimensionless ejection velocities that are slightly higher. In addition, the rebound and ejection angles are 20% to 40% lower.

**Table 4.2** Comparison of model-derived collision statistics with measurements of Willetts and Rice (1985a, 1989). Values of the collision variables are given as the mean and standard deviation. The experimental sand population is divided into a coarse fraction ( $0.35\text{mm} < D_m < 0.60\text{mm}$ ), medium fraction ( $0.25\text{mm} < D_m < 0.35\text{mm}$ ), and fine fraction ( $0.15\text{mm} < D_m < 0.25\text{mm}$ ). For comparison, a sediment bed constructed from the Great Sand Dunes size-frequency distribution (i.e. Figure 2.1) is similarly divided into a coarse fraction ( $0.30\text{mm} < D_m < 0.5\text{mm}$ ), medium fraction ( $0.23\text{mm} < D_m < 0.30\text{mm}$ ), and fine fraction ( $0.17\text{mm} < D_m < 0.23\text{mm}$ ). The dimensionless rebound velocity is the ratio of the impact to rebound velocities.

	Size Fraction	Sample Size	Impact Speed (m/s)	Impact Angle (deg.)	Dimensionless Rebound Velocity	Rebound Angle (deg.)
Willetts and Rice data	coarse grains	56	$3.38 \pm 0.89$	$12.7 \pm 5.1$	$0.63 \pm 0.16$	$19.1 \pm 13.0$
	medium grains	98	$3.56 \pm 0.94$	$11.7 \pm 5.2$	$0.61 \pm 0.14$	$24.9 \pm 14.2$
	fine grains	80	$3.61 \pm 1.22$	$9.5 \pm 4.6$	$0.57 \pm 0.19$	$38.8 \pm 25.8$
mixed-grain model	coarse grains	113	$2.43 \pm 1.72$	$10.12 \pm 2.29$	$0.41 \pm 0.23$	$14.72 \pm 12.29$
	medium grains	229	$2.45 \pm 1.10$	$9.14 \pm 2.19$	$0.38 \pm 0.20$	$20.05 \pm 16.00$
	fine grains	110	$2.47 \pm 1.90$	$8.81 \pm 7.63$	$0.31 \pm 0.19$	$26.57 \pm 20.89$

**Table 4.2 continued.** The dimensionless ejection velocity is the ratio of the impact velocity of the incoming grain to the lift-off velocity of the ejected particle.

	Size Fraction	Sample Size	Dimensionless Ejection Velocity	Ejection Angle (deg.)
Willetts and Rice data	coarse grains	56	0.11	$50.2 \pm 43.5$
	medium grains	98	0.10	$53.5 \pm 43.9$
	fine grains	80	0.09	$46.2 \pm 36.5$
mixed-grain model	coarse grains	113	$0.18 \pm 0.07$	$31.14 \pm 16.16$
	medium grains	229	$0.19 \pm 0.09$	$38.31 \pm 23.69$
	fine grains	110	$0.18 \pm 0.05$	$37.07 \pm 14.12$

Possible explanations for the differences between the measured and predicted statistics include the fact that the sand mixtures are not identical; the wind-tunnel sample has a slightly broader range of grain sizes than the Great Sand Dunes sands. The higher predicted ejection speeds and lower ejection angles might be a result of the model constraint that only one ejection occurs per collision. Willetts and Rice recorded up to ten ejections during a single collision and, consequently, their ejection statistics include the collection of ejecta with very low velocities that distribute from the collision site over a broad range in angles with the horizontal. On the other hand, the model predicts a broader range in impact and rebound velocities, and a population of low-energy rebounding saltations that were not observed experimentally. A graph of the impact speed versus rebound speed for the three fractions looks similar to that shown for the sand population composed from the Yamasaka and Ikeda (1988) size-frequency distribution (Figure 4.3), in that there exists a dense concentration of points in the low-velocity spectrum, representing about 25% of the moving population. In contrast, the graph of the Willetts and Rice experimental results of impact versus rebound speed (e.g. see McEwan *et al.*, 1992; Fig. 7) does not show this subset of low-energy saltations. Computational models of uniform-grain-size saltation (e.g. Anderson and Haff, 1991) similarly predict the existence of a low-energy population of saltating grains. The difficulty in distinguishing low-energy collisions during wind-tunnel sand-transport experiments has been discussed extensively in the literature. Despite these and other complications, however, it is encouraging that the predicted results for the grain-trajectory parameters of each size fraction display the same trends and relative magnitudes as the measured data.

#### 4.4 Summary

Recent experimental and theoretical advances in the mechanics of grain collisions have provided a more solid physical understanding of the influence of grain-bed interactions in shaping the form of the bedload-flux profile and have provided a framework for modelling the evolution of bed stratigraphy over time (e.g. Forrest and Haff, 1992). Thus far, numerical models principally have focused on uniform-size materials or on mixtures of two grain sizes. The theoretical model presented here seeks to extend this base of knowledge by addressing the dynamics of grain collisions

in naturally distributed grain-size mixtures. Empirical data on the influence of grain mass on the dynamics of grain-grain collisions are limited, however, and the model results discussed here lie beyond the current observational base in many respects. Nonetheless, general observations of the dependency of grain-bed collisions on the sediment size-frequency distribution are predicted quite well by the mixed-grain collision algorithm, which has encouraged further quantitative investigations of the differences in collision dynamics between mixed-grain and uniform sediments, as well as the interactions of discrete size fractions within a natural mixture.

The mixed-grain collision algorithm depends on the models of the computer-generated sediment bed and the fluid mechanics of eolian mixed-grain transporting flows, described in previous chapters, for input of all variables important to the collision problem. These are: (1) the impact speeds and angles of approach of the incoming grain, derived from the fluid-mechanical and ballistic components of the model; (2) the site of collision, which can be found deterministically because the progress of each grain downwind is located temporally and spatially with respect to the simulated bed surface; (3) the geometry of the collision site, which is a function of the grain impact angle, the size of the impacted bed grain relative to the incoming grain, and the geometric properties of the bed pocket in which the impacted grain resides, given by the sediment-bed algorithm; (4) the momentum transfer via collision, which depends on the geometric configuration of the collision, the masses of the involved grains, the momentum of the incoming grain, and the laws of conservation of linear momentum and energy for partially elastic collisions; (5) the components of lift-off velocity for the rebounding and ejected grains, which derive from (4); and (6) the lift-off angles of grains, which are calculated from (3). The important assumptions made are that: (1) the effects of bed microtopography are much greater than the those of intergranular contact (i.e. inelasticity, friction, compressibility) during collision, which is consistent with the theoretical findings of Haff and Anderson (1993); and (2) the probability of ejecting more than one grain capable of saltating downwind is low. Although more than one ejection per collision has been observed, the general thought is that the low-energy, secondary ejecta contribute little to the bedload flux or modification of the wind profile under flat-bed, moderate-flow conditions. Predicted values of the collision variables agree, in terms of general trend and magnitude, with measurements for similar

size-frequency distributions made by Willetts and Rice (1985a, 1989). The validity of the model and these assumptions will be tested further in Chapter 5 by comparing measured and predicted bedload fluxes.

The numerical model quantifies two observations that have been discussed, largely conceptually, in the literature for several decades. The first is that there exists a definite and substantial variation in collision behavior between grain-size fractions within a mixture. The second is that collision outcomes vary with the grain-size distribution of the sediment bed. Calculations of collision variables for the sediment mixture ( $D_{50} = 0.70\text{mm}$ ; e.g. Figure 3.1) over a range of transport stages show that the particles from the finer fractions collide with the bed more energetically on average than the median and coarse fractions, with correspondingly higher impact and rebound speeds, higher hop heights, longer trajectories, and greater distances travelled downwind.

Collision outcomes depend on the relative sizes of particles involved. Small grains have greater access to the surface area of bed grains exposed to the flow. Consequently, they execute more head-on collisions than coarse grains, such that their vertical component of rebound velocity exceeds the vertical component, and they launch upward energetically. Grains of the coarse fraction cannot penetrate the smaller interstices, so that their collisions are relegated to the upper surfaces of exposed grains. They tend, therefore, to execute more glancing collisions than do particles of the finer fraction, which tends to promote low-angle, forward trajectories. Variation in hop characteristics between size fractions are also a function of mass-dependent inertial forces and fluid forces acting on the grain as it leaves the bed. The relative masses of colliding grains dictates the ability of incoming grains to eject bed grains, as well as the lift-off energy of each grain. Ejection statistics computed by the model show that small grains rarely eject particles greater than about 1.5 times their size, except in those infrequent occasions when larger particles perched precariously on the surface can be knocked forward with minimal energy transfer. On the other hand, coarse grains eject a range of particle sizes because of their mass relative to the median and smaller percentiles of grains composing the bed. Their ability to dislodge the smallest fraction is greatly reduced by the fact that these grains often are in bed pockets too small to be entered by the larger grains. The model predicts, however, that grains eject like-sized grains in at least 50% of the colli-



sions they execute.

The degree of topographic inhomogeneity of the bed surface also dictates the nature of bed collisions. The coarser the grain mixture composing the surface, the more variable the collision outcomes, with the greatest variation predicted for the smallest and coarsest fractions of the mixture. The model predicts significant variations in collision histories between grains moving over a same-sized bed, and the same grains moving over the mixed-size bed. Collisions of the finer fractions with the heterogeneous bed are more energetic, on average, than on the uniform bed. The median and coarse grains, however, are less energetic, resulting in lower particle velocities and shorter hop trajectories than predicted in the uniform-grain case. For example, the model shows that maximum impact and rebound speeds, as well as hop heights and lengths, of fine grains colliding with the mixed-grain bed are almost 50% higher than values calculated for the same grains colliding with a bed of similar-sized grains.

The sensitivity of the mechanics of grain-bed collisions to the size-frequency distribution of the sediment surface suggests that modelling the sediment bed as accurately as possible is a critical ingredient to the mixed-grain, bedload-transport problem. In addition, the dependency of collision responses on grain-size information highlights the great need for additional experiments that can quantify the relationships between particle size and grain-bed interactions for a range of sediment mixtures and flow conditions.

## Chapter 5: Model Calculations of Mixed-Grain Bedload Transport

Most quantitative studies of eolian bedload transport have focused on the total transport rate and its relationship to aerodynamic parameters, such as the fluid shear stress, to characterize the sediment-moving capacity of the wind. As discussed in previous chapters, the movement of particles in a naturally distributed eolian mixture is governed by the other grains, both at the level of the sediment bed and within the wind column. At the bed surface, small grains often are sheltered in bed pockets from collisions with larger grains that would propel them into the flow, whereas the coarser particles protrude from the bed surface and are more likely to be impacted by saltating particles. Once the finer grains are mobilized, however, they extract relatively more momentum from the airflow, thereby modifying the wind's response to all saltating particles. Inertial forces acting on the finer grains are smaller than those acting on the moving coarse grains, such that the small particles will be accelerated more rapidly and to greater heights above the bed surface than the coarser particles and, hence, interact more vigorously with the wind at all levels. Because of their mass relative to the masses of grains composing the sediment bed, however, coarse grains are more likely to eject a range of particle sizes than are the finer fractions. As a result, each size fraction in a mixture has a unique transport rate which depends on the total size-frequency distribution of particles comprising the sediment bed.

The considerable variation in sediment size distributions among depositional environments complicates the development of universal, predictive bedload functions for sand mixtures because these disparities are difficult to characterize analytically and require extensive calculations if derived numerically. Semi-empirical, sediment-transport relationships have assumed that the size-frequency distribution follows a log-normal or Gaussian curve and typically employ the mean, median, or  $D_{84}$  percentile to describe the entire mixture (e.g. Bagnold, 1941; Chepil, 1945; Zingg, 1953; Horikawa and Shen, 1960; Tsuchiya, 1970; Hsu, 1973; Hsu and Blanchard, 1991). Other researchers have proposed exponential laws to describe the dependence of total flux on height above the bed (e.g. Williams, 1964; Nalpanis, 1985; White and Mounla, 1991), or bedload expressions that include the shear velocity raised to some power (e.g. White, 1979; Rasmussen and

Mikkelsen, 1991; Sorensen, 1991), which require empirical input from experiments conducted with a specified sand mixture. Theoretical treatments of eolian bedload transport, thus far, have dealt only with uniform-sized sediments. As discussed in Chapter 2, a large percentage of eolian sediment distributions are skewed or bimodal, rather than log-normally distributed. Consequently, total-bedload functions dependent on one or two grain-size parameters, or on the sediment and flow conditions of a single study, may yield inconsistent results. For example, several researchers (e.g. Berg, 1983; Sarre, 1988) have compared the available total-bedload equations using one set of experimental data and have found considerable variation among the mass-flux profiles calculated with different bedload relationships.

The goal of this work, therefore, has been to develop a theoretical model for the bedload transport of eolian mixtures capable predicting the mechanics of grain movement for individual size fractions of naturally sorted sediments. Because the sediment size-frequency distribution is input directly to the sediment-bed construction algorithm, the model can address any sand mixture commonly found in coastal, inland dunefield, and eolian-fluvial transitional environments. Coupling the numerical sediment bed, fluid-mechanical, and collisional algorithms yields a self-contained model in which the variables necessary for predicting fractional bedload-transport rates may be obtained directly from the theory for the dynamics of particle-fluid interactions and grain-grain interactions between moving particles and the sediment bed. The numerical model is not dependent on any set of empirical observations, other than the sedimentological characteristics of the sand sample used; therefore, it may be tested independently with experimental data.

Very few measurements exist of fractional transport rates in eolian systems, largely because experimental and field research has focused on total bedload transport and because constituent flux rates of individual size fractions in a simultaneously transported mixture are difficult to measure. The only known published data set is that of Yamasaka and Ikeda (1988). Consequently, the grain-size frequency distribution of their experimental sands has been used throughout much of this study, for the purpose of utilizing their data in an independent test of the model's ability to predict the fluid and particle dynamics of grain mixtures. In the following sections, the model calculations of bedload transport and their comparison with the data set of Yamasaka and Ikeda are discussed.

### 5.1 Theoretical calculations of bedload transport

The volume discharge of bedload sediment per unit width of airflow,  $Q_s$ , is defined as:

$$Q_s = \int_{\eta}^{\delta_B} C_s u_s dz \quad (5.1)$$

where  $C_s$  is the sediment concentration of the mixture as a function of height  $z$  above the bed,  $u_s$  is the downwind component of sediment velocity,  $\eta$  is the elevation of the nonmoving portion of the sediment bed, and  $\delta_B$  is the maximum height of the saltation layer. In mixture-transporting flows, the total bedload flux,  $Q_s$ , is the sum of the fractional volume discharges of all  $m$  sediment components,  $(Q_s)_m$ , in the bedload layer:

$$Q_s = \sum_{m=1}^M (Q_s)_m = \sum_{m=1}^M \left[ \int_{\eta}^{(\delta_B)_m} C_m u_m dz \right] \quad (5.2)$$

where  $C_m$  and  $u_m$  are the concentration and forward particle velocity of sediment component  $m$ , respectively, and  $(\delta_B)_m$  is the maximum height of the saltation trajectories of component  $m$ . The volume discharge of each sediment component  $m$  may be rewritten according to the previously defined relationship (i.e. section 3.6, Chapter 3) of the concentration at any height  $z$  to its value normalized by the concentration at the bed:  $C_m = (C_m)_\eta (C_*)_m$ . Hence, the bedload-discharge equation for each sediment component becomes:

$$(Q_s)_m = (C_m)_\eta \int_{\eta}^{(\delta_B)_m} (C_*)_m u_m dz . \quad (5.3)$$

The method for calculating the movement of sediment within the saltation layer has been discussed previously and is summarized here. Input parameters required by the model are the grain-size frequency distribution, the grain densities, the fluid density and viscosity, and the boundary shear stress. Similar to the experimental conditions of Yamasaka and Ikeda (1988), the grain density is  $\rho_s = 2.65 \times 10^3 \text{ kg/m}^3$  and the fluid viscosity is  $\nu = 1.50 \times 10^{-5} \text{ m}^2/\text{s}$ . The computer algorithm for carrying out the calculations attempts to recreate as much of the natural trans-

port process as possible. A boundary shear stress, specified by the flow conditions of interest, is applied to the computer-generated sediment bed (see Figure 3.1; derived from the size-frequency distribution of Yamasaka and Ikeda), and a few grains, for which the critical stress for the initiation of grain motion has been exceeded, are entrained aerodynamically from exposed positions on the bed surface. Once mobilized, the saltation trajectories of each grain are computed, according to equation 3.11, as a function of time and position relative to the bed surface over which they pass. Some of these grains collide sufficiently energetically with the bed to eject other particles, and the sediment load develops through subsequent ejections of stationary bed particles through impact by saltating grains. The model accounts for all moving grains as they roll, creep, or saltate from the collision site in a single hop or series of continuous trajectories. The characteristics of grain impact with the bed are defined by the speed and angle (with the horizontal) of the incoming grain, the relative mass of the particle relative to that of the grain it strikes and the masses of other grains composing the bed, the geometries of the collision between grains and the array of bed particles in the vicinity of the collision site, and the magnitude of momentum transfer between grains. The rebound and ejection characteristics of grains are calculated from the geometry of the collision and the balance of momentum and energy during impact. The equations for particle launch velocity are given in Chapter 4 (i.e. equations 4.16b, g, h). The motion of each particle is followed from beginning to end, and any ejections it produces from its multiple impacts with the bed similarly are accounted. Grains that hop off the downwind end of the  $1000D_{50}$ -long bed are recirculated from the upwind edge to effect a bed of infinite length. The momentum extracted by each moving particle at each level in the flow is calculated as the product of the drag force acting on the particle times the sediment concentration. To compare model results with the experimental data, the particles are binned into seven size fractions, such that the momentum extracted by each size fraction as a function of height above the bed is the sum of the momentum extracted by each grain belonging to that fraction. The numerical solution of the grain-fluid interaction problem requires iteration because the nature of each particle trajectory, the unique characteristics of each grain-bed collision, the form of the vertical profile of fluid velocity, and the concentration of moving grains at successive levels in the flow are not known at first. The first iteration requires the input of a fluid-

velocity profile, which can be established in a number of ways; it was found in Chapter 3, however, that the velocity profile scales with the height of the bedload layer for the  $D_{50}$  fraction, so that an appropriate choice for the initial form of the velocity profile modified by all moving grains is that for the  $D_{50}$  fraction. Convergence of the vertical profile of fluid velocity and the concentration profile for sediment grains in the bedload layer is obtained when all moving grains and the transporting flow achieve equilibrium. For the horizontally uniform, steady-state problem, this occurs when each terminating grain is replaced, on average, by an ejected particle and when the size-frequency distribution of the moving population equals the distribution of grain sizes within the bed.

The volume discharge of each grain-size fraction in the mixture,  $(Q_s)_m$ , is obtained by multiplying the horizontal component of the particle velocity ( $u_m$ ) for each particle by the nondimensional grain concentration  $(C_*)_m$ , summed over all grains of the size fraction, over all levels in the flow between  $\eta$  and  $(\delta_B)_m$ . This term is then multiplied by the fractional sediment concentration at the bed,  $(C_m)_\eta$ , that is, the concentration at  $z = 0$  of all moving grains of the specified size fraction; therefore,

$$(C_m)_\eta = \sum_{m=1}^M (C_m)_\eta; (Q_s)_m = (C_m)_\eta \sum_{m=1}^M (C_*)_m u_m. \quad (5.4)$$

As described in Chapter 3, the grain concentration as a function of height above the bed  $C_m(z)$ , is proportional to the time that a particle spends at that level ( $\Delta z = 0.1D_{50}$ ), both on the upward and downward limbs of its trajectory ( $\Delta t/\Delta z$ ). This term, as well as the particle velocities, are calculated by the saltation-trajectory algorithm. The concentration of each grain size at the bed is computed from equation 3.15, shown again here, as:

$$(C_m)_\eta = \frac{(\tau_T)_m - (\tau_\eta)_m}{[(F_D)_m/V_m]_\eta D_m}$$

where  $[(F_D)_m/V_m]_\eta$  is the drag force per unit volume acting on  $D_m$  at the level of the bed, and  $(\tau_\eta)_m$  is the critical shear stress for initiation of saltation of a grain  $D_m$ , the values of which are derived theoretically as described in Chapter 3. For each sediment-transport calculation, the moving population consists of 200-300 grains (i.e. approximately 1200-1500 saltation trajectories).

## 5.2 Comparison of calculated fluxes with bedload-transport measurements

The experiments of Yamasaka and Ikeda (1988) were conducted with the sand mixture whose grain-size frequency distribution is shown in Figure 2.1. A discussion of their methods appears in the 1988 paper and in Ikeda (1982a, b). The laterally inclinable, wind tunnel used in the experiments had a working reach of 4 meters and a cross-sectional aperture of 10 cm by 30 cm. A 2-meter tunnel section upwind of the working reach allowed air passage prior to flow in the main chamber of the tunnel, in order to develop steady, horizontally uniform flows. The airflow velocity across the test reach was measured with a Pitot tube and a differential manometer. An unconsolidated, mobile bed surface was prepared with the sand mixture and smoothed by drawing a plate along guides attached to the wind tunnel. Sediment was introduced at the upwind end of the tunnel, collected at the downwind end through a filter, sieved, and weighed to calculate the flux of each size fraction. These measurements of longitudinal flux rates over a flat bed were obtained during a larger study investigating the mechanics of lateral sediment transport of poorly sorted sand mixtures.

To obtain the mean bed shear stress during the experiments, Yamasaka and Ikeda measured, by means of a static pressure tube, the longitudinal pressure gradient between two stagnant pressure holes spaced 2.2 meters apart. This is equivalent to the energy slope,  $dh/dx$ , in their equation for the mean boundary shear stress:  $\bar{\tau}_B = \rho g (A_b/B) (dh/dx)$ , where  $B$  is the width of the wind tunnel and  $A_b$  is the wind-tunnel area dynamically affected by flow adjacent to the bed. They found  $A_b$  to be a function of the Reynolds number for the temporal mean velocity along the central longitudinal axis of the wind tunnel (Ikeda, 1982a),  $A_b = a(Re^x)A_{\perp}$ , where  $A_{\perp}$  is the total cross-sectional area of the wind tunnel and the coefficients  $a$  and  $x$  are dependent on the size-frequency distribution of the sand mixture.

The sediment fluxes measured by Yamasaka and Ikeda (1988) for seven grain-size fractions are reproduced in Figure 5.1. Data are plotted logarithmically as a function of the dimensionless Shields stress for each grain-size fraction ( $D_m$ ),  $(\tau_*)_m = [\tau_b / (\rho_s - \rho) g D_m]$ , and the dimensionless volume discharge of size fraction  $D_m$  per unit bed width, according to its probability ( $P_m$ ) in the size distribution,  $(Q_*)_m / P_m = (Q_s)_m / [(\rho_s / \rho - 1) g D_m^3]^{1/2}$ . The grain size frac-

tions identified by the authors are:  $D_5 = 0.20\text{mm}$ ,  $D_{18} = 0.35\text{mm}$ ,  $D_{40} = 0.50\text{mm}$ ,  $D_{50} = 0.70\text{mm}$ ,  $D_{70} = 1.0\text{mm}$ ,  $D_{86} = 1.4\text{mm}$ , and  $D_{95} = 1.8\text{mm}$ . Data for each size fraction are represented symbolically, as well as described by a curve derived from the equation:

$$\frac{(Q_*)_m}{P_m} = K (\tau_*)_m^{1.5} \left[ 1 - \frac{[(\tau_*)_{cr}]_m}{(\tau_*)_m} \right]^{1/2} \quad (5.5)$$

where  $K = 10$  for poorly sorted sediments (see equation 9 in Yamasaka and Ikeda, 1988).

In order to make the comparison between measured and predicted fractional transport rates, it is necessary to replot Figure 5.1 in terms of the transport stage,  $(T_*)_m = [\tau_b/(\tau_{cr})_m]$ , because the critical Shields stresses for each size fraction determined semi-empirically do not match those predicted by the theoretical model. Yamasaka and Ikeda took the critical Shields stress for each size fraction to be the value for which the measured sediment transport rate was 1% of the rate calculated from a bedload power-law function:  $(Q_*)_m/P_m = 10 (\tau_*)_m^{3/2}$ . Their values of the critical shear stress for each size fraction are approximately equivalent, leading the authors to suggest that the critical stresses for incipient motion of all sizes are independent of grain size and lie in the vicinity of the impact threshold. Critical shear stresses calculated by the model (equation 3.10), however, predict a greater sensitivity of each grain size to the particle-scale geometry of the bed surface (i.e.  $D_m/k_s$ ), indicating that small particles resting in relatively larger bed pockets require greater shear stresses to move than would be the case for larger particles occupying the same bed pockets. Consequently, the model predicts a stronger dependence of the critical shear stress on grain-size and bed-pocket-geometry characteristics. The range in critical shear stresses between the empirical and theoretical study are shown in Table 5.1, as the dimensionless critical Shields stress for each size fraction  $[(\tau_*)_{cr}]_m$  and the critical shear stress  $(\tau_{cr})_m$ . The values calculated by the model are for the average case where the bed-pocket angle geometry is formed by the grain and a grain of median diameter; that is,  $D_m/k_s = D_m/D_{50}$ .

The difference in the methods used to compute the boundary  $(\tau_b)$  and critical  $(\tau_{cr})_m$  shear stresses obviously have a considerable influence on the compatibility of the experimental and theoretical results. The ratio of the dimensionless Shields stress  $(\tau_*)_m$  to the critical Shields stress



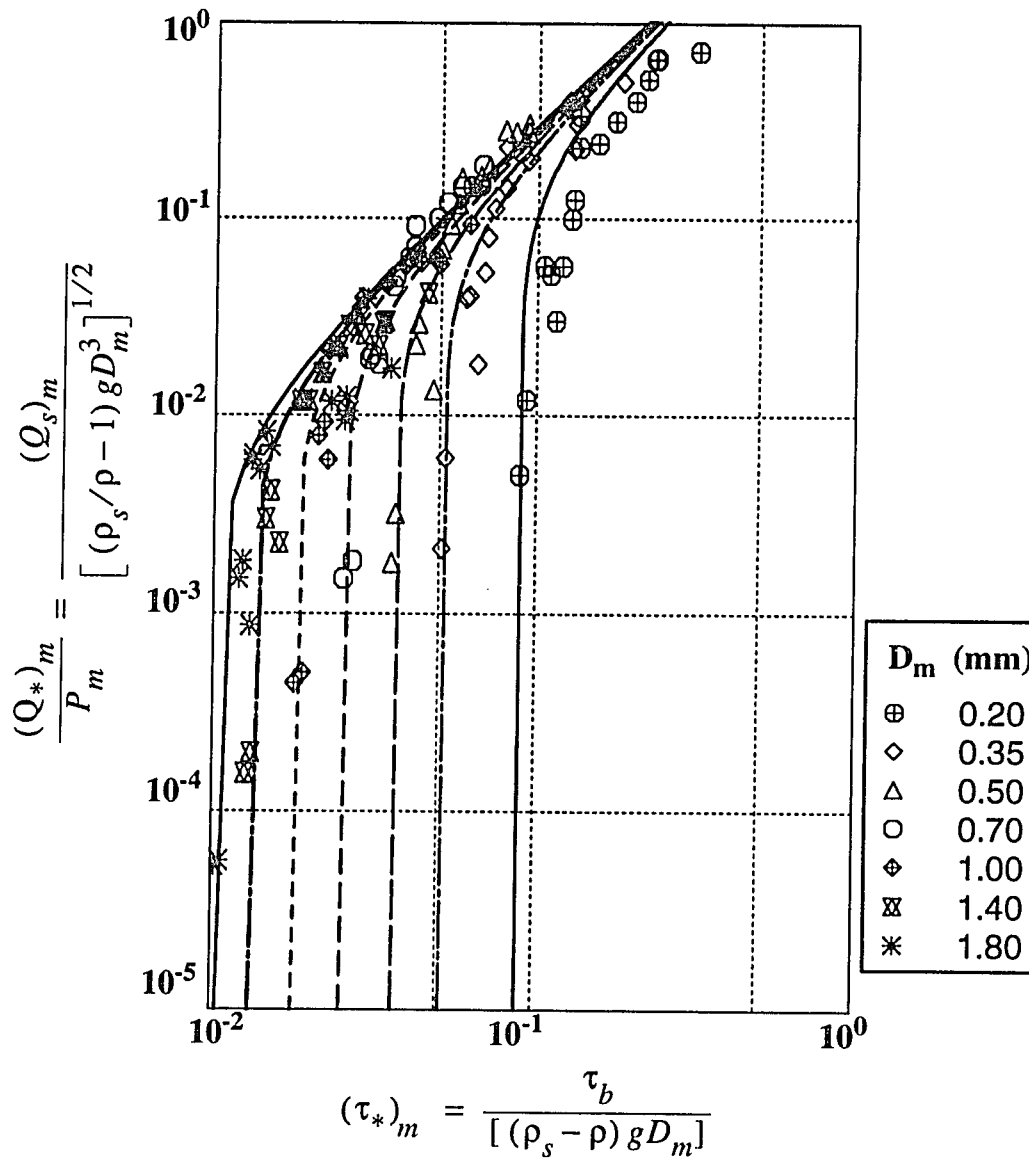


**Figure 5.1** Fractional transport rates measured by Yamasaka and Ikeda (1988; see Fig. 2) as a function of the dimensionless Shields stress  $(\tau_*)_m$  for each grain-size fraction ( $D_m$ ) and the dimensionless volumetric discharge per unit bed width  $(Q_*)_m$ , weighted by the probability density of each size fraction ( $P_m$ ). The grain-size probability distribution is given in Figure 2.1. The figure legend above displays the graphic symbols for each size fraction. Curves fit to the data are derived semi-empirically through equation 5.5. The median grain diameter is  $D_{50} = 0.70\text{mm}$ .

**Table 5.1** Values of the dimensionless critical Shields stress  $[(\tau_*)_{cr}]_m$  and the critical shear stress  $(\tau_{cr})_m$  determined semi-empirically for each grain-size fraction ( $D_m$ ) of the sand mixture by Yamasaka and Ikeda (1988), compared with values predicted by the numerical model. See text for discussion.

grain size (mm)	empirical $[(\tau_*)_{cr}]_m$	predicted $[(\tau_*)_{cr}]_m$	empirical $(\tau_{cr})_m$ $\times 10^{-1} \text{ N/m}^2$	predicted $(\tau_{cr})_m$ $\times 10^{-1} \text{ N/m}^2$
0.20	0.0891	0.1910	4.63	9.92
0.35	0.0515	0.1052	4.68	9.56
0.50	0.0366	0.0727	4.75	9.44
0.70	0.0253	0.0492	4.60	8.94
1.00	0.0180	0.0360	4.67	9.35
1.40	0.0132	0.0289	4.79	10.51
1.80	0.0104	0.0245	4.85	11.45

$[(\tau_*)_{cr}]_m$ , however, varies self-consistently for the measured fractional transport rates, as do the values predicted by the model. Hence, the ratio of the stresses, or the transport stage  $(T_*)_m = (\tau_*)_m / [(\tau_*)_{cr}]_m$  provides a means for reducing the measurements and the predicted values of the fractional transport rates to a common denominator. The experimental data are replotted in Figure 5.2 as a function of the transport stage,  $(T_*)_m$ , and the dimensionless sediment-transport rate. Brackets in the figure denote the range in the experimental observations about the curves derived for each size fraction from equation 5.5.

Model predictions of the fractional transport rates for the mixture are presented in Figure 5.3. The computed discharge rates of six size fractions, for transport stages  $1.5 \leq (T_*)_m \leq 6.0$ , are plotted with the empirical curves and data brackets shown in the previous figure. Two principal differences between the model and empirical results are that the model investigated bedload transport at higher transport stages than those measured experimentally, and that the model did not predict transport of the largest size fraction,  $D_{95} = 1.8\text{mm}$ . The computer-generated bed lacked grains of this size fraction in its surface layers. The 5% (by weight) of the coarsest fraction present in the simulated bed are at depths too great to have been exposed to grain-grain collisions at the bed surface.

The calculated transport rates for six size fractions of the sediment mixture are in very good agreement with the experimental data, when compared by the transport-stage versus volumetric-discharge relationship. The predicted values as a whole are lower than the empirically derived curves at the low end of the transport-stage range and higher at the upper end, but the calculated values for each size fraction fall well within the bracketed range of the experimental data. The predicted fractional discharges for the  $(T_*)_m = 1.5$  case average 15% lower than the values of the empirical curves, 10% lower for the  $(T_*)_m = 3.0$  case, with the exception of the predicted flux for the  $D_{86} = 1.40\text{mm}$  fraction which is 10% higher than the average measured value, and 14% higher for the  $(T_*)_m = 6.0$  case. These variations in the predicted results compared with the empirical curves are reasonable, however, given the considerable scatter in data points to which the empirical curves are fit.

The model results are described more closely by a transport equation of a slightly different

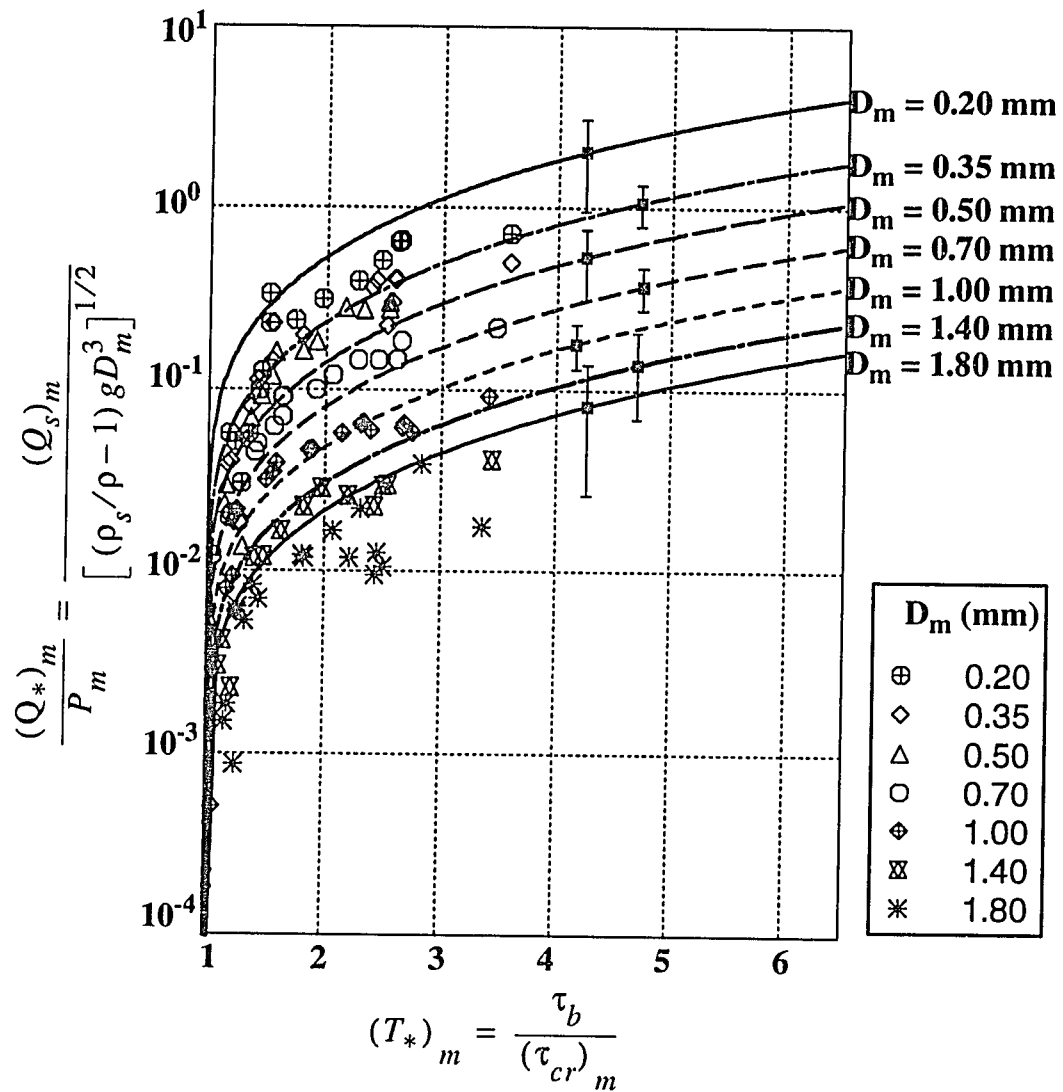


**Figure 5.2** Experimental bedload-transport data, replotted from Figure 5.1 in terms of the transport stage  $(T_*)_m$  and the dimensionless sediment-transport rate  $(Q_s)_m/P_m$ , where  $(T_*)_m$  is the ratio of the boundary shear stress to the critical shear stress of each grain-size fraction,  $(T_*)_m = \tau_b/(\tau_{cr})_m$ . The empirically derived values of  $\tau_b$  and  $(\tau_{cr})_m$  are used. Brackets about the empirical curves derived from equation 5.5 define the range of experimental observations for each grain-size fraction.

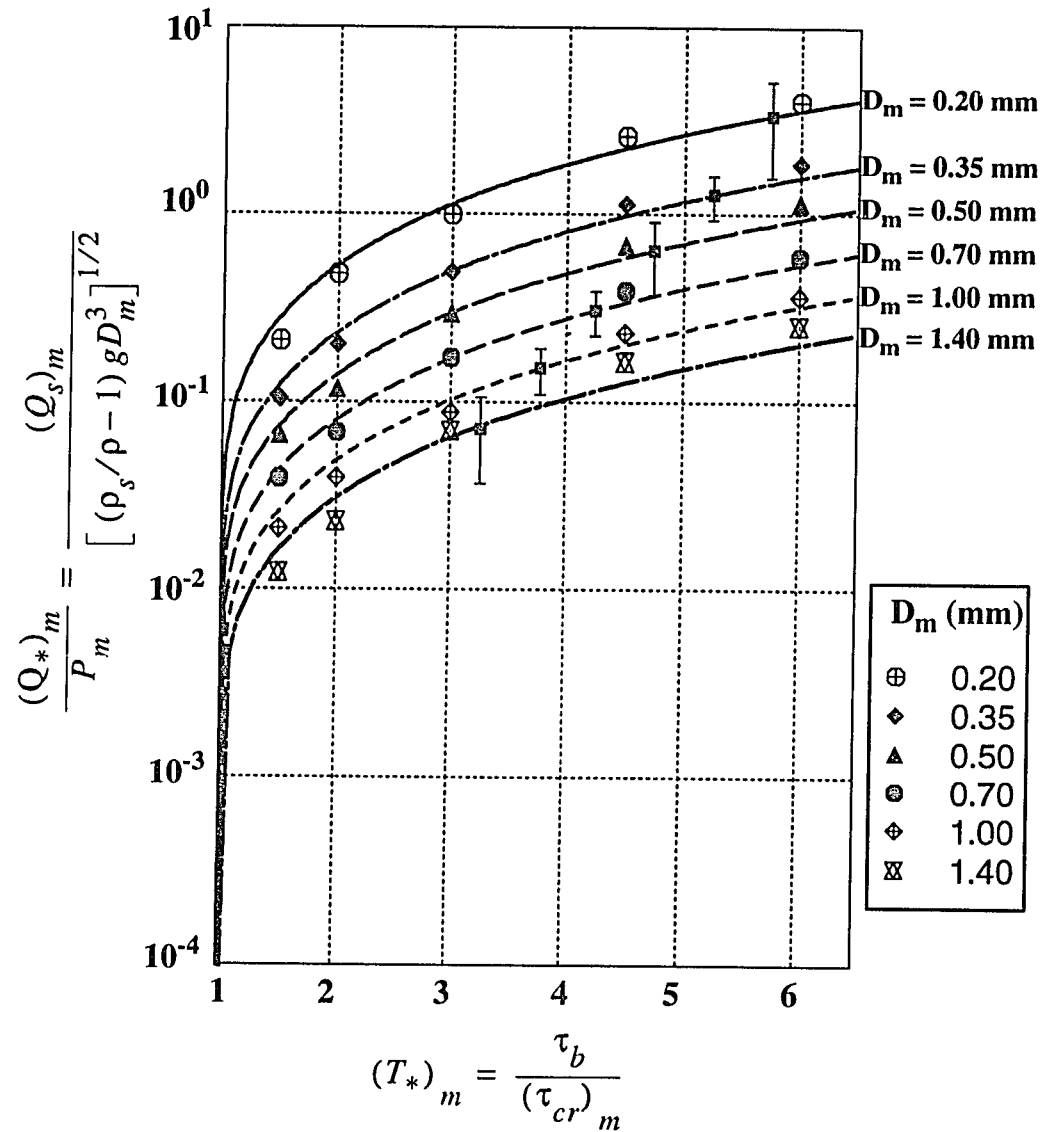


**Figure 5.3** Comparison of fractional transport rates predicted by the numerical model with the best-fit curves from the experimental data of Yamasaka and Ikeda (1988). Brackets indicate the range in the wind-tunnel data for each grain size fraction. Curves and brackets are identical to those shown in Figure 5.2 with the experimental data points. Predicted flux rates are graphed as a function of the transport stage  $(T_*)_m$ , the model-calculated shear stresses  $(\tau_{cr})_m$ , and the dimensionless sediment discharge  $(Q_*)_m$ , weighted by the grain probability density  $(P_m)$ .

form than that given by Yamasaka and Ikeda (1988) in equation 5.5. It is:

$$\frac{(Q_*)_m}{P_m} = K (\tau_*)_m^{1.5} \left[ 1.5 - \frac{[(\tau_*)_{cr}]_m}{(\tau_*)_m} \right] \left[ 1 - \frac{[(\tau_*)_{cr}]_m}{(\tau_*)_m} \right]^{1/2} \quad (5.6)$$

in which the new value of the coefficient is  $K = 9$  if the curves are calculated using the empirically derived values of  $(\tau_b)$  and  $(\tau_{cr})_m$ , and  $K = 3$  for the model-calculated values of  $(\tau_b)$  and  $(\tau_{cr})_m$ . Equation 5.6 provides a better fit to the theoretical results, especially in the low- and high- transport regimes (Figure 5.4). This equation is more similar in form to the sediment-transport relationship formulated by Ashida and Michiue (1972; see Yamasaka and Ikeda, 1988) for subaqueous flows, which Yamasaka and Ikeda modified to fit their wind-tunnel data. The equation for water is:

$$\frac{(Q_*)_m}{P_m} = K (\tau_*)^{1.5} \left[ 1 - \frac{(\tau_*)_{cr}}{\tau_*} \right] \left[ 1 - \left( \frac{(\tau_*)_{cr}}{\tau_*} \right)^{1/2} \right] \quad (5.7)$$

in which Ashida and Michiue determined a value of 17 for the coefficient  $K$ .

The main difference between the experimentally and theoretically derived transport relationships, therefore, is an additional term that contains the critical Shields stress, which reflects the greater dependence of the predicted grain flux on the conditions of initial motion (e.g. the bed-pocket geometry angles and the  $D_m/k_s$  relationship) than observed by Yamasaka and Ikeda. They conclude, on the basis of their observations and physical reasoning, that in the neighborhood of  $(T_*)_m = 1.0$  all grain sizes are saltating simultaneously. As described earlier, model calculations suggest that full saltation of all grain sizes occurs at a higher transport stage of  $(T_*)_m \approx 1.5$  (e.g. see Figure 3.7).

Calculations of the fractional discharge rates below the transport stage  $(T_*)_m = 1.5$  show that the transport relations between the size fractions become more complex, and that the model is very sensitive to the transport behavior of the coarser and finer size fractions at low shear velocities. The transport stage  $(T_*)_m = 1.5$  represents the threshold for the flow conditions in which grains of all size fractions are extracting momentum from the wind. At this transport stage, the largest moving grains are very nearly at the critical stress for initiation of saltation, so that these

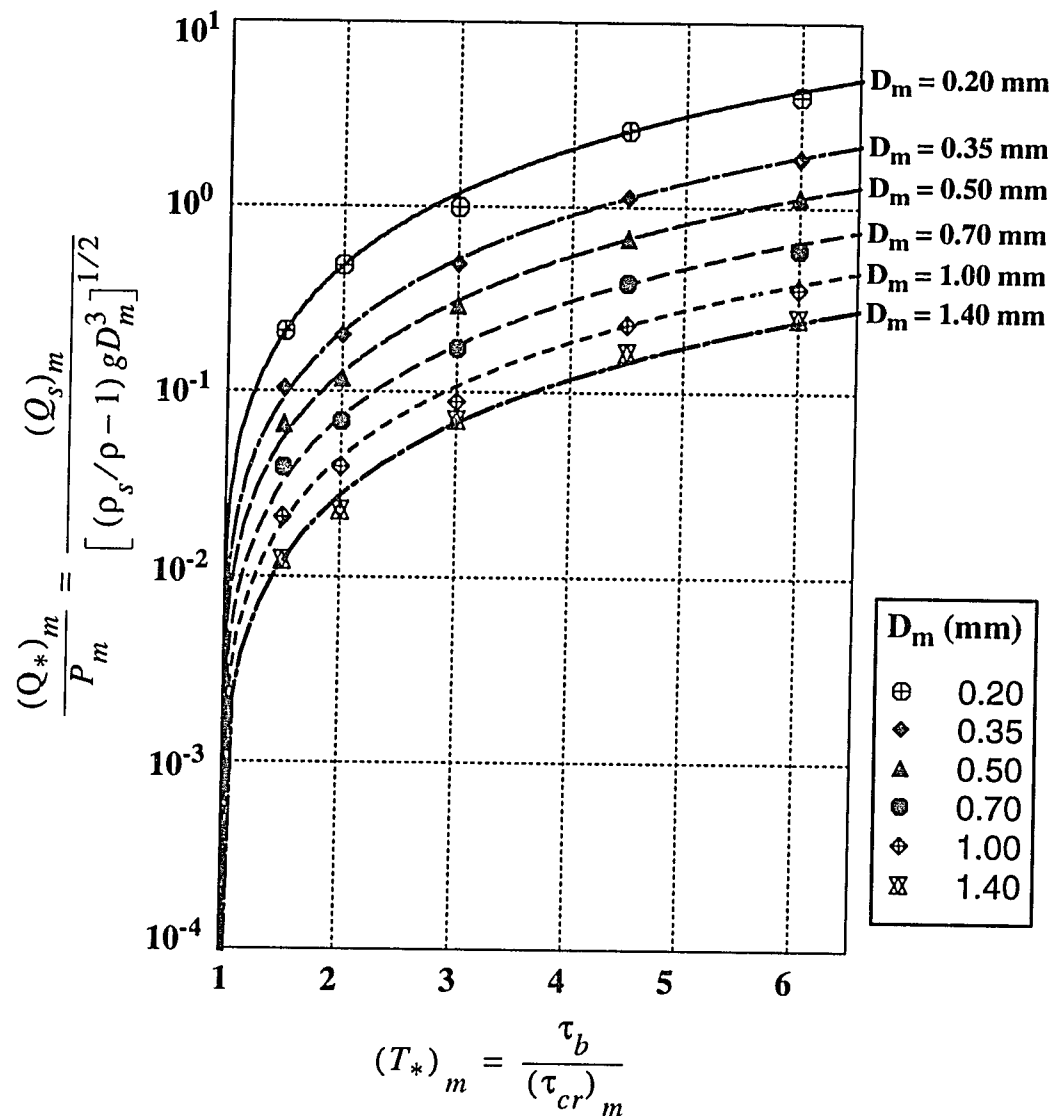


**Figure 5.4** Model-predicted transport rates for the size fractions, fit to new curves derived with equation 5.6 and the theoretical values of  $(\tau_b)$  and  $(\tau_{cr})_m$ . These curves describe the calculated transport rates in the low- and high- transport regimes slightly better than do the transport curves given by Yamasaka and Ikeda (1988) and shown in Figure 5.3. Model results are plotted as a function of the transport stage  $(T_*)_m$  and the dimensionless sediment discharge  $(Q_s)_m/P_m$ .

particles are rolling or moving only in short, low hops of a few grain diameter's distance and are interacting negligibly with the flow. As the transport stage drops to within the vicinity of  $(T^*)_m = 1.0$ , fewer of the grain-size fractions contain energetically saltating grains that extract momentum from the flow. In addition, as the transport stage decreases and the finer fraction becomes less energetic, small grains possess correspondingly lower particle impact velocities and higher impact angles. Consequently, they tend to become trapped in bed pockets more frequently than at higher transport stages. At fractional transport stages less than 1.5, therefore, particle motion is highly sensitive to the distribution of bed-pocket angle geometries and the differences in particle mass between the moving and stationary bed particles.

Although the model predictions of a threshold for simultaneous saltation have not been described empirically for the eolian environment, similar phenomena have been witnessed in flume studies of incipient sand motion. For example, Wilcock and Southard (1989) found that the fine and coarse fractions of a sand mixture appear, in general, to be less mobile than the medium fractions and that the size-dependent variation in grain mobility increases with decreasing transport stage. In the water case, the finer fractions appear to be fully mobile at  $(T^*)_m = 1.5$ , whereas the coarser fractions are not simultaneously mobile. In contrast, all grains of the eolian mixture appear to be fully mobile (i.e. simultaneously saltating) at  $(T^*)_m = 1.5$ . This difference is explained in part by the dominance of fluid forces in water versus the relatively greater importance of the forces of intergranular collisions in air, which contribute to a more energetically moving bedload in the low transport-stage range.

The total or bulk sediment-discharge rates predicted by the numerical model are shown in Figure 5.5 as a function of transport stage. These results are compared with the model-predicted discharge rates for the  $D_{50} = 0.70\text{mm}$  fraction of the mixture and for the case where grains of diameter  $D = 0.70\text{mm}$  are saltating across a uniform-sized sediment bed ( $D/k_s = 1$ ). The bulk discharge rate ( $Q^*$ ) is the sum of the fractional fluxes at a given  $T^*$ ; the curve fit to the data is found by summing the theoretically derived curves for the six size fractions (e.g. Figure 5.4). This curve coincides with that calculated using equation 5.6, in which  $K = 3$  and  $(\tau^*)_m$  and  $[(\tau^*)_{cr}]_m$  correspond to the smallest grain size present in the mixture ( $D_i = 0.16\text{mm}$ ;  $\tau_{cr} = 1.21 \text{ N/m}^2$ ). The best-



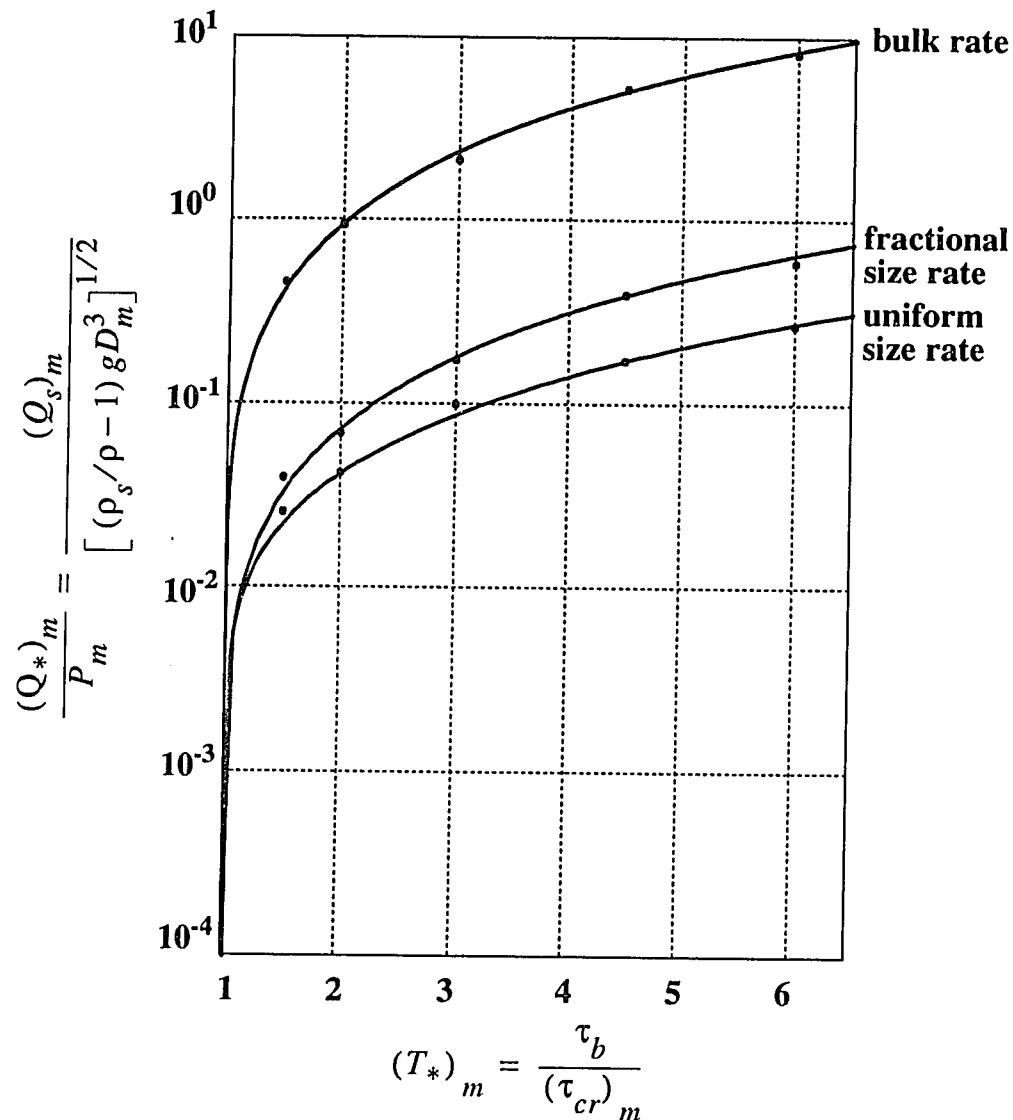


**Figure 5.5** Comparison of model-predicted curves for the bulk discharge of the mixture ( $\Sigma D_m$ ), the fractional discharge of the median grain size ( $D_{50} = 0.70\text{mm}$ ), and the total discharge of uniform-sized sediment ( $D = k_s = 0.70\text{mm}$ ). Best-fit curves are calculated in the bulk-rate case by summing the fractional curves in Figure 5.4, in the fractional-rate case by equation 5.6 with  $K = 3$  and  $(\tau_{cr})_{50} = 8.94 \times 10^{-1} \text{ N/m}^2$ , and in the uniform-size rate case by equation 5.5 with  $K = 10$  and  $\tau_{cr} = 2.74 \times 10^{-1} \text{ N/m}^2$ . The curve for the bulk-rate case coincides with that obtained through equation 5.6 with  $K = 3$  and the critical shear stress,  $(\tau_{cr})_m = 1.21 \text{ N/m}^2$ , of the smallest grain size present,  $D_i = 0.16\text{mm}$ .

fit curve through the predicted flux rates for the uniform-sized grains obtains from equation 5.5 (i.e. the semi-empirical relationship of Yamasaka and Ikeda for uniform-size sand) with  $K = 10$  and  $(\tau_{*})_{cr} = 1.51 \times 10^{-2}$  [or  $\tau_{cr} = 2.74 \times 10^{-1} \text{ N/m}^2$ ]. Similar to the results of the study by Yamasaka and Ikeda (1988), the slopes of the curves for the uniform-size and mixed-size cases are sufficiently different to warrant separate best-fit equations.

Comparison of the curves in Figure 5.5 demonstrates that for the same values of the transport stage, flux rates of the sand mixture are about 1.3 orders of magnitude greater than those of the uniform-size transport case. In addition, the flux rates of the median size fraction of the mixture are about 40% greater than those of the uniform-size case at low to moderate transport stages  $[(T_{*})_m < 3.0]$  and about 60% greater at the higher transport stages  $[(T_{*})_m > 3.0]$ . These results are in keeping with observations quantified in previous chapters regarding the dynamical behavior of inhomogeneous mixtures. In Figures 4.7 through 4.12, it was shown that for grain-bed collisions in which the ratio of the incoming to impacted masses  $m_0/m_2 < 1$ , the rebounding grain was considerably more energetic than for a similar-sized grain on a bed composed of the same grains, on average travelling higher, faster, and farther than its counterpart. Conversely, for  $m_0/m_2 > 1$ , the uniform-size grains were comparatively more energetic. The mixture, however, consists of a relatively higher percentage of grains with diameters less than or equal to the median size, so that the bulk sediment-discharge rates reflect the higher fluxes of the smaller and median size fractions. Flux rates of the uniform-grain case most closely approach the values for the  $D_{86} = 1.40\text{mm}$  fraction of the mixture.

Figure 5.5 bears some important implications for field and laboratory estimations of mixed-grain sediment-transport rates. Semi-empirical equations of bedload transport typically employ the mean or median diameter to represent the sorting characteristics of the sand mixture (e.g. Bagnold, 1941; Williams, 1964; Hsu, 1971; Berg, 1983; Sarre, 1988). The results of this study suggest that using experimental or theoretical flux data for uniform sortings as estimates of bedload transport in more poorly sorted mixtures yields values that are considerably low. Furthermore, employing the mean or median diameter in estimates of mixed-size transport also leads to low estimates. Earlier it was shown that the bulk transport rates could be calculated with equation 5.6, using  $D =$

$D_i$  as the characteristic grain diameter. This suggests that the use of  $D < D_{10}$  as the characteristic grain size in semi-empirical equations of bedload transport might result in significantly more accurate results.

### 5.3 Summary

The sediment-transport model presented in this study differs from existing methods of calculating discharge in the bedload layer in that it incorporates the full grain-size frequency distribution of a mixed-size sediment population and derives from the fundamental physics of grain-grain and grain-fluid interactions without depending on empirical measurements. The high degree of similarity between the theoretical bedload-transport calculations and available wind-tunnel data lends support to the validity of the numerical model in describing the fluid and particle dynamics of eolian mixed-grain deposits. Not only can fractional and total bedload-transport rates be predicted for a range of sediment sortings, but the collisional and fluid-mechanical behavior of grains of unequal size can be examined in detail. This numerical model also yields a bedload-transport relationship (i.e. equation 5.6) that can be employed theoretically to obtain bedload-transport rates outside the range of the current experimental database, and it provides an alternative semi-empirical equation to those published in the literature.

Comparisons of predicted bulk transport rates for mixed-grain sands with rates calculated for a uniformly sorted population, in which  $D = D_{50}$  of the mixture, highlight the sensitivity of the particle flux rates to the sedimentological characteristics of the bed. Calculations demonstrate that bulk transport rates of a sand mixture computed with the characteristic grain diameter  $D < D_{10}$  yield substantially more correct values than when the mean or median grain size is used, as is customarily done in semi-empirical, eolian bedload-transport equations. These results underscore the importance of accurately characterizing the grain-size frequency distributions in theoretical models of heterogeneous systems.

## Chapter 6: Summary and Conclusions

All natural sediments contain a range of particle sizes. The physics of bedload transport in heterogeneous sedimentary deposits, therefore, is complicated by the interactions of moving particles with a sediment bed whose surface topography varies spatially due to the particle-size distribution and sorting characteristics of the grain mixture. In eolian systems, grain collisions with the bed primarily are responsible for entraining particles from the bed into the airstream, and the dynamics of intergranular impacts are controlled largely by the differences in particle mass of the involved grains, as well as the range of bed-pocket geometries of particles composing the bed surface. Each grain-size fraction also responds differently to the fluid flow. There is no single threshold fluid shear stress, as exists in the well-sorted (e.g. uniform grain) case but, rather, a unique value for each size fraction of the mixture. Consequently, each size fraction experiences a different mode of transport at low shear velocities, although these variations decrease with increasing shear velocity. The magnitudes of the momentum and energy transfer to stationary particles during collision vary depending on their mass, and mixed-size particles are ejected into the windstream with differing particle velocities; hence, grains of a particular size fraction travel, on average, to different heights in the wind column than particles of another fraction. The vertical profile of wind velocity, therefore, responds differently to each size fraction, with some fractions extracting relatively more momentum from the flow than others. As a result, each grain-size fraction has a different effect on the wind-grain feedback process that dictates flow and particle velocities within the bedload layer. This, in turn, results in different bedload transport rates for each size fraction in the granular mixture.

A relatively good understanding of bedload-transport dynamics in well-sorted sediments has been achieved over the past few decades through rigorous experimental and numerical-modeling work. The purpose of this dissertation, therefore, has been to extend numerical theory into the arena of mixed-size eolian sediments. Relatively fewer experimental observations of the mechanics of poorly sorted sediment transport exist, providing more limited information with which to test the validity of the mixed-grain theoretical model presented here; however, model results have

been tested whenever possible against field and experimental understanding of heterogeneous sand deposits.

The contribution of this work is a unified numerical theory for the fluid and particle mechanics of sediment mixtures in wind. It yields a bedload-transport relationship that can be used to predict the bulk discharge rates of heterogeneous sediments, as well as the fluxes of each of its size fractions, without empirical measurements. The applications of the numerical model include predicting the flux rates of granular mixtures, important to an understanding of erosion and deposition in modern eolian environments, and characterizing the evolution of poorly sorted sediment beds, essential for interpreting the stratigraphy of modern and ancient sand bodies. The model comprises four dynamical components that are coupled to predict the bedload-transport rates of grain-size fractions within a mixture: (1) a computer-generated sediment bed that fully characterizes the size-frequency distribution of the sediment mixture of interest; (2) a deterministic saltation component that describes the initial motion and ballistic trajectories of grains rolling or saltating in continuous hop sequences across the bed; this algorithm follows the approach of Wiberg and Smith (1985) for particle trajectories in Newtonian fluids; (3) a collisional algorithm that treats the stochastic behavior of grain collisions in a deterministic manner, by calculating the momentum transfer between particles and the geometry of the grain-grain collision from the granular configuration of the collision site and the energetics of grains as they approach the bed; and, (4) a fluid-mechanical element that predicts the extraction of momentum from the fluid by each grain-size fraction. The model assumes two-dimensional, steady, horizontally uniform flow conditions. Input required to run the model includes the grain-size frequency of the sediment mixture, the grain densities, and the fluid density and viscosity.

The sediment-bed algorithm presented here develops two-dimensional granular arrays from measured grain-size frequency distributions, choosing grains of varying size at random from the distribution and placing them in the sediment bed according to geometric arguments. A fluid-mechanical element smooths the resulting bed surface of any precarious grain clusters created by randomly stacking grains to form the bed, in a manner analogous to that used to plane wind-tunnel surfaces prior to experimental flows. The initial beds, hence, are randomly sorted which allows

investigation of the mechanical processes by which grain sorting and packing evolves during flow events. Comparison of computer-generated bed characteristics with available measurements of natural and experimental bulk sediment properties and bed-surface friction angles for mixtures of similar grain-size distributions yields good agreement.

In addition to its use in the sediment-transport problem, the sediment-bed computational algorithm may have some application to stratigraphic analyses of internal bed morphology. Extending the model to address the three-dimensionality of sediment beds, and incorporating the fluid and particle mechanics of bedform generation, would allow quantification of the processes by which wind-ripple stratigraphy and other depositional features, such as surface coarsening, develop in poorly sorted materials. It was found that the topographic relief of the computer-generated sediment surface has an established but irregular amplitude and wavelength, generally on the order of 4-6 median grain diameters ( $D_{50}$ ) between the topographic lows (bed pockets) and highs (protruding coarse grains or grain clusters) and 10-20  $D_{50}$  in the downwind direction, which is consistent with observations of wind-tunnel beds prior to airflow (e.g. Willetts; see Anderson and Haff, 1991). These bumps and depressions appear to serve as nuclei for development of grain sorting. Bed-smoothing calculations during preparation of the computer-generated sediment beds demonstrate that selective clustering of grains by size commences with movement of the first grains along the surface, whereby the finer grains tend to cluster in bed pockets and topographic lows, and the coarser grains pile up against each other when one or several grains becomes lodged in a prominent position on the bed surface. It is suspected that these uneven, small-scale topographic perturbations might form the nuclei for development of bed patchiness and other bedform features, even at flow stages prior to the onset of full saltation, although this theory needs to be tested further with the fully posed sediment-transport model. A commonly held theory is that the creeping population of lowest-energy moving grains defines the spacing and sorting of bedforms (e.g. see discussions in Pye and Tsoar, 1990, Anderson *et al.*, 1991; Forrest and Haff, 1992). The model suggests that small-scale perturbations, although irregularly spaced, already exist by virtue of the geometric packing of disproportionately sized grains forming the sediment bed.

Model calculations of the aerodynamic effects of bed-surface roughness demonstrate that,

for sand deposits, protruding surface grains exert negligible drag on the near-bed airflow. The major influence of the bed surface on the vertical profile of fluid velocity, therefore, lies in controlling the grain-size probability distribution of particles leaving the bed, which considerably affects the concentration of each grain size in motion. Model results show that the distribution of bed-pocket geometries and the relative masses of colliding and ejected grains govern the ability of each particle to be propelled into the flow. Once ejected, sediment grains reach different heights in the flow depending on the balance between mass-dependent inertial forces and drag forces acting on the grains. The extraction of momentum by accelerating grains of a particular size fraction depends principally on the horizontal (downwind) component of the drag force times the concentration of moving grains of that size fraction. In addition to being regulated by the size-frequency distribution of the sediment bed, the concentration of each size fraction is limited by the magnitude of momentum available to sustain grains in the wind column. Model calculations show that even though the central fractions contain larger absolute numbers of moving grains, due to their dominance of the size-frequency distribution, the finer fractions actually extract proportionately greater amounts of momentum from the flow. For a given flow velocity, small grains are accelerated more by the wind than coarser ones because inertial forces acting on them are less; hence, the small grains reach a higher maximum height in the airstream. Consequently, they extract relatively more momentum, especially at heights above the bed not attained by the coarser fractions.

Calculation of the momentum extracted by each size fraction depends on knowing the fluid shear stress threshold below which the flow is not capable of initiating saltation. Model results demonstrate that particles rolling or moving in low-energy trajectories (e.g. the "creep" and "splash" populations) extract relatively little momentum from the flow, regardless of grain size. It is the saltating population, consequently, that dictates the form of the momentum-extraction profile. The critical fluid shear stress for initiation of saltation is grain-size dependent and ranges from 6% higher than the critical stress for initial motion (i.e. the critical Shields stress) for the finest grains to 30% higher for the coarsest grains in the sand mixtures investigated. For these mixtures, the transport stage (ratio of the boundary to critical shear stresses) of the saltation threshold ranges from 1.05 to 1.5, such that full saltation of the entire mixture (i.e. all grains potentially able

to saltate) occurs at  $(T^*)_m \geq 1.5$ . The model shows that the critical shear stress of saltation is not only dependent on grain size, but also on transport stage. At a transport stage of  $(T^*)_m = 3.0$ , the bedload layer of the windstream is saturated with moving grains extracting momentum from the flow, such that the near-bed flow velocity begins to decrease. Hence, the local fluid shear stress affecting each grain size reduces to a level just sufficient to maintain saltation; this is accomplished through reduction of the critical shear stress for saltation, which is reduced incrementally with increases in transport stage. Model calculations clearly demonstrate that the critical shear stress for saltation varies semi-logarithmically with transport stage above  $(T^*)_m = 3.0$ , and reduces uniformly for all grain sizes. At a transport stage of  $(T^*)_m = 6.0$ , the critical stresses for maintaining saltation of each size fraction are still slightly greater than those for sustaining particle motion (e.g. the critical Shields stress).

Calculations of momentum-extraction profiles for grain-size fractions within a mixture indicate that the median grain diameter  $D_{50}$  is an appropriate length scale for characterizing the momentum extraction of mixtures, that is, all curves may be normalized in the vertical by  $z/D_{50}$ . As expected, the coarser fractions extract relatively less momentum than the central fractions, whereas the finer fractions extract relatively more. The total momentum extracted by the moving mixture is the sum of momentum extracted by each of its components. Furthermore, model analyses demonstrate that the profiles of total momentum extraction for a range of transport stages collapse to essentially one curve when the height axis is nondimensionalized by the maximum height of the saltation layer in each case. The model predicts a linear increase in the maximum height of the saltation layer to a transport stage of 3. Again, the reduction of the local fluid stress necessary to compensate for the high concentration of moving grains demonstrates its influence. The reduction in the critical shear stress of saltation results in a metering of the velocities of particles in all size fractions, such that the grain trajectories of all fractions achieve a more uniform height. Hence, above  $(T^*)_m = 3.0$ , the maximum thickness of the saltation layer increases asymptotically with increasing transport stage. This effect has been discussed qualitatively by Gerety and Slingerland (1983) from their experiments with eolian sand mixtures, and has also been measured in flume studies of grain mixtures (Wilcock and Southard, 1989), although the abruptness of the tran-



sition in fluid response to increasing concentration was not witnessed in the subaqueous case.

Model results indicate that equilibrium between the flow and the moving grains is attained when the grain-size frequency distributions of grains in the bedload layer match those of the sediment bed. This means that each terminated grain of each moving size fraction is being replaced, on average, by a similar-sized grain. Model calculations of the grain-bed collision process predict that grains eject like-sized grains in at least 50% of the collisions in which they are involved. The remaining 50% of the grain replacements to the bedload layer through ejection, for a particular grain-size fraction, occur through collisions with incoming grains that are relatively larger. Small grains rarely eject particles larger 1.5 times their own size, except in the case where a precariously perched grain can be knocked from its pocket with minimal momentum expended. Large grains, on the other hand, eject a range of grain sizes, but rarely eject the finer fractions because small grains often lie in bed pockets inaccessible to the larger grains. Hence, the finest grains are dislodged primarily by like-sized particles that can penetrate the small confines of bed pockets, or when the bed pocket is exhumed by removal of the adjacent surface grains. These observations, of course, are only valid at low to moderately high transport stages. At high transport stages, when the bed is actively eroding or being deformed by high-energy bombardments (e.g. bed cratering), large grains are more likely to impact the bed with such force to release a wide range of particle sizes. This has been observed experimentally by a number of researchers (e.g. Bagnold, 1941; Mitha *et al.*, 1986).

The grain-bed collision model quantifies some of the experimental observations of mixed-size sediment transport that have been discussed qualitatively in the literature. These include the variation in the mechanics and outcome of grain collisions between size fractions within a mixture, and the modifications in grain-collision behavior with variations in sorting characteristics of the sediment surface. The coarser the grain mixture composing the surface, the more variable the collision outcomes, with the greatest variation predicted for the smallest and the coarsest fractions of the mixture. The model predicts significant variations in collision histories between grains moving over a uniform-sized bed and the same grains moving over a mixed-size bed. Small grains tend to be more energetic on a mixed-grain bed, where the range of particle-collision geometries is greater

and the grains are more likely to rebound upward from the exposed surfaces of grains that are much larger than themselves. For example, the model shows that maximum rebound speeds, hop heights, and trajectory lengths of fine grains colliding with the mixed-grain bed are almost 50% higher than calculated for the same particles bouncing over a bed of like-sized particles. This results in higher sediment discharge rates for the mixture than for the uniform-sized deposit, as has been documented experimentally by Yamasaka and Ikeda (unpublished data; 1988).

The full bedload-transport model couples the algorithms for the sediment bed, the fluid-mechanics of sediment-transporting flows, grain motion within the flow, and grain collisions with bed to predict the fractional transport rates of individual size fractions within the mixture. The model calculates the product of the forward particle velocities times the grain concentration for each size fraction and integrates over the height of the bedload layer to yield fractional volume discharges per unit airflow width. The model predictions compare very well with measurements made by Yamasaka and Ikeda (1988). In order to make the comparison, the simulated sediment bed was composed from the same grain-size frequency distribution used in the experiments, and the same environmental conditions (e.g. temperature, flow velocities) were used in the model. The small discrepancies between the calculated and measured fractional transport rates probably are related to the differences between the critical Shields stresses predicted by the model and those derived from the measurement of shear stresses during the experiment. Another source of variability between the predicted and calculated values is that the model extended the range of calculations to higher values of the transport stage, which might account for the difference in slopes of the curves fit to the measured versus the predicted fractional-transport rates.

Based on their measurements and physical reasoning, Yamasaka and Ikeda suggested that the critical Shields stress for each fraction is independent of grain size because the incipient motion of sand particles in air flows is assumed to be at the impact threshold, which lies below the fluid threshold for initiation of grain motion. The model, however, predicts a strong independence of the critical Shields stress on grain size. The effects of the difference in critical Shields stresses were removed by comparing the discharge rates as a function of the transport stage. The measured and predicted values differ by a slight amount in the lower and upper ranges of the transport stage.

A set of curves fit to the predicted values yield a bedload-transport equation that accounts more strongly for the dependence of the critical Shields stress on grain size than the equation offered by Yamasaka and Ikeda (1988). The otherwise close agreement lends support to the validity of the model in predicting the fluid and particle mechanics of mixed-grain bedload transport. Further testing of the model, however, awaits further experimentation, as the Yamasaka and Ikeda data set represents the only measurements of eolian fractional-bedload rates currently available.

The sensitivity of the model predictions of grain-fluid and grain-bed interactions to the size-frequency distribution of the sediment mixture suggests the importance of accurately accounting for grain-size variations in numerical modelling of heterogeneous sediments. Comparisons of bulk transport rates, calculated from the sum of the fractional bedload-transport rates, with discharge rates of uniform-size sediments in which  $D = D_{50}$  demonstrate a difference of over an order of magnitude. Similarly, bedload-transport rates for  $D_{50}$  grains saltating over the mixed bed are roughly 50% lower in magnitude than the bulk discharge rates. These results underscore the strong influence of grain sorting on bedload discharge of natural sediment mixtures and suggest that the use of mean and median grain sizes as the characteristic grain diameter in semi-empirical bedload equations can result in substantially low estimates.

Model results show that the particle-flux, concentration, and momentum-extraction profiles of each grain size are scaled by the respective profiles of the  $D_{50}$  fraction for the range of mixtures studied here. In addition, variations in the vertical profile of fluid velocity and the total bedload flux rate with increasing transport stage are scaled by the height of the saltation layer. These observations are important in that they suggest a more analytical approach to some of the bedload-transport and fluid-velocity parameters, including the form of the momentum-extraction profile with varying grain size and transport stage. Hence, this model lays some of the necessary groundwork for an analytical solution to the problem of mixed-size sediment transport. While at present the model focuses on mixed-grain transport over flat beds, it also provides the basic framework for the logical next step, which is modelling the evolution of small-scale bedforms in poorly sorted sediments.

## LIST OF REFERENCES

- Ahlbrandt, T.S., 1979, Textural parameters of eolian deposits. *IN* McKee, E.D., ed., *A Study of Global Sand Seas*, U.S. Geol. Surv. Prof. Pap. No. 1052, p. 21-60.
- Anderson, R.S., 1986, *Sediment Transport by Wind: Saltation, Suspension, Erosion, and Ripples*. Ph.D. dissert., Univ. Washington, Seattle, Wash.
- Anderson, R.S., 1987, A theoretical model for aeolian impact ripples. *Sedimentology* **34**: 943-956.
- Anderson, R.S., and P.K. Haff, 1988, Simulation of eolian saltation. *Science* **241**: 820-823.
- Anderson, R.S., and P.K. Haff, 1991, Wind modification and bed response during saltation of sand in air. *Acta Mech. Suppl.* 1: 21-51.
- Anderson, R.S., and B. Hallet, 1986, Sediment transport by wind: Toward a general model. *Geol. Soc. Amer. Bull.* **97**: 523-535.
- Anderson, R.S., Sørensen, M., and B.B. Willetts, 1991, A review of recent progress in our understanding of aeolian sediment transport. *Acta Mech. Suppl.* 1: 1-19.
- Andrews, S., 1981, Sedimentology of Great Sand Dunes, Colorado. *IN* Ethridge, F.G., and R.M. Flores, eds., *Recent and Ancient Nonmarine Depositional Environments: Models for Exploration*, Soc. Econ. Paleontol. Mineral. Spec. Publ. 31, Tulsa, Okla., p. 279-291.
- Ashida, K., and M. Michiue, 1971, Study on bed load transportation for nonuniform sediment and river bed variation. *Disaster Prevention Res. Inst. Ann.*, Kyoto Univ., No. 14B, p. 259-273 (in Japanese).
- Bagnold, R.A., 1936, The movement of desert sand. *Proc. R. Soc. London, Ser. A.* **157**: 594-620.
- Bagnold, R.A., 1941, *The Physics of Blown Sand and Desert Dunes*. Methuen and Co., London, 265 pp.
- Bagnold, R.A., 1954, Experiments on a gravity-free dispersion of large solid spheres in a Newtonian fluid under shear. *Proc. R. Soc. London Ser. A* **225**: 49-63.
- Bagnold, R.A., and O.E. Barndorff-Nielsen, 1980, The pattern of natural grain size distributions. *Sedimentology* **27**: 199-207.
- Barndorff-Nielsen, O.E., and B.B. Willetts, 1991, editors, *Aeolian Grain Transport*. Proc. Sandberg Workshop, May 1990, *Acta Mech.*, Suppl. 1, vol. 1-2, Springer-Verlag Inc., NY.
- Barndorff-Nielsen, O.E., Jensen, J.L., and M. Sørensen, 1982, On the relation between size and distance travelled for wind-driven sand grains - Results and discussion of a pilot experiment

- using coloured sand. *Euromech 156: Mechanics of Sediment Transport*, Istanbul, July 1982, p. 55-64.
- Barndorff-Nielsen, O.E., Møller, J.T., Rasmussen, K.R., and B.B. Willetts, 1985a, editors, *Proceedings of the International Workshop on the Physics of Blown Sand*. Dept. of Theoretical Statistics, Inst. of Mathematics, Univ. of Aarhus, Memoirs No. 8, Vol. 1-3, 693 pp.
- Barndorff-Nielsen, O.E., Jensen, J.L., Nielsen, H.L., Rasmussen, K.R., and M. Sørensen, 1985b, Wind tunnel tracer studies of grain progress. *IN Barndorff-Nielsen, O.E., Møller, J.T., Rømer Rasmussen, K., and B.B. Willetts, eds., Proceedings of the International Workshop on the Physics of Blown Sand*. Dept. of Theoretical Statistics, Inst. of Mathematics, Univ. of Aarhus, Memoirs No. 8, Vol. 2, p. 243-252.
- Beard, D.C., and P.K. Weyl, 1973, Influence of texture on porosity and permeability of unconsolidated sand. *Amer. Assoc. Petrol. Geol. Bull.* **57**: 349-369.
- Belly, P.Y., 1964, *Sand Movement by Wind*. U.S. Army, Corps Eng., Coastal Eng. Research Ctr., Tech. Memo. 1.
- Berg, N.H., 1983, Field evaluation of some sand transport models. *Earth Surf. Proc. Landforms* **8**: 101-114.
- Bigarella, J.J., 1972, Eolian environments - their characteristics, recognition, and importance. *IN J.K. Rigby and W.K. Hamblin, eds., Recognition of Ancient Sedimentary Environments*, Soc. Econ. Paleontol. Mineral., Spec. Publ. No. 16, Tulsa, Okla., p. 12-62.
- Binda, P.L., 1983, On the skewness of some eolian sands from Saudi Arabia. *IN Brookfield, M.E., and T.S. Ahlbrandt, eds., Eolian Sediments and Processes*. Elsevier Press, Amsterdam, Netherlands, p. 27-40.
- Bui, E.N., Mazzullo, J.M., and L.P. Wilding, 1989, Using quartz grain size and shape analysis to distinguish between aeolian and fluvial deposits in the Dallol Bosso of Niger (West Africa). *Earth Surf. Proc. Landforms* **14**: 157-166.
- Burford, A.E., 1961, Petrology of the Great Sand Dunes, Colorado. *West Virg. Acad. Sci.* **33**: 87-90.
- Calder, S.R., 1987, *Mechanics of Bedload Transport by Wind*. Unpubl. M.S. research paper (non-thesis option), Univ. Washington, Seattle, Wash., 50 pp.
- Calder, S.R., and J.D. Smith, 1989, Effects of grain sorting on the near-bed wind velocity field. *EOS, Trans. Amer. Geophys. Union* **70(43)**: 1109.
- Chepil, W.S., 1945, Dynamics of wind erosion: II, Initiation of soil movement. *Soil Science* **60**: 397-410.
- Chepil, W.S., 1959, Equilibrium of soil grains at the threshold of movement by wind. *Proc. Soil*

- Sci. Soc. Amer.* **23**: 422-428.
- Chepil, W.S., 1961, The use of spheres to measure lift and drag on wind-eroded soil grains. *Proc. Soil Sci. Soc. Amer.* **25**: 343-345.
- Chepil, W.S., and N.P. Woodruff, 1963, The physics of wind erosion and its control. *Adv. Agron.* **15**: 211-302.
- Chiu, T.Y., 1972, *Sand Transport by Wind*. Dept. Coastal Oceanogr. Eng., Tech. Rep., TR-040, Univ. Florida, Gainesville.
- Christiansen, C., and D. Hartmann, 1988, On using the log-hyperbolic distribution to describe the textural characteristics of eolian sediments. Discussion and reply. *Journ. Sedim. Petrol.* **58(1)**: 159-162.
- Cleveland, W.S., 1979, Robust locally weighted regression and smoothing scatterplots. *Journ. Amer. Statist. Assoc.* **74(368)**: 829-836.
- Cundall, P.A., and O.D.L. Strack, 1979, A discrete numerical model for granular assemblies. *Geotechnique* **29(1)**: 47-65.
- DePloey, J., 1980, Some field measurements and experimental data on wind blown sands. *IN M. de Boodt and D. Gabrieli, eds., Assessment of Erosion*, Wiley, Chichester, p. 541-552.
- Deresiewicz, H., 1958, Mechanics of granular material. *Advd. Appl. Mech.* **5**: 233-306.
- Dietrich, W.E., 1982, *Flow, Boundary Shear Stress, and Sediment Transport in a River Meander*. Ph.D. dissert., Univ. Washington, Seattle, Wash., 261 pp..
- Dietrich, W.E., Kirchner, J.W., Ikeda, H., and F. Iseya, 1989, Sediment supply and the development of the coarse surface layer in gravel-bedded rivers. *Nature* **340**: 215-217.
- Draga, M., 1983, Eolian activity as a consequence of beach nourishment - Observations at Westerland (Sylt), German North Sea coast. *Z. Geomorph. Suppl. Band* **45**: 303-319.
- Drake, T.G., and R.L. Shreve, 1987, *Bed-load Transport, Duck Creek, Wyoming*. 13 min., 16mm sound and color film, Office of Instructional Dev., Univ. California, Los Angeles.
- Drake, T.G., Shreve, R.L., Dietrich, W.E., Whiting, P.J., and L.B. Leopold, 1988, Bedload transport of fine gravel observed by motion-picture photography. *J. Fluid Mech.* **192**: 193-217.
- Eagleson, P.S., and R.G. Dean, 1961, Wave-induced motion of bottom sediment particles. *Trans. Amer. Soc. Civ. Eng.* **126(1)**: 1162-1186.
- El-Baz, F., and M.H.A. Hassan, 1986, editors, *Physics of Desertification*. Martinus Nijhoff, Dordrecht.

- Ellwood, J.M., Evans, P.D., and I.G. Wilson, 1975, Small scale aeolian bedforms. *Journ. Sedim. Petrol.* **45**: 554-561.
- Fieller, N.R.J., Gilbertson, D.D., and W. Olbricht, 1984, A new method for the environmental analysis of particle size data from shoreline environments. *Nature* **311**: 648-651.
- Flenley, E.C., 1985, Use of mixture distributions in the modelling of sand particle sizes. *IN* Barn-dorff-Nielsen, O.E., Møller, J.T., Rømer Rasmussen, K., and B.B. Willetts, eds., *Proceedings of the International Workshop on the Physics of Blown Sand*. Dept. of Theoretical Statistics, Inst. of Mathematics, Univ. of Aarhus, Memoirs No. 8, Vol. 3, p. 633-648.
- Flenley, E.C., Fieller, N.R.J., and D.D. Gilbertson, 1987, The statistical analysis of 'mixed' grain size distributions from aeolian sands in the Libyan Pre-Desert using log skew Laplace models. *IN* Frostick, L., and I. Reid, eds., *Desert Sediments: Ancient and Modern*, Geol. Soc. Spec. Publ. No. 35, Blackwell Scientific Publ. Inc., Palo Alto, Calif., p. 271-280.
- Folk, R.L., 1971, Longitudinal dunes of the northwestern edge of the Simpson Desert, Northern Territory, Australia: 1. Geomorphology and grain size relationships. *Sedimentology* **16**: 5-54.
- Forrest, S.B., and P.K. Haff, 1992, Mechanics of wind ripple stratigraphy. *Science* **255**: 1240-1243.
- Freeze, R.A., and J.A. Cherry, 1979, *Groundwater*. Prentice-Hall, Inc., Englewood Cliffs, NJ, 604 pp.
- Frostick, L.E., and I. Reid, 1987, editors, *Desert Sediments: Ancient and Modern*. Geol. Society Spec. Publ. No. 35, Blackwell Scientific Publ. Inc., Palo Alto, Calif., 401 pp.
- Fryberger, S.G., Ahlbrandt, T.S., and S. Andrews, 1979, Origin, sedimentary features, and significance of low-angle eolian "sand sheet" deposits, Great Sand Dunes National Monument and vicinity, Colorado. *Journ. Sedim. Petrol.* **49**(3): 733-746.
- Fryberger, S.G., and C.J. Schenk, 1981, Wind sedimentation tunnel experiments on the origins of aeolian strata. *Sedimentology* **28**: 805-822.
- Fryberger, S.G., and C.J. Schenk, 1988, Pin stripe lamination: A distinctive feature of modern and ancient eolian sediments. *Sedim. Geology* **55**: 1-15.
- Fryberger, S.G., Krystinik, L.F., and C.J. Schenk, 1990, *Modern and Ancient Eolian Deposits: Petroleum Exploration and Production*. Rocky Mtn. Section Soc. for Sedim. Geology (SEPM), Denver, Colo., 248 pp.
- Gerety, K.M., 1984, *A Wind-Tunnel Study of the Saltation of Heterogeneous (Size, Density) Sands*. Ph.D. dissert., Penn. State Univ.
- Gerety, K.M., 1985, Problems with determination of  $u_{*c}$  from wind-velocity profiles measured in

- experiments with saltation. *IN* Barndorff-Nielsen, O.E., Møller, J.T., Rømer Rasmussen, K., and B.B. Willetts, eds., *Proceedings of the International Workshop on the Physics of Blown Sand*. Dept. of Theoretical Statistics, Inst. of Mathematics, Univ. of Aarhus, Memoirs No. 8, Vol. 2, p. 271-300.
- Gerety, K.M., and R. Slingerland, 1983, Nature of the saltating population in wind tunnel experiments with heterogeneous size-density sands. *IN* Brookfield, M.E., and T.S. Ahlbrandt, eds., *Eolian Sediments and Processes*. Elsevier Press, Amsterdam, Netherlands, p. 115-131.
- Gilbert, G.K., 1914, The transporting of debris by running water. *U.S. Geol. Surv. Prof. Paper 86*, chap. IX.
- Goldsmith, W., 1960, *Impact: The Theory and Physical Behavior of Colliding Solids*. Edward Arnold, Ltd., London.
- Grant, W.D., and O.S. Madsen, 1982, Movable bed roughness in unsteady oscillatory flow. *Journ. Geophys. Res.* **87(C1)**: 469-481.
- Greeley, R., and J.D. Iversen, 1985, *Wind as a Geological Process* (on Earth, Mars, Venus and Titan). Cambridge Univ. Press, Cambridge, Mass., 333 pp.
- Greeley, R., White, B.R., Pollack, J.B., Iversen, J.D., and R.N. Leach, 1977, Dust storms on Mars: Considerations and simulations. NASA Tech. Memo., 78423.
- Greeley, R., Gaddis, L., Lancaster, N., Dobrovolskis, A., Iversen, J., Rasmussen, K., Saunders, S., van Zyl, J., Wall, S., Zebker, H., and B. White, 1991, Assessment of aerodynamic roughness via airborne radar observations. *Acta Mech. Suppl.* **2**: 77-88.
- Haff, P.K., and R.S. Anderson, 1993, Grain scale simulations of loose sedimentary beds: The example of grain-bed impacts in aeolian saltation. *Sedimentology* **40**: 175-198.
- Hesp, P.A., and S.G. Fryberger, 1988, editors, *Special Issue on Eolian Sediments*. *Sediment. Geol.* **55**.
- Horikawa, K.S., and H.W. Shen, 1960, *Sand Movement by Wind Action*. U.S. Army, Corps Eng., Beach Erosion Board, Tech. Memo. 119.
- Hsu, S.A., 1973, Computing aeolian sand transport from shear velocity measurements. *J. Geol.* **81**: 739-743.
- Hsu, S.A., 1974, Computing eolian sand transport from routine weather data. *Proc. 14th. Coastal Eng. Conf.*, Copenhagen, vol. II, p. 1619-1626.
- Hsu, S.A., and B.W. Blanchard, 1991, Shear velocity and eolian sand transport on a barrier island. *IN Coastal Sediments '91*, Amer. Soc. Civ. Eng., p. 220-234.
- Hunt, J.C.R., and P. Nalpanis, 1985, Saltating and suspended particles over flat and sloping sur-



- faces: I. Modelling concepts. *IN* Barndorff-Nielsen, O.E., Møller, J.T., Rømer Rasmussen, K., and B.B. Willetts, eds., *Proceedings of the International Workshop on the Physics of Blown Sand*. Dept. of Theoretical Statistics, Inst. of Mathematics, Univ. of Aarhus, Memoirs No. 8, Vol. 1, p. 9-36.
- Hunter, R.E., 1977, Basic types of stratification in small eolian dunes. *Sedimentology* **24**: 361-387.
- Ikeda, S., 1982a, Incipient motion of sand particles on side slopes. *Journ. Hydraul. Div., Proc. Amer. Soc. Civil Eng.* **108(HY1)**: 95-113.
- Ikeda, S., 1982b, Lateral bed load transport on side slopes. *Journ. Hydraul. Div., Proc. Amer. Soc. Civil Eng.* **108(HY11)**: 1369-1373.
- Iseya, F., and H. Ikeda, 1987, Pulsations in bedload transport rates induced by a longitudinal sediment sorting: A flume study using sand and gravel mixtures. *Geografiska Annaler* **69(A)**: 15-27.
- Iversen, J.D., Wang, W.P., Rasmussen, K.R., Mikkelsen, H.E., and R.N. Leach, 1991, Roughness element effect on local and universal saltation transport. *Acta Mech. Suppl.* **2**: 65-75.
- Jensen, J.L., and M. Sørensen, 1982, On the mathematical modeling of aeolian saltation. *Euro-mech 156: Mechanics of Sediment Transport*, Istanbul, July 1982, p. 65-72.
- Jensen, J.L., and M.Sørensen, 1986, Estimation of some aeolian saltation transport parameters: A re-analysis of Williams' data. *Sedimentology* **33**: 547-558.
- Jiang, Z., and P.K. Haff, 1993, Multiparticle simulation methods applied to the micromechanics of bed load transport. *Water Resour. Res.* **29(2)**: 399-412.
- Johnson, R.B., 1967, *The Great Sand Dunes of Southern Colorado*. U.S. Geol. Surv. Prof. Pap. No. 575-C, p. 177-183.
- Kawamura, R., 1964, *Study of Sand Movement by Wind*. Hydraulic Eng. Lab. Tech. Rep. HEL-2-8, Univ. California, Berkeley, Calif., p. 99-108.
- Kennedy, W.J., Jr. and J.E. Gentle, 1980, *Statistical Computing*. Marcel Dekker Inc., NY., 591 pp. Chap. 6, "Random Numbers", p. 133-264.
- Kirchner, J.W., Dietrich, W.E., Iseya, F., and H. Ikeda, 1990, The variability of critical shear stress, friction angle, and grain protrusion in water-worked sediments. *Sedimentology* **37**: 647-672.
- Kocurek, G., 1988, editor, *Late Paleozoic and Mesozoic Eolian Deposits of the Western Interior of the United States*. Spec. Issue, *Sediment. Geol.* **56**.
- Kocurek, G., and R.H. Dott, Jr., 1981, Distinctions and uses of stratification types in the interpretation of eolian sand. *Journ. Sedim. Petrol.* **51**: 579-595.

- Kolbuszewski, J., 1953, Note on factors governing the porosity of wind deposited sands. *Geol. Mag.* **90**: 48-56.
- Kolbuszewski, J., Nadolski, L., and Z. Dydacki, 1950, Porosity of wind deposited sands. *Geol. Mag.* **87**: 433-435.
- Lancaster, N., Greeley, R., and K.R. Rasmussen, 1991, Interaction between unvegetated desert surfaces and the atmospheric boundary layer: A preliminary assessment. *Acta Mech. Suppl.* **2**: 89-102.
- Leopold, L.B., Wolman, M.G., and J.P. Miller, 1964, *Fluvial Processes in Geomorphology*. W.H. Freeman and Co., San Francisco, 522 pp.
- Li, Z., and P.D. Komar, 1986, Laboratory measurements of pivoting angles for applications to selective entrainment of gravel in a current. *Sedimentology* **33**: 413-423.
- Lindholm, R.C., 1987, *A Practical Approach to Sedimentology*. Allen & Unwin Inc., Winchester, Mass., 276 pp.
- Lisle, T.E., Ikeda, H., and F. Iseya, 1991, Formation of stationary alternate bars in a steep channel with mixed-size sediment: A flume experiment. *Earth Surf. Proc. Landforms* **16**: 463-469.
- Lisle, T.E., Iseya, F., and H. Ikeda, 1993, Response of a channel with alternate bars to a decrease in supply of mixed-size bed load: A flume experiment. *Water Resour. Res.* **29(11)**: 3623-3629.
- Ludwick, J.C., 1956, A volumeter for measuring porosity of incoherent sands. *Journ. Sedim. Petrol.* **26(3)**: 276-283.
- Lun, C.K.K., and S.B. Savage, 1986, The effects of an impact velocity dependent coefficient of restitution on stresses developed by sheared granular materials. *Acta Mech.* **63**: 15-44.
- Mazzullo, J., Sims, D., and D. Cunningham, 1986, The effects of eolian sorting and abrasion upon the shapes of fine quartz sand grains. *Journ. Sedim. Petrol.* **56(1)**: 45-56.
- McEwan, I.K., 1993, Bagnold's kink: A physical feature of a wind velocity profile modified by blown sand? *Earth Surf. Proc. Landforms* **18**: 145-156.
- McEwan, I.K., and B.B. Willetts, 1991, Numerical model of the saltation cloud. *Acta Mech. Suppl.* **1**: 53-66.
- McEwan, I.K., Willetts, B.B., and M.A. Rice, 1992, The grain/bed collision in sand transport by wind. *Sedimentology* **39**: 971-981.
- Middleton, G.V., and J.B. Southard, 1984, *Mechanics of Sediment Movement*, 2nd. edition. Soc. Econ. Paleontol. Mineral. Short Course No. 3 Lect. Notes, Providence, RI., 401 pp.

- Miller, R.L. and R.J. Byrne, 1966, The angle of repose for a single grain on a fixed rough bed. *Sedimentology* **6**: 303-314.
- Mitha, S., Tran, M.Q., Werner, B.T., and P.K. Haff, 1986, The grain-bed impact process in aeolian saltation. *Acta Mech.* **63**: 267-278.
- Mulligan, K.R., 1988, Velocity profiles measured on the windward slope of a transverse dune. *Earth Surf. Proc. Landforms* **13**: 573-582.
- Nalpanis, P., 1985, Saltating and suspended particles over flat and sloping beds: II. Experiments and numerical simulations. *IN* Bårdorff-Nielsen, O.E., Møller, J.T., Rømer Rasmussen, K., and B.B. Willetts, eds., *Proceedings of the International Workshop on the Physics of Blown Sand*. Dept. of Theoretical Statistics, Inst. of Mathematics, Univ. of Aarhus, Memoirs No. 8, Vol. 1, p. 38-66.
- Nickling, W.G., 1986, editor, *Aeolian Geomorphology*. Proc. 17th. Annual Binghamton Geomorph. Symp., Allen & Unwin Inc., Winchester, Mass., 311 pp.
- Nickling, W.G., 1988, The initiation of particle movement by wind. *Sedimentology* **35**: 499-511.
- Nikuradse, J., 1933, Laws of flow in rough pipes. *VDI-Forschungsheft 361* (Engl. translation in NACA Technical Memo. No. 1292, Natl. Advisory Comm. Aeronautics, Wash. D.C., 1950, 62pp).
- Nordstrom, K.F., Psuty, N.P., and R.W.G. Carter, 1990, editors, *Coastal Dunes: Form and Process*. Wiley, Chichester.
- Owen, P.R., 1964, Saltation of uniform grains in air. *Journ. Fluid Mech.* **20**: 225-242.
- Pomeroy, J.W., and D.M. Gray, 1990, Saltation of snow. *Water Resour. Res.* **26**(7): 1583-1594.
- Pryor, W.A., 1973, Permeability and porosity variations in some Holocene sand bodies. *Amer. Assoc. Petrol. Geol. Bull.* **57**: 162-189.
- Pye, K., and H. Tsoar, 1990, *Aeolian Sand and Sand Dunes*. Unwin Hyman Inc., Cambridge, Mass., 396 pp.
- Rasmussen, K.R., and H.E. Mikkelsen, 1991, Wind tunnel observations of aeolian transport rates. *Acta Mech. Suppl.* **1**: 135-144.
- Raupach, M.R., 1991, Interaction between saltating particles and the airflow. *Acta Mech. Suppl.* **1**: 83-96.
- Reichardt, H., 1951, Vollständige darstellung der turbulenten geschwindigkeitsverteilung in glatten leitungen. *Zeitschrift für Angewandte Mathematisch Mechanik*, band 31, no. 7, p. 208-219.
- Reizes, J.A., 1978, Numerical study of continuous saltation. *Journ. Hydraul. Div., Amer. Soc.*

Civil Eng. **104**(HY9): 1305-1321.

- Rubin, D.M., and R.E. Hunter, 1987, Field guide to sedimentary structures in the Navajo and Entrada Sandstones in southern Utah and northern Arizona. *IN* G.H. Davis and E.M. VandenDolder, eds., *Geologic Diversity of Arizona and its Margins: Excursions to Choice Areas*, Geol. Soc. America Field-Trip Guidebook, Ariz. Bur. Geol. and Min. Tech., Geol. Surv. Branch, Spec. Paper 5, p. 126-140.
- Rumpel, D.A., 1985, Successive aeolian saltation: Studies of idealized collisions. *Sedimentology* **32**: 267-275.
- Sarre, R.D., 1987, Aeolian sand transport. *Prog. Phys. Geogr.* **111**: 157-182.
- Sarre, R.D., 1988, Evaluation of aeolian sand transport equations using intertidal zone measurements, Saunton Sands, England. *Sedimentology* **35**: 671-679.
- Schenk, C.J., 1983, Textural and structural characteristics of some experimentally formed eolian strata. *IN* Brookfield, M.E., and T.S. Ahlbrandt, eds., *Eolian Sediments and Processes*. Elsevier Press, Amsterdam, Netherlands, p. 41-50.
- Schlichting, H., 1979, *Boundary-Layer Theory*, 7th. edition. McGraw-Hill Book Co., NY., 817pp.
- Serrano, A.A., and J.M. Rodriguez-Ortiz, 1973, A contribution to the mechanics of heterogeneous granular media. *Proc. Symp. Plasticity and Soil Mech.*, Cambridge, Mass.
- Sharp, R.P., 1963, Wind ripples. *Journ. Geol.* **71**: 617-636.
- Shepard, F.P., and R. Young, 1961, Distinguishing between beach and dune sands. *Journ. Sedim. Petrol.* **31**: 196-214.
- Sherman, D.J., 1992, An equilibrium relationship for shear velocity and apparent roughness length in aeolian saltation. *Geomorphology* **5**: 419-431.
- Siever, R., 1988, *Sand*. Scientific Amer. Library, W.H. Freeman and Co., NY., 237 pp.
- Smith, J.D., 1977, Modeling of sediment transport on continental shelves. *IN* E.D. Goldberg, ed., *The Sea*, vol. 6, John Wiley, NY.
- Smith, J.D., and S.R. McLean, 1977, Spatially averaged flow over a wavy surface. *Journ. Geophys. Res.* **82**: 1735-1746.
- Sørensen, M., 1985, Estimation of some aeolian saltation transport parameters from transport rate profiles. *IN* Barndorff-Nielsen, O.E., Møller, J.T., Rømer Rasmussen, K., and B.B. Willetts, eds., *Proceedings of the International Workshop on the Physics of Blown Sand*. Dept. of Theoretical Statistics, Inst. of Mathematics, Univ. of Aarhus, Memoirs No. 8, Vol. 1, p. 141-190.

- Sørensen, M., 1991, An analytic model of wind-blown sand transport. *Acta Mech. Suppl.* 1: 67-81.
- Symon, K.R., 1971, *Mechanics*, 3rd. edition. Addison-Wesley Publ. Co., Reading, Mass., 639 pp.
- Tatara, Y., and N. Moriwaki, 1982, Study on impact of equivalent two bodies (coefficients of restitution of spheres of brass, lead, glass, porcelain, and agate, and the material properties). *Jap. Soc. Mech. Eng. Bull.* 25: 631-637.
- Thomas, D.S.G., 1989, editor, *Arid Zone Geomorphology*. Belhaven Press, London.
- Tickell, F.G., and W.N. Hiatt, 1938, Effect of angularity of grain on porosity and permeability of unconsolidated sands. *Amer. Assoc. Petrol. Geol. Bull.* 22(9): 1272-1274.
- Tsuchiya, Y., 1969, On the mechanisms of saltation of a spherical sand particle in a turbulent stream. *Proc. 13th. Cong., Intern. Assoc. Hydraul. Res.* 2: 191-198.
- Tsuchiya, Y., 1970, Successive saltation of a sand grain by wind. *Proc. 12th. Coastal Eng. Conf., Amer. Soc. Civil Eng.*, vol. 1, p. 1417-1427.
- Tsuchiya, Y., and Y. Kawata, 1972, Characteristics of saltation of sand grains by wind. *Proc. 13th. Coastal Eng. Conf., Amer. Soc. Civil Eng.*, vol. 2, p. 1617-1625.
- Ungar, J., and P.K. Haff, 1987, Steady state saltation in air. *Sedimentology* 34: 289-299.
- Walker, D.J., 1981, *An Experimental Study of Wind Ripples*. Unpubl. M.S. thesis, Mass. Inst. Technology, Cambridge, Mass., 145 pp.
- Werner, B.T., 1987, *A Physical Model of Wind-Blown Sediment Transport*. Ph.D. dissert., Calif. Inst. Technology, Pasadena, Calif., 442 pp.
- Werner, B.T., 1990, A steady-state model of wind-blown sand transport. *J. Geol.* 98(1): 1-17.
- Werner, B.T., and P.K. Haff, 1986, A simulation study of the low energy ejecta resulting from single impacts in eolian saltation. *IN Arndt, R.E.A. et al., eds., Advancements in Aerodynamics, Fluid Mechanics, and Hydraulics*, Proc. Amer. Soc. Civil Eng., p. 337-345.
- Werner, B.T., and P.K. Haff, 1988, The impact process in aeolian saltation: Two-dimensional simulations. *Sedimentology* 35: 189-196.
- White, B.R., 1979, Soil transport by winds on Mars. *J. Geophys. Res.* 84: 4643-4651.
- White, B.R., 1982, Two-phase measurements of saltating turbulent boundary layer flow. *Intern. Journ. Multiphase Flow* 8(5): 459-473.
- White, B.R., 1985, The dynamics of particle motion in saltation. *IN Barndorff-Nielsen, O.E., Møller, J.T., Rømer Rasmussen, K., and B.B. Willetts, eds., Proceedings of the International*

- Workshop on the Physics of Blown Sand*. Dept. of Theoretical Statistics, Inst. of Mathematics, Univ. of Aarhus, Memoirs No. 8, Vol. 1, p. 101-140.
- White, B.R., and H. Mounla, 1991, An experimental study of Froude number effect on wind-tunnel saltation. *Acta Mech. Suppl.* 1: 145-157.
- White, B.R., and J.C. Schulz, 1977, Magnus effect in saltation. *Journ. Fluid Mech.* **81**: 497-512.
- Whiting, P.J., and W.E. Dietrich, 1990, Boundary shear stress and roughness over mobile alluvial beds. *Journ. Hydraul. Eng.* **116**: 1495-1511.
- Whiting, P.J., Dietrich, W.E., Leopold, L.B., Drake, T.G., and R.L. Shreve, 1988, Bedload sheets in heterogeneous sediment. *Geology* **16**(2): 105-108.
- Wiberg, P.L., 1987, *Mechanics of Bedload Sediment Transport*. Ph.D. dissert., Univ. Washington, Seattle, Wash., 133 pp.
- Wiberg, P.L. and D.M. Rubin, 1989, Bed roughness produced by saltating sediment. *Journ. Geophys. Res.* **94**(C4): 5011-5016.
- Wiberg, P.L., and J.D. Smith, 1985, A theoretical model for saltating grains in water. *J. Geophys. Res.* **90**(C4): 7341-7354.
- Wiberg, P.L., and J.D., Smith, 1987a, Initial motion of coarse sediment in streams of high gradient. *IN Erosion and Sedimentation in the Pacific Rim*, Proc. Corvallis Symp., Intern. Assoc. Hydrol. Sci., no. 165, p. 299-308.
- Wiberg, P.L., and J.D. Smith, 1987b, Calculations of the critical shear stress for motion of uniform and heterogeneous sediments. *Water Resour. Res.* **23**: 1471-1480.
- Wiberg, P.L., and J.D. Smith, 1989, Model for calculating bed load transport of sediment. *Journ. Hydraul. Eng.*, Amer. Soc. Civil Eng. **115**(1): 101-123.
- Wiberg, P.L., and J.D. Smith, 1991, Velocity distribution and bed roughness in high-gradient streams. *Water Resour. Res.* **27**(5): 825-838.
- Wilcock, P.R., 1987, *Bedload Transport of Mixed-Size Sediments*. Ph.D. dissert., Johns Hopkins Univ., Baltimore, MD., 205 pp.
- Wilcock, P.R., and J.B. Southard, 1989, Bed-load transport of mixed-size sediment: Fractional transport rates, bedforms, and the development of a coarse bed-surface layer. *Water Resour. Res.* **25**(7): 1629-1641.
- Willetts, B.B., 1983, Transport by the wind of granular material of different grain shapes and densities. *Sedimentology* **30**: 669-679.
- Willetts, B.B., and I.K. McEwan, 1993, Particle dislodgement from a flat sand bed by wind: A re-

- analysis of Willetts & Rice's data. *IN* Pye, K., and N. Lancaster, eds., *Aeolian Sediments: Ancient and Modern*, Spec. Publ. No. 16, Intern. Assoc. Sedim., p. 3-12.
- Willetts, B.B., and M.A. Rice, 1985a, Inter-saltation collisions. *IN* Barndorff-Nielsen, O.E., Møller, J.T., Rømer Rasmussen, K., and B.B. Willetts, eds., *Proceedings of the International Workshop on the Physics of Blown Sand*. Dept. of Theoretical Statistics, Inst. of Mathematics, Univ. of Aarhus, Memoirs No. 8, Vol. 1, p. 83-100.
- Willetts, B.B., and M.A. Rice, 1985b, Wind tunnel tracer experiments using dyed sand. *IN* Barndorff-Nielsen, O.E., Møller, J.T., Rømer Rasmussen, K., and B.B. Willetts, eds., *Proceedings of the International Workshop on the Physics of Blown Sand*. Dept. of Theoretical Statistics, Inst. of Mathematics, Univ. of Aarhus, Memoirs No. 8, Vol. 2, p. 225-242.
- Willetts, B.B., and M.A. Rice, 1986a, Collision in aeolian transport: The saltation/creep link. *IN* Nickling, W.G., ed., *Aeolian Geomorphology*, Allen & Unwin, London, p. 1-17.
- Willetts, B.B., and M.A. Rice, 1986b, Collisions in aeolian saltation. *Acta Mech.* **63**: 255-265.
- Willetts, B.B., and M.A. Rice, 1988, Particle dislodgement from a flat sand bed by wind. *Earth Surf. Proc. Landforms* **13**: 717-728.
- Willetts, B.B., and M.A. Rice, 1989, Collisions of quartz grains with a sand bed: The influence of incident angle. *Earth Surf. Proc. Landforms* **14**: 719-730.
- Willetts, B.B., McEwan, I.K., and M.A. Rice, 1991, Initiation of motion of quartz sand grains. *Acta Mech. Suppl.* **1**: 123-134.
- Williams, G.P., 1964, Some aspects of the eolian saltation load. *Sedimentology* **9**: 89-104.
- Williams, J.J., Butterfield, G.R., and D.G. Clark, 1990, Rates of aerodynamic entrainment in a developing boundary layer. *Sedimentology* **37**: 1039-1048.
- Yamasaka, M., and S. Ikeda, 1988, Lateral sediment transport of heterogeneous bed materials. *IN Proc. 6th. Congr. Asian and Pacific Div.*, Intern. Assoc. Hydraul. Res., Kyoto, Japan, p. 43-50.
- Zingg, A.W., 1953, Wind-tunnel studies of the movement of sedimentary material. *IN Proc. 5th. Hydraul. Conf.*, *Univ. Iowa Studies in Engineering Bull.* **24**: 111-135.

## BIOGRAPHICAL NOTE

**Name:** Susan Calder Shaw

**Born:** Port Angeles, Washington  
December 17, 1958

**Education:** Canyon del Oro High School, Oro Valley, Arizona  
A.B. with High Honors, Geology, Oberlin College, Oberlin, Ohio, 1981  
Title: Microbiota of the Late Proterozoic Ryssö Formation,  
Nordaustlandet, Svalbard  
M.S., Geology, University of Washington, Seattle, Washington, 1987  
Title: Mechanics of Bedload Transport by Wind  
Ph.D., Geology, University of Washington, Seattle, Washington, 1994  
Title: Bedload Transport of Mixed-Size Sediments by Wind